Signal Processing Methods for the Analysis of the Electrocardiogram

Zur Erlangung des akademischen Grades eines

DOKTOR-INGENIEURS

von der Fakultät für

Elektrotechnik und Informationstechnik

des Karlsruher Instituts für Technologie (KIT)

genehmigte

DISSERTATION

von

Gustavo Lenis, Dipl.-Ing.

geb. in Cali, Kolumbien

Tag der mündlichen Prüfung:	09.05.2017
Referent:	Prof. Dr. rer. nat. Olaf Dössel
Korreferent:	Prof. Dr. Pablo Laguna

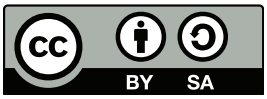

Zusammenfassung

Das Elektrokardiogramm (EKG) zeichnet die elektrische Aktivität des Herzens auf der Brustoberfläche auf. Dieses Signal kann einfach und kostengünstig aufgenommen werden und wird daher in einer Vielzahl von mobilen und stationären Anwendungen genutzt. Es ist über die letzten 100 Jahre zum Goldstandard bei der Diagnose vieler kardiologischer Krankheiten geworden. Herzerkrankungen bleiben ein relevantes Thema in unserer Gesellschaft, da sie zu 30 % aller Todesfälle weltweit führen. Allein die koronare Herzkrankheit ist die häufigste Todesursache überhaupt. Weiterhin sind 2 bis 3 % der Europäer von Herzrhythmusstörungen wie Vorhofflimmern und Vorhofflattern betroffen. Die damit verbundenen geschätzten Kosten in der Europäischen Union belaufen sich auf 26 Milliarden Euro pro Jahr. In allen diesen Fällen ist die Aufzeichnung des EKGs der erste unumgängliche Schritt für eine verlässliche Diagnose und erfolgreiche Therapie.

Im Rahmen dieser Dissertation wurden eine Reihe von Algorithmen zur Signalverarbeitung des EKG entwickelt, die automatisch die rhythmischen und morphologischen Eigenschaften aus dem EKG extrahieren und dadurch den diagnostischen Prozess und die Entscheidungsfindung des Arztes unterstützen. In einem ersten Projekt wurde das Phänomen der postextrasystolischen T-Wellen-Änderung (PEST) untersucht. Die aus der PEST extrahierten Biomarker haben wir als Prädiktoren für Herzversagen postuliert. Ein zweites Projekt handelte vom Entwurf eines akkuraten Algorithmus zur Detektion und Annotation der P-Welle im EKG. Als Referenz während der Entwicklung wurden intrakardial gemessene Signale verwendet. Eine dritte Untersuchg hatte das Ziel, das physiologische Phänomen der respiratorischen Sinusarrhythmie (RSA) besser zu verstehen. In diesem Projekt wurde ein Algorithmus zur Trennung der Herzratenvariabilität (HRV) in ihre atmungsabhängige und ihre atmungsunabhŋgige Komponente untersucht. Letzterer Anteil der HRV könnte neue Erkenntnisse über die Regulationsmechanismen des kardiovaskulären Systems liefern. In der vierten und letzten Studie wurde der Einfluss mentaler Belastung auf das EKG während der Autofahrt untersucht. Eine Vielzahl von Deskriptoren wurden gefunden, die eine gefährliche mentale Beanspruchung detektieren und somit den Fahrer vor einem möglichen Unfall schützen können.

Wir schließen aus diesen Untersuchungen, dass gut entwickelte Methoden der Signalverarbeitung des EKG das Potential haben, die Belastung der Patienten, die an Herzerkrankungen leiden, und die Anzahl der Verkehrsunfälle zu reduzieren.

Abstract

The electrocardiogram (ECG) captures the electrical activity of the heart that is projected onto the surface of the body. This signal can be recorded in a simple and cost effective manner making it available for a wide variety of mobile and stationary applications. Thus, over the last 100 years, the ECG has become the gold standard for the diagnosis of many cardiac afflictions. This is still relevant nowadays because cardiovascular diseases are a major topic of concern for our society accounting for almost 30 % of all causes of death worldwide. In particular, the ischemic heart disease is the single most common cause of death. Other cardiac arrhythmias, such as atrial fibrillation and atrial flutter, affect approximately 2 to 3 % of the population in the European Union leading to estimated costs of about 26 billion euros per year. In all these cases, the ECG is the mandatory first step leading to a reliable diagnosis and successful treatment.

In this thesis, we have developed a series of signal processing algorithms capable of automatically extracting rhythmical and morphological properties from the ECG with the aim of supporting the decision making in the diagnostic process. In our first research project, we investigated a phenomenon called postextrasystolic T wave change (PEST) and postulated that the biomarkers obtained from the ECG during PEST could be used to predict pump failure progression death (PFD). The second project dealt with the creation of an algorithm to accurately detect and delineate the P wave in the ECG using as ground truth the electrograms recorded inside the atria. Our third investigation aimed at a deeper understanding of a physiological phenomenon called respiratory sinus arrhythmia (RSA). Here, we developed an algorithm that separates the heart rate variability (HRV) into a respiration driven component and a respiration independent part. The respiration free HRV could deliver new insights about the regulation of the cardiovascular system. In the fourth and final study, we investigated the impact of mental workload on the ECG while driving a car and discovered a variety of features that can help to detect a dangerous state of mind and protect the driver from a car crash.

We conclude that well designed signal processing methods for the ECG have the potential of reducing the burden for the cardiac patient and the amount of accidents on the road.

Acknowledgments

This thesis is the result of my scientific work carried out from June 2012 to Mai 2017 at the Institute of Biomedical Engineering (IBT) at the Karlsruhe Institute of Technology (KIT). It has been made possible by the contribution of many people. I would like to thank them for their support.

I would like to start by thanking Prof. Olaf Dössel for giving me the opportunity to work in his research group, for the financial support he provided over all these years, and for his impressive enthusiasm and interest for my research topic. He would not only spend a significant amount of time supervising my projects but he would also give me the chance to develop my own ideas, manage my own scientific projects and grow as a professional research engineer. In addition, the amazing working atmosphere in the laboratory kept me motivated and full of joy every day at work.

I would also like to thank Prof. Pablo Laguna from the University of Zaragoza in Spain for the strong partnership we have built over the last four years. He has been also of great help serving as a referee for my thesis and being an indispensable member of the dissertation committee. I can only be grateful for the opportunity he gave me to work in his laboratory and to the support he and his research team gave during my time at the University of Zaragoza. We have achieved a fruitful scientific collaboration in which we have shared a significant amount of data and knowledge. I truly wish that he continues to cooperate with our group in the future.

Ich danke auch meinen Kollegen am IBT für die Unterstützung, die sie mir über die letzten 10 Jahre gegeben haben. Durch starke Kooperationen innerhalb des Instituts, haben wir verschiedene Projekte in der Wissenschaft und Lehre erfolgreich abgeschlossen. Besonders danke ich dem "Colega" Oesterlein für seine nette und sehr kompetente Arbeitsweise und für seinen tollen Einsatz in der LEN-Übung. "Colega Lion" danke ich für seinen außerordentlichen Einsatz für die Gruppe, die Einblicke in die Welt der Modellierung und Simulation und für den interessanten Austausch über Management und Leadership. Zum Schluss danke ich auch der Burn-Out Klicke (Thomas, Walther, Danila, Wachter, Baron und Schuler) für die vielen netten Abende, die wir zusammen verbracht haben. Mit euch hat die Arbeit sehr viel Spaß gemacht. Sehr hilfsbereit waren auch die Mitarbeiter des Instituts Frau Günter, Ramona und Herr Schroll, die mich häufig bei verschiedenen Schwierigkeiten gerettet haben.

Für ihren außergewöhnlichen Einsatz danke ich auch allen Studierenden, die mich bei meinen Forschungsprojekten unterstützt haben. Am längsten habe ich das Vergnügen gehabt, mit Pilia, Menges, Reichensperger, Kircher und Ritter zu arbeiten. Durch viele

wissenschaftliche Diskussionen, tolle Teamarbeit und konstruktives Feedback haben wir nicht nur unsere Ziele erreichen können sondern auch eine Menge Spass gehabt. Durch die Zusammenarbeit mit meinen Studierenden habe ich meine Leidenschaft für die Arbeit als Teamleiter entdeckt.

Por último me queda agradecerle a los parceros del concejo de la mensa y en especial a Jaco, Dano, Paula, Rooney y Jimmy, por todo el tiempo libre que pasamos juntos, por las interesantes conversaciones a la hora de la comida y por la lora tan seria que dimos todos estos años en Karlsruhe. Sin ellos esta experiencia no hubiera sido tan divertida. A mis papás les agradezco el apoyo moral constante y su motivación ejemplar de seguir camellando en lo que más les gusta. A mi queridísima Don Lexi le agradezco su compañía, su apoyo incondicional y las tan enriquecedoras discusiones que hemos tenido en los mas de 20 años viviendo juntos. Al fin y al cabo es ella quien ha hecho de mi una mejor persona.

Contents

Abbreviations

AEB	atrial ectopic beat
AFib	atrial fibrillation
AFlu	atrial flutter
ANS	autonomic nervous system
AP	action potential
AR	autoregressive
ARMA	autoregressive moving average
AUC	area under the curve
AWGN	additive white Gaussian noise
AWLN	additive white Laplacian noise
BIC	Bayesian information criterion
CD	cardiac death
CHF	chronic heart failure
DFT	discrete Fourier transform
ECG	electrocardiogram
ECGI	electrocardiographic imaging
EGM	electrogram
FFT	fast Fourier transform
FIR	finite impulse response
HRT	heart rate turbulence
HRV	heart rate variability
LCT	lane change task
LTI	linear time invariant
MA	moving average
MCO	morphological change onset
MCS	morphological change slope
NASA-TLX	NASA task load index
NLEO	non-linear energy operator
NPV	negative predictive value
PCA	principal component analysis
PEST	postextrasystolic T wave change
PFD	pump failure progression death
πCA	periodic component analysis

PPV	positive predictive value
PSD	power spectral density
ROC	receiver operating characteristic
RSA	respiratory sinus arrhythmia
SCD	sudden cardiac death
SEN	sensitivity
SNR	signal-to-noise ratio
SPE	specificity
SVM	support-vector-machine
SWT	stationary wavelet transform
TM	total mortality
TO	turbulence onset
TS	turbulence slope
VEB	ventricular ectopic beat
VEBs	ventricular ectopic beats
VFF	ventricular far field
WPA	wavelet packet analysis

CHAPTER 1

Introduction

1.1 Motivation

Electrocardiography is the medical procedure of recording the electrical activity of the heart on the chest of a subject [1]. It is characterized by a simple and inexpensive recording device making it available in many mobile and stationary scenarios. Over the last 100 years, the electrocardiogram (ECG) has become not only the gold standard for the initial evaluation of the health state of the heart but also a powerful diagnostic tool in other areas of medicine and life sciences [2].

Cardiovascular diseases have become a topic of major concern for our society accounting for almost 30 % of all causes of death worldwide [3]. In particular, the ischemic heart disease is the single most common cause of death accounting for 7.6 million diseases only in 2012 worldwide [4]. Furthermore, cardiovascular diseases are the most expensive ones and accounted for 253.9 billion dollars or almost 17 % of the total expenditures from the National Health Expenditure Accounts in the United States in 2005. Only the three most relevant heart afflictions, that include coronary heart disease, congestive heart failure and dysrhythmias, accounted for a total expenditure of 123.1 billion dollars in that same year [5]. In addition, four heart-related medical operations were among the top 20 procedures having the highest aggregate cost in 2011. The heart valve procedures and the coronary artery bypass were the two most costly medical operations per hospital stay with mean costs of 53.400 dollars [6]. For many of these pathologies, the ECG is the mandatory first step in the diagnostic procedure.

From the ECG, the so-called biomarkers can also be computed. These are mainly rhythmical and morphological features of the signal that have been found to be related to particular diseases and can be used to assess the risk of worsening of that pathology. Other biomarkers can be used to stratify the risk of dying of a cardiac related complication in patients with a history of infarction or chronic heart failure [7, 8]. Many markers arriving, for example, from the heart rate variability (HRV) [9], the heart rate turbulence (HRT) [10], or the dispersion of repolarization [11] have been proven to be strong predictors. By using them,

the physician can make a well-founded decision about the best treatment for the patient. In this thesis, we investigated a phenomenon called postextrasystolic T wave change (PEST) and hypothesized that it could be used to predict pump failure progression death (PFD) and identify high risk patients suffering from chronic heart failure (CHF).

Among the serious cardiac arrhythmias, the most common one is atrial fibrillation (AFib) [12]. It affects approximately 2 % to 3 % of the population in the European Union and USA. The prevalence of this disease increases with age and impacts 4 % of the population between 60 and 70 years old and up to 14 % of the octogenarians [13]. Estimated costs for the European Union are about 26 billion euros per year [14]. Again, the ECG is the initial step to diagnose this pathology. However, in the early stages of AFib, the arrhythmia appears and vanishes after a short period of time leaving no rhythmical changes in the ECG. This fact makes paroxismal AFib hard to diagnose. To address this problem, special biomarkers based on the P wave in the ECG have been created and have been found to be related to AFib [15]. For that purpose, a very precise detection and delineation of the P wave in the ECG must be performed automatically. Thus, a part of this thesis was devoted to the accurate detection and delineation of the P wave. For that purpose, we proposed a new method based on the stationary wavelet transform (SWT) and used intracardiac signals as reference in the development of the algorithm.

The regulation of the cardiovascular system is another source of interest for physicians. The controlled interdependence between respiration, blood pressure and heart rate is carried out by the autonomic nervous system (ANS). In order to study the ANS, the previously mentioned HRV and its relation to the complete cardiovascular system is analyzed. A curious phenomenon closely related to HRV and its regulation is called respiratory sinus arrhythmia (RSA) [16]. In the healthy RSA, the heart rate and the respiration tend to synchronize in order to optimize gas transfer in the lungs. When HRV is analysed in the presence of RSA, the HRV parameters capture an RSA dependet component. Motivated by this, another part of this thesis was devoted to the separation of the effect of respiration on the HRV with the aim of achieving a discriminated HRV analysis and possible new insights about the regulation of the cardiovascular system [17].

The ECG is also frequently used in other fields of research such as psychology and ergonomics. This signal is in fact the most common physiological measure utilized to monitor mental workload because it allows a direct, cost-effective and continuous measurement [18]. This procedure relies on the idea that alterations in the ECG appear as a consequence of activity of the central nervous system [19]. Hence, the response of the ANS to the external stressor affects the regulation of the heart and becomes observable in the HRV [20]. One of the applications that has gained attention in the last years is the monitoring of mental workload while driving a car. Since stress is one of the major causes of traffic accidents for professional drivers, it is of interest to detect such a dangerous psychological state and protect the driver from a potential car crash [21]. In this thesis, we investigated the impact of mental workload on the ECG while driving a car and discovered a variety of features that are closely related to an increased mental workload.

It is therefore of highest priority to obtain as much reliable information as possible from the ECG and to support the further decision making of the cardiologist or psychologist using it. Thus, well designed signal processing methods for the ECG have the potential of reducing the burden for the cardiac patient and the amount accidents on the road.

1.2 Aim of the Thesis

In this thesis, four major research projects are presented, each of them with the goal of creating new signal processing methods that improve the amount and quality of information gained from the ECG. The four research projects address the following topics:

- The aim of the first project is to learn more about the dynamical change of the postextrasystolic T wave and to introduce new parameters to quantify it. On the clinical side, the goal is also to investigate how this phenomenon manifests on healthy subjects and to evaluate if it can be used to predict cardiac death (CD) in patients with chronic heart failure.
- The second project has the goal of creating a new P wave delineation technique that is developed using intracardiac measurements as golden truth to achieve a higher accuracy when detecting the beginning of the P wave.
- The aim of the third project is to develop a method to quantify coupling between respiration and HRV and to use linear filtering to separate the respiration dependent part of HRV. On the clinical side, the goal is also to analyze how coupling varies with breathing rate and how the independent HRV parameters relate to the coupled ones.
- The fourth project has the goal of developing a large variety of rhythmical and morphological ECG features and to examine their suitability for the measurement of the mental workload of a driver.

1.3 Structure of the Thesis

The thesis is dived into the following six big portions and each of them is divided into related chapters:

Part 1: The first part presents the medical and mathematical fundamentals relevant for this thesis.

- Chapter 2 gives an introduction to the anatomy and physiology of the heart. Special attention is put to the origination of the ECG and its constitutive waves. The autonomic regulation of the heart is then described and the concepts of HRV and RSA are explained. The chapter ends with a brief introduction to the pathology called chronic heart failure.
- Chapter 3 outlines the theory behind the mathematical and signal processing fundamentals relevant for this thesis. It begins with an introduction to signals

and systems. It then explains the Fourier and wavelet transforms and continues with the principal component analysis. It concludes with the introduction of two similarity measures and some general concepts on the analysis of time series.

Part 2: The second part of the thesis introduces the concept of PEST and presents three different studies in this field.

- Chapter 4 outlines the study analyzing the morphological change of the postextrasystolic T waves in a cohort of 14 patients suffering from congestive heart failure. Special attention is put to the maximal amplitude of the T wave. The two parameters used to characterize PEST are introduced in this chapter.
- Chapter 5 studies the manifestation of PEST in patients with structural healthy ventricles. A quantification algorithm based on a new similarity measure is introduced in this chapter.
- Chapter 6 evaluates the hypothesis of PEST being capable of predicting CD in patients with chronic heart failure. A larger cohort of over 500 patients was used for the statistical analysis.

Part 3: The third part of the thesis deals with the delineation of the P wave in the surface ECG.

- Chapter 8 presents the method created to detect the beginning of the P wave. For the development of the method, intracardiac signals were used as reference and the SWT was applied for the detection and delineation of the P wave.

Part 4: The fourth part of the thesis deals with the coupling between respiration and heart rate.

- Chapter 8 presents the method created to measure coupling between respiration and heart rate. It also outlines the results for the decoupling procedure and discusses the respiration independent HRV parameters.

Part 5: The fifth part of the thesis deals with the analysis of driver's mental workload and its impact on the ECG.

- Chapter 9 presents the results of the experiment conducted to investigate what ECG features are related to mental workload while driving a car simulator.

Part 6: The sixth part of the thesis centers on its closing remarks.

- Chapter 10 summarizes the thesis giving the most important conclusions of the four research projects.
- Chapter 11 introduces some open questions interesting for future research projects.
- A list of publications and supervised student projects is given at the end of the thesis.

PART I

FUNDAMENTALS

CHAPTER 2

Medical Fundamentals

In this chapter, the foundations of the most relevant medical topics for this thesis are presented. The goal is to give the reader an introduction to the field of cardiology so that the signal processing methods and clinical studies presented later can be better understood. The chapter begins with a description of the anatomy and physiology of the human heart. Afterwards, the basic concepts of cardiac electrophysiology and the electrocardiogram are explained. Further, the autonomic regulation of the heart and heart rate variability (HRV) are introduced and special attention is put on respiratory sinus arrhythmia (RSA). The chapter then finishes with a short description of the cardiac phenomenon called heart rate turbulence (HRT). The interested reader is invited to refer to the cited literature for a deeper description.

2.1 Anatomy and Physiology of the Human Heart

The heart is one of the most important organs because it is responsable for pumping blood through the vessels and maintaining adequate circulation throughout the body [22]. It is a hollow muscle with four chambers and it is located between the lungs in the center of the thorax in an area called the mediastinum. It is surrounded by a fibrous sac called pericardium and attached in its superior part to the great vessels. In terms of measure, the heart of an adult is around 9 cm wide at the base, 6 cm from anterior to posterior part at its broadest point, and 13 cm from base to apex. The weight of the heart is about 300 g accounting for approximately 4.5 % of the human body. In terms of physiology, the heart is actually constituted by two pumps. Its left side collects the oxygenated blood coming from the lungs and pumps it through the systemic circuit delivering nutrients and oxygen to the other organs of the body. The right side of the heart collects the deoxygenated blood from the body and pumps it through the lungs to reoxygenate it. The pumping function of the heart is characterized by a rhythmic contraction leading to a circulation of 8000 l of blood per day. In resting conditions, The blood pressure in the systemic circuit is maintained between 80 mmHg and 120 mmHg, while in the pulmonary circuit it lies around 30 mmHg. To ensure unidirectional blood flow, the heart is equipped with 4 valves. The atria and ventricles on both sides of the heart are

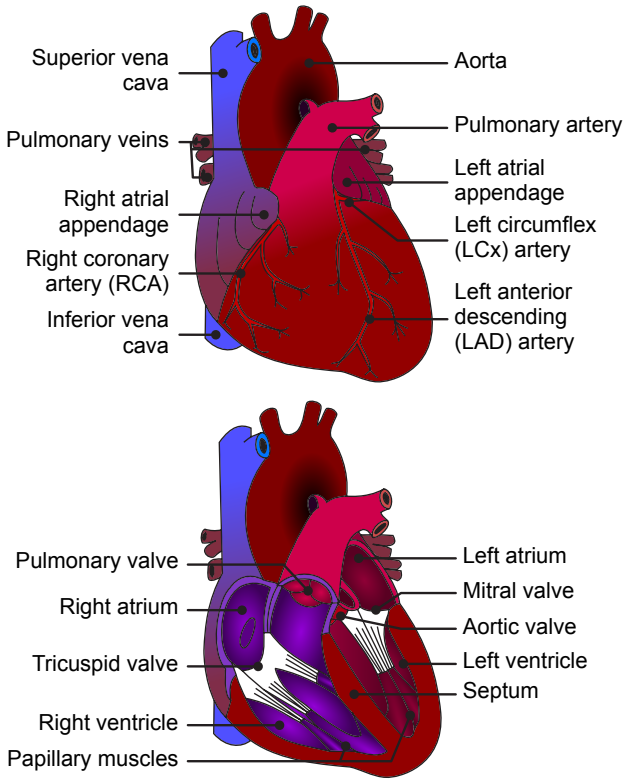

Figure 2.1: Anatomy of the human heart. In the upper part of the figure, the great vessels and coronary arteries are presented while the lower part displays the interior of the organ. This figure was reprinted from publication [24] with permission from the author.

separated each by a valve. The outflow tract of each ventricle is also sealed by a valve [23]. Figure 2.1 gives an overview of the anatomy of the heart.

2.2 Cardiac Electrophysiology

Every cell in the body, and the cardiac myocyte is not the exception, is enclosed by a phospholipid bilayer called cell membrane that separates the outside environment from the interior of the cell. In contrast to the majority of the cells, the cardiac myocyte is electrically excitable. This is possible because the cell membrane is equipped with selectively permeable ion channels, pumps and exchangers allowing ionic currents to flow between the intra and extracellular space. The transport of different ions through the cell membrane leads to different ionic concentrations on each side of the membrane and to a potential difference across it. This is the so-called transmembrane voltage. Under resting conditions, this potential difference is approximately equal to -80 mV for cardiac myocytes. If an external

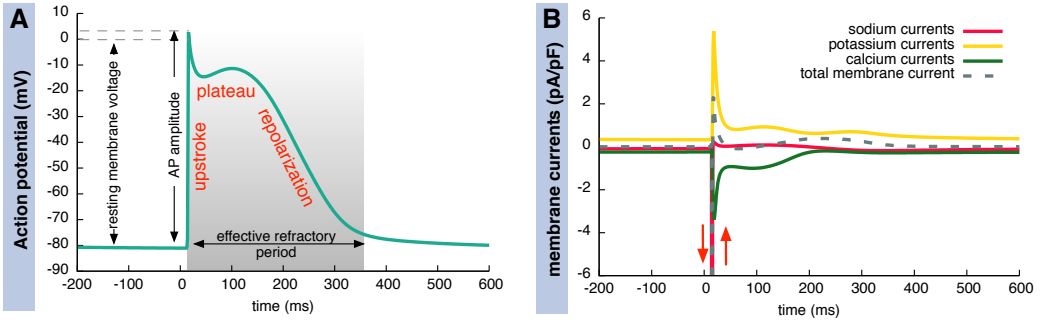

Figure 2.2: The left figure shows the course of the transmembrane voltage during the AP of a cardiac myocyte and its different phases. The right figure displays the most important ionic currents through the membrane. The sodium current reaches an amplitude of ≈−70 pA/pF. The calcium exchange with the sarcoplasmic reticulum is not considered. The Courtemanche et al. model optimized for atrial myocytes was used to compute the courses [25]. This figure was reprinted from publication [26] with permission from the author and was originally inspired by [27].

stimulus drives the transmembrane voltage above a certain threshold between -50 and -60 mV, an action potential (AP) is triggered.

The AP can be divided into three major parts: depolarization, plateau phase and repolarization. The depolarization phase begins with a fast sodium inward current leading to a rapid upstroke in the transmembrane voltage and an overshooting to positive values. Afterwards, the sodium channels deactivate and remain in this state until the AP has reached again a lower threshold voltage. This interval, in which no further AP can be triggered, is called effective refractory period. After the sodium channels have closed, the potassium channels open and cause an outward potassium current leading to a slight repolarization of the cell membrane. This is followed by the activation of the calcium channels and an inward calcium current. This calcium inflows triggers in the cell a further calcium release from the sarcoplasmatic reticulum. The outward potassium current and the increasing calcium concentration inside the cell almost compensate leading to the plateau phase. The calcium channel then closes and the potassium current increases again repolarizing the membrane. Finally, the resting state potential is reached and the initial ionic concentrations are restored by pumps and exchangers, like the sodium potassium APTase or the sodium calcium exchanger. Figure 2.2 shows the course of an AP.

2.3 Cardiac Conduction System

Neighboring cardiac myocytes are linked to each other with special channels called gap junctions. Through these entities various molecules and ions are directly transferred allowing the propagation of the electrical excitation from one cell to the next one until the complete heart has been activated. The type and amount of gap junctions in the cells determines how quickly an electrical pulse travels within the tissue [28].

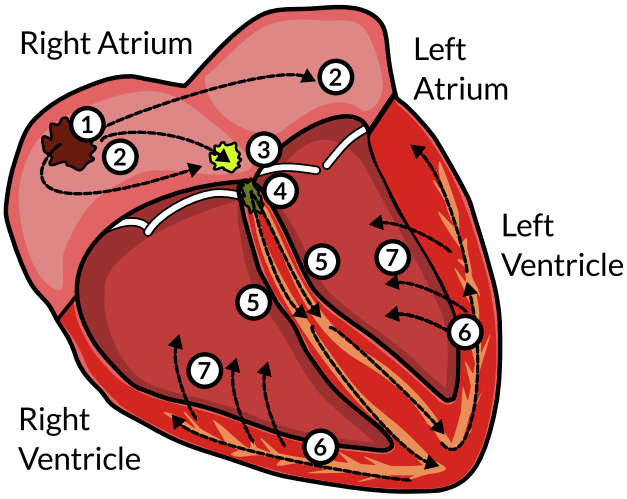

Figure 2.3: Schematic of the electrical conduction system of the heart. (1) Sinus node and origin of the electrical pulse. (2) Atrial cardiac muscle. (3) Atrioventricular node. (4) Bundle of His. (5) Left and right bundle fibers. (6) Purkinje fibers. (7) Ventricular cardiac muscle. This figure was reprinted from publication [30] with permission from the author and was originally inspired by [1].

The origin of the electrical pulse in the heart takes place in the right atrium close to the superior vena cava and is triggered by a group of cells called sinus node. This initial depolarization wave travels through the atria, triggers the contraction of them, activates the atrioventricular node and ends in the left atrial appendage. In general, the atria are electrically isolated from the ventricles. In order to activate the ventricles, the pulse has to first travel after a short delay from the atrioventricular node to the bundle of His. The His bundle is the origin of the depolarization wave in the ventricles. From here, the electrical activation spreads through the left and right bundle branches in the septum and the Purkinje fiber network reaching the cardiac muscle and leading to a coordinated contraction of the ventricles. Figure 2.3 shows a schematic of the electrical conduction system of the heart [29] [1].

If an electrical pulse does not originate in the sinus node, it is considered abnormal. These beats are called ectopic and they appear typically prematurely in the cardiac cycle disturbing the existing cardiac rhythm. They are classified depending on their origin and the instant within the cardiac cycle they are triggered. The community around *physionet.org* [31] distinguishes between 19 different types of ectopic beats. The most relevant for this work has its origin in the ventricles and is called ventricular ectopic beat (VEB) [32].

2.4 Electrocardiogram

The electrical activity in the heart, and in concrete the electrical current flowing in the cardiac tissue, generates also time varying potential differences on the surface of the body. The electrocardiogram (ECG) is the recording of those potential differences. This biosignal is

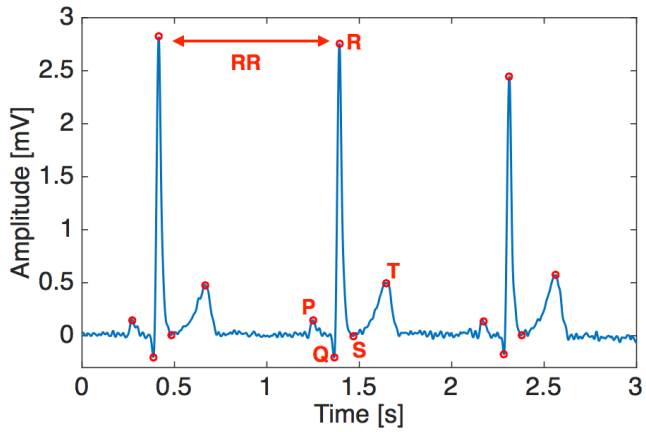

Figure 2.4: Electrocardiographic recording of a healthy subject. The sequence of distinguishable ECG waves can be seen in three beats. This figure was reprinted from publication [33] with permission from the publisher.

however not a direct measure of the depolarization and repolarization of each cell but rather the resulting collective electrical activity from the different AP in every region of the heart. In order to make a recording possible, electrodes have to be placed on the surface of the body and attached to an amplifier with high input impedance. The ECG signal is also characterized by a sequence of distinguishable waves that reflect the electrical activity in each part of the heart. They are called P wave, PQ segment, QRS complex, ST segment and T wave. They can be described as follows [23]:

- P wave: The electrical depolarization of the cardiac tissue in the atria leads to the P wave in the ECG. It has typically a duration of 50 to 100 ms.
- PQ segment: After the P wave, the ECG remains at the isoline level. During this interval, the complete atrium is depolarized and the AV node delays the pulse.
- QRS complex: The QRS complex starts 160 ms after the beginning of the P wave when the excitation reaches the bundle of His. It is decomposed into three characteristic peaks, the Q wave, the R peak and the S wave. The highest amplitude of the QRS complex is the R peak which is achieved when the ventricular tissue depolarizes. The QRS complex has a typical duration of 120 to 200 ms.
- ST interval: During the plateau phase of the AP in the ventricles, a slowly changing signal appears in the ECG. This is the ST segment.
- T wave: This wave arises from the heterogeneous repolarization of the ventricles. The time segment between the beginning of the QRS complex and the end of the T wave is called QT interval and has a duration of about 400 ms.

For the measurement of the ECG, a standardized 12 lead system is used in clinical practice. To acquire the standard ECG, a total of ten electrodes are needed. From those, three are used to record the bipolar leads according to Einthoven (I, II and III) and further three unipolar leads according to Goldberger (aVR, aVL, aVF). They are placed on the torso but close to the right and left arms, and to the left leg. As reference, another electrode is placed

on the torso close to the right leg. Further six electrodes are placed on the left side of the chest close to the heart to derive the unipolar Wilson leads (V1 to V6) [34].

2.5 Autonomic Nervous System

The autonomic nervous system (ANS) is part of the peripheral nervous system and plays an important role in the regulation of many vital functions of the body such as the heart rate, blood pressure, respiration, digestion and metabolism. It is called autonomic because the regulation takes place unconsciously. The most important control center is the hypothalamus. The ANS is divided into two components: the sympathetic and the parasympathetic nervous systems. Depending on the organ and type of regulatory task, these two subsystems can have opposing or complementary effects but they can also work together or independent from each other. In general, the parasympathetic system dominates when the body is resting and is active during "breed-and-feed" and "rest-and-digest" situations. On the other hand, the sympathetic nervous system is primary active during "fight-or-flight" situations and activates during exercise, stress or emergencies [29].

In the cardiovascular system, the regulation of sympathetic and parasympathetic systems is antagonistic. The activation of sympathetic tone leads to an increasing of heart rate, respiration rate and blood pressure. The transport of energy from the reserves to the organs where is currently needed is also triggered. The parasympathetic system has the opposed effect. In the case of the heart, the electrical conduction system and the heart muscle are innervated in order to regulate heart rate and muscular strength to adapt to changing environmental conditions. The parasympathetic system acts through the neurotransmitter acetylcholine reducing the frequency of the sinus node and slowing down the transit time of the pulse in the AV node. The sympathetic system operates through the cathecolamines adrenaline and noradrenaline increasing the pulse rate in the sinus node, reducing the transit time in the AV node and increasing the contractility and relaxation speed of the cardiac muscle [35].

2.6 Heart Rate Variability

Consecutive heart beats arise in a non-constant rhythm. The physiological phenomenon in which the duration of the heart period varies over time is called HRV. The beat-to-beat time is called RR interval and a collection of subsequent RR intervals is called RR time series. The HRV characterizes also the ability of the body to adapt to external conditions and internal demands and is regulated by the ANS. Thus, the HRV makes possible a non-invasive measurement of the state of the ANS allowing the quantification of the tone of the sympathetic and parasympathetic systems. Through the HRV, it is also possible to evaluate the health of the heart because a reduced or an increased HRV has been shown to correlate with different diseases or psychological states [9].

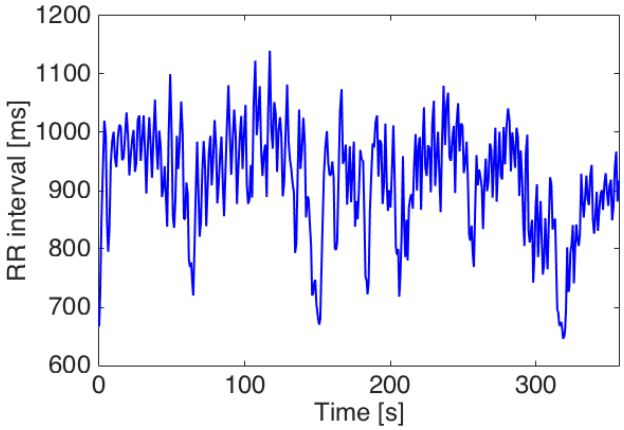

Figure 2.5: RR time series obtained from a driver during an experiment for the assesment of mental workload. The series has a length of six minutes and the RR intervals range from 646 to 1140 ms. This figure was reprinted from [33] with permission from the publisher.

In order to quantify HRV and explore its diagnostic value, a large variety of parameters can be obtained from the RR time series [36]. Depending on the representation of the series, they can be classified into time or frequency domain parameters. They can also be categorized depending on their mathematical nature into linear or nonlinear features. Many quantitative methods have also been used to create these parameters including geometry, statistics, chaos theory, information theory, or time-frequency analysis, just to name a few. Finally, depending on the length of the series, the HRV analysis is divided into a short-term (around five minutes) and a long-term (24 hours). Figure 2.5 shows an example of a short term RR time series.

2.7 Respiratory Sinus Arrhythmia

In healthy subjects, the heart rate tends to couple to respiration and varies with it synchronously. This physiological phenomenon is called RSA and it is the greatest influence from the ANS on the heart and recorded through the RR time series in a non-invasive way. During RSA, the heart rate increases when a person inspires and decreases during expiration [16]. Figure 2.6 shows an example of the RSA phenomenon. Even though the purpose of RSA in the human body is not fully understood, it is believed to be there for two reasons. Its first goal is to minimize the mechanical work of the pumping function of the heart while maintaining the necessary concentration of gases in the blood. Second, it is supposed to optimize gas exchange during respiration by matching blood flow in the lungs to breathing rate [37–39].

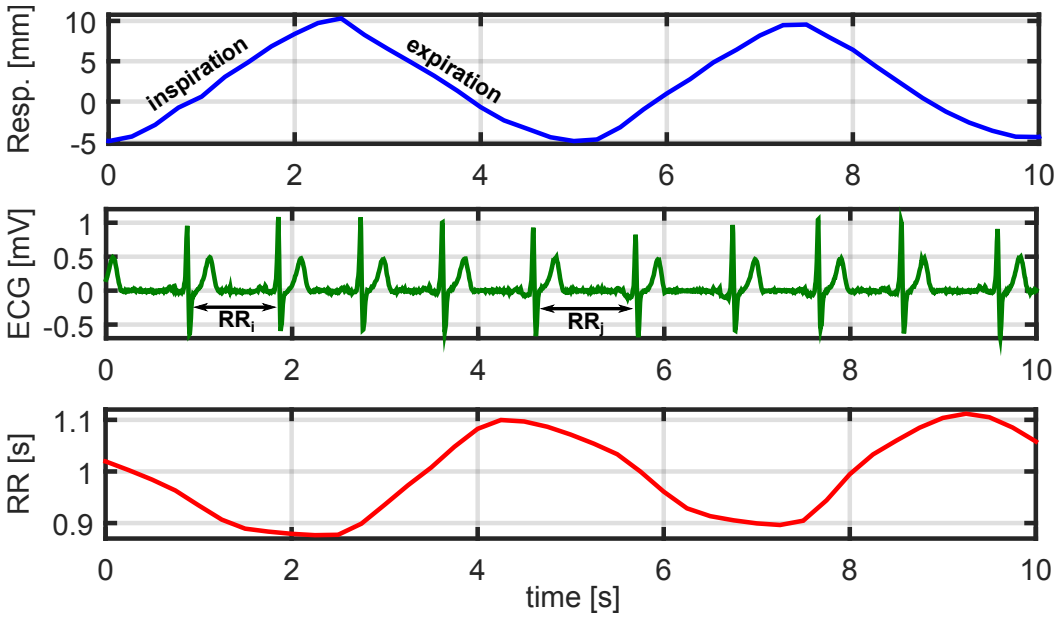

Figure 2.6: An example of the RSA phenomenon. The upper figure shows a surrogate measure of the tidal volume of the lungs, the figure in the middles displays the ECG recorded synchronously and the lower figure shows the RR time series derived from the ECG. This figure was reprinted from publication [40] with permission from the author.

2.8 Heart Rate Turbulence

The HRT is the short-time response of the sinus rhythm to a VEB. In healthy persons, the HRT is characterized by an initial shortening of the RR intervals followed by a deceleration of the heart rate to even lower values than before the VEB and finally a restitution of the original RR interval length [10]. In order to obtain the HRT curve, a tachogram is constructed with five normal beats before and another 15 after every VEB. Averaging all post-ectopic responses over a long period of time delivers the resulting HRT curve used for medical analysis [7].

For quantification and further diagnosis, the parameters turbulence onset (TO) and turbulence slope (TS) were introduced. TO is a relative measure of the initial shortening of the RR interval after the VEB. It is measured in percentage and given by the following equation:

$$TO = \frac{(RR_2 + RR_3) - (RR_{-1} + RR_{-2})}{(RR_{-1} + RR_{-2})}$$

TS captures the recovering slope at which the cycle length returns to higher values. It is defined as the maximal positive slope of a regression line over five consecutive RR intervals after the VEB. It is measured in milliseconds per beat. The accurate estimation of the two parameters is compromised if low signal quality and artifacts in the ECG are present, wrong classifications of the VEB are perfomed or the recording device has a low sampling rate.

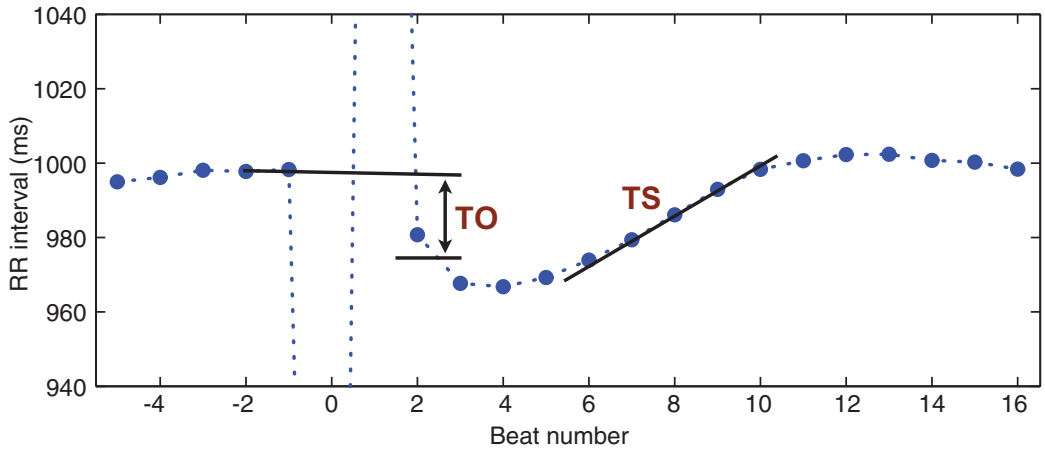

Figure 2.7: Normal HRT curve with an ilustration of the parameters TO and TS. This figure was reprinted from publication [41] with permission from the publisher.

Thus, a set of rules to ensure a high quality HRT curve were defined and should by fulfilled in any HRT-based diagnosis [10]. Figure 2.7 shows a normal HRT curve and an illustration of the parameters TO and TS.

The HRT parameters TO and TS have been shown to be independent and a powerful predictor of sudden cardiac death (SCD) in patients with a history of myocardial infarction [7]. The thresholds TO$<$0 % and TS$>$2.5 ms/beat are considered normal. The two parameters combined are able to predict SCD with a sensitivity of 30 % and a positive predictive value of 32 %. Furthermore, TS is also a strong risk stratifier with a relative risk of up to 3.5 [42].

CHAPTER 3

Mathematical Fundamentals

In this chapter, the mathematical foundations relevant to understand the signal processing methods used in this thesis are presented. The chapter begins with a short introduction to the theory of signals and systems followed by two of the most important signal transformations, the Fourier transform and wavelet transform. The chapter continues with an overview of random variables, probability theory and central moments. Continuing with the study of random variables, special attention is put to similarity measures and the analysis of principal components. The chapter then finishes with an introduction to the analysis of time series focusing on autoregressive moving average models. For further information or mathematical demonstrations of particular results, the reader in invited to refer to the cited literature.

3.1 Signals and Systems

3.1.1 Signal

A signal can be defined as the time dependent measurement of a quantity that contains relevant information for an observer [43]. In a more mathematical way, a signal is a function of time and it is typically defined as a mapping from the real valued time t to a real, complex or integer valued signal $x(t)$ [44].

$$x(t) \text{ with } t \in \mathbb{R} \text{ and } x(t) \in \mathbb{R}, \mathbb{C} \text{ or } \mathbb{Z} \tag{3.1}$$

In the particular case of discrete time signals, the mapping goes from integer valued time k to a real, complex or integer valued function $x(k)$.

$$x(t) = x(k) \text{ with } t = k,\ k \in \mathbb{Z} \text{ and } x(k) \in \mathbb{R}, \mathbb{C} \text{ or } \mathbb{Z} \tag{3.2}$$

In modern science and engineering, many signal processing algorithms are performed by a computer using digitized signals. For that purpose, the continuous-time signal is sampled at

Figure 3.1: The system T maps the input signal $x(t)$ to the output signal $y(t)$.

a fixed rate so that $x(t) = x(k \cdot t_s)$. The time interval t_s is called sampling time and corresponds to the distance between two consecutive sample points. The inverse of the sampling time $f_s = 1/t_s$ is called sampling frequency. In many biological or medical applications, the time distance between consecutive samples is not necessarily constant. An example of this is the RR time series obtained from the electrocardiogram (ECG).

3.1.2 Energy Signal

An important property of signals is their energy content. Mathematically speaking, a bounded, piecewise continuous signal $x(t)$ is said to have finite energy if the following equation holds [44]:

$$E_s = \int_{-\infty}^{\infty} |x(t)|^2 dt < \infty \tag{3.3}$$

where E_s is the energy of the signal. An analogous definition exists for the discrete-time energy signal:

$$E_s = \sum_{k=-\infty}^{\infty} |x(k)|^2 < \infty \tag{3.4}$$

If finite energy is assumed in the universe, then only signals with finite energy can be recorded. Thus, all physically measurable signals (including ECG) are energy signals [45]. However, in theory, other kind of signals can be defined and investigated.

3.1.3 System

A system can be defined as any entity that responds to an input signal $x(t)$ with an output signal $y(t)$. In science and engineering, systems are used to model physical phenomena in the real world. In mathematical terms, the system is a transformation T from the input signal $x(t)$ to the output signal $y(t)$ as can be seen in figure 3.1:

$$y(t) = T\{x(t)\} \tag{3.5}$$

If the transformation T is linear and independent of time t, the system is called linear time invariant (LTI). This kind of systems is characterized by a linear differential equation with constant coefficients as follows:

$$\sum_{n=0}^{N} a_n \cdot \frac{d^n y(t)}{dt^n} = \sum_{m=0}^{M} b_m \cdot \frac{d^m x(t)}{dt^m} \tag{3.6}$$

Analogously, a discrete-time LTI system is defined by a linear difference equation with constant coefficients:

$$\sum_{n=0}^{N} a_n \cdot y(k-n) = \sum_{m=0}^{M} b_m \cdot x(k-m) \tag{3.7}$$

3.2 Fourier Transform

The Fourier transform is a linear integral operator that converts a signal in its freqeuncy domain representation. It arises as a generalization of the Fourier series for non-periodic signals.

3.3 Continuous Fourier Transform

The Fourier transform of a continuous-time energy signal $x(t)$ is a linear integral transform defined as follows:

$$\mathscr{F}\{x(t)\} = X(f) = \int_{-\infty}^{\infty} x(t) \cdot e^{-j2\pi ft} dt \tag{3.8}$$

In the theory of Hilbert spaces, the Fourier transform can be represented as the inner product of the function $x(t)$ with the complex exponential function $e^{j2\pi ft}$. Preserving the notation used in [44], the Fourier transform can be given as:

$$\mathscr{F}\{x(t)\} = X(f) = \left\langle x(t), e^{j2\pi ft} \right\rangle_t \tag{3.9}$$

From a given Fourier transform $X(f)$, it is possible to reconstruct the original signal $x(t)$. The inverse Fourier transform is given by [44]:

$$\mathscr{F}^{-1}\{X(f)\} = x(t) = \int_{-\infty}^{\infty} X(f) \cdot e^{j2\pi ft} df \tag{3.10}$$

The function $X(f)$ is called the spectrum of $x(t)$.

3.4 Discrete Fourier Transform

An analogous definition exists also for discrete-time signals $x(k)$. In that case, the discrete Fourier transform (DFT) is given by:

$$DFT\{x(k)\} = X(n) = \sum_{k=0}^{K-1} x(k) \cdot e^{-j2\pi \frac{nk}{K}} \tag{3.11}$$

where K is the total length of the signal $x(k)$. The discrete Fourier transform $X(n)$ has the same length K. From a given $X(n)$, the inverse discrete Fourier transform reconstructs the discrete-time domain signal as follows:

$$x(k) = \frac{1}{N} \sum_{n=0}^{N-1} X(n) \cdot e^{j2\pi \frac{nk}{N}} \quad \text{with} \quad N = K \tag{3.12}$$

3.5 Wavelet Transform

The wavelet transform is a further member of the family of linear transforms that delivers a time-frequency representation of the original time domain signal. Other members of this family are the short-time Fourier transform and the Wigner-Ville distribution. The wavelet analysis is based on the comparison (measurement of similarity) of the time signal with a scaled and shifted version of a wavelet function. The latter is characterized by compactness in the time-frequency domain so that the whole procedure allows the localization of signal power in the time-frequency plane [46].

3.5.1 Continuous Wavelet Transform

For continuous-time energy signals, the wavelet transform is defined as follows [46]:

$$W_x^{\psi}(a,b) = \left\langle x(t), \psi_{a,b}^*(t) \right\rangle_t = \int_{-\infty}^{\infty} x(t) \cdot \psi_{a,b}^*(t) dt \tag{3.13}$$

where the function $\psi_{a,b}^*(t)$ is the scaled and shifted version of the complex conjugate mother wavelet. This one is given in the following manner:

$$\psi_{a,b}(t) = \frac{1}{\sqrt{|a|}} \cdot \psi\left(\frac{t-b}{a}\right) \quad \text{with} \quad \psi_{a,b}(t) \in \mathbb{C} \tag{3.14}$$

A function is considered to be a wavelet if it fulfills the following criteria [47]:

1. A wavelet $\psi(t)$ must have finite energy which is typically normalized to be one.

$$\int_{-\infty}^{\infty} |\psi(t)|^2 dt < \infty \tag{3.15}$$

2. The Fourier transform of the wavelet $\Psi(f)$ must fulfill also the following admissibility condition:
$$C_\psi = \int_{-\infty}^{\infty} \frac{|\Psi(f)|^2}{|f|} df < \infty \tag{3.16}$$
3. For complex wavelets a third requirement exists. The Fourier transform of a complex wavelet must be real and it is not allowed to have negative frequency components.

The first two criteria mean that a wavelet must be an energy signal with zero mean that is also localized in time and frequency.

From a given wavelet transform $W_x^\psi(a,b)$ obtained using the analysis wavelet $\psi_{a,b}^*(t)$, the time signal $x(t)$ can be reconstructed using a synthesis wavelet $\overline{\psi}_{a,b}^*(t)$ in the following manner:

$$x(t) = \frac{1}{C_{\psi\overline{\psi}}} \int_{-\infty}^{\infty}\int_{-\infty}^{\infty} W_x^\psi(a,b) \cdot \frac{1}{\sqrt{a}} \overline{\psi}_{a,b}(t) \frac{da}{a^2} db \tag{3.17}$$

The reconstruction is only possible if the analysis and synthesis wavelets fulfill admissibility condition for different wavelets:

$$C_{\psi\overline{\psi}} = \int_{-\infty}^{\infty} \frac{\Psi^*(f) \cdot \overline{\Psi}(f)}{|f|} df < \infty \tag{3.18}$$

The continuous wavelet transform in its "classical" definition delivers an analysis dependent of wavelet scales. However, a time-frequency representation of the signal can be more interesting in some application. For that purpose, it is necessary to reformulate the definition in terms of frequencies instead of scaling parameters. Thus, the scaling parameter a is replaced by the multiplicative inverse of a normalized frequency. It can be shown that $a = \frac{f_\psi}{f}$ is a valid replacement, where f_ψ is a representative (often the center) frequency of the wavelet $\psi(t)$. The wavelet transform is then redefined to include time shifts and frequency variations in the following manner [46]

$$W_x^\psi(f,\tau) = \sqrt{\left|\frac{f}{f_\psi}\right|} \int_{-\infty}^{\infty} x(t) \cdot \psi^* \left(\frac{f}{f_\psi}(t-\tau)\right) dt \tag{3.19}$$

3.5.2 Discrete Wavelet Transform

In computerized signal processing, time-discrete signals are used and a counterpart for the continuous wavelet transform is needed. An optimal (non-redundant) representation can be achieved discretizing the scaling parameter a and the shifting parameter b using a dyadic

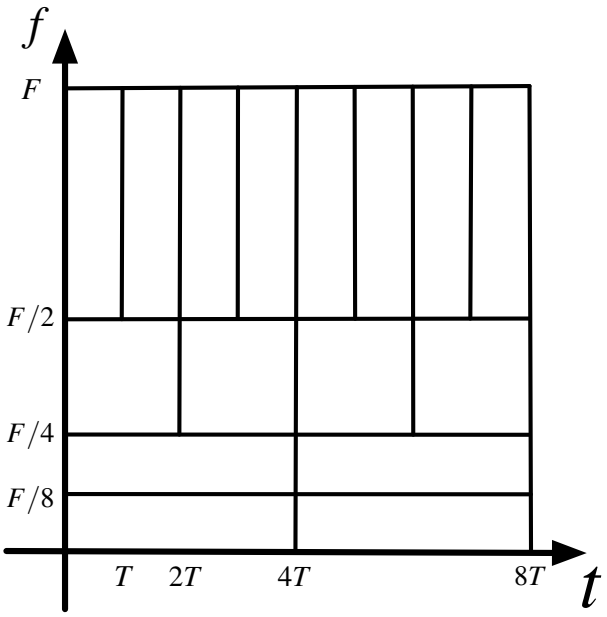

Figure 3.2: Time-frequency plane generated using a dyadic grid for the discrete wavelet transform. Figure inspired by [46].

grid. Scales are then a power of two and shifts are an integer factor of the same power of two. The discrete wavelet transform is defined in the following manner [46]:

$$W_x^{\psi}(k,m) = \sum_{n=-\infty}^{\infty} x(n) \cdot 2^{-\frac{k}{2}} \psi(2^{-k}n - m) \tag{3.20}$$

The discrete wavelet transform produces a time-frequency (or rather time-scale) plane that is also discrete. This leads to a low frequency resolution at shorter time and a high frequency resolution at longer times. This is conform with the Heisenberger's uncertainty principle of the Fourier transform [47]. Figure 3.2 shows the time frequency-plane generated using a dyadic grid.

In order to achieve an optimal (non-redundant) representation of the discrete-time signal $x(n)$, orthonormal wavelets are used. They fulfill the following criterion:

$$\left\langle \psi(k,m), \psi(k',m') \right\rangle = \delta(k-k') \cdot \delta(m-m') \tag{3.21}$$

In practice however, a scaling function $\phi(k,m)$ associated with the wavelet function $\psi(k,m)$ is introduced to facilitate a multiresolution representation of the signal. The scaling function is orthonormal to the wavelet function and has low-pass characteristics. It is responsible for the approximation $a_m(n)$ of the signal $x(n)$ at the scale m. On the other hand, the wavelet function has band-pass behavior and it captures the details $d_m(n)$ of the signal $x(n)$ at that same scale. A multirate representation of the signal means that at any given

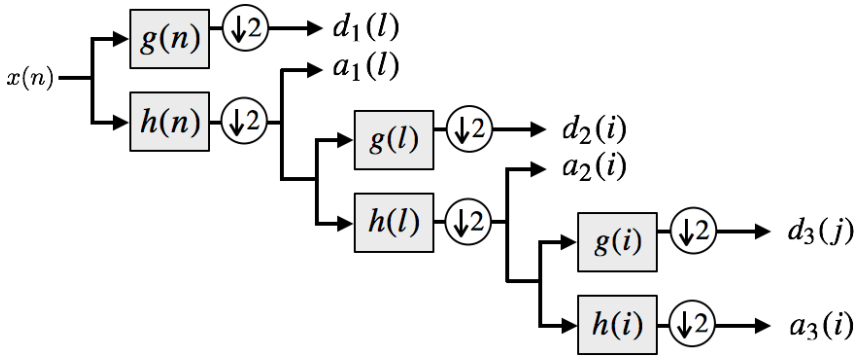

Figure 3.3: Filter bank used to compute the wavelet coefficients using the algorithm known as the fast wavelet transform.

scale m, the sum of detail and approximation of the signal produce the approximation at the previous scale (next higher resolution).

$$a_{m-1}(n) = a_m(n) + d_m(n) \tag{3.22}$$

The use of a multirate filter bank leads to a very efficient computation of the discrete wavelet transform and is known as the fast wavelet transform. Similar to the fast Fourier transform, the approximation and detail signals at a given scale are calculated recursively from the approximation signals at the previous scale. This computation is performed using the low-pass and high-pass filters associated with the scaling and wavelet function through a convolution of the impulse response of the filters with approximation of the signal at the given scale. Thus, for every scale the following relationship holds:

$$a_{m+1}(l) = a_m(n) * h(n)|_{n=2l} \tag{3.23}$$

$$d_{m+1}(l) = a_m(n) * g(n)|_{n=2l} \tag{3.24}$$

The discrete wavelet decomposition begins with the signal $x(n)$, which is the approximation itself at the first scale. The signal is filtered by the low-pass and band-pass filters to produce the approximation and detail coefficients at the next scale. The resulting approximation coefficients are decimated by a factor of two and the procedure is repeated. Figure 3.3 shows how this procedure is done.

The synthesis of the original signal $x(n)$ from its wavelet coefficients is performed in a analogous manner. Again, a filter bank is used and the process begins with the wavelet coefficients at the highest scale. These coefficients are upsampled, filtered using the low-pass and high-pass synthesis filters and summed to create the approximation coefficients at the previous scale. From here, the procedure is repeated until the original signal has been reconstructed.

One of the disadvantages of the discrete wavelet transform is that it is not translation invariant and can thus become unsuitable for some applications such as detection of edges or spikes. To overcome this problem, the stationary wavelet transform was introduced [48]. In

this method, the downsampling of the signal at each stage of the filter bank is replaced by an upsampling of the filter coefficients. By doing so, the transformed signal has the same amount of samples at each stage at the cost of redundancy.

3.5.3 Wavelet Packet Decomposition

The wavelet packet analysis is a generalization of the discrete wavelet transform that allows a flexible time-frequency representation of the signal. The generalization is achieved by creating wavelets that split the time-frequency plane into the desired intervals and give the user the chance of creating a custom made analysis. A filter bank realization is also used for the wavelet packet decomposition but instead of recursively processing only the approximation coefficients, the detail coefficients are also further filtered [49]. Figures 3.4a and 3.4b show an example of a possible filter bank realization and its corresponding time-frequency plane.

3.6 Principles of Probability Theory and Statistics

3.6.1 Random Variable

A random variable X is a function that maps the sample space S of possible outcomes of an experiment to a real number. If x is a fixed value and X is a random variable, then $P(X \leq x)$ denotes the probability of the random variable X being less or equal than the given value x.

3.6.2 Probability Density Function and Cumulative Distribution Function

The cumulative distribution function of a continuous random variable X is the real valued function $F_X(x)$ defined by:

$$F_X(x) = P(X \leq x) \text{ with } x \in \mathbb{R} \tag{3.25}$$

A cumulative distribution function must fulfill the following criteria:

1. $0 \leq F_X(x) \leq 1$
2. $F_X(x_1) \leq F_X(x_2)$ if $x_1 \leq x_2$
3. $\lim_{x \to \infty} F_X(x) = 1$
4. $\lim_{x \to -\infty} F_X(x) = 0$
5. $\lim_{x \to a^+} F_X(x) = F_X(a^+) = F_X(a)$

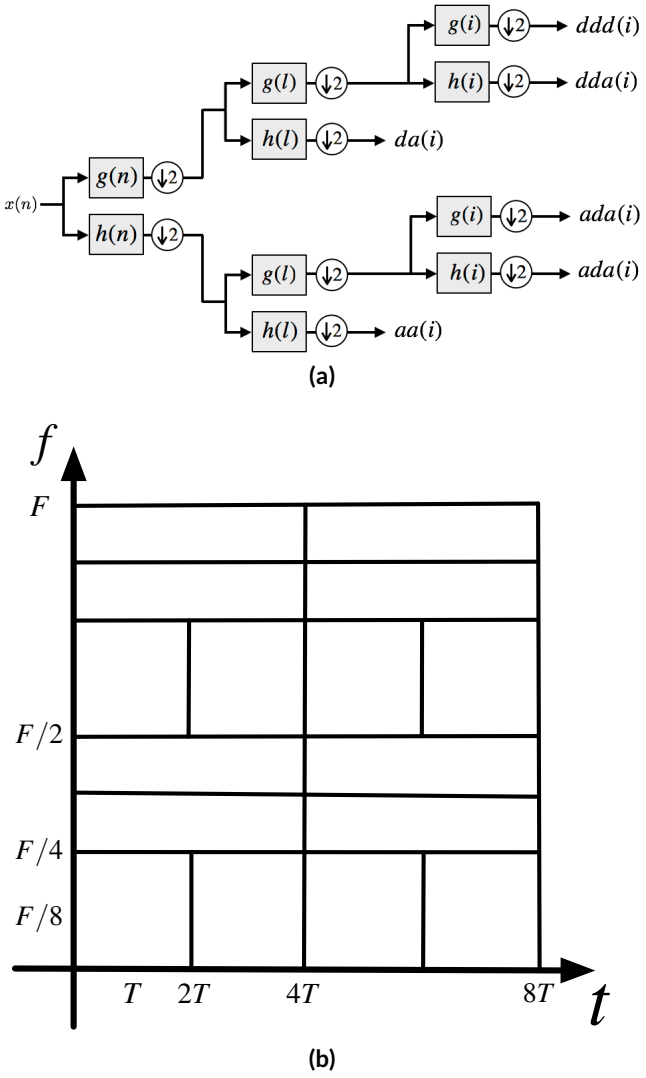

Figure 3.4: (a): An example of a possible filter bank used to compute the wavelet coefficients of a wavelet packet decomposition. (b): Time-frequency plane generated using the wavelet packet decomposition displayed in figure (a).

From the cumulative distribution function $F_X(x)$, the probability density function $f_X(x)$ can be obtained in the following manner:

$$f_X(x) = \frac{dF_X(x)}{dx} \tag{3.26}$$

The following properties are fulfilled by $f_X(x)$:

1. $f_X(x) \geq 0$
2. $\int_{-\infty}^{\infty} f_X(x)dx = 1$
3. $f_X(x)$ is piecewise continuous
4. $P(a < X \leq b) = \int_{a}^{b} f_X(x)dx$

3.6.3 Random Process

A random process $X(x;t)$ is a collection of random variables indexed by the parameter $t \in T$ and defined over the sample space S [50]. The parameter t is typically called time. For a fixed time $t = t_0$, the random process becomes a random variable $X(x;t_0)$. On the other hand, when the sample point is fixed $x = x_0$, the random process becomes a function $X(x_0;t)$ of the index t, which is also called a realization of the process. If both, the index t and the sample x are fixed, the random process $X(x_0;t_0)$ becomes a real number. For a given time t, the cumulative distribution function $F_X(x;t)$ and the probability density function $f_X(x;t)$ are defined as:

$$F_X(x;t) = P(X(t) \leq x) \text{ with } x,\ t \in \mathbb{R} \tag{3.27}$$

$$f_X(x;t) = \frac{dF_X(x;t)}{dx} \tag{3.28}$$

In order to study the relationship between random variables of the process at different times, the nth order cumulative distribution function is introduced as follows:

$$F_{X_1,X_2,\ldots,X_n}(x_1,x_2,\ldots,x_n;t_1,t_2,\ldots,t_n) = \tag{3.29}$$

$$P(X_1(t_1) \leq x_1, X_2(t_2) \leq x_2, \ldots, X_n(t_n) \leq x_n) \tag{3.30}$$

A random process $X(t)$ is considered to be stationary if its nth order cumulative distribution function for every set of indexes $t_i \in T,\ i = 1,2,\ldots,n$ and for all n is not affected by any time shift τ. Thus, stationary is defined as [51]:

$$F_{X_1,X_2,\ldots,X_n}(x_1,x_2,\ldots,x_n;t_1,t_2,\ldots,t_n) = \tag{3.31}$$

$$F_{X_1,X_2,\ldots,X_n}(x_1,x_2,\ldots,x_n;t_1+\tau,t_2+\tau,\ldots,t_n+\tau) \tag{3.32}$$

If the equality holds only for $n \leq 2$, the process is said to be stationary in the weak sense. This kind of random processes have the advantage of being representable with arbitrary precision by autoregressive moving average (ARMA) models (introduced later in section 3.9.1) [52].

3.6.4 Central Moments

The expected value (or mean) of a random variable X is defined as the center of mass of its probability density function $f_X(x)$:

$$\mu_X = E\{X\} = \int_{-\infty}^{\infty} x f_X(x) dx \tag{3.33}$$

$E\{\cdot\}$ denotes the expectation operator. The moment of order n of the probability density function $f_X(x)$ around its mean μ_X is defined as follows:

$$\mu_{X,n} = E\{(X - E\{X\})^n\} = \int_{-\infty}^{\infty} (x - \mu_X)^n f_X(x) dx \tag{3.34}$$

The set of central moments are characterizing features of a random variable. Particularly relevant for many applications are the second, third and fourth central moments. The second central moment σ^2 is called variance and is a measure of the dispersion or width of the $f_X(x)$ around its mean. The positive square root of the variance is called standard deviation. The variance is given by:

$$\sigma^2_{X,n} = E\{(X - E\{X\})^2\} = \int_{-\infty}^{\infty} (x - \mu_X)^2 f_X(x) dx \tag{3.35}$$

The third central moment is a measure of symmetry of the probability density function. If it is equal to zero, the probability density function is symmetrical around its mean. A negative third central moments arises from a longer tail on the left side of the mean. The third central moment is used to define the skewness $\nu\{X\}$ of the random variable:

$$\nu\{X\} = \frac{E\{(X - E\{X\})^3\}}{\sigma_X^3} \tag{3.36}$$

Finally, the fourth central moment is a measure of how much probability mass is concentrated in the tails of the distribution. This is often referred to as the "tailedness" of the distribution. The fourth central moment is used to define the kurtosis $k\{X\}$ of the random variable:

$$k\{X\} = \frac{E\{(X - E\{X\})^4\}}{\sigma_X^4} \tag{3.37}$$

3.6.5 Similarity Measures

A similarity measure is a real-valued function that quantifies the degree of association or dependency between two random variables [53]. In general, similarity measures are opposite to distance metrics.

3.6.5.1 Correlation Coefficient

The correlation coefficient ρ_{XY} measures the linear relationship or linear degree of association between two random variables X and Y. It is defined in the following manner:

$$\rho_{XY} = \frac{Cov\{X,Y\}}{\sigma_X \cdot \sigma_Y} \tag{3.38}$$

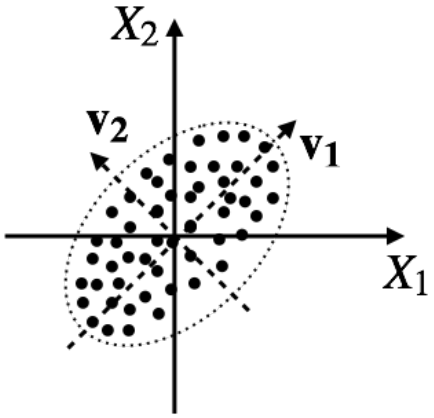

Figure 3.5: Principal components of a two dimensional random variable $\mathbf{X}$. This figure was adpated from publication [56] with permission from the author.

The covariance $Cov\{\cdot\}$ of the two random variables X and Y is defined by:

$$Cov\{X,Y\} = E\{(X-\mu_X)(Y-\mu_Y)\} \tag{3.39}$$

The correlation takes values in the interval $[-1;+1]$. It maximizes when a perfect positive linear relationship is present between X and Y and becomes -1 in case of perfect negative linear association. If the two variables are not correlated, ρ_{XY} is equal to zero. Furthermore, the correlation coefficient is independent of scaling or shifting of either of the random variables.

3.6.6 Principal Component Analysis

The principal component analysis (PCA) is a linear mapping of an n dimensional, zero mean random variable $\mathbf{X} = [X_1, X_2, ..., X_n]^\top$ to a new coordinate system in which the variance of each component is maximal [54].

For that purpose, an orthonormal matrix $\mathbf{V}$ has to be found, such that each projection $\mathbf{p} = \mathbf{V} \cdot \mathbf{X}$ of the random variable $\mathbf{X}$ with respect to each of the basis vectors of $\mathbf{V}$ have maximal variance. This is an optimization problem that begins by finding the first orthonormal basis vector $\mathbf{v_1}$ that is going to generate the projection p_1 with greatest variance [55].

$$\mathbf{v_1} = \underset{\mathbf{v_1}}{argmax}\{var\{p_1\}\} = \underset{\mathbf{v_1}}{argmax}\{var\{\mathbf{v_1} \cdot \mathbf{X}\}\} \text{ subject to } |\mathbf{v_1}| = 1 \tag{3.40}$$

The further principal components are found by projecting the random variable $\mathbf{X}$ onto a hyperplane orthogonal to the previously found basis vector and repeating the maximization procedure. The algorithm ends when no more projections can be done and thus n principal components have been found. The basis vectors of $\mathbf{V}$ are called the principal components of $\mathbf{X}$ and the projections p_i are called scores. The maximized score variances λ_i are the principal values. The idea behind PCA is displayed in figure 3.5.

Furthermore, it can be shown that the solution to this optimization problem can be found analytically [55]. The eigenvectors of the covariance matrix $\mathbf{Cov}\{\mathbf{X},\mathbf{X}\}$ represent its principal components and its eigenvalues are the principal values. A singular value decomposition is performed to find them.

$$Cov\{\mathbf{X},\mathbf{X}\} = E\{(\mathbf{X}-\mu_{\mathbf{X}})(\mathbf{X}-\mu_{\mathbf{X}})^{\top}\} = E\{X \cdot X^{\top}\} = \mathbf{V}^{\top}\Lambda\mathbf{V} \tag{3.41}$$

PCA is a method that can be very useful to reduce the dimensionality of a random variable but at the same time retain as much information (variance) as needed in its scores [54]. In other fields of science, this technique is also known as Karhunen-Loève transform.

3.7 Statistical Classification

In the field of machine learning, the classification task consists of assigning a set of observations, each characterized by well-defined properties (also called features or patterns), to a category (also called class). The computed features of a new object are used to separate it from others and predict its class automatically. In order to develop a classifier, two stages are needed: training and testing. Depending on the application, a third stage called validation may also be required [54].

The technical implementation of a classifier begins with the training phase for which a set of observations is needed. These are labeled by an expert, so that a class is assigned to each of them. The features of each observation are placed on a training vector $\mathbf{x}$ and its corresponding category is placed in the class label d. This information is then used to generate a weighting vector $\mathbf{w}$ that describes some sort of discriminant function used to divide the space of features into non-overlapping zones. Each zone corresponds to a class.

Once the classifier has been trained, the test phase begins. Here, a set of new observations, for which the labels are known to the user but unknown to the classifier, are used to evaluate the performance of the classification system. Training and testing with different observations each time can be iterated to improve the performance of the classifier. Once the best possible classifier has been achieved, another data set unknown up to this point to the classifier, can again be use to validate the measured performance.

A large variety of classifiers have been created in the field of machine learning. They range from a simple threshold to support-vector-machine (SVM) or artificial neuronal networks capable of performing various tasks better than a human being [57].

3.7.1 Support-Vector-Machine

The SVM is a classifier from the field of supervised learners that has the aim of finding a linear separating hyperplane by maximizing the distance from the separating plane to the observation in each class. In general, this procedure is a heuristic that minimizes the risk of

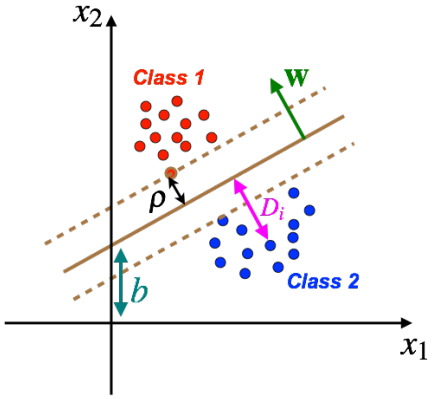

Figure 3.6: Linear SVM used to separate two classes in a two dimensional feature space. The margin ρ is maximized with the aim of minimizing the classification error in general.

misclassification [58]. Figure 3.6 displays the classification problem in a two dimensional feature space.

In order to solve this classification task, it has to be reformulated as an optimization problem. The margin ρ, which is the distance from the closest observation to the separating line, has to be maximized in order to minimize the risk of misclassification. In this procedure, the optimal parameter of the separating plane (normal vector $\mathbf{w}$ and offset b) are found. Using the same notation displayed in figure 3.6, the optimization problem can then be formulated as follows:

$$\underset{\mathbf{w},b}{argmax}\ \rho^2 \ \text{ subject to:} \tag{3.42}$$

$$D_i \geq \rho \text{ for all } i, \text{ and} \tag{3.43}$$

$$\rho \geq 0 \tag{3.44}$$

This maximization problem can again be rewritten as a minimization problem of a quadratic polynomial subject to a linear inequality as constraint. Quadratic programming is the name of this kind of optimization problems. They can be solved very efficiently in polynomial time. This kind of SVM are called hard margin because they do not allow classification errors during the training phase. For that case, the soft margin SVM has been developed that accounts for classification errors and regularizes them. In addition, the SVM has also been extended to allow non-linear separating surfaces applying the so called kernel trick [57].

3.8 Statistical Hypothesis Testing

A very common way of evaluating the significance of a result obtained in a scientific study are statistical tests [59]. Depending on the properties of the study and the distributions underlying the populations being analyzed, a large variety of tests have been developed.

The majority of them have in common that they assess the probability (also called p-value) of making a mistake when a previously set hypothesis is rejected. The hypothesis being evaluated is typically called null hypothesis H_0 and its counterpart is called alternative hypothesis H_1. In order to measure how significant a result may be, the probability p is used. It can be said in general, that the lower p, the lower also the error probability when rejecting H_0 and thus the more significant the hypothesis H_1 becomes. Four significance levels (also called α levels) of p have been introduced in literature and are defined as follows [59]:

- $p < 0.1$: slightly significant
- $p < 0.05$: significant
- $p < 0.01$: highly significant
- $p < 0.001$: most significant

It is important to mention that the p-value is dependent on two factors, the number of observations used to calculate it and the probability distribution assumed for the population. Thus, the interpretation of a p-value must always be done taking them into account. Furthermore, the p-value delivers no information about the causality of a result or its relevance for the scientific community. Two very popular tests in the field of signal processing because of their non-parametric nature and simplistic assumptions are the Wilcoxon rank sum and Wilcoxon signed rank test.

3.9 Time Series Analysis

A time series $x(n)$ with $n \in \mathbb{N}$ is defined as a time or index dependent sequence of data points. Time series are commonly used in different fields of science for the empirical analysis of the dynamical properties and behavior of real-world systems [60]. In cardiology, typical examples for time series are obtained from the ECG when the time intervals between the various waves are tracked. Probably, the best known time series is the RR tachogram (displayed in figure 2.5). In general, the analysis of time series is based on the representation of the signal using a mathematical model, which can be used to obtain more information about the underlying phenomenon and predict future events.

3.9.1 Autoregressive Moving Average Models

The ARMA model of a time series $x(n)$ is a parametric representation of the underlying stochastic process being analyzed. These models are very popular because they can describe with arbitrary precision weak-sense stationary random processes. The ARMA model is divided into two separated processes, the autoregressive (AR) and the moving average (MA)

parts. For model orders P and Q_ε, that correspond respectively to the AR and MA parts of the model, the following holds [61]:

$$x(n) = \sum_{k=1}^{N} x(n-k) + \sum_{k=0}^{Q_\varepsilon} \varepsilon(n-k) \tag{3.45}$$

where $\varepsilon(n)$ is commonly a white Gaussian noise process. This model can be extended to include a second time series $y(n)$ of order Q as exogenous input creating an ARMAx model in the following manner:

$$x(n) = \sum_{k=1}^{N} x(n-k) + \sum_{k=1}^{Q} y(n-k) + \sum_{k=0}^{Q_\varepsilon} \varepsilon(n-k) \tag{3.46}$$

In many applications, the model order Q_ε of the MA part is set to one. The other model orders P and Q can be estimated using methods proposed in literature such as the Akaike information criterion, the Bayesian information criterion (BIC) or the Box-Jenkins method [62]. The identification of the model coefficients is typically carried out using least squares estimation [51]. ARMA models can also be used to study causal dependencies between two or more processes [63].

PART II

POSTEXTRASYSTOLIC T WAVE CHANGE

CHAPTER 4

Influence of Ventricular Ectopic Beats on Subsequent Waves in the Electrocardiogram

4.1 Introduction

The stratification of risk of death or other complications because of cardiac afflictions is a relevant research topic [64]. The prognosis of a patient after myocardial infarction or during heart failure are typical examples in which cardiologists have to reliably decide on the treatment of the patient. For this purpose, risk stratifiers such as the left ventricular dysfunction, non-sustained ventricular tachycardia, abnormal heart rate variability (HRV) and frequent ventricular ectopic beats (VEBs) are used. However, statistical analysis demonstrates that they are not strong predictors even when they are combined. On the other hand, the heart rate turbulence (HRT) seems to be a more powerful predictor achieving a sensitivity (SEN) of 30% and a positive predictive value (PPV) of 32% in a variety of studies.

Risk of sudden cardiac death (SCD) after myocardial infarction can be stratified using the HRT parameters. A normal patient has a turbulence onset (TO) of $TO < 0\,\%$ and a turbulence slope (TS) of $TS > 2.5\,ms/beat$. An HRT curve from a normal patient can be seen in figure 2.7. If one of the parameters is abnormal, the patient is classified as risk 1 and if both parameters are not in the normal range, the patient is classified as risk 2. Even with this approach, the total number of false positives remains high [65]. Hence, new approaches could be introduced to analyze not only the rhythmical properties of the ECG during HRT but also the morphology of the ECG waves.

In this work, we propose a new interpretation of HRT based on the theory of dynamic systems and generated from this interpretation two new descriptors of HRT. In addition, we created an algorithm for the study of the morphology of electrocardiogram (ECG) waves during HRT and demonstrated its applicability using the amplitude of the T wave. During the development of this algorithm, we also introduced special signal processing methods capable

of dealing with ECG signals recorded from different devices and with diverse properties. The aim of this project was also to evaluate if these new signal processing algorithms were suitable for the study of postextrasystolic change of ECG waves. The results shown here were published in form of a journal paper [41] and presented in two conferences [66, 67].

4.2 Materials and Methods

4.2.1 Data

For the analysis of HRT phenomena, ECG data recorded from patients suffering from frequent VEBs are needed. In addition, algorithms for the automatic detection and classification of ventricular ectopic beat (VEB) are also required. Thus, in this work, we used separated data sets that allowed us to work with the following two applications.

For the development (training and testing) of our classification algorithm, the MIT-BIH Arrhythmia Database from *physionet.org* was used [31]. A total of 81,844 beats were used for training and testing. In this data set, a two channel ECG signal with a sampling rate of 360 Hz was available. In this work, only one of the two channels was used to avoid redundancy of information. The ectopic beats in the database were manually annotated by experts. In order to validate the algorithm, another data set provided by the company Biosigna GmbH was used. The data set contained 56 patients with frequent ectopic beats was used. In this second data set, the signals were recorded for one hour using a standard 12 lead configuration and a sampling rate of 500 Hz. The ectopic beats were also manually annotated by experts. A total of 290,149 beats were used in the validation process.

For the system theoretical approach to HRT and the analysis of postextrasystolic T waves, a subgroup of the validation data set was considered. Only the patients having at least eight VEB fulfilling the HRT rules were used. In addition, a further recording provided by Prof. Dr. rer. nat. Wilhelm Stork and his research group at the Institute for Information Processing Technologies (ITIV) at the Karlsruhe Institute of Technology (KIT) was also included so that a total of 14 patients were incorporated in this study. This recording had a duration of 9.5 days and a sampling rate of 256 Hz.

4.2.2 Signal Processing Workflow

In order to perform an HRT analysis, a sequence of processing steps are needed. The workflow begins with the filtering of the raw ECG signals to remove the typical artifacts. It then continues with the detection of the QRS complexes and the T wave. In order to classify the QRS complexes and separate the normal ones from the VEB, a support-vector-machine (SVM) is used. The features given to the SVM are of rhythmical and morphological nature and were computed to reflect deviations from a template beat. The signal processing steps will be explained in the following section.

4.2.2.1 Filtering the ECG Signal

Depending on the application and kind of information that should be gained from the ECG, the filtering process can be adapted. For the detection of the QRS complexes, the ECG was first filtered with a band-pass in the band from 2 to 40 Hz. For the T wave detection the cutoff frequency of the high-pass filter was set at 0.3 Hz in order not to affect the morphology of the T wave. However, once the ECG waves have been detected, a new filtering process was used prior to the classification step. The idea behind this procedure is to retain as much information as possible from the template beat so that the classifier can fulfill its separating task. An adaptive approach was chosen, where the cutoff frequencies of the filter are chosen depending on the spectral properties of the template beat. They were respectively chosen at the frequency values where 2 and 95 % of the total spectral power was located. Mathematically speaking, we used the following equations to compute the upper cutoff frequency:

$$f_{lowpass} = f \left| \left\{ \frac{\int_0^f |\mathscr{F}\{template(t)\}|^2 df'}{\int_0^{f_{nyquist}} |\mathscr{F}\{template(t)\}|^2 df'} = 0.95 \right\} \right. \tag{4.1}$$

The operator $\mathscr{F}\{\cdot\}$ denotes the Fourier transform of the signal. For the cutoff frequency of the high-pass filter, an analogous equation was used.

$$f_{highpass} = f \left| \left\{ \frac{\int_0^f |\mathscr{F}\{template(t)\}|^2 df'}{\int_0^{f_{nyquist}} |\mathscr{F}\{template(t)\}|^2 df'} = 0.02 \right\} \right. \tag{4.2}$$

The frequency $f_{nyquist}$ is defined as half of the sampling rate of the discrete-time ECG. It is assumed that the sampling rate has been properly chosen to avoid aliasing in the discrete signal.

4.2.2.2 Detecting the QRS Complex

The detection of the QRS complexes was based on the stationary wavelet transform and the Haar wavelet was used for decomposition [47]. The first step of the procedure was to extract the absolute valued detail coefficients $D_n(t)$ at the corresponding decomposition level around 15 Hz. An adaptive (time and signal dependent) threshold was chosen dependent of the moving average of the absolute detail coefficients. Values above the threshold were marked as QRS complexes.

$$Th(t) = k \cdot MA\{|D_n(t)|\} \tag{4.3}$$

The operator $MA\{\cdot\}$ denotes the moving average. The threshold was optimized varying the parameter k so that the variance of the resulting RR time series was minimized.

4.2.2.3 Detecting the T Wave

The method used to detect and delineate the T wave was based on the correlation of each local T wave with a T wave template. For that purpose, the T wave template had to be built first. This procedure began with the detection of the maximal amplitude of the ECG signal in the interval after the QRS complex and before the P wave. This point was labeled as the peak of the T wave. From there, an interval of $\pm$ 160 ms was extracted. The template was then created averaging the T waves of higher quality. For that purpose the T waves having a corrupted morphology were removed from the group. Those outliers were found performing a principal component analysis (PCA) on all the extracted T waves and calculating the Hotelling's T statistics [68]:

$$T_k^2 = \sum_{i=1}^{m} \frac{z_{k,i}^2}{\lambda_i} \quad k = 1,2,...,K \tag{4.4}$$

The kth T wave in the data set has a Hotelling's T^2 value of T_k^2. The letter i corresponds to the index of the principal component for which the scores $z_{k,i}$ were computed as projections onto that same component. Those same scores have a variance of λ_i. The T waves chosen to build the template are the ones having a T_k^2 value below the average among all T_k^2. Once the template has been established, it is delineated using the tangential method [69], which delivers the beginning and end of the wave.

For the delineation of each T wave in the ECG signal, the template was used as reference. For this purpose, the T wave template was shifted within the interval after the QRS complex and before the P wave. In addition, the width of the template was also varied to account for heart rate dependent variations. The combination of shift and width that maximized the correlation between the template and the local T wave was used to delineate the local T wave. The beginning and end points of the matching template were set as beginning and endpoint of the local T wave.

4.2.2.4 Generating a Patient Specific Template

A normal beat can look different depending on patient and ECG lead. Thus, our approach to classify ectopic beats assumed that for each patient and each ECG lead, ectopic beats were different (in morphology and rhythm) from normal beats in the same signal. Hence, a template must be a good representative of the normal beats not only in their morphology but also in their rhythmical properties. In order to build such a template, the rhythmical properties were assessed first. A Poincaré plot was built using the RR time series and the points placed near the bisectrix of the graph were considered for a second stage. Here, the morphology was taken into consideration. Using the correlation coefficient, the beats having

too little similarity with the other beats were excluded. At the end, an average signal was built that represents the template. Figure 4.1 shows the process of building the template.

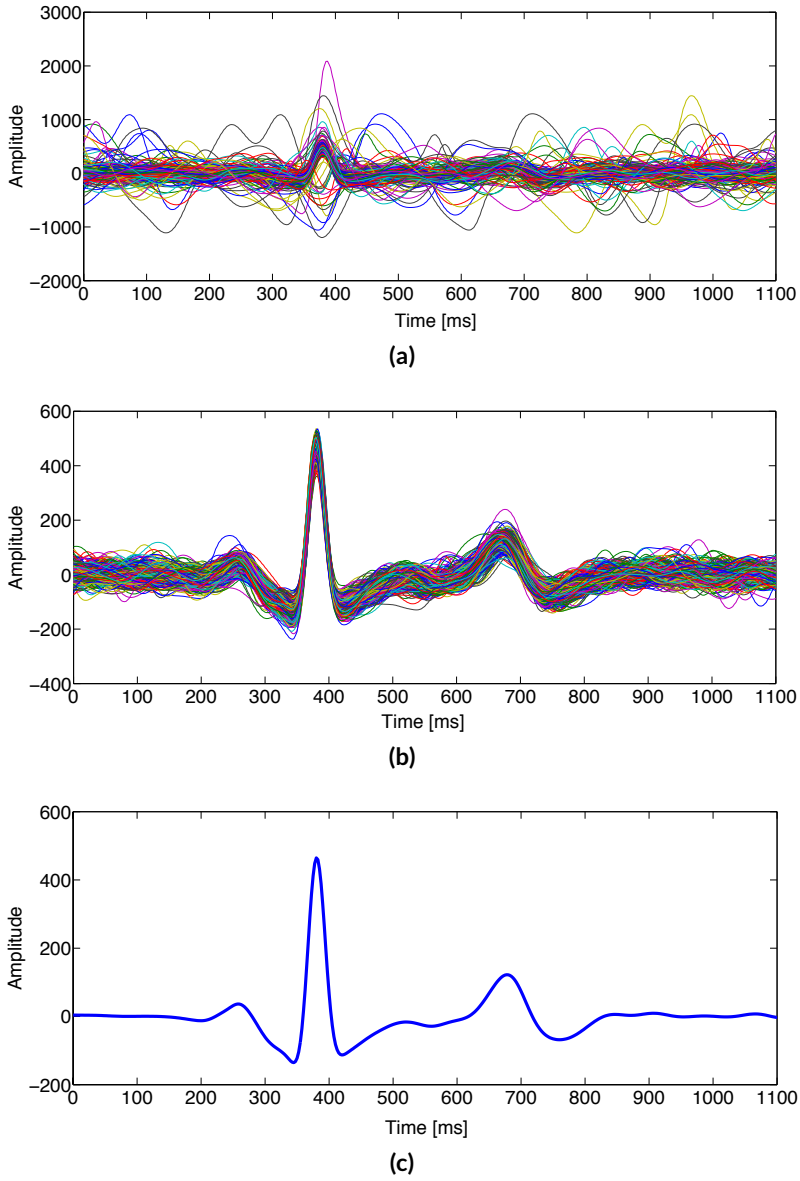

Figure 4.1: (a): All beats extracted from a 30 minute ECG signal. (b): Selected beats to compute the template. (c): The template is a clean smooth signal and a good representative of the normal beats. This figure was reprinted from publication [41] with permission from the publisher.

4.2.2.5 Feature Extraction from the QRS Complex

A classifier, in our case the SVM, assigns a class depending on the feature values computed from each observation. In this work, we developed an SVM that differentiates between

three classes, normal beat, VEB, and atrial ectopic beat (AEB) by examining only the QRS complex. The AEB differ from normal beats only in their rhythmical properties, while the VEB have different morphological and rhythmical characteristics. Therefore, features were created to capture the two types of properties.

The rhythmical features were obtained from the RR time series and its reciprocal time series, the instantaneous heart rate. All ectopic beats were expected to have a shortened coupling interval and a longer compensatory pause. Using this idea, a total of 20 rhythmical features were created that included in its calculation the information coming from one or more beats prior and after the current beat being analyzed. In addition, another 35 properties were extracted from the morphology of the QRS complex. Some examples of those features are computed from maximal and minimal amplitude of the beat, area under the curve, maximal and minimal slope, width, symmetry, central moments, statistical properties of the amplitude distribution, spectral properties, wavelet coefficients or PCA scores. In total, 55 properties of the QRS complex were used to train and test the SVM.

4.2.2.6 Classifying Beats with the SVM

As mentioned previously, the features obtained from normal beats should be similar to the ones from the template, while ectopic beats should have strongly different properties. Therefore, the feature values obtained from every patient and every signal were normalized using the values from the template. The resulting deviations were used to train the SVM. We chose a soft margin SVM with Gaussian kernel and found the optimal parameters for it to be $log(\Gamma) = 1.9$ and $log(C) = 0.14$. The optimal parameters were found using the grid search optimization.

4.2.2.7 Artifact Detection

Some artifacts coming from movement, loose electrodes, muscular activity or electromagnetic interference can overlap in spectrum with the ECG signal and are not removed after the filtering process. If they affect the normal morphology of a QRS complex, they can also lead to wrong classifications. Therefore, it is important to remove beats labeled as VEB that were probably wrongly classified.

Beats having amplitudes or energies too large to be physiologically possible were detected comparing the energy of the beat with the one from the template. Normal beats that were wrongly classified as ectopic because they are too noisy can be found calculating the complex coherence between the template and the other beat [70]. Artifacts spreading over various beats so that a sequence of wrongly classified ectopic beats appeared were detected using the normal beats at the border of the sequence. Those normal beats were also corrupted but not that strongly. A lower correlation coefficient between the template and local beat as the border of the artifact was expected in that case.

4.2.2.8 Multichannel Analysis

A multichannel ECG signal was processed lead by lead. This procedure can have the drawback that the detected and classified beats can vary among channels. So for example, a QRS complex is found in some of the channels but in others it is not, or a QRS complex is classified as normal in some channels but in others it is labeled as ectopic. In order to synchronize information among all channels, a voting algorithm is used in which the location of the QRS complexes, the T waves and the classification of the beats is decided by letting every ECG channel have one vote. The decision having the majority of the votes is then made and generalized for all channels. If a tie arises, the most probable case is chosen according to a-priory knowledge.

4.2.3 System Theoretical Approach to HRT

Different interpretations of the HRT curve have been introduced in the past. For example, Schneider et al. [71] proposed an approximation using a sine function with time-dependent frequency and hypothesized that the parameters describing that frequency could predict mortality in patients with chronic heart failure. We proposed that HRT is the response of a feedback controlled loop to an external disturbance. In this case, the perturbation was the VEB and the drop in blood pressure it causes while the regulated variable is the RR time series adapting to compensate the pressure drop. In terms of system theory, we defined the HRT curve as the step response of a discrete second order linear time invariant (LTI) system. The following mathematical model is used:

$$y(k) + a_1 \cdot y(k-1) + a_2 \cdot y(k-2) = b_0 \cdot x(k) + b_1 \cdot x(k-1) + b_2 \cdot x(k-2) \tag{4.5}$$

The input variable $x(k)$ is a unitary step while the output signal $y(k)$ is the recorded RR time series after the coupling interval and compensatory pause of the VEB. The coefficients of the difference equation were estimated using the least squares method [51]. The two solutions $z_{\infty 1}$, $z_{\infty 2}$ of the characteristic equation of the difference equation (also called poles of transfer function) were also computed because they contain valuable information about the dynamical properties of the system:

$$z^2 + a_1 z + a_2 = 0 \tag{4.6}$$

The two solutions $z_{\infty 1}$, $z_{\infty 2}$ were then mapped to their continuous time counterparts using the following transformation:

$$s_{\infty i} = \frac{1}{T_{mean}} \cdot ln(z_{\infty i}) \tag{4.7}$$

Here, T_{mean} is the mean RR interval during HRT and the $ln(\cdot)$ denotes the complex natural logarithm. Using the two parameters $z_{\infty 1}$, $z_{\infty 2}$, the damping coefficient d and the

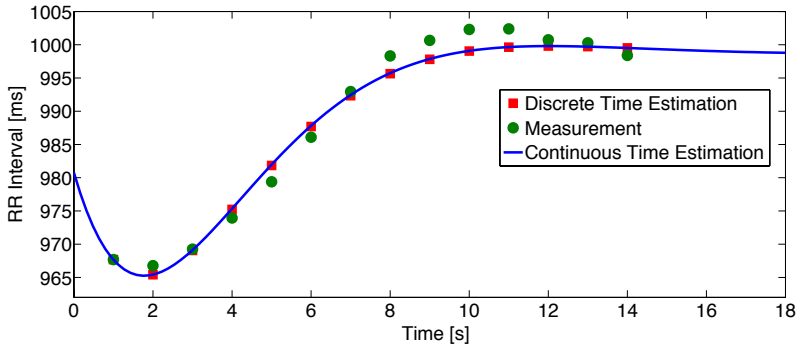

Figure 4.2: A normal HRT curve together with the approximations from the step response of a discrete and continuous LTI system. The parameters $d = 0.73$ and $\omega_0 = 0.45\,s^{-1}$ were estimated for this system. This figure was reprinted from publication [41] with permission from the publisher.

resonance frequency ω_0 of the continuous time second order system were calculated in the following manner:

$$\omega_0^2 = s_{\infty 1} \cdot s_{\infty 2} \tag{4.8}$$

$$d = \frac{s_{\infty 1} + s_{\infty 2}}{2\omega_0} \tag{4.9}$$

The interpretations of these two parameters can be given from the theory of vibrations. The damping coefficient d is a measure of the stability of the system. The higher d, the lower the amplitude of the oscillation. For $d = 0$, the system is critically stable and the oscillation does not decay, while for $d \geq 1$ the system does not oscillate. On the other hand, the resonance frequency ω_0 is a measure of how fast a system responds to an external input or how fast it oscillates. Figure 4.2 shows the HRT curve displayed in figure 2.7 together with its discrete time approximation and its continuous time counterpart.

4.2.4 Influence of a VEB on Subsequent ECG Waves

In order to quantify changes in the ECG signal, several morphological descriptors have been used in the past. The mean value of the descriptor or its variation can be used to predict a particular outcome for a given patient. For example, Zabel et al. used morphological features of the T wave to stratify risk of cardiac death (CD) in patients with a history of myocardial infarction [72]. For the investigation of the influence of a VEB on the subsequent ECG waves, we developed an algorithm that resembles closely the procedure used to quantify HRT. In the algorithm the following steps were carried out:

- First, after signal preprocessing, all VEB in the signal were found and the ones fulfilling all HRT rules were selected. The rules can be found in [73].
- Second, five waves prior and 15 after each VEB were segmented and their morphological features were computed generating a local time series for each feature.
- Third, for every ECG signal, so many time series for a given feature were generated, as the number of VEB present in the signal. The time series are averaged producing

one smooth sequence of morphological values. The same procedure was carried out with the segmented waves so that the evolution of the wave morphology from beat to beat can be visualized too.

- Fourth, the time series of each feature was quantified with the two parameters presented in the next section.

The feasibility of the algorithm was investigated using the T wave and its maximal amplitude as morphological descriptor. It is important to mention that the same procedure can be applied to the other ECG waves and all possible features. Figure 4.3 shows the changes of a postextrasystolic T wave in comparison to a T wave prior to the VEB. The change in morphology of the postextrasystolic T wave is called postextrasystolic T wave change (PEST) for short.

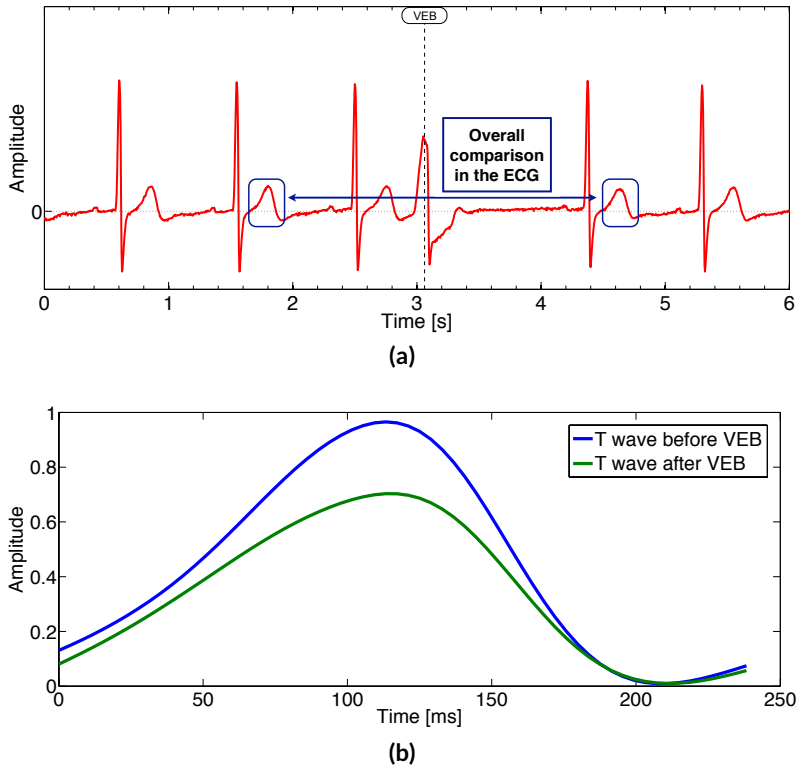

Figure 4.3: (a): ECG signal in the vicinity of a VEB. To visualize PEST, the last T wave prior and the first wave after the compensatory pause are compared. (b): From the averaged sequence of segemented T waves in the vicinity of the VEB, the last wave prior to the VEB and the first wave after the compensatory pause are displayed here. A reduction in T wave amplitude, width and a higher asymmetry can be observed. This figure was reprinted from publication [41] with permission from the publisher.

4.2.5 Quantification of Postextrasystolic Change

The shape of the postextrasystolic T wave went through an initial change and recovered with every beat that passed by. A dynamical behavior of the amplitude of the T wave can be observed in figure 4.4a. It seems to be described by an exponential trend. A discrete and a continuous-time approximation of this evolution using a first order difference equation is also presented in 4.4b.

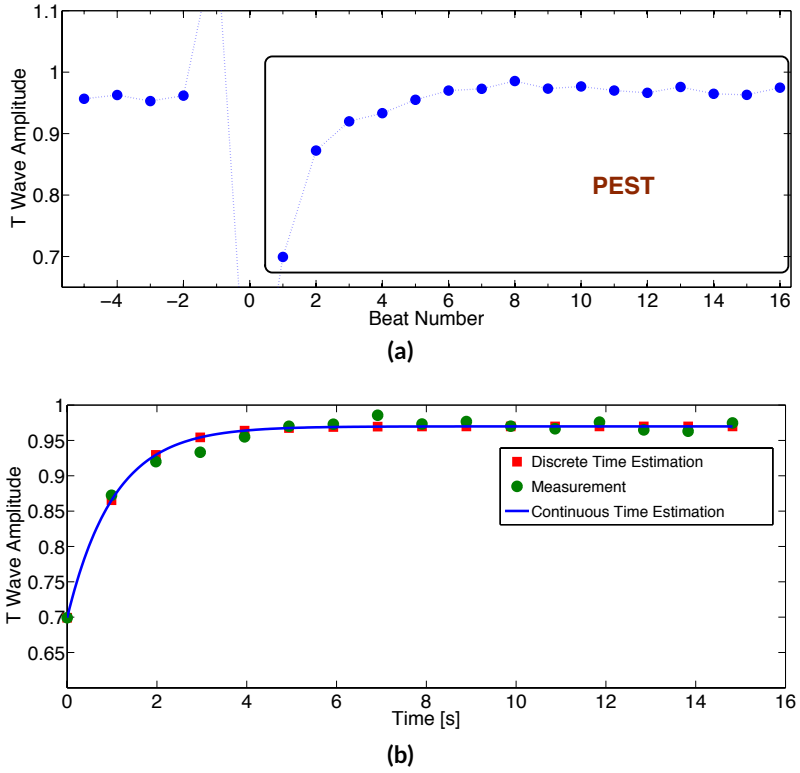

Figure 4.4: (a): Time evolution of the amplitude of the T wave in the vicinity of VEB. A clear reduction of the amplitude can be observed after the compensatory pause followed by an exponential restitution to its original value. (b): The PEST sequence was approximated with an exponential curve arising from a first order difference equation. The discrete and continuous time approximations are displayed. This figure was reprinted from publication [41] with permission from the publisher.

In order to characterize the PEST time series, we introduced two descriptors resembling the HRT parameters: morphological change onset (MCO) and morphological change slope (MCS). We defined them as follows:

$$MCO = \frac{MF(1) - \frac{1}{4}\sum_{i=-5}^{-2} MF(i)}{\frac{1}{4}\sum_{i=-5}^{-2} MF(i)} \tag{4.10}$$

$$MCS = \frac{MF(2) - MF(1)}{t(2) - t(1)} \tag{4.11}$$

$MF(i)$ is the morphological feature at the position i, in our case the maximal amplitude of the T wave. $t(i)$ is the time at which the ith maximum of the T wave is located. The difference $t(2) - t(1)$ corresponds with first RR interval after the compensatory pause. Figure 4.5 shows the PEST and its characterizing parameters for the same subject used in figure 4.4.

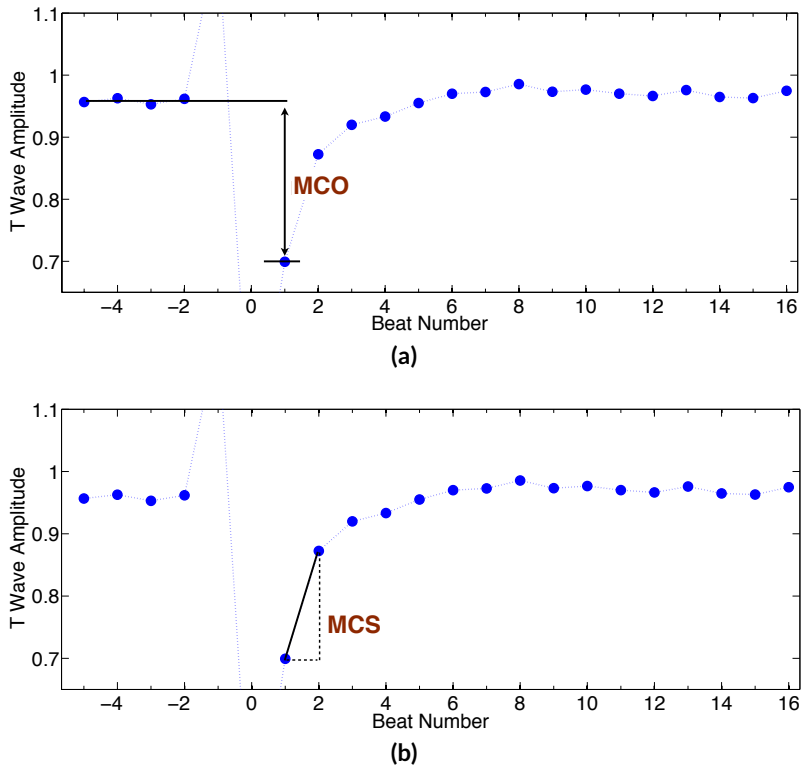

Figure 4.5: (a): Graphical representation of the parameter MCO used to quantify the inital change in morphology of the postextrasystolic T wave. (b): Graphical representation of the parameter MCS used to quantify the inital change in morphology of the postextrasystolic T wave. This figure was reprinted from publication [41] with permission from the publisher.

4.3 Results

The first goal of this work was to evaluate whether the signal processing workflow developed to detect and classify VEBs was indeed suitable for the later HRT analysis. In a second step,

we investigated if the proposed algorithm was capable of capturing morphological changes in the posextrasystolic waves. The results achieved for these two goals are presented in the first and second parts of this section respectively.

4.3.1 Evaluation of the Classification Algorithm

The classification algorithm used to find the VEB was evaluated using the validation data set. Three scenarios were compared. In the first one, no multichannel synchronization and no artifact detection were used. In the second variant, we allowed only the multichannel synchronization but left the artifact detection out. In the third scenario, we included both the artifact detection and the multichannel synchronization. Again, multichannel analysis and artifact detection were introduced in section 4.2.2.8 and 4.2.2.7. Table 4.1 presents the results obtained in this study. The best configuration was achieved using the multichannel synchronization and the artifact reduction. Here, a correct rate of 99.38 %, a SEN of 86.38 % and a PPV of 77.24 % were achieved. For the computation of SEN and PPV, we grouped the AEB and the VEB together and labeled their annotation as a positive event. The normal beats were marked as a negative event.

Table 4.1: Results of Evaluation of the Classification Algorithm

Adaptive filter	Artifact detection	Multichannel analysis	Correct Rate [%]	SEN [%]	PPV [%]
no	no	no	98.31	90.84	44.26
yes	yes	no	98.75	88.73	51.24
yes	yes	yes	99.38	86.38	77.24

4.3.2 PEST Among Patients in the Study

We also investigated whether a modification of the postextrasystolic T wave could be captured by the algorithm introduced in this work. We considered a T wave to be modified if any of its 12 morphological features changed significantly. For statistical significance testing, we compared the mean feature value of the waves prior and after the VEB using an ANOVA test. A change was considered significant if the statistical test delivered an error probability of $p < 0.05$. Table 4.2 shows the results of this study. A significantly modified postextrasystolic T wave was observed in 12 of the 14 patients. For the sake of completeness, we also included the HRT risk class in the table.

Table 4.2: Results of the study done to investigate the influence of a VEB on the T wave of the first subsequent normal beat

Subject number	Number of VEB	HRT risk class	Modified T wave
1	8	0	yes
2	11	0	yes
3	11	1	no
4	12	0	yes
5	15	2	yes
6	15	0	yes
7	21	1	yes
8	25	1	yes
9	26	0	no
10	33	0	yes
11	35	0	yes
12	42	0	yes
13	80	0	yes
14	590	0	yes

4.4 Discussion

A signal processing workflow was created for the detection and classification of ectopic beats in the ECG. The achieved correct rate of 99.38 % in the detection of the VEBs gave us confidence in the developed signal processing workflow and demonstrated the applicability of the classification algorithm. However, it is important to mention that even though the correct rate seemed high at first sight, it may be influenced by the strong imbalance of the classes within the data set. We had predominantly more normal beats in the training set than ectopic ones. This leads to a classification system dealing better with normal beats than with their ectopic counterparts. The lower SEN of 86.38 % and the PPV of 77.24 % were still within the range of other published studies [7, 74, 75] leading us to the conclusion that although the classification method can still be improved, it is good enough to the study the HRT-related phenomena.

A system theoretical approach to HRT was introduced and the interpretation of the HRT curve as a step response of a second order system was proposed. An algorithm for the estimation of the parameters damping coefficient d and resonance frequency ω_0 was developed with the aim of characterizing the HRT curve. We believe that these parameters give a global characterization of the HRT curve because they consider all points and could be used to better characterize the control process performed by the autonomic nervous system after the blood pressure drop because of a VEB.

The influence of the VEB on subsequent ECG waves was studied by means of the T wave. Specifically, the time evolution of the maximal amplitude of the T wave was observed. We found that a VEB can lead to an initial change in T wave morphology followed by (what could be) an exponential recovery to its original shape. For the characterization of this recovery phase, the parameters of a discrete first order LTI system were proposed. We also observed that PEST was present in 12 from 14 patients. This demonstrates on one hand that

our algorithm is capable of capturing PEST phenomena, and on the other hand that PEST appears to be common among randomly selected patients with frequent VEB. However, the HRT risk classification did not coincide with the significant presence of PEST. Due to the small number of patients, it is impossible to generalize this finding. Nevertheless, if HRT risk classification is indeed uncorrelated to significant PEST, this finding would demonstrate that morphological changes in the ECG contain new undiscovered information not found in its rhythmical properties. This possible conclusion motivates also the idea of proposing PEST as a risk stratifier and investigating its predictive power for outcomes like CD in patients with a history of myocardial infarction or chronic heart failure (CHF).

The results of this study raise also the question of the physiological mechanisms behind PEST. It is well known that the shape of the T wave depends, among other factors, on instantaneous heart rate [69]. Thus, a simple explanation for PEST could be that the morphological change arises from the acceleration of heart rate after the VEB. However, normal HRT is characterized by a very small initial reduction of the RR interval. As can be seen in figure 2.7, the initial reduction of the RR interval is around 50 ms. In addition, the RR intervals in HRT have an oscillatory behavior, while PEST is characterized by a monotonic restitution. For these reasons, we conclude that instantaneous heart rate changes are probably not the mechanisms behind PEST. A more promising explanation could be given based on the findings of in-silico studies. Keller et al. [76] demonstrated that the shape of the T wave arises from the heterogeneities in the repolarization of the ventricles and the delayed rectifier potassium current I_{Ks} plays a major role in this process. Thus, we believe that PEST must be somehow related to changes in either the ionic concentrations or the membrane currents at cellular level. In any case, it is impossible to definitely conclude alone from this study what the physiological explanation for PEST may be and what diagnostic power it may have.

4.5 Outlook

In order to investigate the predictive power of PEST, a larger clinical study is needed. The parameter MCO and MCS could be evaluated as risk predictors in a retrospective follow-up study. A data set with patients suffering from CHF with a known outcome of CD would be ideal for this study.

On the other hand, in order to better understand the mechanisms behind PEST, it would be very interesting to study this phenomenon also in healthy subjects. By doing so, we could learn if PEST is a normal phenomenon that manifest in everyone when a VEB appears and how large is its effect on the ECG. The study can also be complemented by an in-silico study in which the ionic concentrations and currents at cellular level would be observed directly and could deliver insights on the mechanisms behind PEST.

These two studies were indeed carried out and their results are presented in the next two chapters of this thesis.

4.6 Conclusion

In this work, we introduced a new interpretation of the HRT based on the theory of LTI systems and proposed an algorithm to obtain the damping coefficient and the resonance freqeuncy of the HRT curve. Furthermore, we created and optimized the signal processing algorithm and observed that PEST was a phenomenon characterized by an initial change of the postextrasystolic T wave morphology followed by a recovery to initial shape. More research is needed to conclusively understand the underlying mechanisms behind PEST and its clinical value.

CHAPTER 5

Postextrasystolic T Wave in Healthy Subjects

5.1 Introduction

In the previous chapter, the concept of postextrasystolic T wave change (PEST) was introduced and defined as the short-time variation of T wave shape after a ventricular ectopic beat (VEB). We also showed that morphology of the wave undergoes an initial modification and recovers steadily with every beat. The PEST phenomenon has been known for more than one hundred years [77] and it has been observed in patients with different pathological conditions [78, 79]. However, the physiological mechanisms behind PEST are not fully understood. Some authors have proposed that PEST may be related to cardiac memory and prematurity of the VEB, while others believe it is rather a consequence of the increased blood preasure after a long compensatory pause [80–83]. It is also unknown if PEST has any diagnostic value. As a matter of fact, it is unclear if PEST is a normal phenomenon present in healthy subjects and if so, how does it manifest.

In order to shed light on this topic, we studied PEST in a group of ten patients with structurally healthy ventricles. In concrete, we turned our attention to two open questions. First, is PEST present in healthy subjects, and if so, what are its properties. Second, are the PEST parameters correlated to the heart rate turbulence (HRT) parameters or the basal heart rate of the patients. In addition, a large multiscale electrophysiological simulation was performed with the aim of recreating PEST and gaining more information about the electrophysiological mechanisms behind it. A total of 15 beats were simulated in the temporal vicinity of a VEB. This work was carried out in close cooperation with the group BSICoS at the University of Zaragoza and the Department of Signal Theory and Communications at the University Rey Juan Carlos in Madrid. It was published in form of an internationl conference paper [84].

5.2 Materials and Methods

5.2.1 Clinical and Simulated Data

The clinical study used for this work had been previously designed to investigate HRT and its dependency on coupling interval and resting heart rate. It was recorded at the Arrhythmia Unit at University Hospital Virgen de la Arrixaca de Murcia, Spain and provided to us from our cooperation partners at the Department of Signal Theory and Communications of the Rey Juan Carlos University in Madrid, Spain and the BSICoS Group at the University of Zaragoza, Spain. This study was also used in the past to investigate other related topics such as the measurement of HRT using only a photoplethysmographic sensor [85]. The data contained the recordings of ten patients with structurally healthy ventricles that had to go through catheter ablation therapy because of a supraventricular tachycardia. After the ablation procedure was finished but before leaving the electrophysiology laboratory, each patient underwent a protocol of right ventricular stimulation triggering ectopic beats from the apex. The stimulation was performed every 20 sinus beats so that at the end of the procedure, between 11 and 20 VEB (depending on the patient) were suitable for HRT and PEST analysis. The electrocardiogram (ECG) was recorded at a sampling rate of 1 or 2 kHz.

On the other hand, the in-silico study was performed with the electrophysiological model from ten Tusscher et al. [86] and a monodomain simulation was carried out with the software acCELLerate [87, 88]. The full torso geometry was obtained segmenting a magnetic resonance image from a healthy subject. Anisotropic electrical conductivities were chosen appropietely for each tissue class including ventricles, skeletal muscle, fat, blood, lung, liver and spleen. In the simulation, the depolarization wave of the normal beats originates in the Purkjnie muscle junctions and propagates to the neighboring voxels triggering each time an action potential (AP). For the repolarization scheme (responsible for the generation of the T wave in the ECG), regional dependencies of the AP were included in the model together with transmural heterogeneity [89, 90]. It is also important to mention that no ion channels dependent on mechanical stretch were included so that only electrophysiological phenomena could be analyzed. In total, five sinus beats prior to the VEB, the VEB itself (including the coupling interval and the compensatory pause) and another nine normal postextrasystolic beats were simulated. The RR time series used for this simulation was obtained from the recording presented in figure 2.7 and corresponded with a normal HRT. The simulated ECG had a sampling frequency of 1 kHz. The simulated ECG signal was treated in the same way (the same algorithms were applied) like the other ten from the electrophysiological study. Thus, the simulation was treated as if it had been the 11th patient of the electrophysiological study. Figure 5.1 shows a portion of the simulated ECG including the leads Einthoven I, II and Wilson V1. In the same figure, the ventricular anatomy displaying the transmembrane voltages in the heart tissue and the origin of the ectopic beat can be observed.

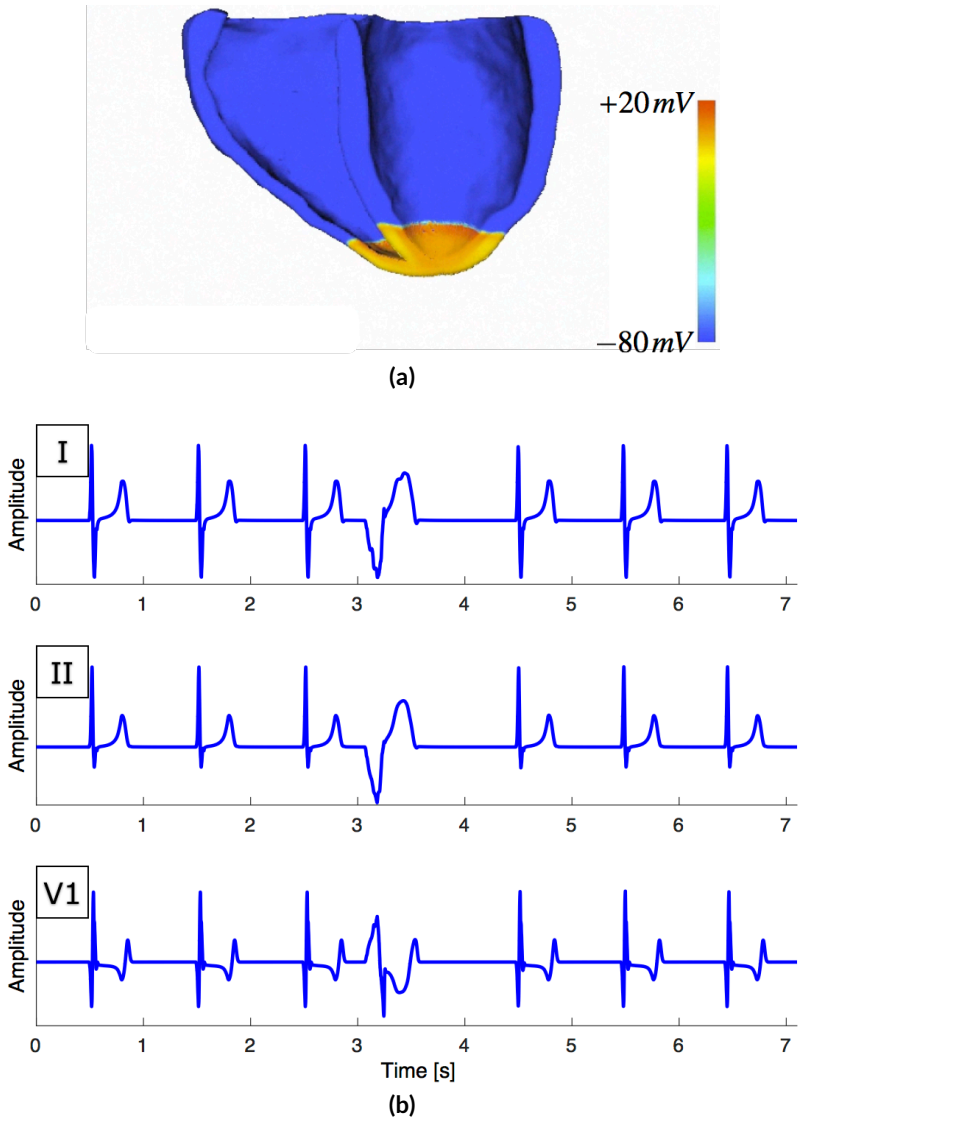

Figure 5.1: (a): Cut of the ventricular anatomy displaying the transmembrane voltage coded in color. The ectopic depolarization wave can be seen originating in the ventricular apex. (b): A portion of the simulated ECG centered around the VEB. This figure was reprinted from publication [84] with permission from the authors.

5.2.2 Signal Processing Workflow

The signal processing steps carried out to obtain the needed information from the ECG were described in the previous chapter and were intended to remain the same in this work. However, a challenging task arose when detecting the paced VEB in the ECG. The solution proposed to overcome this problem will be presented in the next section.

5.2.3 QRS Detection and Classification

As it turned out, the VEB had a very low amplitude in many of the ECG channels. This lead to a large amount of VEB not being detected and not being used for further HRT and PEST analysis. To overcome this problem, we had the idea of finding an optimal patient specific linear combination of the ECG channels that delivered a large VEB amplitude facilitating automatic detection. However, the task was actually more complex than that. The required linear transformation had to be performed before the automatic QRS complex detection because otherwise the VEB would not even have had the chance of being detected. To solve this problem, we came up with an indirect approach. If the reason for the low amplitude of the VEB relied on the fact that those beats were perpendicular to the normal ones in the ECG lead space, then we could first find the direction that maximizes the normal beats and look afterwards for an orthogonal subspace in which the direction that maximizes the amplitude of the VEB can be found.

In order to first find the mixing vector $\mathbf{w}$ that maximizes normal QRS complex amplitude, the multichannel ECG signal was interpreted as a realization of a multidimensional random process $\mathbf{X}$ in the ECG lead space and only the linearly independent channels were taken into consideration. By plotting the ECG leads against each other, a new parametric representation was obtained, where every ECG wave builds a loop. This representation is shown in figure 5.2a for one of the signals in the study. Since there are 20 times more normal beats than ectopic ones in the signal, we assumed that the normal beats would dominate the ECG lead space and that a vector pointing in the direction of the center of mass of all data points would probably also point in the direction of the the normal QRS loop. Thus, the center of mass is defined as the mixing vector $\mathbf{w}$. This is the red vector in figure 5.2a. This vector $\mathbf{w}$ spanned an orthogonal subspace, in which a further principal component analysis (PCA) was performed. Since the normal QRS complex has little power on this plane, the first principal component should point in the direction of the projected VEB loop. All principal components together with the first mixing vector $\mathbf{w}$ span an orthonormal basis $\mathbf{W}$. The ECG is then projected onto this basis ($\mathbf{Y} = \mathbf{X} \cdot \mathbf{W}$) for further analysis.

From the transformed ECG signal $\mathbf{Y}$, we retained only the channels with highest amount of energy containing together at least 90 % of the total energy of the original signal. Typically, no more than three transformed channels fulfilled this criterion. Finally, the transformed ECG was processed with the standard multilead algorithm that includes synchronization among leads. Now, the VEB could be detected in two out of three channels and the HRT and PEST analysis were possible. Figure 5.2b shows the resulting linearly combined channels with highest energy. The first channel is characterized by a spiky normal QRS complex. In the second channel, the amplitude of the VEB is largest. The third channel is orthogonal to both the normal QRS complex and the VEB and is thus characterized by similar amplitudes in all QRS complexes.

The algorithm can be summarized as follows:

- First, the ECG was filtered. In particular the offset was removed and a stable isoline was achieved.

- Second, the mixing vector **w** was computed and the data points were projected onto the orthogonal plane perpendicular to **w**.
- Third, in the orthogonal subspace, a PCA was performed with the aim of maximizing the amplitude of the VEB. For further analysis the number of transformed channels preserved must contain at least 90 % of the original energy of the signal.
- Fourth, the standard multilead processing of the ECG signal that includes synchronization among channels was performed with the resulting linearly combined leads.

5.2.4 Maximizing T Wave Amplitude

Since the idea behind PEST is to measure changes in T wave morphology, it would be of great help if those changes could be somehow amplified to prior the analysis. For this purpose, we combined the linearly independent ECG leads to create a transformed channel with maximal T wave amplitude. By maximizing T wave amplitude, we expected PEST to be also amplified. To achieve maximization of T wave amplitude, we applied a similar procedure as the one used with the normal QRS complexes in the previous section. In this case, however, we used T wave templates instead of the complete signal. The advantage of using the templates bases on the fact that the T wave loop is very clean and the direction of maximization can be found very precisely. Figure 5.3 shows the T wave templates from three leads of the same signal, the T wave loop and the resulting linearly combined channel with a spiky T wave.

5.2.5 Quantifying PEST with One General Feature

In the last chapter, we proposed that the quantification of PEST could be carried out using any morphological feature characterizing the T wave such as the amplitude, the width, the symmetry and so on. However, it would be of great help if we could find a feature that captures the general change in morphology and accounts for changes in all properties. A possible candidate for this task would be the correlation coefficient between the postextrasystolic T waves and a beat prior to the VEB. The squared correlation coefficient has the property of being a number between 0 and +1 making it a very intuitive measure of similarity. So, for example, a large PEST would be characterized by a number significantly lower than +1. However, for this application, the correlation coefficient has the disadvantage of being independent of scaling or offsetting any of the two waves. To overcome this problem, we proposed a new measure of similarity called the $l\_operator$ because it is closely related to the Euclidean norm (or simply the length $l(k)$) of the difference between two time-discrete signals $x(k)$ and $y(k)$ being compared. It is defined in the following manner:

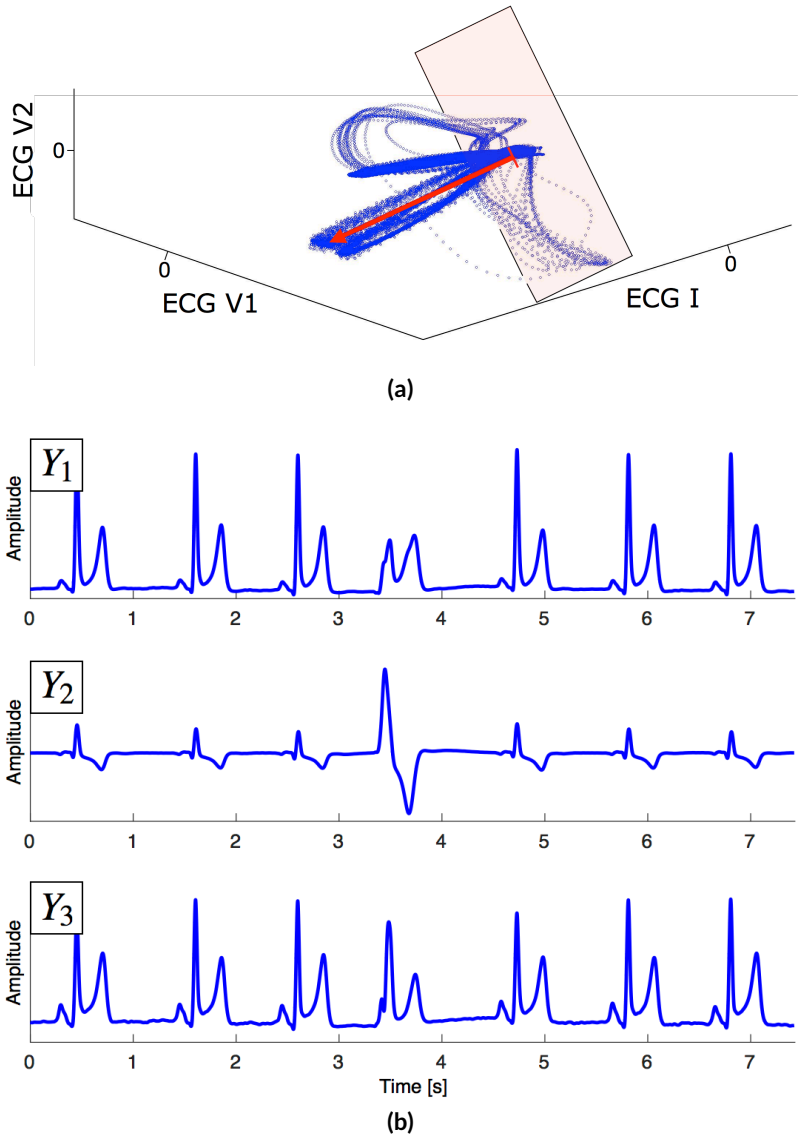

Figure 5.2: (a): ECG signal displayed as a three dimensional parametric representation, where the lead Einthoven I, Wilson V1 and V2 are plotted against each other. The red arrow points towards the center of mass of all data points which is also the direction of the normal QRS loop. The red vector is defined as is the mixing vector $\mathbf{w}$ for the linear transformation. A plane is spanned perpendicular to $\mathbf{w}$. In this plane the direction that maximizes VEB energy is found using a PCA. (b): The first three leads of the transformed ECG signal with respect to the basis $\mathbf{W}$ demonstrate how the first lead has high normal QRS amplitude, while the second lead is characterized by a large amplitude of the VEB. This figure was reprinted from publication [84] with permission from the authors.

$$l\_operator\{x(k),y(k)\} = 1 - \frac{||l(k)||^2}{||x(k)||^2+||y(k)||^2} \tag{5.1}$$

$$= 1 - \frac{||x(k)-y(k)||^2}{||x(k)||^2+||y(k)||^2} \tag{5.2}$$

$$= \frac{2\langle x(k),y(k)\rangle}{||x(k)||^2+||y(k)||^2} \tag{5.3}$$

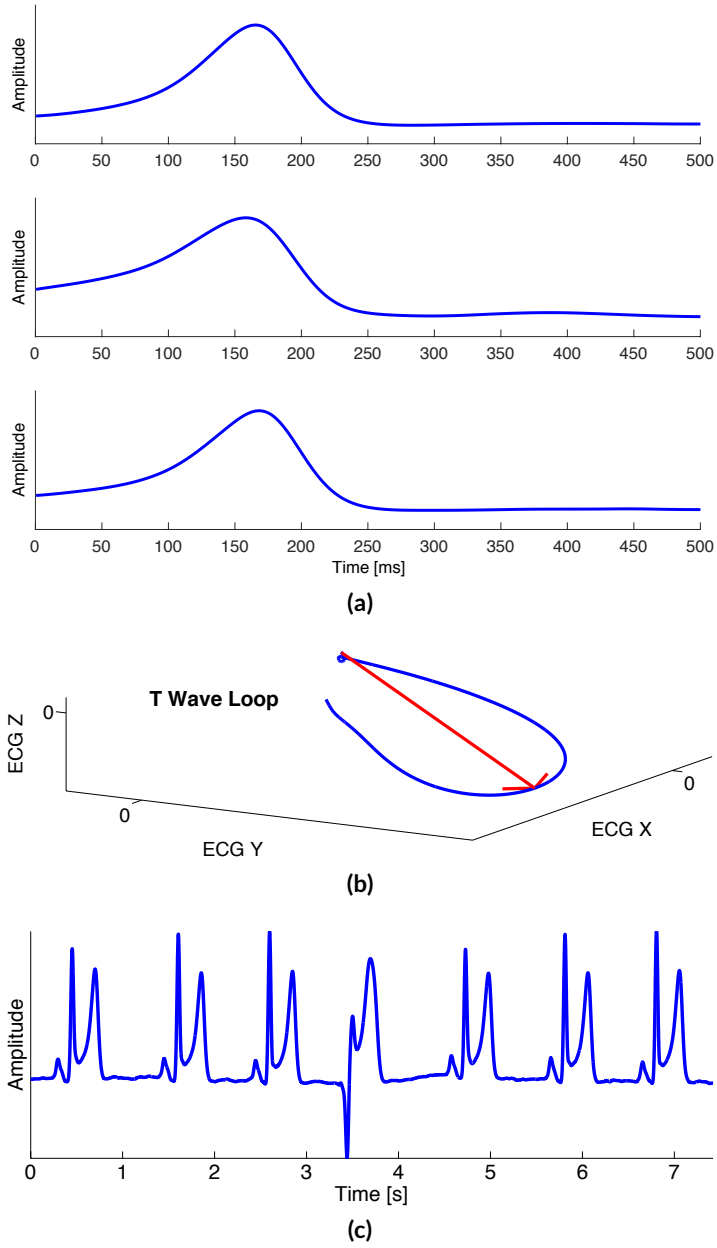

Figure 5.3: (a): T wave template from three leads of the same ECG signal. This kind of templates were used to create a multidimensional T wave loop and find the linear combination that maximizes T wave amplitude. (b): T wave loop and direction of maximal T wave amplitude. (c): ECG signal for which the T wave amplitude was maximized. The signal is characterized by the spiky shape of the T wave. This figure was reprinted from publication [84] with permission from the authors.

The $l\_operator$ is a similarity measure originally based on distance. It has similar properties to the correlation coefficient because it delivers also a number in the interval $[-1,+1]$. However, $+1$ can only be achieved if the two signals are perfectly equal. Scaling or offsetting any of the two signals will deliver a lower value. As for the correlation coefficient, orthogonal signals have also a similarity of 0 when compared using the $l\_operator$. Furthermore, it

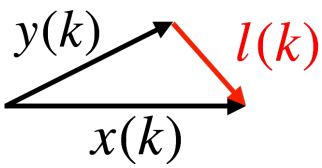

$$||l(k)||^2 = ||x(k) - y(k)||^2$$

Figure 5.4: The *l_operator* is a measure of similarity between the two time-discrete signals $x(k)$ and $y(k)$. It is baser, however, on the Euclidian distance (length of difference) $||l(k)||$ between the two time-discrete signals $x(k)$ and $y(k)$.

resembles the Sørensen-Dice coefficient commonly used in information theory to compare similarity between two binary vectors [91, 92].

The next step in the quantification of PEST was to create a time series of morphological features in the vicinity of the VEB. For that purpose, five T waves prior to each VEB and another 15 afterwards were segmented. A T wave template was created averaging the T waves prior to each VEB. The template was then compared to all waves in its vicinity. Mathematically speaking, the morphological feature was calculated as follows:

$$lop(n) = l\_operator\{T_n(t), Template(t)\} \tag{5.4}$$

Using the mean time series of *l_operator* values, the parameters to quantify PEST were computed using the equations 4.10 proposed in the last chapter. Figure 5.6 shows an example of a time series of *l_operator* values and the PEST parameters.

$$MCO = \frac{lop(1) - \frac{1}{4}\sum_{i=-5}^{-2} lop(i)}{\frac{1}{4}\sum_{i=-5}^{-2} lop(i)} \tag{5.5}$$

$$MCS = \frac{lop(2) - lop(1)}{t(2) - t(1)} \tag{5.6}$$

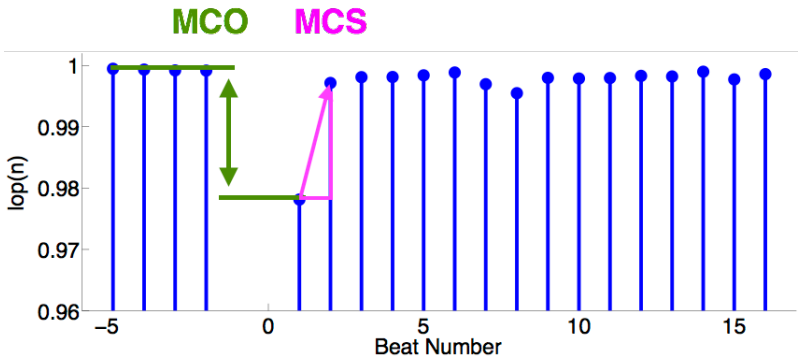

Figure 5.5: Example of a time series of *l_operator* values and the PEST parameters. This figure was reprinted from publication [84] with permission from the authors.

5.3 Results

The parameters morphological change onset (MCO) and morphological change slope (MCS) were computed for all patients in the study and are presented in table 5.1. In the table, the patient number and the amount of VEB used for the analysis are also presented. It is important to recall that patient number 11 is the simulated subject. The table presents also the basal RR interval length and the parameter turbulence onset (TO) and turbulence slope (TS) from the analysis of HRT together with the overall results in the study.

Table 5.1: Results showing HRT and PEST parameters for the patients examined. Patient number 11 is the simulated subject. The overall statistics are given as median and interquartile range (med±iqr). This table was reprinted from publication [84] with permission from the authors.

Patient # Nr.	Basal RR [ms]	Nr. of VEB	TO [%]	TS [ms/beat]	MCO [‰]	MCS [‰/s]
1	1074	14	-3.75	10.90	-0.68	0.65
2	940	20	0.51	2.71	-11.17	11.41
3	851	16	-1.65	7.09	-7.72	7.78
4	1147	17	0.53	27.57	-5.10	2.38
5	736	11	-1.05	1.77	-1.17	1.44
6	911	18	-0.81	4.16	-12.70	14.22
7	708	12	-5.59	12.49	-14.50	20.47
8	744	13	-1.20	7.09	-49.64	66.29
9	952	18	-2.94	7.05	-7.03	7.38
10	1140	11	-7.52	22.50	-2.41	2.10
11	998	1	-2.31	6.20	-1.07	1.16
overall	940±284.25	14±6.50	-1.65±2.68	7.09±7.42	-7.03±10.83	7.38±1.61

5.3.1 Manifestation of PEST among healthy subjects

All patients presented a small but measurable PEST. Even though the strength of PEST was different in every patient, they all had in common that PEST was characterized by an initial reduction of $l\_operator$ value followed by a restitution within one or two postextrasystolic beats. However, the kind of postextrasystolic change was different in every patient. This change could be a reduction (or an increase) in T wave amplitude, a greater T wave width or other changes in symmetry or slope. To illustrate this, figure 5.5 shows PEST in patient number 2, 7 and 11.

In patient number 2, PEST was characterized by a reduction in T wave amplitude in the first postextrasystolic wave and an almost complete restoration of morphology within the next beat. The second postextrasystolic wave had only a slightly lower amplitude than the original one. The third wave had already normal morphology.

On the other hand, PEST in patient number 7 was characterized by an alternating T wave amplitude. The first postextrasystolic wave had a larger amplitude than the template while the second wave had a reduced one. The third postextrasystolic wave was again normal.

Finally, the simulated patient had a very small PEST characterized by an almost unnoticeable increase in amplitude in the first postectopic T wave.

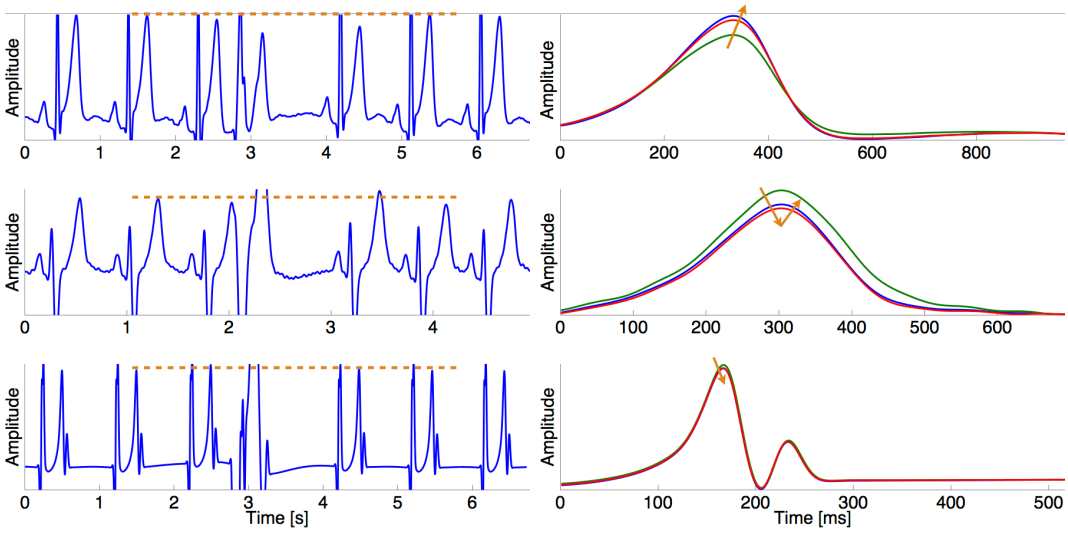

Figure 5.6: The manifestation of PEST was different among the patients from the study. Patient number 2 (upper panel) had a decreased postectopic T wave amplitude. Patient number 7 (middle pannel) had alternating postextrasystolic T wave amplitude. Simulated patient number 11 (lower panel) had almost no PEST. This figure was reprinted from publication [84] with permission from the authors.

5.3.2 Correlation to HRT and Heart Rate

A simple statistical analysis was carried out to investigate if PEST parameter MCO and MCS are related to the HRT parameters TO and TS or the sinus rhythm (basal RR interval) of the patients. Table 5.2 shows the results of the correlation analysis. In general, very low correlations were found between PEST and HRT. On the other hand, PEST and heart rate at rest seem to have a stronger correlation.

Table 5.2: Correlation coefficient between the PEST and HRT together with PEST and basal RR.

	MCO [‰]	MCS [‰/s]
Basal RR [ms]	0.51	-0.55
TO [%]	-0.14	0.08
TS [ms/beat]	-0.18	0.13

5.4 Discussion

The first part of this study suggest that PEST is a normal phenomenon present in subjects with structurally healthy ventricles. This result extends the knowledge found in literature where PEST has been primarily observed in patients with different cardiac diseases. We also found that the strength of the morphological change of the postextrasystolic T wave was patient specific. According to the results of the second part of the study, the patient specific PEST could be related to some extent to the resting heart rate of the patient. However, other patient specific properties of the ECG or the VEB such as duration of the coupling interval, the blood pressure drop after the VEB or the increase in blood pressure at the end of the compensatory pause could also play an important role. More research is needed to definitely conclude what the mechanisms behind PEST are. For now, we can assure that this is an interesting research topic with many open questions to be addressed.

In the first part of the study we also realized that the simulated patient had almost no PEST. We can give two possible explanations for this fact. First, the model did not include ion channels dependent on mechanical strech. This means that the possible reduction of blood pressure after the coupling interval or increase after the compensatory pause does not have any influence on the electrophysiology. This would support the idea that PEST could be related to electromechanical coupling of the heart and postectopic potentiation of contractile strength [93]. Second, the ten Tuscher model is characterized by strong long term stability. This means that the model can be used to simulate many subsequent beats without drifting away from the normal behavior. Even though the VEB pushes the electrophysiological simulation away from its operating point at a stable action potential duration and diastolic interval, the change in those parameters is too little to trigger any modifications at cellular level that can be captured in the surface ECG [94]. Thus, at this moment, we cannot conclude definitely that the explanation for PEST comes from pure electrophysiological phenomena or whether or not it is related to mechanical stress in the myocard. We also do not know if the autonomic nervous system (ANS) is playing a role here.

Even though the number of patients was small, they all had in common that PEST was characterized by an initial change in morphology and a recovery within one or two beats after the compensatory pause. If this result can be generalized, this could mean that structurally healthy ventricles are capable of restoring original electrphysiological conditions within one or two seconds after the initial change. Thus, patients with a higher risk of cardiac afflictions may diverge from this behavior and present, for example, a slower recovery.

Finally, we also found that PEST could be independent from HRT due to the low correlation coefficients. It is thus plausible to believe that PEST parameters are independent biomarkers that can be used for the prediction of cardiac death (CD) (or other complications) in patients with heart afflictions, complement HRT parameters and increase its sensitivity and positive predictive value.

It was also interesting to see that all patients had a relatively small PEST. The median MCO was -7.03 ‰. Such a low number can only be measured accurately if very high signal

quality is given, strong filtering techniques or averaging over a large number of VEB are applied. Otherwise, a PEST analysis may not be possible.

5.5 Outlook

The main priority of a future project in this field should be a larger data set that ensures a stronger statistical power of the study. It would also be interesting to have longer signals with more VEB and other portions free of VEB. This would allow a comparison with other ECG biomarkers coming from the heart rate variability (HRV) or the QT time. In addition, the electrophysiological model used for the simulation can be extended to include electromechanical coupling and stress dependent ion channels. Furthermore, the same simulation can be repeated with a different model, one that has a more sensitive relationship between action potential duration and diastolic interval. By doing so, the changes triggered by a VEB could lead to a larger PEST.

On the clinical side, it would be interesting to investigate PEST parameters as risk stratifiers of CD (or other complications). As a matter of fact, we carried out such a study with patients suffering from chronic heart failure (CHF). The results of that study are presented in the next chapter of this thesis.

5.6 Conclusion

In this work, we showed that PEST is a normal phenomenon that manifest in a different manner among the patients in the data set. PEST is, however, characterized by an initial change of postextrasystolic T wave morphology and a rapid recovery to its original shape within one or two beats. Yet, we did not observe this in the simulation. This is probably because of how the electrphysiological model was conceived. In addition, we also showed that PEST parameter were uncorrelated to HRT parameters, and that they may be related to other patient specific features such as the resting heart rate. More research is needed to evaluate the power of PEST as a risk parameter.

CHAPTER 6

Predicting Pump Failure Progression Death

6.1 Introduction

In the previous chapter, we showed that postextrasystolic T wave change (PEST) is a phenomenon that is present in subjects with structurally healthy ventricles. It is characterized by an initial change in T wave morphology (amplitude, width, symmetry and other properties) and a restitution to the original shape within one or two beats. Although PEST has been also observed in patients with coronary artery disease and left ventricular dysfunction [95], its clinical relevance has not been discovered yet. Specifically, the very few clinical studies performed on the identification of high risk patients based on their PEST properties has been impossible so far. Nevertheless, PEST has not been investigated in relation to chronic heart failure (CHF) and cardiac death (CD). Thus, the aim of this work was to investigate if PEST can be used to identify high risk patients suffering from CHF and complement the predictive power of the heart rate turbulence (HRT) parameters.

In a previous study, PEST was demonstrated to correlate with postectopic contractile potentiation [93]. This is a phenomenon in which the strength of the myocardium increases in the first normal beat after a ventricular ectopic beat (VEB). In the mentioned study, it was observed that PEST was more prominent if myocardial contractility was reduced. This result lead us to postulate that PEST, and in concrete the parameters morphological change onset (MCO) and morphological change slope (MCS), could be used as non-invasive biomarkers to predict pump failure progression death (PFD) as a consequence of CHF. This work was carried out in close cooperation with group BSICoS at the University of Zaragoza and published in form of an international conference paper [96].

6.2 Materials and Methods

6.2.1 Clinical Data

The data set we used for the investigation of risk assessment based on PEST parameters is called MUSIC (MUerte Súbita en Insuficiencia Cardiaca) [97]. This data set was the result of a prospective, longitudinal multicenter study carried out in Spain with the goal of evaluating non-invasive electrocardiogram (ECG)-based biomarkers for the prediction of different types of cardiac death in ambulatory patients with CHF. A total of 992 patients marked with the New York Heart Association (NYHA) class I and II were enrolled and prospectively followed up for a median of 44 months (range: 28 to 51). The medications taken by the patients were not withdrawn for this study. A large portion of the patients included in the data set did not have sinus rhythm because of other heart afflictions such as atrial fibrillation (AFib) or had implantable pace makers or defibrillators. In such cases, an HRT analysis is not possible. For this work, we included only the patients having sinus rhythm for which an HRT analysis could be performed. The resulting cohort contained 537 patients, from which 410 (76.4 %) were survivors at the end of the follow-up period. The non-survivors where classified as follows: 24 (4.5 %) died of non-cardiac causes, 44 (8.2 %) died of sudden cardiac death (SCD) and 59 (11.0 %) died of PFD. The latter group is the one this work was intended for. We also defined the class CD as SCD and PFD together and the class total mortality (TM) as all types of cardiac and other unknown causes of death together. A summary of the clinically relevant characteristics of each patient can be found in table 6.2.

For each patient, a 24 hour standard Holter ECG was recorded. The original 12 leads were reduced to two or three orthogonal leads using the linear transformation according to Dower [98]. The signals were acquired at a sampling rate of 200 Hz. The automatic annotations of the QRS complexes and their classification were also available in the database.

6.2.2 Signal Processing Methods

Processing the Holter ECG in the MUSIC database proved to be challenging due to the relatively low quality of the signals. The processing techniques already existing had to be adapted or redesigned. The modifications will be explained in the following sections.

6.2.2.1 Signal Preprocessing

As mentioned in the previous chapter, a clean T wave morphology is very important for PEST analysis because the postextrasystolic changes are very small. In order to remove the artifacts in the ECG but maintain the morphology of the T wave, the filtering process was modified. First, power line hum was eliminated using a Gaussian filter with a center frequency at 50 Hz and a width of 1 Hz and all harmonics. Second, the signal was filtered with a narrower band

pass filter with cutoff frequencies at 0.3 and 20 Hz to match the frequency spectrum of the T wave. Since baseline wander can go above 0.3 Hz, a second baseline wander removal technique was performed. Here, a two stage moving median filter with window lengths of 0.7 and 1.8 s was applied [90].

After T wave detection, a T wave template was created and compared locally to each T wave. The comparison was carried out in frequency domain. If the local T wave had considerably different spectral properties, a low signal to noise ratio was assumed and the local T wave was removed from the analysis.

6.2.2.2 T Wave Detection

In order to achieve a more robust T wave detection, the stationary wavelet transform (SWT) was used in this case [99]. The procedure began with the cancellation of the P wave and the QRS interval. This was done replacing that signal portion with a smooth sigmoid function. The resulting signal was assumed to contain only T waves. It was decomposed using the biorthogonal 3.3 wavelet up to the level four. The maximal amplitude of the SWT in the segment between two consecutive R peaks was labeled as the T wave maximum. This method was repeated in every channel and synchronization among all channels was performed to correct wrongly detected waves.

6.2.2.3 Quantifying of PEST

The way PEST was quantified remained basically the same but two changes were carried out. First, in order to account for possible low quality T waves that may damage the PEST analysis, a further refinement step was carried out. We required the T waves not to be affected by the VEB ($n = [-5,...,-2] \cup n = [3,...,15]$) to have a high $l\_operator$ value of at least 0.96 when compared with the template. This ensures that only high quality T waves are used as reference when measuring PEST. Second, the parameter MCO was reformulated and the average of $l\_operator$ values of the T waves prior to the VEB was removed from the denominator (see equation 6.1). Since $l\_operator$ values are smaller or equal to one, they can potentiate MCO if low quality T waves are present in the analysis. For this reason, the parameters used in this study were redefined as:

$$MCO = lop(1) - \frac{1}{4}\sum_{i=-5}^{-2} lop(i) \cdot 1000 \ [‰] \tag{6.1}$$

$$MCS = \frac{lop(2) - lop(1)}{t(2) - t(1)} \cdot 1000 \ [‰/s] \tag{6.2}$$

The notation $lop(n)$ represents again the $l\_operator$ value when comparing the T wave template with the T wave number n:

$$lop(n) = l\_operator\{T_n(t), Template(t)\} \tag{6.3}$$

6.2.3 Statistical Analysis

There are many ways of quantifying the predictive power of a parameter regarding a given classification problem. Modern approaches such as cross validation have been sucessfully applied in fields like machine learning [100]. However, in medicine, the question if a parameter can be used for risk assessment is carried out in a more traditional way based primarily on statistical tests. First, the participants in the study are separated according to their outcome at the end of the study. Survivors and non-survivors with their corresponding cause of death are compared always one class against all others with respect to their statistical properties. In this work, that comparison was carried out using a two-tailed Wilcoxon-Mann-Whitney test, which is a non-parametric test that does not require any given distribution of the data.

In the second step, the complete population was split into two non-overlapping subgroups for each PEST parameter. The group with the higher values will be labeled using the $+$ sign, while the group with lower parameter values will be marked by the $-$ sign. Thus, the subgroups were called MCO+, MCO-, MCS+ and MCS-. The optimal dividing thresholds for the subgroups were found with a receiver operating characteristic (ROC) curve. The ROC curves calculated for both PEST parameter can be seen in figure 6.1. Using the separated subgroups, we tested with respect to PFD if the observed difference in proportions was indeed statistically significant. The aim of this analysis was to evaluate if high and low risk patients can be discriminated by PEST. For this purpose, a Fisher's exact test was carried out. This test allowed us to assess the predictive power of both parameters.

We also investigated if PEST parameters were related to other relevant but invasive cardiac biomarkers such as reduced left ventricular dysfunction, NYHA class III, etc. The test used here was again Fisher's exact test in the case of categorical variables and the two-tailed Wilcoxon-Mann-Whitney test for continuous variables. This analysis may become interesting because it opens the possibility of replacing the invasive biomarkers with the non-invasive MCO and MCS if a surrogate relationship was to be found.

For all statistical tests, a significance level of $p < 0.05$ was chosen.

6.3 Results

First, the statistical properties of the complete population were analyzed and the parameters MCO [‰] and MCS [$‰/s$] were found to have a median and interquartile range (med$\pm$iqr) of -6.970$\pm$13.657 and 6.377$\pm$15.221 respectively. The results for the statistical analysis with respect to the outcome of the study are presented in table 6.1. No significant differences in any of the comparisons were found.

Second, from the ROC curves, an area under the curve (AUC) of 0.546 and 1-0.452=0.548 were found for MCO and MCS respectively. In addition, the optimal thresholds that maximized the sum of sensitivity (SEN) and 1-specificity (SPE) were MCO=-7.0 ‰ and

Table 6.1: med±iqr for MCO and MCS of each cause of death. The error probability (p value) for the comparisons among classes is also given.

	MCO [‰]			MCS [‰/s]		
	cause of death **med±iqr**	others **med±iqr**	**p-value**	cause of death **med±iqr**	others **med±iqr**	**p-value**
SCD vs. other	-8.22±11.43	-6.79±13.81	0.616	7.10±11.47	6.37±15.48	0.758
PFD vs. other	-5.74±7.68	-7.18±14.03	0.245	4.58±11.65	6.61±15.36	0.227
CD vs. other	-5.98±10.44	-7.14±14.47	0.567	6.20±11.31	6.57±15.40	0.457
TM vs. other	-6.69±11.96	-7.00±14.19	0.917	6.29±13.63	6.48±15.40	0.631

MCS=6.333 $‰/s$. Afterwards, the 537 patients were divided into the positive and negative subgroups. In the group MCO- 265 patients were included, while 272 were part of MCO+. On the other hand, 280 patients were classified as MCS+ and the other 257 as MCS-.

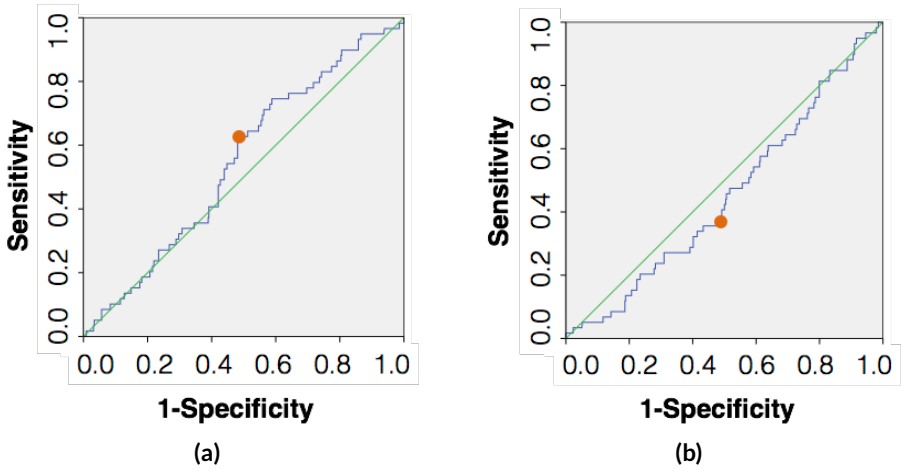

Figure 6.1: (a): ROC curve for the parameter MCO with respect to the outcome PFD and the point for optimal separation are displayed. (b): ROC curve for the parameter MCS with respect to the outcome PFD. The point for optimal separation are displayed. This figure was reprinted from publication [96] with permission from the author.

Third, the results of the test evaluating if high and low risk patients can be discriminated using PEST is displayed in the last row of table 6.2. No significance was found for any of the two PEST parameters. However, the error probability for MCO was p=0.054 which is close to the significance level. The rest of table 6.2 shows the comparison of the PEST parameter to other relevant cardiac biomarkers. The difference in proportions of each subgroup was statistically significant for QRS>120 ms for both MCO and MCS. Significance was also present when comparing average heart rate with MCS.

Table 6.2: Summary of the statistical analysis performed on the predictive power of the PEST parameters MCO and MCS.

	Overall population (N=537)	**MCO-** (N=265)	**MCO+** (N=272)	**p-value**	**MCS-** (N=280)	**MCS+** (N=257)	**p-value**
Age (y)	64±17	64±19	65±15	0.133	65±15	63.5±19	0.148
Gender (men)	389 (72.4%)	187 (70.6%)	202 (74.3%)	0.385	210 (75%)	179(69.6%)	0.177
NYHA class III	101 (18.8%)	54 (20.4%)	47 (17.3%)	0.378	45 (16.1%)	56 (21.8%)	0.098
LVEF $< 35\%$	308 (57.4%)	143 (54.0%)	165 (60.7%)	0.138	171 (61.1%)	137 (53.3%)	0.081
Diabetes	213 (39.7%)	106 (40.0%)	107 (39.3%)	0.930	106 (37.9%)	107 (41.6%)	0.379
Beta blockers	367 (68.3%)	179 (67.5%)	188 (69.1%)	0.711	196 (70.0%)	171 (66.5%)	0.404
Amiodarone	47 (8.8%)	23 (8.7%)	24 (8.8%)	1.000	26 (9.3%)	21 (8.3%)	0.760
ARB or ACE inhibitors	103 (19.2%)	46 (17.4%)	57 (21.0%)	0.324	60 (21.4%)	43 (16.7%)	0.188
Average heart rate (bpm)	71±17	71±17	71±15	0.863	70±15	72±17	**$<10^{-3}$**
Maximum heart rate (bpm)	113±23	114±23	113 ± 21	0.448	113 ± 22	115±25	0.056
Heart rate range (bpm)	64±19	65±21	62±18	0.078	62±18	66±22	0.057
QRS > 120 ms	225 (41.9%)	81 (30.6%)	144 (52.9%)	**$<10^{-3}$**	143 (51.1%)	82 (31.9%)	**$<10^{-3}$**
Nonsustained VT and more than 240 VPB in 24h	145 (27.0%)	66 (24.9%)	79 (29.0%)	0.287	82 (29.3%)	63 (24.5%)	0.243
PFD	59 (11.0%)	22 (8.3%)	37 (13.6%)	0.054	37 (13.2%)	22 (8.6%)	0.098

Data are presented as absolute frequencies and percentages and as med ± iqr.
NYHA = New York Heart Association; LVEF = left ventricular ejection fraction; ACE = angiotensin-converting enzyme;
ARB = angiotensin receptor blocker; VT = ventricular tachycardia; VPB = ventricular premature beat;
MCO+ = morphological change onset positive group; MCO- = morphological change onset negative group;
MCS+ = morphological change slope positive group; MCS- = morphological change slope negative group.
Significant differences between MCO- and MCO+ just as MCS- and MCS+ are indicated in bold.

6.4 Discussion

The results obtained from the Wilcoxon-Mann-Whitney test comparing the distributions of the study outcomes showed that the PEST parameters were not related to any sort of cardiac death. Furthermore, the analysis carried out with the ROC curve delivered an AUC slightly above 0.5 in both cases demonstrating again the low predictive power of the PEST parameters. In addition, the Fisher's exact test to evaluate MCO and MCS as risk predictors also turned out to be negative. These results are in accordance with other findings in literature where PEST also failed to discriminate high risk patients suffering from coronary artery disease or left ventricular dysfunction [95]. Furthermore, these results could also validate the hypothesis presented in the previous chapter of this thesis, where we proposed that PEST may be a normal phenomenon among all patients that is independent of their cardiac disease.

Nevertheless, we have to question if the results obtained here can be trusted. As mentioned previously, a PEST analysis can only be performed accurately if a high signal quality is given. This was not the case in this study. Figure 6.2 shows a typical example of how an ECG in the vicinity of a VEB may look like in the MUSIC database. The beat to beat variation of the T wave because of diverse external perturbations is probably larger than PEST itself. Thus, in this kind of signals, PEST would be lost in noise.

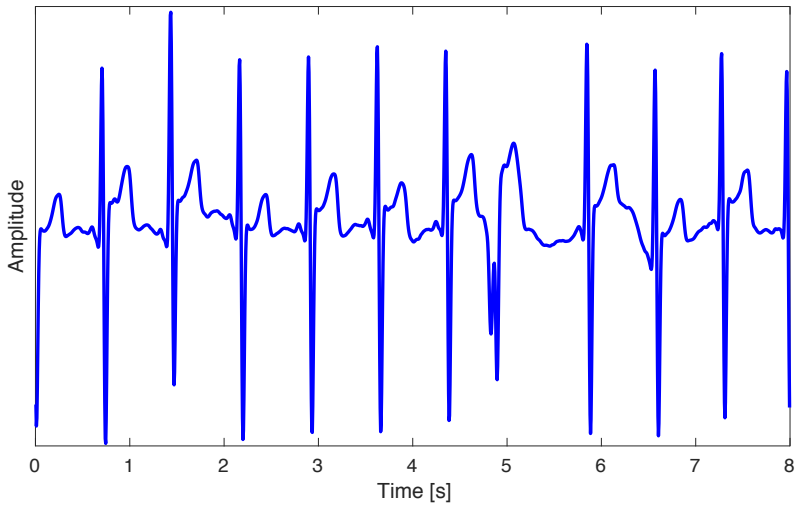

Figure 6.2: Example of an ECG signal extracted for PEST analysis. The low signal quality compromises the accurate estimation of the parameters MCO and MCS.

Finally, the significance test considering MCO+ and MCO- with respect to PFD delivered an error probability of $p = 0.054$ which is close to the significance level. This could mean, that despite the difficulties imposed by the quality of the signals and the relatively low statistical power of the study, the possibility of PEST being a valuable risk stratifier may be realistic and the used algorithm could be the correct one. Furthermore, even though the total amount of patients included in this study was relatively large, the non-survivors PFD

outcome were only 59 (11.0 %). This number is probably too low to generalize the results obtained here and for now, we can only conclude that more research is needed to definitely prove or disprove the predictive power of PEST.

6.5 Outlook

The focus of a future study should lie on the clinical meaning of PEST and its applicability for risk assessment. For that purpose, a data set with similar properties to the one used here but with better signal quality would be necessary. Survivors of myocardial infarction or patients suffering from CHF should remain the target of the study. The statistical analysis can be performed in the same manner as here but it would be interesting to extend the morphological features to include others like the T wave amplitude, width or symmetry. Even though the $l\_operator$ is capable of measuring general morphological changes, it may not be sensitive enough for this task. Thus, including other features in the analysis would deliver a more elaborated quantification of PEST.

6.6 Conclusion

From this study, we concluded that PEST was not capable of identifying PFD patients in the MUSIC data set. This result may have one of the two following explanations. First, PEST is a normal phenomenon that manifest independently of the state of health of the patient, or second, the signal quality and the algorithms we used to capture PEST did not allow us to accurately quantify it. In any case, more research is needed to finally conclude what the true clinical value of PEST may be.

PART III

INTRACARDIAC AND SURFACE ELECTROCARDIOGRAMS

CHAPTER 7

Detecting the Beginning of the P Wave

7.1 Introduction

The P wave in the electrocardiogram (ECG) plays an important role when diagnosing atrial diseases such as recurrent atrial ectopic beats (AEB), atrial fibrillation (AFib) or atrial flutter (AFlu). The latter two are a common cause of stroke [101]. These diseases originate from structural modifications of the heart tissue and remodeling of the electrophysiology of the cardiac myocytes [102]. They lead together to morphological changes of the normal P wave that can be used to identify high risk patients and treat them even before symptoms appear [103–105].

In case that symptoms are already present, and pharmacological treatment does not prove effective, the arrhythmia patient is typically treated with a minimally invasive radiofrequency ablation [106]. Although ablation therapy has been demonstrated to work successfully in many cases, recurrence has been observed in up to 35 % of the patients. The analysis of the shape of the P wave before and after ablation can deliver a more accurate forecast of the success of the ablation [107, 108].

Nevertheless, manual annotation of the P wave in the ECG signal is a subjective and very time demanding task. In addition, the accuracy of the annotations is dependent on the quality of the signal, the chosen ECG lead and the experience of the annotator. Figure 7.1 shows two ECG signals with manually annotated P waves (onset and peak) from the QT database in *physionet.org* [31]. While the annotations seem to be accurate in figure 7.1 (a), the marked peak of the P wave does not seem to match the true maximum of the wave in figure 7.1 (b).

Hence, in this project, we created a new algorithm based on the stationary wavelet transform (SWT) for the automatic detection and delineation of the P wave in the ECG. Using electrograms recorded inside the heart and on the chest of a patient, it was possible to develop an algorithm and find precisely the beginning of the P wave. The algorithm was then

validated with manually annotated ECG signals. The results presented here were published as a journal paper [99] and presented in form of a conference contribution [109].

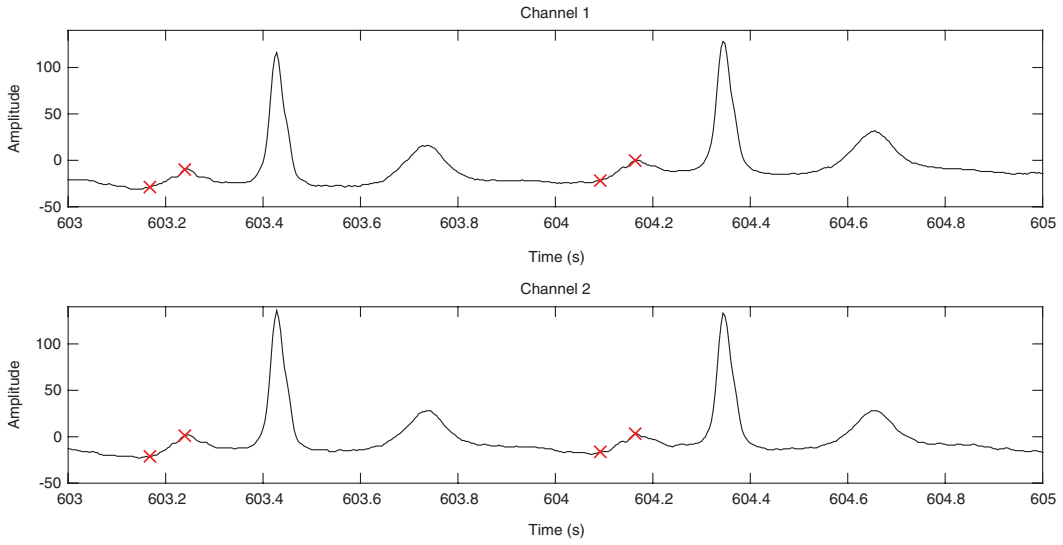

(a)

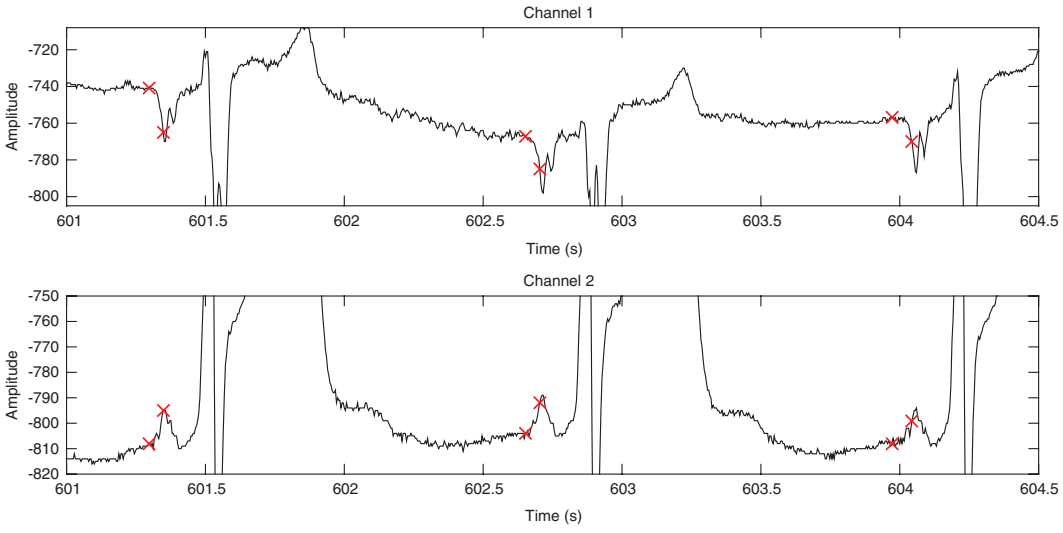

(b)

Figure 7.1: Two examples of the manually annotated signals in the QT database from *physionet.org*. (a): High quality signal with accurate annotation. (b): Lower quality signal for which the annotated peak of the P wave does not match its maximum. The fiducial points were not set consistenly from one wave to the next one. This figure was reprinted from publication [99] with permission from the publisher.

7.2 Materials and Methods

7.2.1 Data

Two data sets were used for the purpose of developing, testing and validating the delineation algorithm presented here. First, for the development and testing process, simultaneously recorded surface ECG and intracardiac electrogram (EGM) during an ablation procedure were used. The data were acquired from a 54 year old female patient suffering from paroxysmal AFib. The recording system was the EnSite NavX Velocity X_1 electroanatomical mapping system using biatrial mapping with two basket catheters. All signals were aquired at a sampling rate of 2032.5 Hz. In this data set, 32 P waves were obtained during sinus rhythm. Since good coverage of the sinus node was given, we assumed that these signals could be used as reference to label the beginning of the P wave in the surface ECG. This data set and its visualization was provided by Dr.-Ing. Tobias Oesterlein in close cooperation with the Städtisches Klinikum in Karlsruhe, Germany and published also in [110].

Second, the algorithm was validated using the QT database from *physionet.org* [111]. This data set contains 105 ECG signals each with a duration of 15 minutes and sampled at 250 Hz. The recordings were manually annotated by two expert physicians. For every signal in the database, two channels were acquired. A total of 3194 P waves were included. Although 7.1 shows a controversial annotation, the majority of the markings in this database are very accurate and thus considered a reliable tool for benchmarking.

7.2.2 ECG Signal Preprocessing

The general signal preprocessing scheme of an ECG was introduced in chapter 4. The procedure remained the same here but a modification of the filtering parameters was carried out. In order to match the spectral properties of the P wave, a phase free band-pass filter with cutoff frequencies at 1 and 15 Hz was applied [112]. These frequencies are not recommended for diagnostic purposes because they may remove too much information from the ECG. In this work, the filtered signal was used only for the detection of the P wave and any diagnostic information was gained from the original signal. Due to the low cutoff frequency of the low-pass filter, no power line hum filter was required.

7.2.3 Phase Free SWT

As mentioned in the mathematical fundamentals, the SWT was defined as a modified version of the discrete wavelet transform to achieve the property of remaining invariant with respect to translations of the original signal. For this purpose, the downsampling process of the signal in every step of the filter bank is replaced by an upsampling of the filter coefficients while maintaining the transformed signal unaltered. The transformed signal is thus invariant

with respect to translations and allows the precise detection of an event of interest like a P wave in the /ECG. The filter bank representation of the SWT can be seen in figure 7.2 (a).

The finite impulse response (FIR) wavelet filters used in the SWT analysis are causal. Thus, their phase differs from zero and it is not necessarily linear. This leads to a transformed signal that is shifted in time with respect to the original signal. So, for example, the maximum of the P wave in the original signal is not necessarily aligned with the maximum (or any other characteristic point) in the transformed signal. In addition, the non-symmetrical wavelet filters have a non-linear phase making an estimation of the time shift highly unpractical. This phenomenon is demonstrated in figure 7.2. A P wave was modeled using two Gaussian bells for the right and left half of the P wave. Each Gaussian bell had a different width producing an unsymmetrical wave. It can be seen in figure 7.2 (c) that the transformed P wave has its zero crossing shifted in time with respect to the maximum of the P wave. Hence, a direct detection of the P wave maximum would not be possible in this case.

In order to eliminate the time shift from the wavelet filter, we introduced a new algorithm that will be explained as follows. First, the SWT of the signal was computed in the standard manner. Second, the original signal was reverted in time and the SWT of the reverted signal was calculated. The resulting SWT was reverted again in time again. The two SWT are then added to produce a resulting signal that is free of phase. This transformed signal was obtained using the biorthogonal wavelet 3.3 at the decomposition level seven. This wavelet together with its scaling function can be seen in figure 7.2 (b).

We proved mathematically that the resulting filter had zero phase in the following manner. The signal being analyzed was called $x(t)$ and its Fourier transform $X(f) = \mathscr{F}\{x(t)\}$. The time inversion produces the signal $x(-t)$ in the time domain and the complex conjugate $X^*(f)$ in the frequency domain. If we choose $H(f) = \mathscr{F}\{h(t)\}$ to be the transfer function of the wavelet filter and $Y(f) = \mathscr{F}\{y(t)\}$ the wavelet transform of $x(t)$, then the following holds:

$$
\begin{aligned}
Y(f) &= X(f)\cdot H(f) + (X^*(f)\cdot H(f))^* && (7.1)\\
&= X(f)\,(H(f) + H^*(f)) && (7.2)\\
&= X(f)\cdot 2\cdot \mathrm{Re}\{H(f)\} && (7.3)
\end{aligned}
$$

Using this procedure, the resulting wavelet filter used to analyze $x(t)$ was in fact $2\cdot \mathrm{Re}\{H(f)\}$. This is a real valued filter that is free of phase. The resulting phase free SWT can be seen in figure 7.3. The maximum of the original signal and its transform are aligned in time so that a direct detection of the maximum was possible. There is a further advantage of this procedure which is demonstrated in figure 7.3. The minima left and right of the maximum correspond with the beginning and end of the P wave. These side minima were used to automatically delineate the P wave. We also postulated a third advantage of this method. Since the wavelet transform is carried out at a higher level, in this example level seven, the high frequency noise and power line hum should be filtered out in the SWT process. Baseline wander should also be canceled out since it is captured by the approximation coefficients

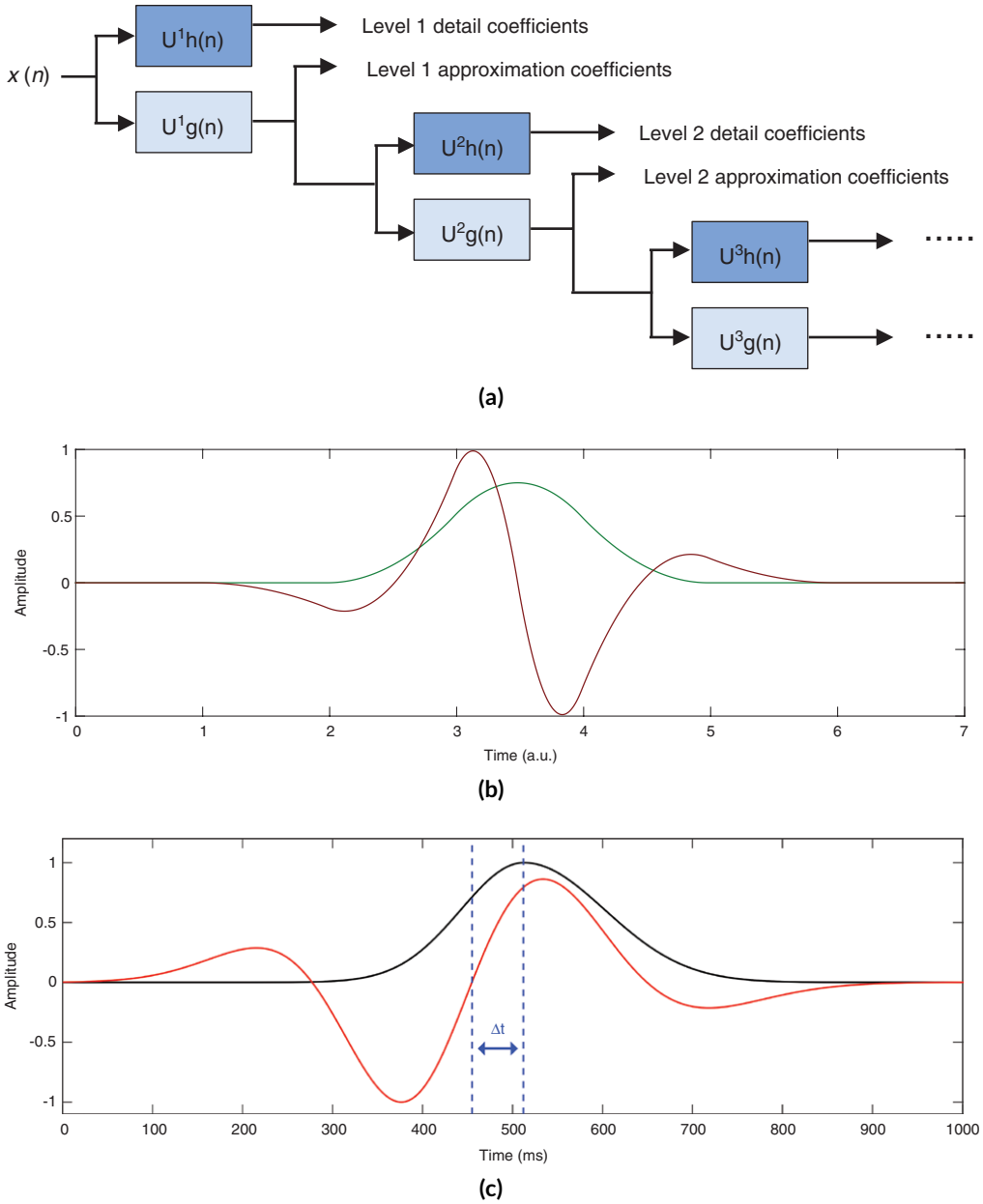

Figure 7.2: (a): Block diagram of the filter bank representation of the SWT. The operator $U^i h(n)$ represents ith upsampling step of the filter $h(n)$. (b): Reverse biorthogonal wavelet 3.3 (brown) and its scaling function (green). (c): Modell of the P wave (black) and its SWT (red) using the reverse biorthogonal wavelet 3.3. A time shift between the maximum of he modelled P wave and the zero crossing of the SWT can be observed. This figure was reprinted from publication [99] with permission from the publisher.

of the SWT and we used the detail coefficients for the analysis. We will demonstrate this advantage in a later section.

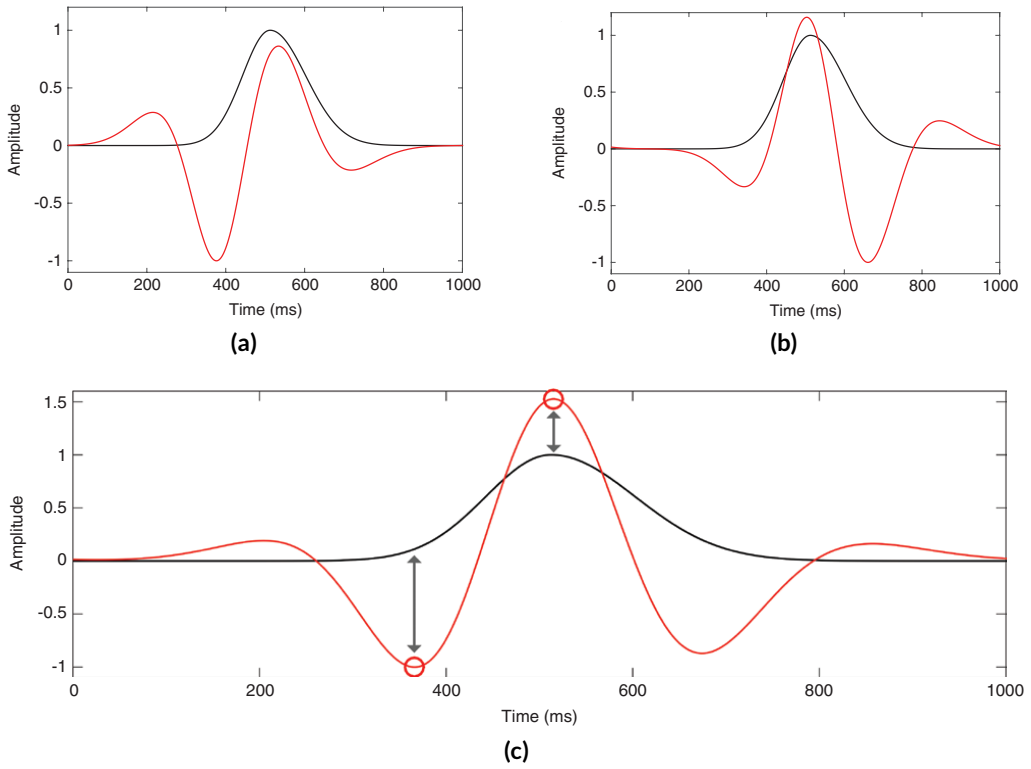

Figure 7.3: (a): P wave model (black) and its SWT (red) with the reverse biorthogonal 3.3 wavelet at the decomposition level seven. (b): P wave model (black) and its reversed-time SWT (red). (c): P wave model (black) and its phase free SWT (red). The red signal is the result of the sum of the transformed signals from (a) and (b). The automatic delineation of the P wave was performed using the extrema in the phase free SWT. This figure was reprinted from publication [99] with permission from the publisher.

7.2.4 Intracardiac Signal Processing

7.2.4.1 Intracardiac Signal Filtering

In this work, we used bipolar signals because they are clean of far field artifacts and baseline wander coming from respiration and other low frequency perturbations. The signal is filtered with a concatenation of two Gaussian filters with cutoff frequencies at 30 and 300 Hz according to the standard procedure found in literature [113]. It is important to mention that the filters applied to the surface ECG and intracardiac EGM were both phase free. This ensured that all signals are aligned in time which was a mandatory requirement since the intracardiac EGM are being used as reference for the beginning of the P wave in the surface ECG.

7.2.4.2 Detecting the Beginning of the Atrial Activation in the Intracardiac EGM

The beginning of the atrial depolarization can be obtained from intracardiac recordings. For this purpose, a good coverage of the area around the sinus node using the basket catheter was required. Figures 7.4 (a) and (b) show the atrial anatomy of the patient undergoing catheter ablation and the exact location of the electrodes of the basket catheter. In order to detect the instant when the atrial activation began, the algorithm presented in [114] was extended. That algorithm was based on the non-linear energy operator (NLEO), which was used to transform the atrial EGM to potentiate atrial depolarization waves and reduce other unwanted signal components. Afterwards, a signal dependent threshold was applied to detect the exact instant at which the depolarization wave reached the catheter. In order to increase the robustness of the procedure, a detected activity was accepted as such if it was detected in at least two neighboring electrode pairs.

Figure 7.4 (c) shows the multichannel intracardiac recording from both basket catheters delivering 56 bipolar EGM traces. The signals in blue originate from the right atrium while the signals in green were recorded in the left atrium. The activity during two P waves can be seen in this figure. The detected beginnings of the depolarization waves are marked with a red line. The simultaneous ECG is displayed in figure 7.4. The beginning of the P wave was marked with the same red line, which became the reference for the development of the delineation algorithm.

7.2.5 P wave Detection and Delineation in the ECG

7.2.5.1 Removing the QT interval

In order to facilitate the detection of the P wave and avoid detecting other ECG waves like the QRS complex or the T wave, the QT interval was canceled. The idea was to replace this interval with a smooth function for which the wavelet coefficients were very low. By doing so, the only remaining wave in the ECG was the P wave and the phase free SWT can be used to detect it. The smooth function chosen was a sigmoid given by the following equation:

$$s(t) = \frac{s_2 - s_1}{1 + e^{-t}} + s_2 \tag{7.4}$$

The parameters s_1 and s_2 characterize the sigmoid function and were set to assure that the resulting signal was continuous:

$$s_1 = x(t_{r1}) \tag{7.5}$$

$$s_2 = x(t_{r2}) \tag{7.6}$$

Here, the original ECG signal is called $x(t)$ and the boundary points of the replacement interval were located 50 ms prior to the Q peak (t_{r1}) and 60 % of the interval into the

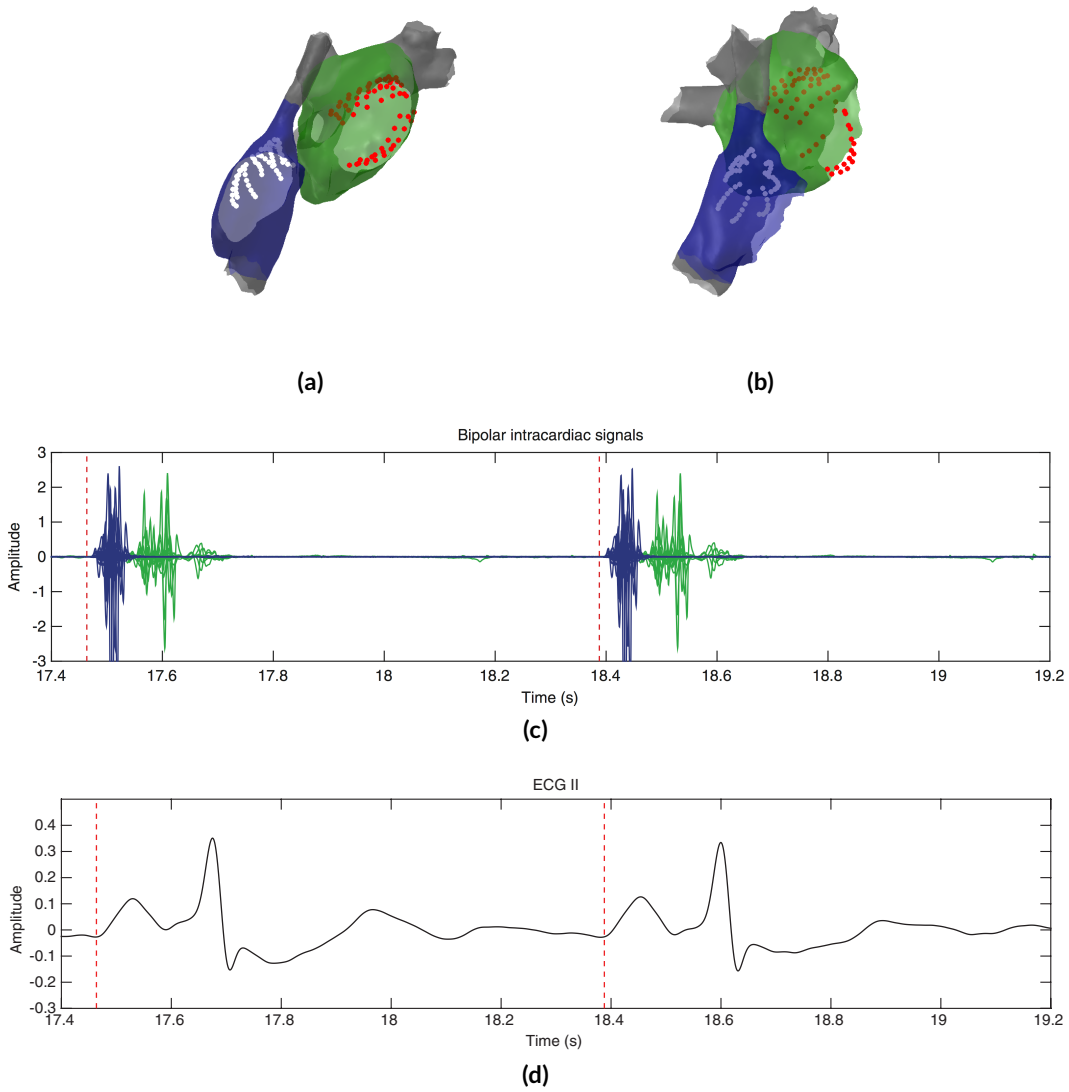

Figure 7.4: (a): Atrial geometry obtained from the patient undergoing catheter ablation. This perspective is called left anterior oblique. The position of the electrodes in the right atrium is marked with white dots. A good coverage of the sinus node can be assumed. (b): Same atrial geometry visualized from the perspective right anterior oblique. (c): Multichannel intracardiac EGM recorded using the biatrial configuration displayed in (a) and (b). The color of the signal corresponds with the atrium it was recorded from. (d): ECG lead Einthoven II recorded simultaneously during the catheter ablation. The beginning of the P wave is marked with the red line in both, the surface and intracardiac signals. This figure was reprinted from publication [99] with permission from the publisher.

succeeding R peak (t_{r2}). Figure 7.5 (a) shows an ECG signal in its original form and the same signal after QT interval removal. The delineation of the P wave is shown in figure 7.5 and was obtained directly from the transformed signal. The delineation process will be explained in detail in the next section.

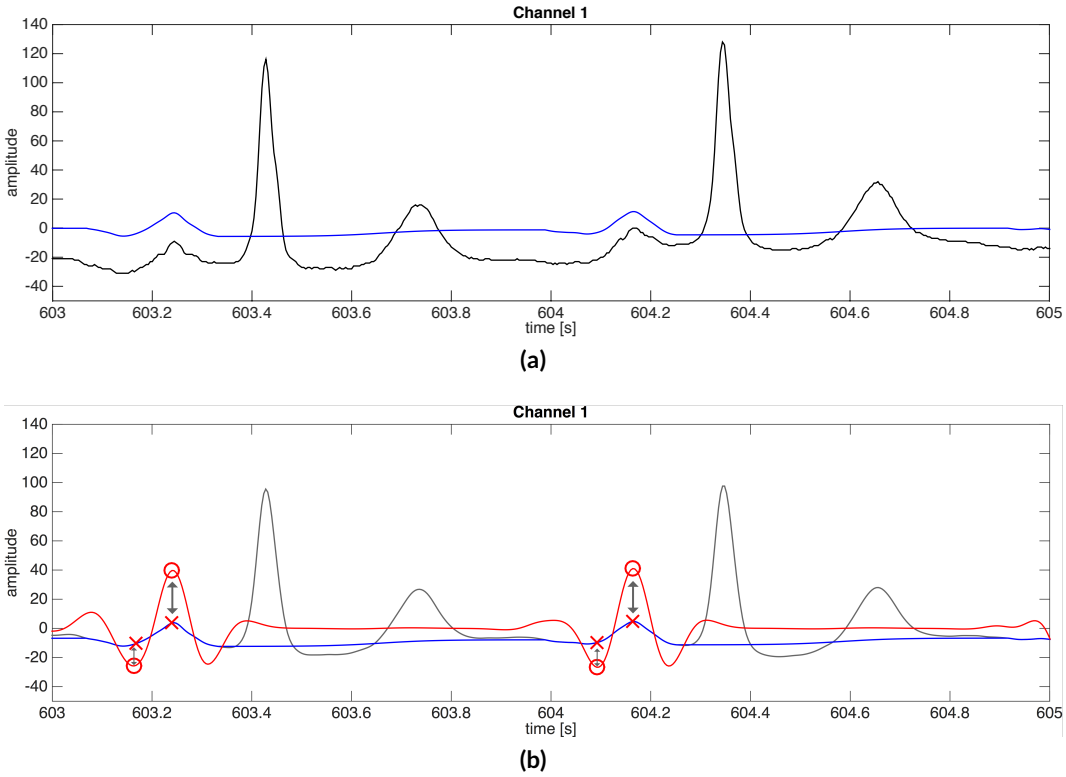

Figure 7.5: (a): ECG signal before and after the QT segment has been replaced and the signal has been filtered. The replacing signal is a smooth sigmoid. The resulting ECG contains only P waves. (b): The SWT of the replaced ECG signal is also displayed in red. The beginning of the P wave and its peak are obtained directly from the phase free SWT. This figure was reprinted from publication [99] with permission from the publisher.

7.2.5.2 Delineating the P wave

The delineation procedure began with the detection of the P wave peak. For that purpose the absolute value of the phase free SWT was computed. This was done to account for inverted P waves that may have a negative polarity. In order to find the peak of the P wave, the final portion of each RR interval was inspected. The largest absolute maximum of the transformed signal in that interval was set as the P wave peak. The side absolute maxima were found to correspond to the beginning and end on the P wave. In the case that more than one side maximum was found when searching for the beginning of the wave, the maximum closest to 10 % of the area under the transformed P wave was chosen. The same procedure was done for the P wave offset. A summary of the signal processing steps to achieve delineation can be seen in figure 7.6.

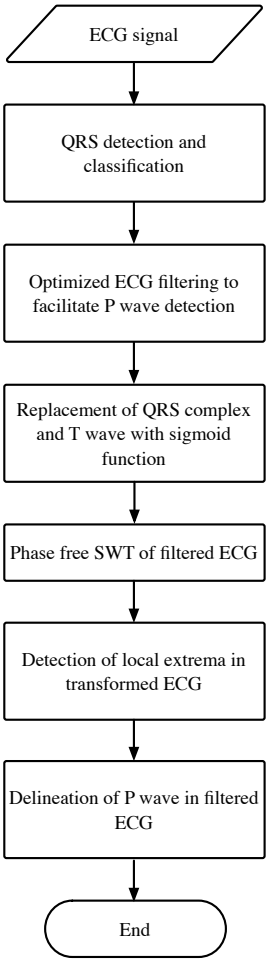

Figure 7.6: Signal processing algorithm displayed as flow diagram for the delineation process of the P wave. This figure was reprinted from publication [99] with permission from the publisher.

7.2.5.3 Evaluating the Method with Synthetic Signals

We created a small study using synthetic signals to evaluate how the method performs with varying morphology of the P wave and in the presence of noise. For this purpose, the morphology and noise patterns of the wave were varied and the delineation algorithm was tested. We then compared the results of the delineation algorithm with a well-known reference. The comparison was carried out subtracting the reference value from the modified one as follows: $P_{on,dev} = P_{on,mod} - P_{on,ref}$ or $P_{peak,dev} = P_{peak,mod} - P_{peak,ref}$. The reference P wave and its delineation can be seen in figure 7.7 (a).

In the first part of the study, the morphology of the P wave was varied. For that purpose, our P wave model was generated from two halves of a Gaussian bell concatenated in the following manner:

$$x_{\Delta\sigma}(t) = \begin{cases} \exp^{\left(-\frac{(t-\mu)^2}{2(\sigma_l+\Delta\sigma)^2}\right)}, & \text{for } t \leq 0, \\ \exp^{\left(-\frac{(t-\mu)^2}{2\sigma_r^2}\right)}, & \text{for } t > 0 \end{cases} \tag{7.7}$$

The parameters $\sigma_l = 70\,ms$ and $\sigma_r = 90\,ms$ were chosen to recreate a realistic P wave with asymmetric shape. The variation of the parameter $\Delta\sigma$ was chosen from -20 to $+20$ ms in steps of 1 ms. Figure 7.7 (c) shows a P wave modeled with $\Delta\sigma = +15\,ms$. In addition, we also allowed the amplitude of the P wave to vary. For that purpose, a constant coefficient a in the range from -2 to $+2$ in steps of of 0.25 was introduced as follows:

$$x_a(t) = a \cdot x(t) \tag{7.8}$$

Figure 7.7 (b) shows a P wave with inverted amplitude at $a = -1$.

In the second part of the study, we evaluated the performance of the algorithm with respect to noise. We chose four models to recreate the typical kind of perturbations present in the ECG signal. All types of noises were added to the reference P wave and the delineation procedure was performed afterwards. The four kinds of perturbations are described as follows:

- additive white Gaussian noise (AWGN) with the following amplitude distribution:

$$f_X(x) = \frac{1}{\sigma\sqrt{2\pi}} \cdot e^{-\frac{1}{2}\left(\frac{x}{\sigma}\right)^2} \tag{7.9}$$

  The variance of the amplitude distribution can be adapted to achieve a different signal-to-noise ratio (SNR).
- additive white Laplacian noise (AWLN) with the following amplitude distribution

$$f_X(x) = \frac{1}{2\lambda} \cdot e^{-\left|\frac{x}{\lambda}\right|} \tag{7.10}$$

  The variance $2\lambda^2$ of the amplitude distribution can be varied to generate different SNR levels.
- Low frequency baseline wander in the band from 0 to 0.4 Hz:

$$bw(t) = A \cdot \sum_{k=1}^{5} cos(2\pi \cdot (k-1) \cdot 0.1\,Hz \cdot t + \phi(k)) \tag{7.11}$$

  The amplitude A of the baseline model was adapted to generate different SNR levels. The random phase $\phi(k)$ came from a uniform distribution in the interval $[0; 2\pi)$.
- Power line hum at 50 Hz and its first four harmonics was modeled as follows:

$$pl(t) = A \cdot \sum_{k=1}^{5} \frac{1}{k} \cdot cos(2\pi \cdot k \cdot 50\,Hz \cdot t + \phi(k)) \tag{7.12}$$

The amplitude A of the power line model was varied to achieve different SNR levels. The random phase $\phi(k)$ came from a uniform distribution in the interval $[0;2\pi)$.

The SNR levels were chosen from -3 to $+30$ dB at an interval of 3 dB. Figure 7.7 (d) shows the P wave reference corrupted by an AWGN at an SNR of $+12$ dB. Further, a total of 1000 realizations of each noise model was generated to create a sufficiently large sample size of each noise configuration.

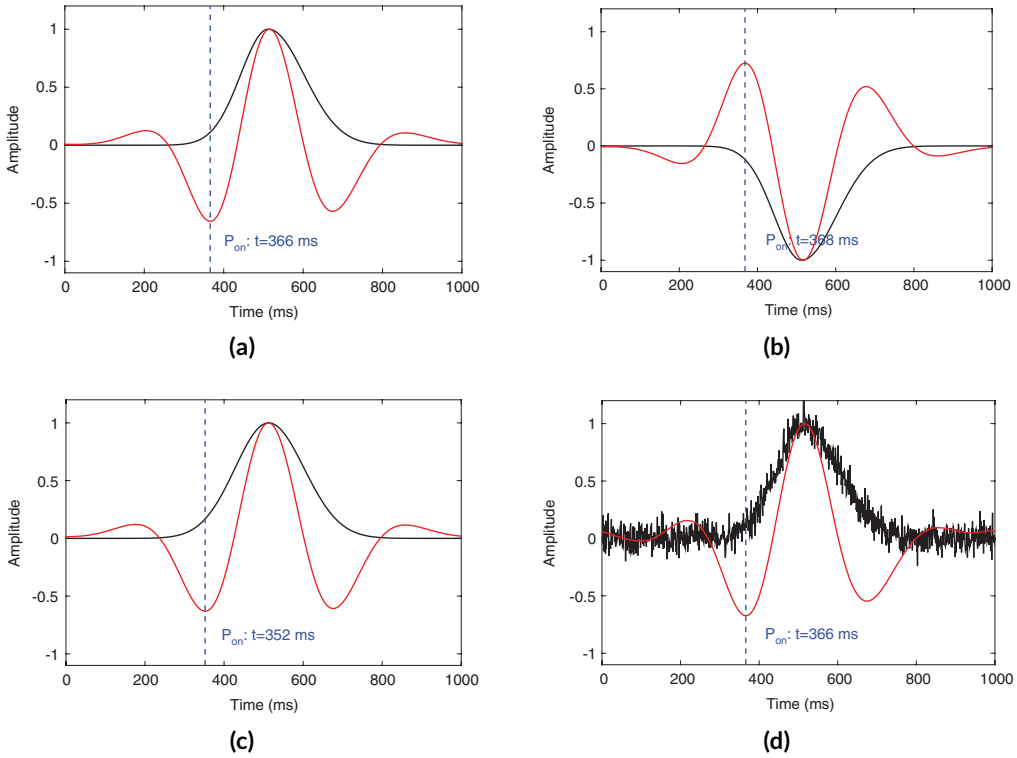

Figure 7.7: (a): P wave model used as reference for the evaluatian of the algorithm. The beginning of the P wave is labeled as P_{on}. (b): Reference P wave with inverted amplitude together with its automatically detected P_{on}. (c): P wave model with a 15 ms wider left side. (d): P wave corrupted by AWGN at an SNR of $+12$ dB. This figure was reprinted from publication [99] with permission from the publisher.

7.2.6 Finding the Optimal Configuration for the Algorithm

The algorithm presented here had two more components that were optimally chosen:

- The wavelet used in the SWT. Different wavelets produce different transforms and thus different delineation points of the P wave. Therefore, we tested the following wavelets and searched for the one that produced the most accurate results: Haar, db2, rbio3.1, rbio3.3, rbio3.5, bior1.3, bior1.5, coif1, sym4, and sym5. We took into account that the shape of the chosen wavelets was similar to the morphology of the P wave.

- The second parameter to choose was the decomposition level of the SWT. The center frequency of the P wave can be used to estimate the decomposition level because in the filter bank representation of the transform, the Nyquist (and sample) frequency of the wavelet coefficients is halved at every stage. Assuming that the center frequency of the P wave is 7 Hz, the approximated decomposition level can be estimated as follows:

$$L \approx \left\lfloor log_2\left(\frac{f_{nyquist}}{f_{center}}\right)\right\rfloor = \left\lfloor log_2\left(\frac{f_{sample}}{f_{center}}\right)\right\rfloor - 1 \tag{7.13}$$

$$= \left\lfloor log_2\left(\frac{2032.5\,Hz}{7\,Hz}\right)\right\rfloor - 1 = 7 \tag{7.14}$$

Finally, we concentrated the evaluation scheme on the ECG lead Einthoven II because this is the lead where the P wave has the largest amplitude.

7.3 Results

7.3.1 Evaluation of the Algorithm with Synthetic Signals

The results obtained from the evaluation carried out with synthetic signals on the onset of the P wave can be seen in figure 7.8. The amplitude of the P wave hardly affected the delineation process. Only for negative amplitudes a small deviation from the reference was observed. In addition, the deviation from the reference in the onset point of the wave had an almost linear dependency from the width of the wave. This means that P_{on} was shifted proportionally to the standard deviation of the Gaussian bell used to model the P wave.

The power line hum and the baseline wander had almost no influence on the delineation process. However, AWGN and AWLN did have a strong impact in the delineating points. Even though the accuracy of the method (measured as the mean of the deviation from the reference) remained high, the robustness of the method (measured as the standard deviation of the deviation from the reference) decrease with lower SNR. For both noise models, the standard deviation of the error for both, P_{on} and P_{peak}, was a bit more than 10 ms at an SNR of -3 dB, which corresponds to approximately 10 % of the full width at halve maximum of the wave.

The results obtained from the evaluation performed with synthetic signals on the onset of the P wave can be seen in figure 7.9. In general, the results were very similar to the ones observed for P_{peak}. The exception was the dependency from the width of the wave. A small linear relationship between the width of the wave and the point labeled as maximum was the result of this study.

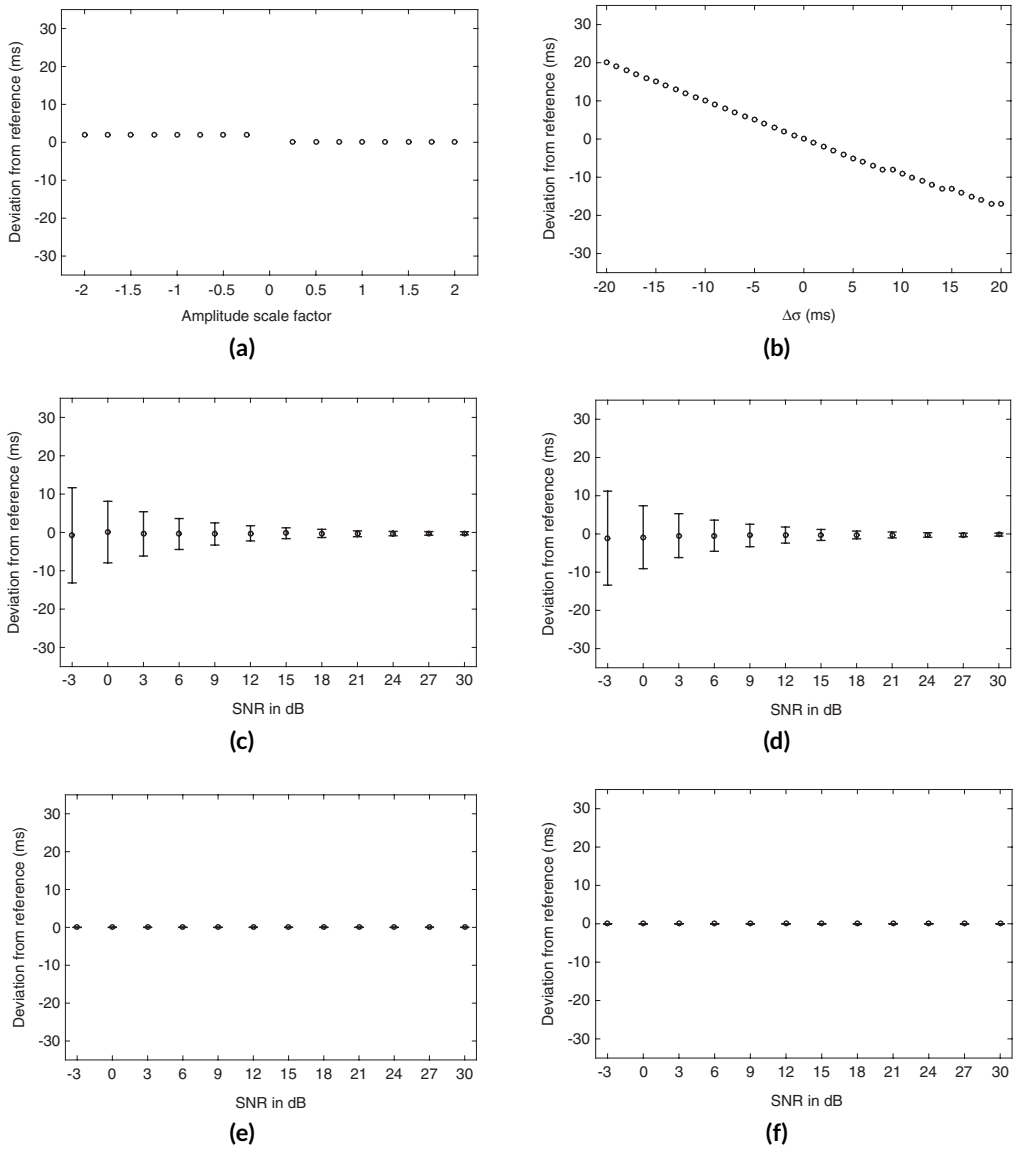

Figure 7.8: Deviations from the reference in the delineation of P_{on} with varying (a): amplitude of the P wave, (b): width of the P wave, (c): SNR under the influence of AWGN, (d): SNR under the influence of AWLN, (e): SNR under the influence of power line hum and (f): SNR under the influence of baseline wander. This figure was reprinted from publication [99] with permission from the publisher.

7.3.2 Optimal Configuration for the Algorithm

We evaluated the optimal configuration of the algorithm based on the delineation error of P_{on} using the intracardiac measurement as reference. The delineation error was defined as $P_{error} = P_{automatic} - P_{reference}$. The mean value of P_{error} is a measure of the accuracy of the algorithm while its standard deviation quantifies the robustness of the method. We chose the best performing configuration based on both, mean and standard deviation. Table 7.1 shows the results of the evaluation process with varying wavelet and decomposition level. The best

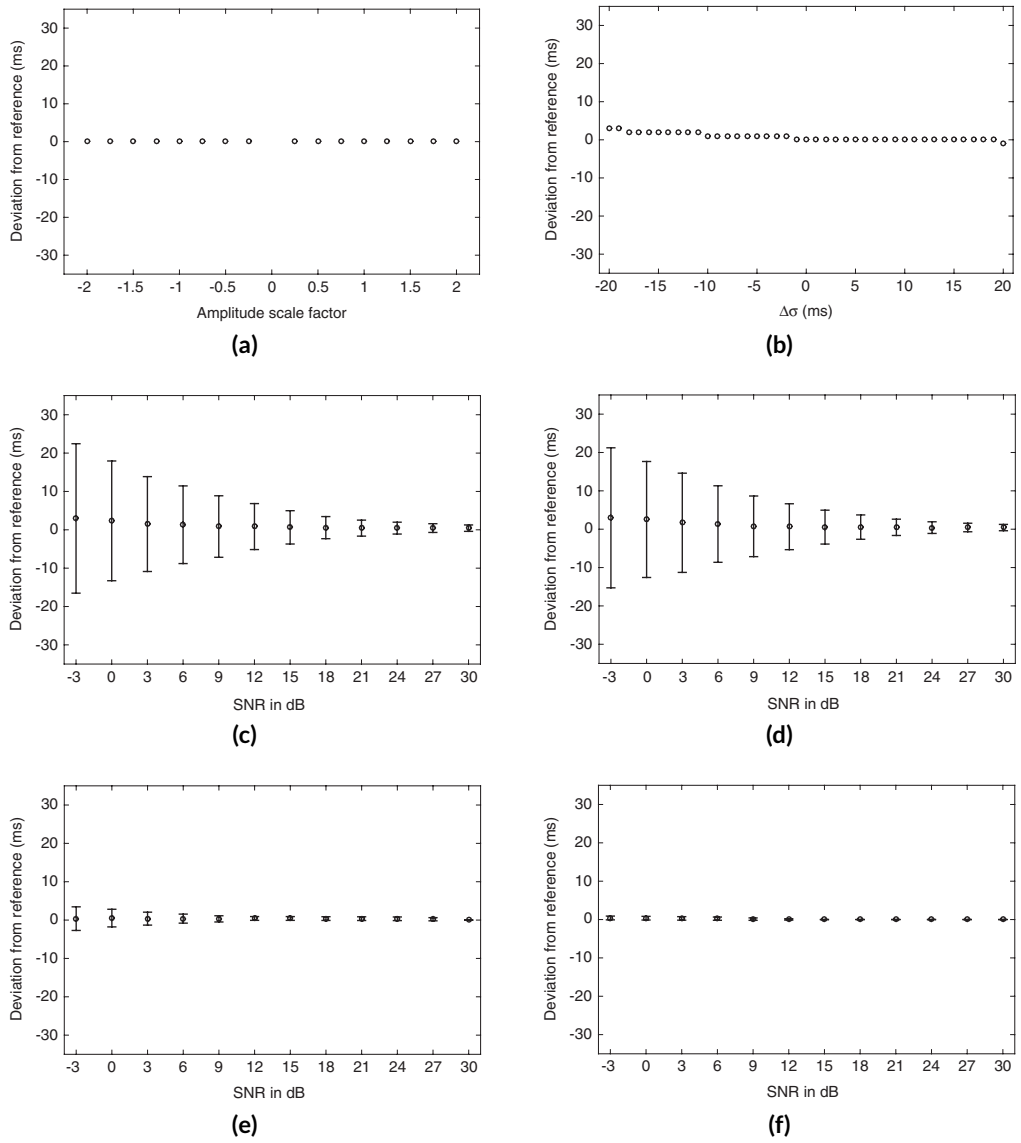

Figure 7.9: Deviations from the reference in the delineation of P_{peak} with varying (a): amplitude of the P wave, (b): width of the P wave, (c): SNR under the influence of AWGN, (d): SNR under the influence of AWLN, (e): SNR under the influence of power line hum and (f): SNR under the influence of baseline wander. This figure was reprinted from publication [99] with permission from the publisher.

performing configuration was the reverse biorthogonal wavelet 3.3 at a decomposition level of seven delivering a delineation error of 1.95 ± 5.61 ms.

7.3.3 Validation of the Algorithm Based on the QT Database

Since the P wave delineation algorithm was created to work independently from intracardiac signals, it was also validated with the manually annotated surface ECG signals from the QT

wavelet	level 4	level 5	level 6	level 7	level 8
haar	14.15 ± 18.65	12.75 ± 10.44	9.72 ± 13.90	1.31 ± 11.80	-34.35 ± 42.82
db2	13.62 ± 14.06	12.18 ± 8.73	8.76 ± 14.25	-3.98 ± 8.54	-70.67 ± 167.10
rbio3.1	14.87 ± 14.12	10.69 ± 13.87	7.83 ± 13.84	-5.01 ± 6.62	-37.28 ± 35.74
rbio3.3	23.12 ± 42.01	4.81 ± 20.01	13.67 ± 13.62	**1.95 ± 5.61**	-46.36 ± 28.39
rbio3.5	17.13 ± 65.59	19.42 ± 32.42	-0.66 ± 15.26	3.13 ± 12.92	-43.44 ± 27.59
bior1.3	16.11 ± 22.29	15.13 ± 14.21	10.11 ± 14.04	2.57 ± 12.35	-33.64 ± 30.25
bior1.5	16.11 ± 22.29	15.18 ± 14.12	10.23 ± 14.16	3.06 ± 12.65	-39.52 ± 29.87
coif1	5.39 ± 23.20	5.39 ± 21.92	0.11 ± 18.51	0.57 ± 81.27	-25.47 ± 39.86
sym4	6.34 ± 46.96	1.92 ± 22.46	-16.37 ± 42.39	3.50 ± 29.00	-9.48 ± 4.59
sym5	17.13 ± 65.81	15.04 ± 32.91	9.11 ± 16.33	-8.71 ± 24.57	-53.94 ± 193.15

Table 7.1: Results of the automatic delineation algorithm for the P wave validated with intracardiac measurements. Mean value and standard deviation (mean ± std) of the delineation error were calculated for the beginning of the wave (P_{on}) and are given in milliseconds. This table was reprinted from publication [99] with permission from the publisher.

database in *physionet.org*. We used the best performing wavelet found in the previous section but had to adapt the decomposition level to the lower sampling frequency of 250 Hz of the signals. The recalculated decomposition level was four. Since two channels were available for each ECG in the databse, we considered the channel that delivered the better delineation results. This procedure was also used by Martínez and we kept it here for comparability reasons [115].

Tables 7.2 to 7.4 present the results obtained for all 115 signals in the database and the summarizing global results. We evaluated only P_{on} and P_{peak} since these were the two delineation points the algorithm was created for. The delineation error was again defined as $P_{error} = P_{automatic} - P_{reference}$. A global average and standard deviation of -0.32 ± 12.41 ms for P_{on} and -5.75 ± 9.12 ms for P_{peak} were achieved.

Figure 7.10 illustrates the performance of the algorithm. Here, the same signals as in figure 7.1 are displayed together with the manual annotations from an expert physician and the automatic delineation delivered by our method. The figure 7.1 (a) shows concordant annotations, while in 7.1 (b) the automatic annotation seems to be more accurate.

7.4 Discussion

7.4.1 Evaluation of the Algorithm with Synthetic Data

In the first part of this study, we investigated the influence of P wave amplitude and width on the delineation procedure. We found that the amplitude of the P wave has very little impact on the delineating points. This is due to the fact that the SWT is a linear transformation. A scaled amplitude modifies the amplitude of the transform but not the location of its extreme

Signal name	Number of P waves	P_{on} mean±std	P_{peak} mean±std
sel100	30	0.27 ± 6.72	10.13 ± 8.83
sel102	0	-	-
sel103	30	-6.93 ± 6.96	1.73 ± 7.62
sel104	17	-18.59 ± 53.03	9.88 ± 45.83
sel114	50	3.04 ± 23.69	-4.48 ± 29.62
sel116	50	-1.84 ± 8.60	2.56 ± 8.23
sel117	30	12.80 ± 13.83	5.33 ± 7.88
sel123	30	10.40 ± 15.60	6.00 ± 9.95
sel14046	31	-1.29 ± 13.56	5.81 ± 7.85
sel14157	28	-8.43 ± 11.84	10.43 ± 4.53
sel14172	50	1.60 ± 9.25	7.76 ± 4.74
sel15814	30	-7.33 ± 10.46	2.13 ± 6.10
sel16265	30	-4.13 ± 6.77	6.13 ± 5.82
sel16272	30	-1.87 ± 6.37	1.73 ± 4.03
sel16273	30	-5.60 ± 11.20	2.53 ± 5.20
sel16420	30	-1.33 ± 5.29	5.07 ± 5.45
sel16483	30	-3.47 ± 6.95	1.07 ± 4.32
sel16539	30	-10.53 ± 12.97	7.20 ± 4.25
sel16773	30	-0.53 ± 4.78	5.33 ± 5.07
sel16786	30	-4.00 ± 6.56	3.20 ± 4.97
sel16795	30	-3.07 ± 10.38	1.07 ± 6.30
sel17152	30	-19.33 ± 6.65	3.60 ± 3.21
sel17453	30	0.00 ± 7.57	3.87 ± 4.64
sel213	71	-5.13 ± 16.59	3.66 ± 7.55
sel221	0	-	-
sel223	31	-16.90 ± 13.13	0.52 ± 6.09
sel230	50	-3.44 ± 11.68	3.92 ± 6.23
sel231	50	1.04 ± 10.34	4.24 ± 7.38
sel232	0	-	-
sel233	30	-0.80 ± 7.31	0.13 ± 6.17
sel30	30	1.20 ± 6.74	5.20 ± 3.66
sel301	30	0.13 ± 6.34	5.60 ± 6.18
sel302	30	-7.60 ± 5.49	2.40 ± 4.28
sel306	36	-5.00 ± 8.13	1.33 ± 14.09
sel307	30	-0.13 ± 7.24	0.93 ± 5.11
sel308	50	-0.32 ± 5.76	-3.36 ± 12.21

Table 7.2: First of three parts of the results obtained for automatic delineation algorithm validated with the QT database from physionet.org. Numeric values are presented as mean and standard deviation (mean $\pm$ std) in milliseconds and represent the difference between automated and the manual annotation. This table was reprinted from publication [99] with permission from the publisher.

Signal name	Number of P waves	P_{on} mean±std	P_{peak} mean±std
sel31	30	2.53 ± 10.79	0.40 ± 4.25
sel310	0	-	-
sel32	30	-7.73 ± 10.34	2.53 ± 5.99
sel33	30	3.73 ± 9.57	2.80 ± 3.95
sel34	30	-15.20 ± 31.13	0.80 ± 10.58
sel35	0	-	-
sel36	1	160.00 ± 0.00	180.00 ± 0.00
sel37	0	-	-
sel38	30	5.20 ± 29.09	23.60 ± 30.58
sel39	30	2.80 ± 7.44	4.13 ± 3.71
sel40	30	15.47 ± 58.79	21.60 ± 61.86
sel41	30	25.73 ± 24.22	15.60 ± 33.22
sel42	30	-26.53 ± 5.41	3.60 ± 3.84
sel43	30	-18.93 ± 11.21	0.80 ± 3.70
sel44	22	-14.55 ± 6.24	-2.00 ± 4.90
sel45	30	-6.80 ± 21.45	-0.13 ± 3.86
sel46	29	-9.52 ± 12.80	1.79 ± 4.85
sel47	30	-2.40 ± 5.81	-0.40 ± 10.52
sel48	30	-6.93 ± 10.81	2.00 ± 7.84
sel49	30	-16.67 ± 9.10	-1.07 ± 3.31
sel50	0	-	-
sel51	30	-6.27 ± 17.03	-2.13 ± 4.55
sel52	30	-0.67 ± 11.41	2.00 ± 5.23
sel803	30	5.20 ± 11.17	6.93 ± 6.72
sel808	30	-2.00 ± 11.15	6.00 ± 6.28
sel811	30	6.67 ± 10.73	0.53 ± 5.43
sel820	30	1.60 ± 10.43	2.13 ± 10.22
sel821	26	-16.00 ± 24.03	-4.62 ± 15.62
sel840	47	-6.21 ± 22.64	0.60 ± 13.24
sel847	33	5.33 ± 8.98	5.58 ± 5.99
sel853	30	2.00 ± 8.96	4.67 ± 9.69
sel871	70	5.49 ± 9.85	1.31 ± 4.24
sel872	30	10.67 ± 8.62	4.00 ± 5.75
sel873	33	-6.55 ± 14.03	0.97 ± 9.28
sel883	30	-4.27 ± 8.46	3.20 ± 13.91

Table 7.3: Second part of the results obtained for automatic delineation algorithm validated with the QT database from physionet.org. Numeric values are presented as mean and standard deviation (mean $\pm$ std) in milliseconds and represent the difference between automated and the manual annotation. This table was reprinted from publication [99] with permission from the publisher.

Signal name	Number of P waves	P_{on} mean±std	P_{peak} mean±std
sel891	58	-2.07 ± 17.43	13.59 ± 19.92
sele0104	30	0.00 ± 5.94	6.13 ± 3.75
sele0106	30	4.93 ± 7.70	3.60 ± 4.74
sele0107	34	3.29 ± 10.30	4.24 ± 6.07
sele0110	30	-6.00 ± 9.32	-0.27 ± 5.03
sele0111	30	-1.60 ± 8.57	4.40 ± 6.92
sele0112	50	3.28 ± 12.56	2.80 ± 7.68
sele0114	30	-4.93 ± 14.16	2.00 ± 9.56
sele0116	30	-16.67 ± 77.24	7.87 ± 70.60
sele0121	30	-2.80 ± 6.40	-0.27 ± 4.19
sele0122	30	-3.60 ± 6.42	6.67 ± 4.50
sele0124	50	4.56 ± 8.04	4.96 ± 8.76
sele0126	30	0.13 ± 8.24	8.80 ± 6.42
sele0129	30	-3.20 ± 11.62	6.93 ± 5.55
sele0133	30	4.00 ± 6.21	8.00 ± 7.05
sele0136	30	-0.53 ± 8.65	1.20 ± 6.49
sele0166	36	2.67 ± 10.25	-1.11 ± 6.53
sele0170	30	2.40 ± 6.09	7.47 ± 4.42
sele0203	30	-3.33 ± 29.97	9.47 ± 24.74
sele0210	30	1.33 ± 20.94	7.20 ± 5.98
sele0211	30	4.27 ± 7.12	4.27 ± 5.14
sele0303	30	-0.93 ± 13.02	1.07 ± 5.03
sele0405	30	-10.40 ± 13.15	0.67 ± 6.13
sele0406	31	-4.52 ± 7.64	3.10 ± 2.87
sele0409	30	-13.07 ± 6.30	3.73 ± 5.25
sele0411	30	-1.07 ± 6.30	2.27 ± 4.89
sele0509	30	-0.13 ± 4.75	4.40 ± 7.74
sele0603	30	-0.27 ± 7.35	8.00 ± 8.00
sele0604	30	-1.33 ± 7.30	-6.13 ± 8.25
sele0606	30	2.93 ± 6.88	6.80 ± 4.35
sele0607	30	-0.13 ± 10.10	3.73 ± 6.21
sele0609	30	-3.47 ± 9.08	6.80 ± 4.35
sele0612	30	28.67 ± 13.46	6.13 ± 5.73
sele0704	30	8.53 ± 17.63	5.33 ± 14.22
global	**3194**	**-0.27 ± 12.20**	**5.75 ± 9.12**

Table 7.4: Third and final part of the results obtained for automatic delineation algorithm validated with the QT database from physionet.org. Numeric values are presented as mean and standard deviation (mean ± std) in milliseconds the difference between automated and the manual annotation. This table was reprinted from publication [99] with permission from the publisher.

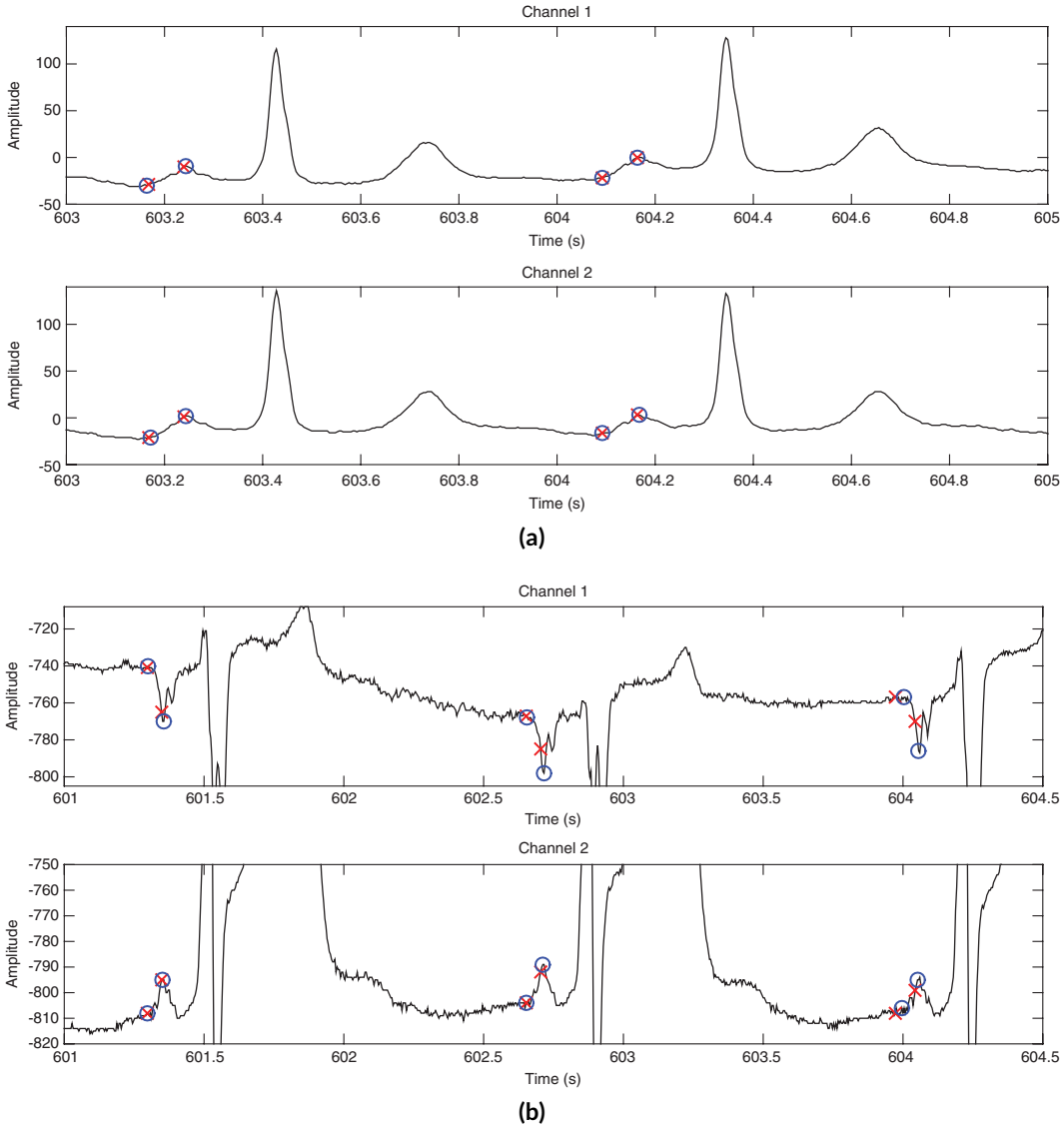

Figure 7.10: (a): Manual and automatic annotations are compared. The blue circle represents the automatic annotation from our algorithm, while the red cross corresponds to the delineation of P_{peak} and P_{on} delivered by the expert physician. (A) High-quality signal for which automatic and manual delineations are in full agreement. (B) ECG signal with abnormal P wave morphology for which the automatic algorithm seems to deliver more accurate delineation. This figure was reprinted from publication [99] with permission from the publisher.

points. We also showed that the point P_{on} would shift proportionally to the width of the P wave. This is probably because the wavelet transform is related to a higher order derivative of the P wave making the extreme points of the transform of the Gaussian bell proportional to its standard deviation.

In the second part of this analysis, we evaluated the impact of noise on the delineation process. We found that the algorithm is very accurate at all SNR levels under the influence of white noise but the robustness lowers with decreasing SNR. This is expected since white noise overlaps in the time and frequency domain with the P wave damaging its morphology

and compromising the delineation procedure. However, the results obtained at standard SNR levels expected from qualitative recording devices are very precise and definitely useful for this application. Furthermore, baseline wander and power line hum did not have a measurable impact on the delineation process. This is due to the fact that these two perturbations are located in a different frequency band than the one used for phase free SWT.

In summary, these results prove that the phase free SWT has very favorable properties relevant for a delineation method.

7.4.2 Plausibility of the Algorithm

In the investigation on the best configuration for the algorithm, we found that the reverse biorthogonal wavelet 3.3 delivered the most accurate and robust delineation. This result is indeed plausible because the scaling function of this wavelet is also bell shaped and thus very similar to the P wave. This wavelet has a higher correlation with the P wave and delivers larger wavelet coefficients in the SWT accounting also for a higher SNR. Furthermore, among the family of the reverse biorthogonal 3.x wavelets, the third one had the best performance. In this family of wavelets, the higher the wavelet order, the sharper it is in the frequency domain but also the broader it is in the time domain. Thus, the reverse biorthogonal 3.3 wavelet should have the best trade-off between spectral sharpness and time concentration for this particular application.

We also found out that level seven was the best performing one in terms of accuracy and robustness. This is also in accordance with our initial guess presented in section 7.2.6. However, since sub-band correlation is a well-known phenomenon in the wavelet theory, it was necessary to test other neighboring levels. As a matter of fact, the reverse biorthogonal 3.5 and coiflet 1 delivered also very good results at level six.

7.4.3 Performance of the Algorithm in the QT Database in Relation to Other Methods

The algorithm was also evaluated in a realistic environment using the QT database. Different P wave morphologies from different patients and ECG leads posed a challenging task for our method. Thus, it was gratifying to see that the algorithm performed very accurately delivering a delineation error of P_{on} below the time resolution of the signal and the error for P_{peak} was just above one sample. Compared to other methods in literature, our algorithm delivered the most accurate delineation of P_{on} and it was within the range of the other methods for P_{peak}. Table 7.5 shows a comparative summary of the methods proposed in literature. The sensitivity (SEN) and positive predictive value (PPV) are also presented in the table and were defined according to Martínez [115]. It is important to mention that a direct comparison is not entirely adequate since other authors considered only P waves of high quality in their analysis, while we included all P waves in the database independent of their quality.

		P_{on}			P_{peak}	
	No.	**mean ± std**	**SEN**	**PPV**	**mean ± std**	**SEN**	**PPV**
This work	3194	-0.27 ± 12.20	100%	88.15%	5.75 ± 9.12	100%	88.15%
Martinez WT [115]	3194	2.0 ± 14.8	98.87%	91.03%	3.6 ± 13.2	98.87%	91.03%
Dumont [116]	N/A	1.9 ± 11.8	98.79%	99.23%	1.4 ± 9	98.39%	98.88%
Laguna [115]	3194	14.0 ± 13.3	97.7%	91.17%	4.8 ± 10.6	97.7%	91.17%
Ghaffari [117]	N/A	1.2 ± 6.3	99.46%	99.46%	4.1 ± 10.5	98.83%	98.83%
Martinez PT [108]	3194	2.6 ± 14.5	98.65%	N/A	32 ± 25.7	98.65%	N/A
Lin [118]	1750	1.7 ± 10.8	99.6%	N/A	2.7 ± 8.1	97.7%	N/A

Table 7.5: Comparison among different delineation algorithms of the P wave found in literature. The abbreviation "No." stands for the number of P waves used in the analysis. The delineation errors are given as mean and standard deviation (mean ± std) in milliseconds. The sensitivity and positive predictive value are denoted by SEN and PPV. Our method delivered the most accurate delineation of P_{on} and competitive performance finding P_{peak}. This table was reprinted from publication [99] with permission from the publisher.

7.4.4 Limitations

The proposed algorithm and the results obtained quantifying its performance have a series of limitations that should be presented as follows. First, the data set used to find the best configuration of the method was not particularly diverse. One single patient and 33 P waves do not necessarily have a strong statistical power. However, it was enough to obtain convincing results in the QT database. Yet, we cannot exclude the possibility that other wavelets and other decomposition levels could perform even better with other unknown signals.

Second, the delineation of P_{on} is dependent on the correct finding of the side maxima in the SWT. In the case that more than one side maximum appears, the one closest to the first 10 % of the area under the transformed P wave are chosen. However, this is a heuristic chosen to match our intuition on the location of the first delineating point in a normal P wave. There could be other P wave morphologies for which this approach may not be the correct one.

Finally, the algorithm was created to work with ECG signals recorded in sinus rhythm for which a P wave is expected prior to the QRS complex. However, supraventricular tachycardias such as AFlu or AFib, for which more than one P wave may appear in a single RR interval, are going to pose a problem for the algorithm. The same is valid for ventricular tachycardias in which no P wave is present in the RR interval.

7.4.5 Outlook

In a future project, it would be very interesting to extend the data set of intracardiac signals to include more patients and other P wave morphologies. The best performing configuration of the method could be further investigated and improved. At some point it may become necessary to extend the algorithm to account for supraventricular arrhythmias. The combined usage of intracardiac and surface recordings can help to understand how complex diseases

such as AFlu or AFib manifest in the surface ECG. Furthermore, the precise delineation of the P wave allows also the investigation of the time evolution of the P wave morphology and it could be used to facilitate diagnosis, risk stratification or preoperative planing.

7.5 Conclusion

The results obtained in this study proved that the phase free SWT fulfills the most important requirements of a delineation algorithm. The points P_{peak} and P_{on} are independent of amplitude of the P wave but linearly dependent of its width. The method remains very accurate under the influence of noise and is robust at high SNR levels. It is also not affected by baseline wander or power line hum. The evaluation on the QT database demonstrated a strong performance in comparison to other methods in literature and validated the configuration chosen for our method. In future, the algorithm should be extended to account for supraventricular and ventricular tachycardias.

PART IV

RESPIRATION AND HEART RATE

CHAPTER 8

Separating the Effect of Respiration on Heart Rate Variability

8.1 Introduction

The rate at which the human heart pumps blood in the body is not constant. As a matter of fact, it is continuously adapting to internal and external factors. This phenomenon is called heart rate variability (HRV) and it is primarily regulated by the two complementary branches of the autonomic nervous system (ANS), the sympathetic and the parasympathetic nervous systems. A healthy person, for whom the regulation of the heart is normal, is expected to have a strong HRV [9]. It is also well known that HRV is tightly coupled to respiration and blood pressure in the cardiovascular system. Moreover, the phenomenon called respiratory sinus arrhythmia (RSA) is the strongest manifestation of the ANS directed to the heart and measured in the RR time series [16].

In RSA, the RR time series and the breathing pattern synchronize leading to a reduction of heart rate during expiration and an increased of heart rate during inspiration [16]. This phenomenon is not fully understood but it is believed to maximize gas transfer between the lungs and the blood vessels while minimizing mechanical work with the aim of maintaining healthy concentration of gases in the body (oxygen and carbon dioxide in blood). In addition, the influence of RSA on HRV is dependent on many factors such as state of health, age, tidal volume and respiration rate of the subject [37–39]. This complicates a direct measurement of the effect of RSA on the HRV parameters. This is the reason why other authors in different applications have tried to control the influence of respiration on HRV either by fixing the respiration rate of the subjects or by subtracting its effect with signal processing methods [17, 119]. These applications have the common hypothesis that respiration free HRV parameters could have a higher diagnostic power or at least deliver new insights about the regulation carried out by the ANS.

In order to shed more light on this topic, we developed a method to quantify coupling between respiration and HRV and separated its respiration dependent part if significant

coupling was present. The quantification of coupling was based on the Granger's causality and significant coupling is detected using statistical hypothesis testing. Furthermore, the method used to separate the respiration dependent part of HRV was carried out depending on the type of respiration being analyzed. For the case of paced respiration, a Gaussian notch filter was developed, while for natural breathing we created a moving average (MA) filter that included respiration as external input. The methods were tested and validated on a theoretical basis using synthetic signals. We further applied the method to separate respiration from HRV in a data set with paced respiration and another one with natural breathing. This work was carried out in close cooperation with group BSICoS a the University of Zaragoza and published as a journal paper [63] and presented in form of a conference contribution [120].

8.2 Materials and Methods

8.2.1 Data

8.2.1.1 Synthetic Signals

For the purpose of testing our algorithms on a theoretical basis, we used synthetic signals for which the ground truth was well-known to perform a simulation study. The RR time series, the respiration pattern and the directional coupling from respiration to RR time series were modeled to reproduce realistic recordings. Figure 8.1 shows the block diagram used for the simulation study. Here, the intrinsic (respiration independent) RR time series is generated as a realization of pink noise. The respiration signal $resp(n)$ was modeled as a sinusoidal function with a time dependent frequency. The directional coupling to create the respiration dependent part in the RR time series $RR_{resp}(n)$ was modeled with an MA filter with transfer function $G(k)$. The intrinsic and respiration dependent parts of the RR time series build together the measured RR time series $RR_{meas}(n)$. The structure used for this model is a particular case of the more general multivariate dynamic adjustment models [121].

More specifically, the models used to reproduce the signals used in this study were defined as follows:

- Respiration was generated using a sinusoidal function having the form $resp(n) = A \cdot \cos(\phi(n))$. The time-dependent phase $\phi(n)$ was defined as the discrete-time approximation of the integral of the time-varying frequency $f(n)$.

$$\phi(n) = \sum_{k=0}^{n} \frac{f(k)}{f_s} \tag{8.1}$$

  The parameter f_s is the sampling frequency in Hz of the respiration signal. We set the sampling frequency to 4 Hz because it is a typical value used in literature for HRV

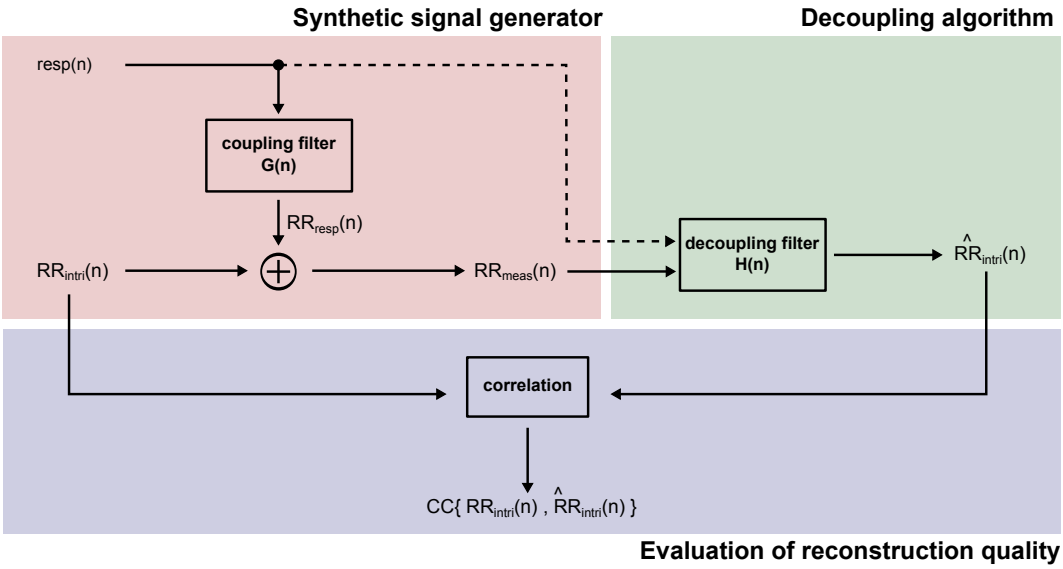

Figure 8.1: Scheme used to synthesize the signals needed to test our algorithms at a theoretical level. This figure was reprinted from publication [63] with permission from the publisher.

analysis [122]. For the time-varying frequency $f(n)$, we used a hyperbolic tangent (tanh) function given by the following equation:

$$f(n) = f_0 + f_1 \cdot \tanh\left(\frac{n - n_0}{f_s \cdot T}\right) \tag{8.2}$$

This is a sigmoid function that was parametrized to obtain the desired signal properties. This function has inferior and superior bounds equal to $f_0 - f_1$ and $f_0 + f_1$ respectively. The product $f_s \cdot T$ is a time-discrete constant that modifies the slope of the sigmoid function. We chose the parameters A, f_0, f_1, T and n_0 in such manner that different physiological scenarios could be recreated. For constant breathing, $f_0 \in [0.1; 0.6]\,Hz$ and $f_1 = 0.005\,Hz$ were chosen to ensure a concentrated spectrum around the breathing frequency f_0. For spontaneous breathing, $f_0 \in [0.1; 0.6]\,Hz$ and $f_1 \in [0; 0.1]\,Hz$ were chosen randomly to mimic variability in the breathing frequency. The other parameters were also obtained from a uniform distribution with the following properties: $A \in [0.2; 0.5]$, $n_0 = [180, 540]$, $T \in [10; 30]\,s$, and a signal length of $N = 720$ sample points equivalent to three minutes was set fixed. In Figure 8.2, four possible realizations of the time varying frequencies are presented.

- The intrinsic RR time series was modeled as a realization of Gaussian pink noise. This type of random process is characterized by a Gaussian distribution of amplitudes $\mathcal{N}(0; \sigma)$ in the time domain and a power spectral density (PSD) proportional to the reciprocal of the frequency $S_{RR_{intri}}(f) \propto 1/f$. This signal can be generated as a low-pass filtered additive white Gaussian noise (AWGN) [123].
- The coupling filter $G(k)$ was modeled as a moving average system applied on the respiration signal. The measured RR time series was then given in the following way:

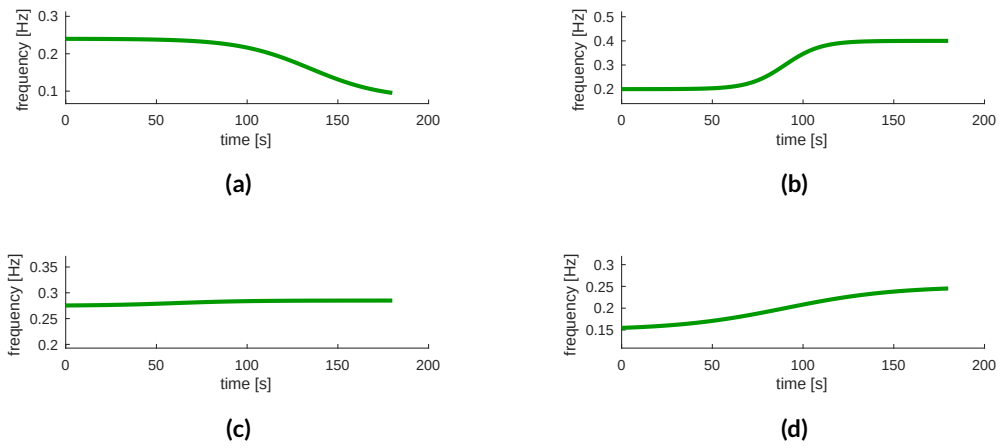

Figure 8.2: Four possible realizations of time-varying respiration frequencies with different parameter sets. The following sets of parameters were used: (a): $f_0 = 0.16$ Hz, $f1 = 0.08$ Hz, $n_0 = 540$, $T = 20$ s. (b): $f_0 = 0.3$ Hz, $f_1 = 0.1\,Hz$, $n_0 = 360$, $T = 10$ s. (c): $f_0 = 0.28$ Hz, $f_1 = 0.005$ Hz, $n_0 = 480$, $T = 20$ s. (d): $f_0 = 0.2$ Hz, $f_1 = 0.05$ Hz, $n_0 = 360$, $T = 30$ s. This figure was reprinted from publication [63] with permission from the publisher.

$$RR_{meas}(n) = \sum_{k=1}^{K} g(k) \cdot resp(n-k) + RR_{intri}(n)$$

Here, the parameter K is the filter order and $g(n)$ is its impulse response. For the study with synthetic signals, the parameter $K \leq 12$ was chosen. Thus, respiration values from up to three seconds in the past could be coupled to the current RR interval [124].

A possible realization of the kind of signals that can be generated using this simulation scheme is presented in figures 8.3 (a) to (h). The time domain signals and their corresponding spectra can be seen. From the shape of the signals, it can be seen that the recorded $RR_{meas}(n)$ is a combination of both, $RR_{intri}(n)$ and $resp(n)$. The last two figures show the results of the decoupling procedure use to reconstruct the original $RR_{intri}(n)$ in an accurate manner. In addition, a comparison between real recordings and synthesized signals can be seen in figure 8.4. Although the real recordings and the simulated signals are not perfectly equal in the time domain, their spectral properties are very similar. This demonstrated the capabilities of the simulation scheme and allowed us to use it to test the decoupling algorithms.

8.2.1.2 Paced Respiration Study

The PRS was conducted by the research group BSICoS at the University of Zaragoza in Spain with the aim of creating a multimodal data set with cardiovascular signals recorded from healthy subjects breathing at a fixed respiration rate. These data were used in a previous

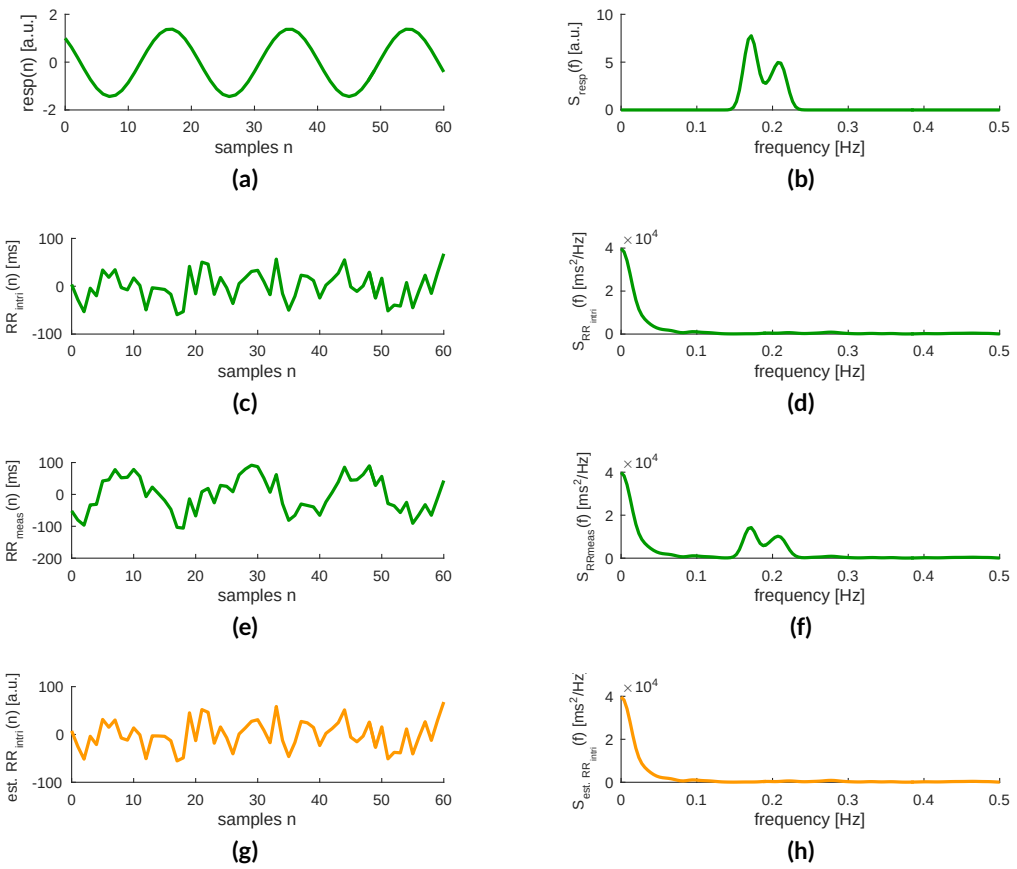

Figure 8.3: Demonstration of the kind of signals that were generated with the simulation scheme. In the left column are the time domain representations while in the right column are the spectra of the signals. (a): Synthesized respiration signal with time-dependent frequency (b): PSD of the signal displayed in (a). (c): Synthesized intrinsic RR time series. (d): PSD of the signal displayed in (c). (e): Synthesized RR time series to recreate a measured one. (f): PSD of the signal displayed in (e). (g): Reconstructed intrinsic RR time series with the decoupling algorithm proposed here. (h): PSD of the signal displayed in (h). This figure was reprinted from publication [63] with permission from the publisher.

research project published in [125]. 19 subjects (6 females, 13 males) participated in the study with ages ranging from 21 to 52 years (median of 28 years). For the study, the subjects were asked to breath at a given constant rate for three minutes, to take a short break afterwards and to breath again at the next given frequency. The respiration frequencies went from 0.1 to 0.6 Hz in steps of 0.1 Hz. A video with a sine wave oscillating at the requested breathing frequency was displayed to the subjects and they were told to follow the pattern with their breathing. The sine wave in the video had a small error of 0.22 ± 1.05 mHz.

Respiratory pattern and electrocardiogram (ECG) were acquired simultaneously with the recorders ABP-10 and POLY-37 from the manufacturer Medicom MTD. The ECG was sampled at a rate of 1000 Hz, with a resolution of 24 bits and the signal was acquired with an orthogonal electrode placement. The respiratory signal was recorded with a chest belt at a sampling rate of 250 Hz. An example of the signals acquired in the PRS study in comparison with synthesized signals with similar properties can be seen in figure 8.4.

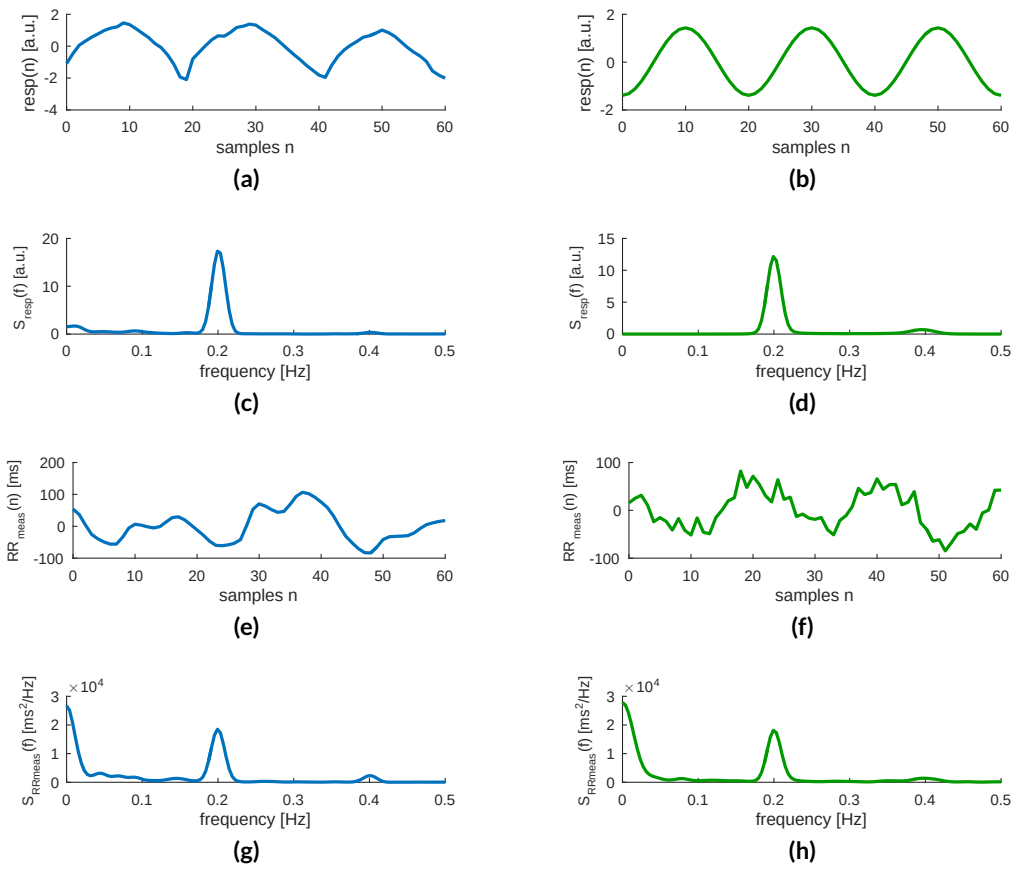

Figure 8.4: Comparison between the signals recorded in the PRS study (left column) and the ones synthesized to test our algorithms (right column). (a): Respiration pattern recorded in the PRS study. (b): Synthetic respiration signal with similar properties to the one presented in (a). (c): PSD of the respiration signal presented in (a). (d): PSD of the respiration signal displayed in (b). (e): RR time series recorded in the PRS study. (f): Synthetic RR time series with similar properties to the one presented in (e). (g): PSD of the RR time series presented in (e). (h): PSD of the R time series displayed in (f). This figure was reprinted from publication [63] with permission from the publisher.

The quality of the recordings was visually inspected and one subject had to be removed from the study because of low signal-to-noise ratio (SNR) and missing signal portions. In addition, we had to be careful with aliasing when dealing with the RR time series and the respiration. The RR time series has an inherent sampling rate that is equal to the heart rate of the subject. Since we wanted to investigate respiration at the exact same moments when the heart beats, aliasing could become a problem if the subject was breathing faster than their mean heart rate divided by two (sampling theorem). This became particularly problematic for the higher breathing rates of 0.5 and 0.6 Hz. For this reason, we had to additionally remove three subjects from the analysis violating the sampling theorem at 0.5 Hz and another nine at 0.6 Hz.

8.2.1.3 Fantasia Database

In order to include signals recorded from subjects breathing at a spontaneous rate in our investigations, we used the Fantasia database from *physionet.org* [126]. This data set was recorded from 20 young and 20 old subjects (20 males and 20 females) while they were watching the Disney movie Fantasia in a supine position at rest. The young subjects were between 21 and 34 years old, while the age of the older participants ranged from 68 to 85 years. An ECG lead and a respiration signal were acquired for each subject in the database. The signals had a duration of 2 hours and were sampled at 250 Hz. An example of the signals in the Fantasia database in comparison with synthesized signals with similar properties can be seen in figure 8.5.

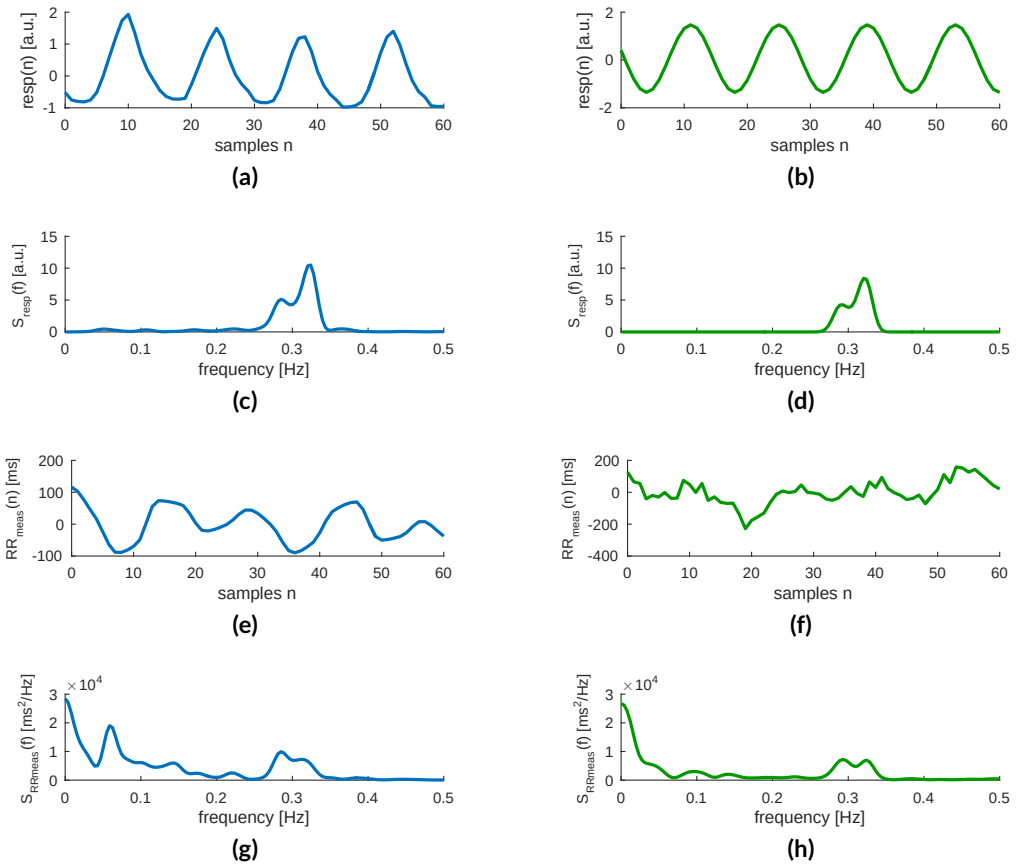

Figure 8.5: Comparison between the signals recorded in the Fantasia database (left column) and the ones synthesized to test our algorithms (right column). (a): Respiration pattern recorded in the Fantasia database. (b): Synthetic respiration signal with similar properties to the one presented in (a). (c): PSD of the respiration signal presented in (a). (d): PSD of the respiration signal displayed in (b). (e): RR time series recorded in the Fantasia database. (f): Synthetic RR time series with similar properties to the one presented in (e). (g): PSD of the RR time series presented in (e). (h): PSD of the R time series displayed in (f). This figure was reprinted from publication [63] with permission from the publisher.

8.2.2 Filtering the ECG and Respiration Signals

The ECG signal was filtered with a Butterworth high-pass filter with a cutoff at 0.5 Hz to remove baseline wander. Power line hum was removed using a Gaussian notch filter at 50 or 60 Hz and its harmonics. High frequency random noise was removed with a Butterworth low-pass filter with a cutoff frequency at 250 Hz. This upper cutoff frequency was chosen particularly high to preserve the R peak in the ECG and achieve an accurate RR time series.

The respiration signal was filtered with a Gaussian high-pass filter with a cutoff at 0.05 Hz to remove baseline wander. Power line hum was removed in the same manner as with the ECG signal. High frequency random noise was removed with a Butterworth low-pass filter with a cutoff frequency at 20 Hz.

8.2.3 Correcting the RR Time Series

The signal processing work flow to obtain the RR time series from the ECG was presented in chapter 4 and was kept unchanged here. However, special attention was payed to the RR time series because detection errors in the R peak can lead to wrong RR intervals and the coupling analysis can be compromised. In order to account for artifacts in the RR time series, we cleaned the series using the method proposed by Malik, in which RR intervals that differ in more than 20 % from the previous or subsequent one are removed [127]. There are other methods to clean the RR time series, yet the removal without replacement seems to be the most conservative one.

8.2.4 Quantifying Coupling with the Granger's Causality

In order to quantify coupling (causality) between respiration and RR time series, we used the method proposed by Granger [128]. In this approach, a time series $y(n)$ was considered to cause another time series $x(n)$, if the prediction of the latter one could be improved when information from the first series was introduced. The initial prediction of the time series $x(n)$ was performed with a linear autoregressive (AR) model. In order to improve the AR estimation of $x(n)$, the series $y(n)$ was introduced through a linear MA model and statistically evaluated to test if it produces a significantly better prediction. The quality of an estimation was measured based on the comparison between the variance of the prediction error of the AR model with respect to the error variance of the MA model. In mathematical terms, the Granger's causality was defined in the following manner:

First, the time series $x(n)$ was modeled as an AR random process:

$$x(n) = \sum_{k=1}^{P} a(k) \cdot x(n-k) + \varepsilon_{AR}(n) \tag{8.3}$$

The AR model was chosen to have an order of P. Further, it is assumed that the prediction error $\varepsilon_{AR}(n)$ was normally distributed having an expected value μ_{AR} and a variance σ^2_{AR}. Typically, the expected value of the prediction error was zero, so that its variance could be estimated by:

$$\sigma^2_{AR} = \frac{1}{N-P-1} \sum_{k=1}^{N-P} \varepsilon^2_{AR}(n) \tag{8.4}$$

In this equation, N was the total number of sample points in the time series. The estimated variance σ^2_{AR} was a random variable distributed according to the χ^2_{N-P} probability density function [129]. Once the AR model has been evaluated, the exogenous input was included into the prediction model with an MAx filter:

$$x(n) = \sum_{k=1}^{P} a(k) \cdot x(n-k) + \sum_{k=1}^{Q} b(k) \cdot y(n-k) + \varepsilon_{ARMAx}(n) \tag{8.5}$$

The MAx model was chosen to have an order of Q and its error variance σ^2_{ARMAx} is χ^2_{N-P-Q} distributed. The quality of the predictions is then compared building the normalized difference of the two error variances [130]:

$$\gamma_{yx} = \frac{\sigma^2_{AR} - \sigma^2_{ARMAx}}{\sigma^2_{ARMAx}} \tag{8.6}$$

$$= \frac{\sigma^2_{AR}}{\sigma^2_{ARMAx}} - 1 \tag{8.7}$$

The ratio $\sigma^2_{AR}/\sigma^2_{ARMAx}$ was again a random variable governed by the F distribution with $N-P$ and $N-P-Q$ degrees of freedom [129]. The null hypothesis that $y(n)$ did not cause $x(n)$ was tested with an F-test allowing a maximal error probability of 5 %. Under these conditions, the threshold for which an improvement in the prediction of $x(n)$ was statistically significant was given by:

$$\gamma^{5\%}_{yx} = F^{-1}(0.05, N-P, N-P-Q) - 1 \tag{8.8}$$

In this equation, F^{-1} stands for the inverse F distribution. Furthermore, the parameter γ_{yx} could be interpreted as a measure of coupling strength. Thus, $\gamma_{yx} = 0$ means that no coupling was present between the two time series. Stronger coupling is reflected in higher values of γ_{yx} and the causality becomes statistically significant if the threshold $\gamma^{5\%}_{yx}$ was exceeded.

In addition, for an optimal estimation of the model orders P and Q, we used the Bayesian information criterion (BIC) [131]. In this method, an optimal trade-off between model order P and precision of the estimation is achieved when the following cost function is minimized:

$$BIC_{AR}(P) = N \cdot \ln(\sigma^2_{AR}) + P \cdot \ln(N) \tag{8.9}$$

The same procedure was applied to find the model order Q for the MAx model. If no minimum is found for this cost function, the optimization process was adapted and a "best guess" was found according to [132]. In our study, $x(n)$ corresponded with the recorded RR time series $RR_{meas}(n)$ while the respiration time series $resp(n)$ was represented by $y(n)$. In addition, the decoupling procedure was only performed if significant coupling between these two series was detected.

8.2.5 Decoupling Paced Respiration

In paced respiration, the spectrum of the RR time series was characterized by a localized peak at the breathing frequency that concentrates coupling to a narrow frequency band. Thus, we assumed that it should be possible to remove this peak using a notch filter and separate the respiration driven part of HRV. For this purpose, we developed an optimal Gaussian notch filter that matched the peak corresponding to respiration in the RR time series and removed it. The HRV spectrum was estimated using Welch's method [133]. Here, a Hamming window with a width of 64 s (256 sample points) and an overlap of 50 % were chosen. The time series was extended with zero padding to generate 1024 points before the fast Fourier transform was carried out.

As mentioned previously, the idea behind this method is to approximate the respiration driven peak in the HRV spectrum and use that approximation to produce a notch filter. The notch filter was then created by inverting the approximated peak. Figure 8.6 demonstrates this principle. The approximation of the spectral peak was carried out with a Gaussian bell for which the amplitude, shift and width were optimized. The optimization problem was formulated as a least squares minimization in the following manner:

$$\begin{aligned} \left|S_{RR}(k) - S_{Gauss}(k)\right|^2 &\rightarrow min \quad \text{for} \quad k \cdot \Delta f \in B_{min} \\ \left|S_{RR}(k) - \mathbf{a} \cdot exp(-\mathbf{b} \cdot (k \cdot \Delta f - f_{resp})^2)\right|^2 &\rightarrow min \quad \text{for} \quad k \cdot \Delta f \in B_{min} \end{aligned}$$

Here, $S_{RR}(k)$ was the PSD of the RR time series and S_{Gauss} was the Gaussian bell with amplitude $\mathbf{a}$ and reciprocal width $\mathbf{b}$. The paced breathing frequency was denoted by f_{resp} and corresponded with the maximum of the peak in the spectrum. The parameter B_{min} was the frequency band in which the estimation is carried out. This interval was chosen between the first side minima left and right from the peak at f_{resp}. Finally, k is the discrete spectral variable and Δf is the spectral resolution.

In its current formulation, the optimization problem has a non-linear dependency from the parameters $\mathbf{a}$ and $\mathbf{b}$. However, the problem can be reformulated using the natural logarithm to generate a linear optimization problem as follows:

$$\left|ln(S_{RR}(k)) - ln(\mathbf{a} \cdot exp(-\mathbf{b} \cdot (k \cdot \Delta f - f_{resp})^2))\right|^2 \rightarrow min \quad \text{for} \quad k \cdot \Delta f \in B_{min}$$
$$\left|ln(S_{RR}(k)) - ln(\mathbf{a}) + \mathbf{b} \cdot (k \cdot \Delta f - f_{resp})^2\right|^2 \rightarrow min \quad \text{for} \quad k \cdot \Delta f \in B_{min}$$

The estimation of $ln(\mathbf{a})$ and $\mathbf{b}$ is carried out with the linear least squares approach. With the two parameters, the decoupling filter is created as an inverted Gaussian bell in the following manner:

$$|H(k)|^2 = \mathbf{a} \cdot (1 - exp(-\mathbf{b} \cdot (k \cdot \Delta f - f_{resp})^2))$$

We carried out the filter step to decouple the two series in the time domain to avoid boundary effects arising from circular convolution. This method has the advantage that a respiration signal is not mandatory. The whole procedure can be carried out using only the RR time series and the paced respiration frequency. Nevertheless, the respiration frequency is assumed to be constant and the method can only work if the coupled spectral power is concentrated around the breathing rate.

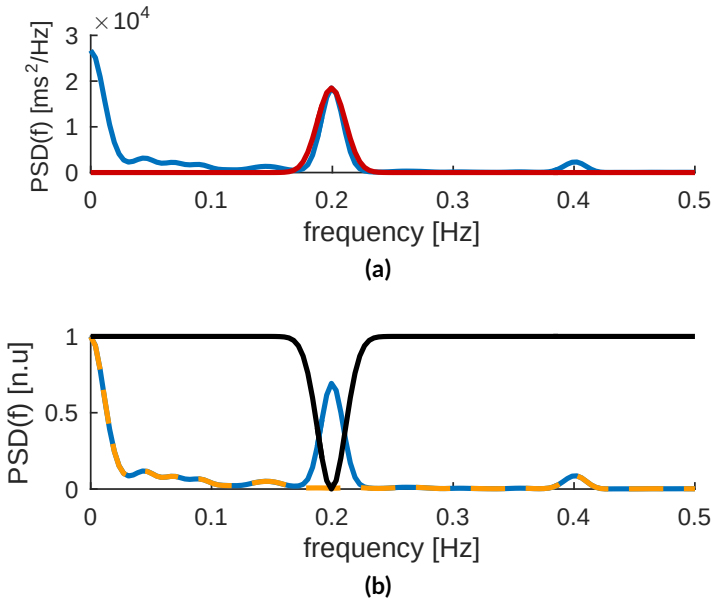

Figure 8.6: Gaussian notch filter used to decouple paced respiration. (a): Respiration driven part of HRV is characterized by a peak in the spectrum concentrated at the breathing frequency (blue). It was approximated using a Gaussian bell (red). (b): The Gaussian bell is inverted to create a notch filter (black). The filtered spectrum (orange) no longer had a peak at the breathing frequency. This figure was reprinted from publication [63] with permission from the publisher.

8.2.6 Decoupling Natural Breathing

In the more general case of spontaneous breathing, the respiration rate could no longer be assumed to be constant and a more general decoupling procedure was required. The idea here, was to model coupling with an MAx filter that interconnects respiration and RR time series. Once the estimation has been performed, it can be subtracted from the measured RR time series. The filter is characterized by its impulse response $h(n)$ and its order Q. The complete coupling model was given by:

$$RR_{meas}(n) = \sum_{k=1}^{Q} h(k) \cdot resp(n-k) + RR_{intri}(n)$$

The model order Q was also found using the BIC. We also assumed that $RR_{intri}(n)$ and the respiration driven part of HRV given by $\sum_{k=1}^{Q} h(k) \cdot resp(n-k)$ to be uncorrelated to each other. By doing so, we were able to reformulate the estimation problem as a minimization one in which $h(n)$ became a decorrelation filter. This was achieved when:

$$\left| RR_{meas}(n) - \sum_{k=1}^{Q} h(k) \cdot resp(n-k) \right|^2 \rightarrow min \quad \text{for} \quad h(k) \in \mathbb{R}$$

The filter coefficients were found using linear least squares minimization and with them, the estimated intrinsic RR time was calculated as:

$$\hat{RR}_{intri}(n) = RR_{meas}(n) - \sum_{k=1}^{Q} h(k) \cdot resp(n-k)$$

In figure 8.7, four exemplary signals demonstrating the decoupling procedure can be seen. The time and frequency domain representations of all signals can be seen before and after decoupling has been applied. Two of the signals come from the simulation study while the other two are real recordings. Two of the signals correspond to paced respiration while the other two are spontaneous breathing.

8.2.7 Evaluating the Algorithm with Synthetic Data

With the aim of evaluating the algorithms developed in this work at a theoretical level, we created two experiments in which the synthetic signals were used. In the first experiment, the Granger's causality was evaluated as a measure of coupling. In particular, the validity of the threshold $\gamma_{yx}^{5\%}$ to detect significant coupling was put to the test. In the second experiment, we tested the performance of the two decoupling algorithms.

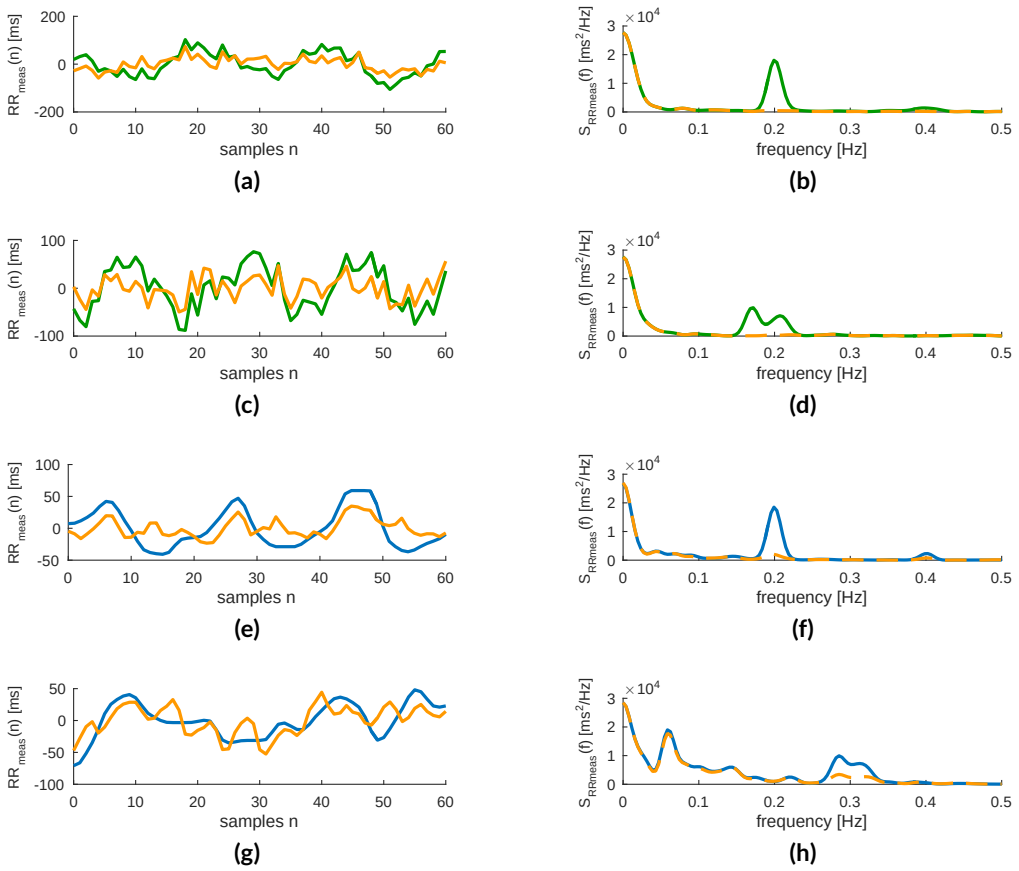

Figure 8.7: (a): Synthetic RR time series with paced respiration before (green) and after (orange) the decoupling algorithm was applied. (b): PSD of the signals presented in (a). (c): Synthetic RR time series with natural breathing before (green) and after (orange) the decoupling algorithm was applied. (d): PSD of the signals presented in (c). (e): Recorded RR time series with paced respiration before (blue) and after (orange) the decoupling algorithm was applied. (f): PSD of the signals presented in (e). (g): Recorded RR time series with natural breathing before (blue) and after (orange) the decoupling algorithm was applied. (h): PSD of the signals presented in (g). This figure was reprinted from publication [63] with permission from the publisher.

8.2.7.1 Evaluating Granger's Causality as a Measure of Coupling

With the purpose of achieving a strong statistical power, we performed this experiment with 200 000 different synthesized signals. The previously introduced parameter A was the amplitude of the respiration signal coupling into the RR time series. It was varied to recreate various coupling strengths and study how the measure γ_{yx} changed in dependency from A. The amplitude $A = \{0, 0.6, 1.4, 2.8, 5\}$ was chosen with the intention of recreating the normal range of the HRV parameter LF/HF $\in [0.2; 5]$. For $A = 0$, no coupling is present while $A > 0$ leads to a coupled respiration signal with $A = 5$ being the strongest coupling.

From the 200 000 realizations, half of them were devoted for the no coupling case of $A = 0$. In every realization, the RR time series, the spontaneous breathing signal and the coupling filter $g(n)$ were generated randomly. In particular, the coupling filter was chosen to

have an order of $Q \leq 12$ and its coefficients were extracted from a uniform distribution in the interval $[-1,+1]$.

8.2.7.2 Evaluating the Decoupling Algorithms

The evaluation of the decoupling measures was carried out with a data set of 100 000 realizations. Half of them were used to test paced respiration while the others aimed at testing natural breathing. The random parameters used to generate this database were introduced in section 8.2.1.1. Decoupling was performed for both cases (paced respiration and natural breathing) with both methods (Gaussian notch filter and MAx filter).

The quality of the reconstructed intrinsic RR time series $\hat{RR}_{intri}(n)$ was quantified with the correlation coefficient. For that purpose, the correlation coefficient between the reconstructed and the original intrinsic RR time series $RR_{intri}(n)$ was estimated. The closer the correlation coefficient is to $+1$, the better the performance of the decoupling procedure.

8.2.8 HRV Analysis

It was also of great interest for this study to investigate how standard HRV parameters change after its respiration driven part has been decoupled. The HRV analysis began with the calculation of HRV parameters from the measured RR time series. Afterwards, the RR time series was decoupled and the same HRV parameters were computed from the estimated intrinsic RR time series.

For the decoupling procedure, the original RR time series was first interpolated to a sampling rate of 4 Hz using monotone cubic splines [134]. There were three reasons for this step. First, the calculation of frequency domain HRV parameters was carried out using Welch's method which required equidistant sampling. Additionally, the increased number of sampling points delivers a spectrum with more information. Third, for the quantification of coupling between respiration and RR time series, the same sampling frequency is required for both signals. Thus, the respiration signal had to be downsampled to achieve a sampling rate of 4 Hz. An anti-alising filter with a cutoff frequency of 2 Hz was applied prior to the downsampling procedure. Third, the monotone cubic splines are important to avoid overshootings in the interpolation step. The overshootings generate larger and shorter RR intervals and could lead to non-accurate estimation of the HRV parameters after decoupling.

For the quantification of HRV, many parameters have been proposed in the past but we concentrated our study on seven parameters, four from the time domain (including one non-linear and one geometrical parameter) and another three from the frequency domain. From the time domain, the parameters SDNN, rMSSD, TINN and Approximate Entropy (ApEn with $r = 0.2 \cdot SDNN$, $m = 2$ and $N = 720$) were computed. The time domain parameters were obtained from the decoupled RR time series resampled at the same positions of the original RR time series. By doing so, we allowed a direct comparison between the HRV parameters before and after decoupling.

The parameters LF, HF and LF/HF were obtained from the frequency domain. Welch's method was used for the estimation of the PSD of the RR time series. Here, a Hamming window with a width of 64 s (256 sample points) and an overlap of 50 % were chosen. The time series was extended with zero padding to generate 1024 points before the fast Fourier transform was carried out achieving a frequency resolution of $\delta f = 3.91 \cdot 10^3$ Hz.

Although the number of HRV parameters chosen for the analysis is not particularly large, the authors assumed it be sufficient for a proper evaluation of the autonomous regulation of the heart.

8.3 Results

8.3.1 Performance of Granger's Causality as a Coupling Measure

The results of the analysis investigating the parameter γ_{yx} as a coupling measure are presented in form of boxplots in figure 8.8 (a). The threshold for statistically significant coupling $\gamma_{yx}^{5\,\%}$ is also displayed in the figure. Using this threshold, the 200 000 realizations were classified into the two subgroups significant and non-significant coupling. The performance of this classification was quantified using the golden truth known from the synthetic signals. A global correct rate of 96.2 % was achieved. Furthermore, a sensitivity (SEN) of 92.6 %, a specificity (SPE) of 100 %, a positive predictive value (PPV) of 100 % and a negative predictive value (NPV) of 93.1 % were achieved. The majority of classification errors were observed for $A = 0.6$ at which coupling was the lowest. In addition, a clear monotonic dependency was observed between the amplitude A and the median of γ_{yx}.

8.3.2 Performance of the Decoupling Algorithms

The results of the analysis investigating the decoupling algorithms to reconstruct $\hat{RR}_{intri}(n)$ from the measured $RR_{meas}(n)$ and the respiration $resp(n)$ are displayed in form of boxplots in figure 8.8 (b). As quality measure, we used the correlation coefficient between reconstructed and synthesized intrinsic RR time series. In the case of paced respiration, the Gaussian filter delivered a median correlation coefficient of 0.968 which turned out to be just below the one obtained with the MAx filter. The lower 25th percentile of two filters were 0.958 and 0.990 respectively demonstrating the high quality reconstruction of both methods.

For natural breathing, we found the MAx filter to be the better performing method. It achieved a median correlation coefficient of 0.992 and an interquartile range of 0.008 demonstrating a very accurate and robust reconstruction. With the Gaussian notch filter, a median correlation coefficient of 0.864 and an interquartile range of 0.111 was achieved. The upper 75th percentile of the performance of this filter was 0.931 proving that even though

this method was not created for this application, it was capable of delivering high quality reconstructions in some cases for which respiration frequency remained relatively constant.

These results proved that the MAx filter worked better in both scenarios. Therefore, for the analysis of the investigation of the coupling measure in γ_{yx} and the analysis of the decoupled HRV parameters we decided to use only the MAx filter.

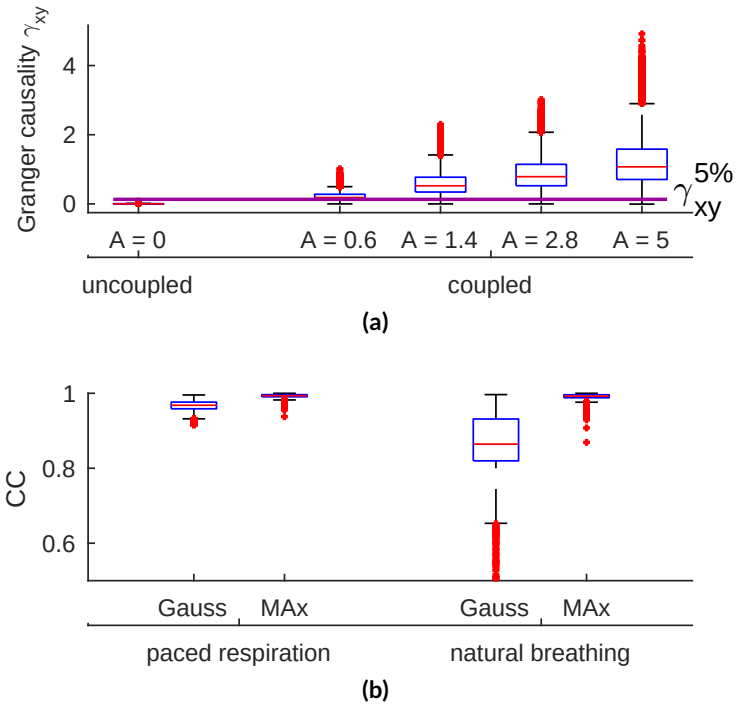

Figure 8.8: Summary of results obtained from the study performed with 200 000 synthetic signals. (a): Coupling measure γ_{yx} obtained from the Granger's causality in dependency of the amplitude of the respiration A. For $A = 0$ no coupling was present while $A = 5$ represented the strongest coupling. $\gamma^{5\%}_{yx}$ is the threshold used to detect significant coupling. This classification system achieved a global correct rate of 96.3 %. (b): Results of the reconstruction of the intrinsic RR time series measured using the correlation coefficient. This figure was reprinted from publication [63] with permission from the publisher.

8.3.3 Coupling between Respiration and RR Time Series

8.3.3.1 Paced Respiration Study

The coupling strength γ_{yx} was investigated in dependency of the paced breathing frequency. The results are presented in figure 8.10. The median coupling was observed to have a clear dependency on the breathing frequency. The threshold for significant coupling is also displayed in the same figure. At 0.1 Hz the median coupling was low and grew with increasing frequency reaching its maximum at 0.3 Hz. Here, significant coupling was present in almost all participants. When the respiration rate was increased further, the coupling

measure γ_{yx} decreased reaching its lowest value at 0.6 Hz. At this frequency, the median coupling was below threshold.

We also did not observe a clear dependency of the intersubject variability, quantified as the interquartile range of the boxplots, and the breathing frequency. However, the lowest interquartile range appeared at the breathing rates 0.1 and 0.6 Hz which were also the frequencies with the lowest coupling strengths. The highest interquartile range appeared at 0.2 Hz.

8.3.3.2 Fantasia Database

The coupling strength was evaluated also in the Fanatasia database. However, the ECG signals in this database have a length of 120 minutes which is significantly larger than the recordings with a duration of three minutes in the PRS study. In order to achieve comparability between the two data sets, we split each signal in the Fantasia database into intervals of the length three minutes and chose the most suited one for the analysis. According to Malik [127], three conditions have to be fulfilled to ensure high quality RR time series:

- No ectopic beats are allowed in the signal.
- The difference between each RR interval and the previous or subsequent one cannot be greater than 20 %.
- Stationarity in the sense of Malik must be given. In this definition, the first RR interval cannot differ in more than 20 % from any other RR interval in the three minute period.

For all the patients, we used initially all the segments that fulfilled the three criteria but kept only the median γ_{yx} for further analysis. Among the selected segments and overall patients, we measured a respiration rate of 0.3 ± 0.09 Hz. Figure 8.9 shows the results obtained in this study in form of a boxplot. The threshold for significant coupling is also shown in the figure. About 75 % of the participants in the study did not have significant coupling. As a matter of fact, median coupling was even lower than the one observed for 0.6 Hz in the PRS study. However, the variability of γ_{yx} among the subjects in the study was similar to the one observed for 0.3 Hz in the PRS study.

8.3.4 Analysis of Heart Rate Variability

We compared the HRV parameters before and after decoupling and tested if a possible change was statistically significant. The error probability (p-value) was computed with the paired Wilcoxon signed rank test and a p-value $p < 0.05$ was considered significant. This procedure was carried out for the PRS study and the Fantasia database. The results were summarized

Table 8.1: The results of the analysis evaluating the change in the HRV parameter value before and after decoupling are summarized in this table. For each parameter, the median and interquartile range (med±iqr), the change in the parameter value given as a ratio and the results of the significance test (p-value) are displayed. The parameter dependency of the paced respiration rate in the PRS study and the spontaneous breathing in the Fantasia database before and after decoupling are shown. This table was reprinted from publication [63] with permission from the publisher.

	0.1 Hz		**0.2 Hz**		**0.3 Hz**		**0.4 Hz**		**0.5 Hz**		**0.6 Hz**		**natural breathing**	
	med	**iqr**	**med**	**iqr**	**med**	**iqr**	**med**	**iqr**	**med**	**iqr**	**med**	**iqr**	**med**	**iqr**
SDNN [ms]	119.89	60.30	57.32	54.02	48.47	41.63	47.74	30.74	34.39	30.58	33.38	19.30	56.92	26.86
$SDNN_{dec}$ [ms]	61.63	32.75	44.53	27.33	40.75	31.85	43.39	26.27	32.41	31.97	30.46	16.66	52.90	35.37
ratio [no u.]	0.51	0.54	0.78	0.51	0.84	0.77	0.91	0.85	0.94	1.05	0.91	0.86	0.93	1.32
p - value	<**0.01**		<**0.01**		<**0.01**		<**0.01**		<**0.01**		<**0.01**		<**0.01**	
rMSSD [ms]	68.50	55.63	41.92	63.80	35.94	65.54	38.11	42.99	30.62	29.54	29.86	20.89	39.26	31.65
$rMSSD_{dec}$ [ms]	47.79	40.40	28.17	32.98	25.12	35.21	24.61	22.49	20.41	23.05	18.39	13.14	34.19	28.40
ratio [no u.]	0.70	0.73	0.67	0.52	0.70	0.54	0.65	0.52	0.67	0.78	0.62	0.63	0.87	0.90
p - value	<**0.01**		<**0.01**		<**0.01**		<**0.01**		<**0.01**		<**0.01**		<**0.01**	
LF [ms^2/Hz]	5791.03	3878.21	260.46	393.07	190.88	384.93	187.18	248.88	167.03	219.68	100.55	118.04	353.88	534.00
LF_{dec} [ms^2/Hz]	357.65	344.31	249.26	389.64	163.36	368.86	222.42	227.77	178.09	214.78	115.24	130.22	297.72	460.94
ratio [no u.]	0.06	0.09	0.96	0.99	0.86	0.96	1.19	0.92	1.07	0.98	1.15	1.10	0.84	0.86
p - value	<**0.01**		**0.04**		**0.01**		0.71		0.76		0.57		0.06	
HF [ms^2/Hz]	512.05	716.17	786.65	2042.61	325.30	757.02	66.53	117.57	34.87	44.58	18.43	16.98	158.74	267.40
HF_{dec} [ms^2/Hz]	438.64	602.99	97.36	198.31	58.74	166.43	49.24	61.47	35.32	47.47	22.91	26.03	111.58	167.30
ratio [no u.]	0.86	0.84	0.12	0.10	0.18	0.22	0.74	0.52	1.01	1.06	1.24	1.53	0.70	0.63
p - value	0.55		<**0.01**		<**0.01**		<**0.01**		0.30		0.42		0.06	
LF/HF [no u.]	9.89	9.16	0.27	0.28	0.86	1.39	2.72	1.33	5.02	3.16	5.63	3.80	1.87	3.76
LF/HF_{dec} [no u.]	0.58	0.92	2.50	2.63	3.32	2.55	4.67	2.44	4.68	2.54	5.42	4.18	2.30	3.97
ratio [no u.]	0.06	0.10	9.14	9.44	3.87	1.84	1.72	1.84	0.93	0.81	0.96	1.10	1.23	1.06
p - value	<**0.01**		<**0.01**		<**0.01**		<**0.01**		0.45		0.12		0.06	
TINN [ms]	396.69	240.55	278.48	193.93	228.63	178.01	232.32	148.07	179.82	128.32	164.36	82.11	253.05	102.71
$TINN_{dec}$ [ms]	291.95	146.65	221.37	111.26	194.18	146.23	199.10	101.96	160.02	141.81	144.10	67.36	225.23	120.83
ratio [no u.]	0.74	0.61	0.79	0.57	0.85	0.82	0.86	0.69	0.89	1.11	0.88	0.82	0.89	1.18
p - value	<**0.01**		<**0.01**		<**0.01**		<**0.01**		<**0.01**		**0.05**		0.12	
ApEn [no u.]	0.68	0.13	0.90	0.13	0.90	0.18	0.99	0.20	0.92	0.14	0.96	0.22	0.82	0.24
$ApEn_{dec}$ [no u.]	0.95	0.10	0.98	0.10	0.94	0.15	0.97	0.14	0.98	0.13	1.01	0.15	0.86	0.16
ratio [no u.]	1.40	0.76	1.09	0.73	1.04	0.82	0.98	0.68	1.06	0.87	1.05	0.70	1.05	0.68
p - value	<**0.01**		<**0.01**		0.55		0.14		**0.03**		**0.02**		**0.02**	

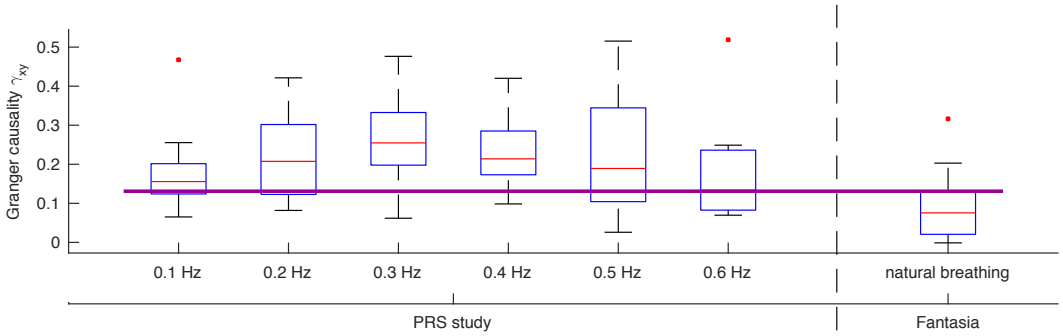

Figure 8.9: Strength of coupling γ_{yx} based on the Granger's causality depicted in dependency of the breathing frequency in paced respiration (PRS study) and natural breathing (Fantasia database). A clear dependency of the coupling strength can be demonstrated in paced respiration with maximal coupling observed at 0.3 Hz. In natural breathing coupling strength was clearly lower with a median value below the significance threshold $\gamma_{yx}^{5\%}$ but intersubject variability was similar to the one observed in the PRS study.

in table 8.1 in the form of median and interquartile range. The boxplots for the parameters SDNN and ApEn are also presented graphically in figure 8.10.

8.3.4.1 Paced Respiration Study

We observed in the PRS study that in general, the decoupled RR time series has less power than the measured one. In addition, the original HRV parameters had a strong dependency of the respiration rate. However, after decoupling, the different median values leveled and became more independent of breathing frequency. Furthermore, the intersubject variability, measured as the interquartile range of the decoupled parameters, was reduced also.

For the time domain parameters, a reduction of SDNN and rMSSD was observed at the lower frequencies (0.1 and 0.2 Hz). Yet, the medians of these two parameters maintained their original values at higher respiration rates (0.3 to 0.6 Hz). The behavior of the geometrical parameter TINN was very similar to the one of SDNN. Interesting were the results obtained for ApEn. This was the only parameter for which its median value increased significantly at the lowest two breathing rates. For the higher breathing frequencies, the changes were more subtle.

In the frequency domain, a significant decrease of the parameter LF at the lowest breathing rate of 0.1 Hz was observed. We were positively surprised by this result because it shows the capability of this procedure to decouple respiration from RR time series even when they have overlapping PSD. This result also matched the observed performance in the study with synthetic signals. Additionally, the parameter HF was observed to be significantly reduced after decoupling for the respiration frequencies 0.2 and 0.3 Hz.

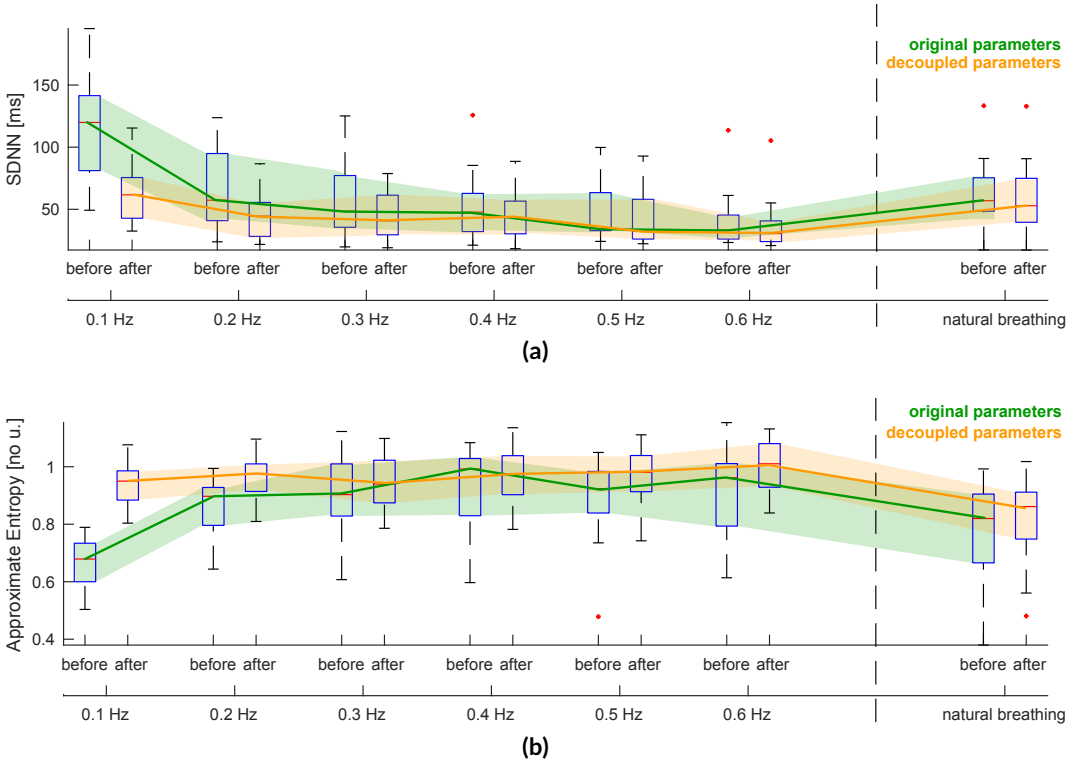

Figure 8.10: Two examples of the results of the analysis evaluating the change in the HRV parameters before and after decoupling. For each parameter, the boxplots in dependency of the paced respiration rate for the subjects in the PRS study and the spontaneous breathing for the subjects in the Fantasia database before and after decoupling are also shown. It can be seen how the boxplots tend to level after decoupling and a strong dependency on breathing frequency is no longer observed. The following HRV parameters are dispayed (a): SDNN. (b): ApEn. This figure was reprinted from publication [63] with permission from the publisher.

8.3.4.2 Fantasia Database

In the analysis done for the Fantasia database, we also observed a slight reduction of the median HRV parameters and their interquartile range. Yet, the decrease was not statistically significant.

8.4 Discussion

8.4.1 Validity of the Chosen Model for Coupling Analysis

The model we chose to couple the exogenous input (respiration) to the RR time series has an open-loop structure and is fully described by the finite impulse response (FIR) filter $g(n)$. However, this can be seen as a restricting model that is not conform with the feedback-loop nature observed in cardiovascular control processes such as the baroreceptor reflex or the cardiopulmonary coupling. As mentioned previously, our open-loop model is a special

case of the larger family of multidynamic adjustment models for which the feedback-loop configuration would have been possible. A larger system with feedback-loop integration would allow the investigation of the origin of cardiovascular oscillations and can also be used to quantify coupling [135]. However, it was our intention to measure coupling according to Granger as an improvement in estimation when the exogenous variable is considered. In the feedback-loop model, this interpretation is no longer given in its original form. Furthermore, it was our intention to quantify the direct coupling from the breathing pattern to the RR time series and for this application, we believe that the open-loop model is appropriate.

8.4.2 Evaluation of Granger's Causality as a Coupling Measure

The coupling measure γ_{yx} delivered intuitive results in the simulation study. First, we observed that it was directly dependent on the amplitude A of the respiration pattern. The larger A the stronger was also the median coupling value among the repetitions carried out in the experiment. In addition, the significance threshold $\gamma_{yx}^{5\%}$, which was derived on a theoretical basis, proved also to be a powerful tool to detect coupling. In 96.3 % of the cases, the classification delivered by this threshold was correct. Even for the lowest coupling strength at $A = 0.6$, the median γ_{yx} was above threshold. Nevertheless, we observed the vast majority of classification errors for $A = 0.6$ which decayed with increasing A. This is an expected result since low amplitude in the respiration signal leads to small respiration dependent part in the RR time series that can no longer be detected by Granger's approach. We believe this should not be a problem in practice since for weak coupling, respiration should have little impact on HRV and the decoupled HRV parameters should not be very different from the coupled ones.

A further point of discussion is the linearity of all the methods used for the study with synthetic signals. Coupling was modeled using the linear filter $g(n)$ and the strength of coupling was calculated with the Granger's causality which is also a linear approach. Thus, our results evaluating γ_{yx} may be overestimated because our quantification problem is matched to the coupling model. Nevertheless, the results of the simulation study were so convincing that we were still interested in the investigation of linearly decoupled HRV parameters in paced respiration and spontaneous breathing.

8.4.3 Evaluation of Separation Algorithms

The results from the study with synthetic signals demonstrated the high performance of both separation algorithms. In particular, the MAx filter turned out to be the better method in both scenarios (paced respiration and natural breathing) achieving in both cases a median correlation coefficient of over 0.99. This is probably due to the fact that this filter incorporates information from both, the measured RR time series and the recorded respiration which combined with a linear model of coupling gives a perfect match for this application. Nevertheless, as mentioned previously, the results may be overestimated because the model

used to couple respiration with RR time series is also linear. In any case, the comparability to the Gaussian notch filter should still be given because the latter is also a linear method.

The Gaussian notch filter demonstrated also a surprisingly good performance in the study with synthetic signals. It was originally developed for paced respiration and it achieved in that case a median correlation coefficient of over 0.96. The method has also the advantage of not requiring a respiration signal making it a viable solution in case no respiration recording device is available. We also observed that in the case of spontaneous breathing, the median performance was above 0.86 and the upper quartile laying above 0.93. This makes the method applicable in the case natural breathing if the breathing frequency remains at an approximately constant rate.

8.4.4 Coupling between Respiration and RR Time Series

8.4.4.1 Paced Respiration Study

The results in the paced respiration study demonstrated that the median coupling strength has a clear dependency on respiration rate and that it maximizes at 0.3 Hz. This is in accordance with the results reported by Pitzalis [124]. However, within the group of subjects analyzed, we observed different coupling strengths ranging from very strong to statistically non-significant for the same breathing frequency. These results suggest that even though a global trend exist, coupling between respiration and RR time series may be a subject specific property with different dependencies from the breathing rate.

The fact that coupling strength maximized at 0.3 Hz was an interesting result because humans tend to breath at about this same frequency naturally. This phenomenon resembles some sort of physiological resonance in which RSA maximizes at the same frequency a person would breath spontaneously which would again lead to an optimized gas transfer on the lungs without further effort. We also found that coupling strength was lowest at 0.1 and 0.2 Hz. We postulated two possible explanations for this result. First, this could be the consequence of the RR time series being very well estimated using only the AR model. In that case, the improvement in estimation measured when respiration is added, would be very low, leading possibly to a non-significant Granger's causality. Second, a physiological explanation would be that other regulation mechanisms below 0.2 Hz such as the baroreceptor reflex, systemic blood pressure and perfusion and body temperature may overlap with the RSA and compromise the MAx estimation.

Finally, a further reduction of coupling strength was observed above 0.4 Hz. This was also in accordance with other results presented in literature showing that RSA decreases with increasing frequency above 0.3 Hz.

8.4.4.2 Fantasia Database

In the Fantasia database, we observed that 75 % of the subjects did not have significant coupling. This could be explained partially because of the older participants who could have a diminished RSA since this phenomenon is believed to decrease with age [136, 137]. Yet, half of the younger participants did not show significant coupling either. As a matter of fact, the median γ_{yx} value in spontaneous breathing was the lowest compared to all paced respiration frequencies. This is probably because in paced respiration, the breathing pattern is very regular which could facilitate synchronization and lead to an increased RSA. We also observed that the intersubject variability in the Fantasia database was very similar to the one observed at 0.3 Hz in the PRS study. This result could mean that the intersubject variability in RSA is best quantified when subjects are told to breathe constantly at their natural frequency.

8.4.5 Analysis of Heart Rate Variability

8.4.5.1 Paced Respiration Study

With the paced respiration study, we realized how HRV parameters can depend on the breathing frequency. For example SDNN, which is a measure of total HRV power went from 119.89 ms on median to less than 40 % of that value at 0.4 Hz. Thus, if a cardiac patient would be diagnosed based only on SDNN, the outcome would be completely different depending on breathing frequency. For this reason, it was also satisfying to see, that after decoupling, the median values among all breathing frequencies leveled and the interquartile ranges decreased. This way, the comparability among subjects is improved facilitating the diagnosis from a physician.

We also observed as a general result that the HRV parameters that quantify power in the RR time series were strongly reduced after decoupling. This demonstrates that RSA is responsible for a major part of the variability in the RR time series. However, we also realized that the way the HRV parameters change after decoupling depends strongly on the breathing frequency. For example SDNN underwent a reduction of 50 % at 0.1 Hz but less than 10 % at 0.4 Hz. Since the majority of the spectral power of the RR time series tends to be concentrated at lower frequencies below 0.2 Hz, the decoupling procedure has a stronger impact on SDNN when respiration has a lower rate. From the frequency domain parameters, we observed a strong reduction of LF at the the breathing frequency of 0.1 Hz. Further, the parameter HF was strongly diminished in the band from 0.2 to 0.4 Hz. These results are very plausible because LF quantifies spectral power between 0.04 and 0.15 Hz while HF ranges from 0.15 to 0.4 Hz.

Another interesting result was the increased median ApEn after decoupling. This parameter is a measure of how chaotic is a signal. The higher the irregularity in the signal, the higher also ApEn. In this case, the increase in ApEn value is probably because the paced

respiration produces a very regular RR time series which after decoupling becomes more chaotic.

8.4.5.2 Fantasia Database

In the Fantasia database, we observed that almost half of the HRV parameters did change significantly after decoupling but the modifications were notoriously smaller than in paced respiration. Furthermore, the change in interquartile range was also relatively small. These results are in accordance with the strength of coupling observed between respiration and HRV in the case of spontaneous breathing. In general, if coupling is weak, then the decoupling procedure will only remove little power from the RR time series so that the HRV parameters remain almost the same.

8.5 Limitations

The method chosen to quantify coupling and decouple the RR time series is based on least squares estimation and linear regression. Although this method turned out to be a good approach for the kind of signals we used here, it does not account for non-linear coupling. We investigated here the relationship between coupling and respiration rate. However, the amplitude of the respiration pattern (breathing depth) plays also an important role and can modify strength of coupling even at constant breathing rates [39]. This phenomenon cannot be included in our model. Furthermore, the Granger's causality is a measure of coupling based on a given model. Thus, if the model is not correctly chosen, the procedure may fail. One of the critical points here is the model order which we chose using the BIC. This is an approach that tends to favor lower model orders and could lead to underestimated dynamics that do not capture the true behavior of the time series.

The intention of the study based on synthetic signals was to validate our methods on a theoretical basis. The results were convincing and motivated us to use the method on real recordings. However, the results could be overestimated. We modeled coupling with a linear transfer function from respiration to RR time series. We then decouple respiration using again a linear model which is a perfect match for this problem. In addition, we modeled respiration with a sinusoidal function and RR time series with pink noise. In reality, these time series are more complex and the performance of the method is probably lower in those cases.

The population used for the both studies is also an aspect that can be considered a limitation. For the PRS study, 19 subjects enrolled while in the Fantasia database 20 participants were present, which is a good number for comparison. However, the two groups are fairly different. The population in the PRS study was predominantly masculine and young while in the Fantasia database, half of the people were older and an equal distribution of men and women was given. Thus a direct comparison between these two groups is not ideal. Yet it can help us postulate new hypotheses to be tested in future prospective studies.

The last topic that could be considered a limitation is possible aliasing that remained unnoticed in the time series we analyzed here. Even though we tried to minimize aliasing by removing from the study the subjects that did not fulfill the Shannon-Nyquist theorem, it is still possible that the higher harmonics of the respiration pattern lead to aliasing errors. However, we also observed that the shape of the respiration signal is close to a sinusoidal function leading to low energy in the higher harmonics. This result was corroborated by the synthetic signal study in which aliasing did compromise the performance of the filters.

8.6 Outlook

The first step in a future project would be the extension of our model to include blood pressure and feedback loops between the three most relevant variables in the cardiorespiratory system. We believe this should improve the current description of the dynamical interactions between RR time series, respiration and blood pressure. In addition, it would be also interesting to introduce non-linear models that include respiration amplitude (depth of breathing) into the coupling measure. However, we would have to go away from the Granger's causality to a new non-linear measure of coupling.

In this work, we investigated the impact of respiration and coupling on the HRV parameters. This kind of study could be extended to analyze the dependency of other variables such as age, gender, fitness or, state of health. They could be combined to examine imbalances of the ANS that are associated with other diseases such as diabetes mellitus, hypertension, chronic heart failure (CHF) or myocardial infarction [138–141]. In these afflictions, a reduced HRV is a predictor of cardiac death. Hence, it would be of great help for the medical community if the decoupled HRV parameter could improve the predicting power of standard HRV even further.

Finally, we would like to study, if the problems that arise from aliasing in the RR time series at higher respiration rates could be avoided, if the respiration signal is sampled at the same points where the RR time series is sampled at. In this work, the RR time series was interpolated to 4 Hz but respiration was downsampled to the same 4 Hz after low-pass filtering. Thus, we could postulate that by sampling respiration at the same points of the RR time series without any further preprocessing, the aliasing effect should be the same on both series and the decoupling procedure would include it and lead to a more accurate γ_{yx} and a better decoupled RR time series. More research is definitely needed to prove this idea.

8.6.1 Conclusion

In this work, we used the idea behind Granger's causality to create a method that is capable of measuring coupling strength between respiration and RR time series and identify statistically significant coupling. We also developed two linear filters, a Gaussian notch and an MAx filter to decouple respiration from the RR time series. The methodology was validated at a

theoretical level using synthetic signals demonstrating that the MAx filter was the better one applicable in paced respiration and spontaneous breathing.

We learned from the analysis of the PRS study that coupling strength is clearly dependent on respiration rate and that it maximizes at 0.3 Hz. We also observed that the median HRV parameters varied among breathing frequencies but leveled after decoupling. The interquartile range was diminished after decoupling suggesting that part of the intersubject variability arises from different manifestations of RSA in each subject. In addition, the decoupling procedure led to a significant reduction of the HRV parameters that quantify power in the RR time series corroborating the notion that RSA is a very relevant component of HRV in the case of paced respiration.

The Fantasia database delivered very different results from the ones observed in paced respiration. The coupling strength between respiration and RR time series was notoriously lower and in 75 % of the subjects, it did not reach the significance level. We also observed that for the subjects with significant coupling, the decoupled HRV parameters underwent a relatively small change. From these results, we concluded that paced respiration probably facilitates coupling and the physiological mechanisms responsible for RSA are potentitated when breathing rate remains constant.

Finally, we concluded that the analysis of decoupled HRV parameters could help us to better understand the role they play in the description of the ANS regulation. Furthermore, the decoupled parameters may have an undiscovered diagnostic power that could help to predict the outcome of cardiac diseases such as diabetes mellitus, hypertension, CHF or myocardial infarction. More research is needed to definitely prove this idea.

PART V

THE IMPACT OF MENTAL WORKLOAD ON THE ELECTROCARDIOGRAM

CHAPTER 9

Electrocardiographic Markers for the Assessment of Mental Workload

9.1 Introduction

The quantification of mental workload plays an important role in the field of ergonomics because it helps to predict human performance for a given task [142]. This is due to the fact that under the influence of mental workload, the processing capabilities of a subject are viewed limited. Even though the community does not have an overall accepted definition of mental workload, the majority of researchers agree that it is directly related to the amount of resources required to carry out a given task. It is also dependent on the person performing the task and the way the task is conceived [143].

In this research project, we were interested in measuring how the driving performance of a subject is affected by mental workload. For that purpose, the quantification of the mental workload that a person is perceiving would be required for a further correlation analysis. In the past, three main approaches for the quantification mental workload have been proposed: (1) subjective measures (2) performance based measures (3) physiological measures [18]. The third approach is particularly interesting for the community because it allows a continuous recording and assessment of the workload. Among the biosignals that can be recorded from the human body, the electrocardiogram (ECG) is the most commonly used technique for this purpose. This is because mental workload is known to have a direct influence on the autonomic nervous system (ANS) and thus on the normal regulation of the heart rate and the heart rate variability (HRV) [144]. However, not only rhythmical features extracted from the RR time series can be modified but also morphological parameters obtained from all ECG waves tend to change under the influence of mental workload. In the past, several studies done for different applications have demonstrated that it is relevant for

the analysis of mental workload to investigate both, morphological and rhythmical features [145–148].

Therefore, in this work, we studied subjects driving a car simulator under the influence of mental workload and investigated in an explorative manner, which of the ECG features are affected by mental workload and how these features change when the degree of difficulty of the given task is increased. This work was performed in close cooperation with the Institute of Human and Industrial Engineering (IfAB) at Karlsruhe Institute of Technology (KIT) and published as a journal paper [33].

9.2 Materials and Methods

9.2.1 Data

9.2.1.1 Participants of the Study

A total of 33 students participated in the study, However, due to a technical problem with the ECG recording device, the first five had to be removed. A further participant was removed as well because of severe difficulties driving the car simulator. Thus, the resulting sample for the study consisted of N=27 participants (1 female, 26 males) with ages ranging from 18 to 30 years (mean of 22.9 years). To motivate participation, all subjects had the chance of winning one of three gift cards worth 25 € from a major online retailer.

9.2.1.2 Primary Task: Lane Change task

The lane change task (LCT) was originally developed to quantify distraction in drivers. This task uses a driving simulator in which the subject has to control a car at the constant speed of 60 km/h and has to regularly change lanes according to appearing signs on the sides of the road [149]. The signs are placed at an average distance of 150 m so that the driver has to change lanes every 9 s. The test takes place in a circuit specially designed so that one lap takes around 3 minutes to complete. A driver is expected to be able to drive for several laps without the need of a pause to rest. In order to quantify driving performance, the mean deviation from a norm driving path was computed for each participant [150].

The simulator consisted of a force feedback wheel (Logitech G27) placed on a table and foot pedals localized under the table paced on the floor. The arrangement mimicked the construction of a car. A standard PC running the driving software together with a projector were used to display the LCT on the screen. Figure 9.1 shows a screenshot of an ongoing LCT.

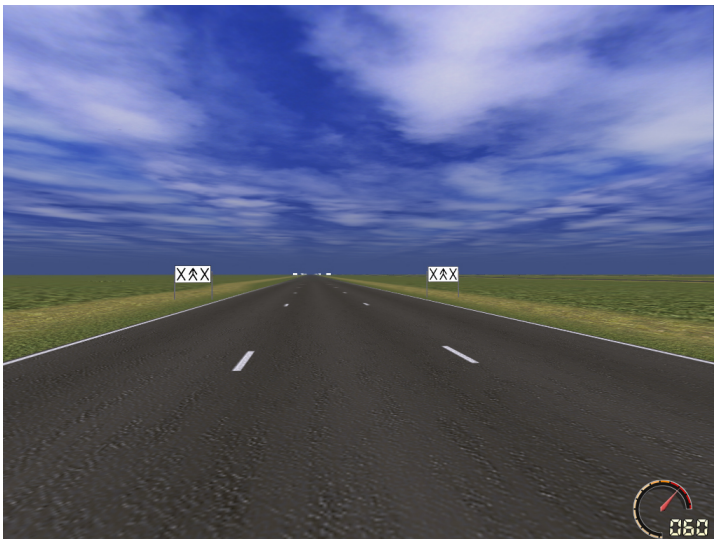

Figure 9.1: Screenshot of an ongoing LCT. Here, the participants drive at a given constant speed and change lanes according to the signs appearing regularly on the side of the road. This figure was reprinted from publication [33] with permission from the publisher.

9.2.1.3 Secondary task: N-Back Task

Simultaneously to the driving task, we carried out the n-back task (also called digital recall task) with the aim of inducing mental workload [151]. Here, the participants listened to a recorded voice saying a sequence of single numeric digits from the interval zero to nine. In every sequence, all 10 numbers were mentioned once but their order was different. The subjects were ask to repeat the digit mentioned n times before (n-back) the current one right after they have heard the digit. Three levels of difficulty were introduced (L1 (0-back), L2 (1-back), L3 (2-back)) and mistakes made by the participants were annotated by the experimenter. Every sequence was spoken in 25 s and a short pause of 5 s was given between two levels. Figure 9.2 shows a schematic representation of the three levels in the n-back task.

9.2.1.4 NASA Task Load Index

The NASA task load index (NASA-TLX) was conceived as a set of subjective questions with the aim of quantifying mental workload [152]. Six topics regarding mental demands, physical demands, temporal demands, performance, effort and frustration level are addressed in a questionnaire and can be answered in a 10 point scale being 10 the highest and 1 the lowest. The average of all six items was defined as a general measure of mental workload. The NASA-TLX has been shown to be a reliable source of measurement for different degrees of mental workload [153, 154].

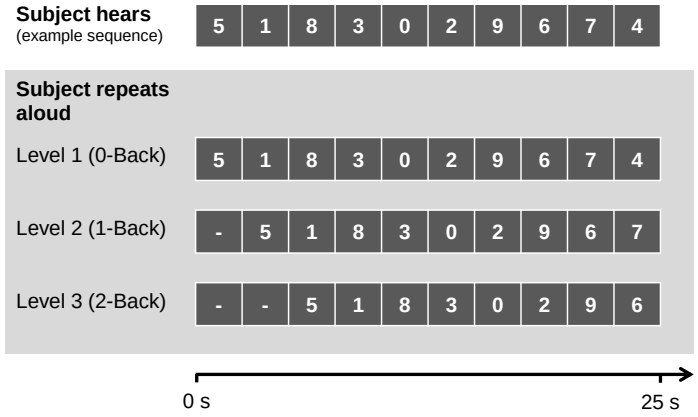

Figure 9.2: Schematic representation of how an n-back task is supposed to be performed. The upper row shows a sequence of 10 digits. Depending on the difficulty level (second to fourth row), the participant is supposed to repeat the digit mentioned n times before the current one. This figure was reprinted from publication [33] with permission from the publisher.

9.2.1.5 ECG Data

The ECG signals were recorded with the device Microvit MT 101 from the manufacturer Schiller AG. Three ECG leads building a quasiorthogonal configuration according to the instructions manual of the recording device were used. The sampling rate of the signals was 1000 Hz and its resolution was 12 bits. We inspected the quality of the signals visually before the signal processing algorithms were applied.

9.2.2 Procedure of the Study

Every repetition of the experiment was carried out in the following manner. First, each participant was welcomed by the experimenter in the room with the driving simulator and was given a consent form to read and sign. Subsequently, the electrodes for the ECG recording were placed on the chest of the subject and the LCT was introduced. Afterwards, the participants had the chance to drive two laps to accustom to the simulation system before the experiment started. Consequently, the experimenter brought the participant to a room close by to record an ECG in resting conditions sitting on a chair. The participant was given a book with pictures from the Himalayas to look at will. This measurement lasted 15 minutes and the participant was brought back to the simulator room to perform the actual LCT with three levels of difficulty (L1, L2 and L3) in the secondary task. The possibility to practice the n-back task and the driving simulator at the beginning of every level was also given to the participant and the measurement began once they had familiarized with it. The participant then drove for two laps before concluding the n-back task and they were asked to fill a NASA-TLX questionnaire before the next level of difficulty started. After the three levels of difficulty were accomplished, the experimenter brought the participant back to the

Figure 9.3: Flow diagram of the experiment performed in this study. The experiment started with 15 minutes of ECG recording in resting conditions. The participant then completed the LCT with the three levels of difficulty in the secondary n-back task. At the end, a second 10 minute ECG recording in resting conditions was carried out. This figure was reprinted from publication [33] with permission from the publisher.

room close by for another 10 minute recording of the resting ECG. Figure 9.3 shows a flow diagram of the components of the experiment.

9.3 Methods

9.3.1 ECG Signal Processing

In this section, the signal processing steps to compute all rhythmical and morphological features will be explained. Figure 9.4 shows a typical example of the ECG signals recorded in this study and its RR time series extracted from the first resting phase of the experiment together with common HRV parameters from the time domain analysis. Figure 9.5 shows a graphical representation of other HRV features from the frequency domain analysis and wavelet packet analysis (WPA). A T wave template used for morphological analysis is also shown in this figure. Table 9.1 shows a summary of the features that turned out to be most relevant for the assessment of mental work load.

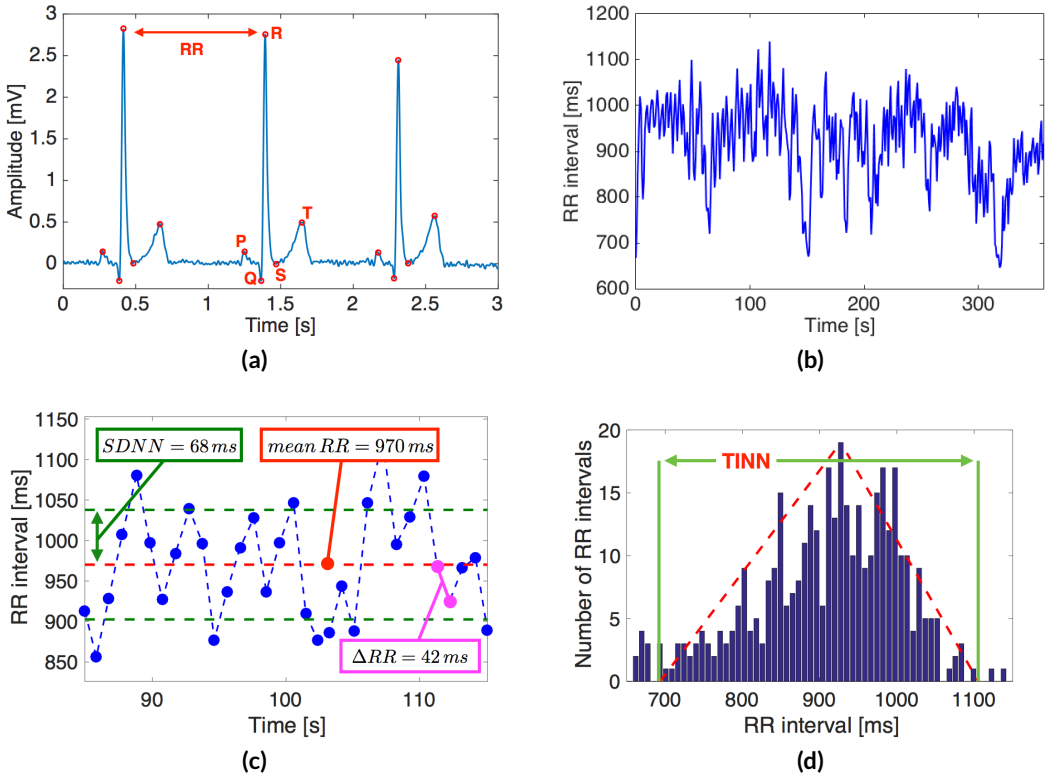

Figure 9.4: (a): Typical ECG signal recorded in this study together with the automatic detection and delineation of each wave in the ECG. (b): Series of RR intervals obtained from the first resting phase of the ECG signal displayed in (a). (c): A portion of the RR time series from figure 9.4 (b) is displayed together with three time domain features. (d): The geometrical parameters like TINN are calculated from the histogram of the RR time series with a bin width of 1/128 s such as the one displayed here. This figure was reprinted from publication [33] with permission from the publisher.

9.3.1.1 Filtering the ECG Signal

For the reduction of baseline wander at the lower frequencies, the ECG signals were filtered with a Gaussian high-pass filter with a cutoff frequency at 0.3 Hz. The attenuation of the high frequency random noise was performed with a low-pass Gaussian filter with a cutoff frequency at 40 Hz. No other sources of noise or perturbations were identified in the signals.

9.3.1.2 Preprocessing the ECG Signal

The detection and delineation of the ECG waves were introduced in chapters 4 and 7. We preserved those approaches in this work. In addition, the creation and filtering of the RR time series was performed in the same manner as described in chapter 8. However, for this work, we extended the HRV analysis to compute more standard parameters and introduced the WPA to quantify HRV in the time frequency domain. The HRV analysis will be explained in detail in the next section.

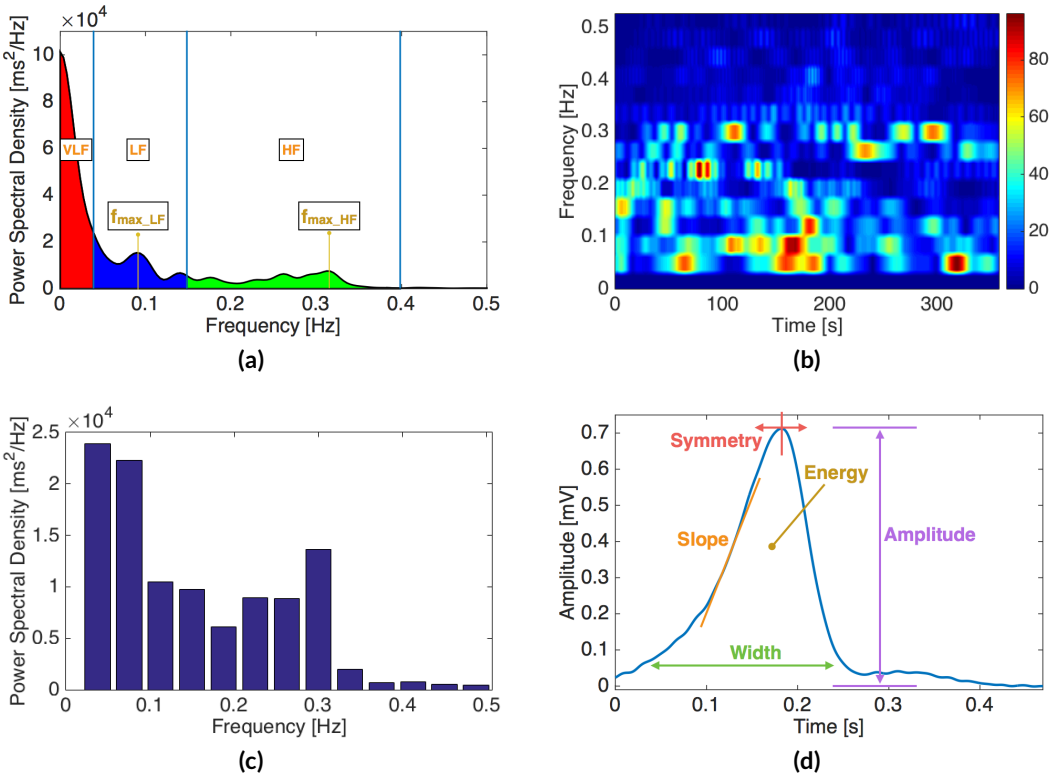

Figure 9.5: (a): PSD of the RR time series shown in figure 9.4 (b) was calculated using Welch's method. The colors represent the area under the curve equivalent to the signal power in each frequency of the bands relevant for HRV analysis. (b): WPA was used to analyze the RR time series and create the time frequency representation shown here. The color coding corresponds with the magnitude of the wavelet coefficients. (c): PSD obtained using WPA from the wavelet coefficients displayed in figure 9.5 (b). (d): T wave template together with its morphological features. This signal was obtained from the ECG shown in figure 9.4 (a). This figure was reprinted from publication [33] with permission from the publisher.

9.3.2 HRV Analysis

The HRV analysis performed in this work concentrated on the extraction of features that quantify the variation of the RR time series in the time domain, the frequency domain and the combined time frequency domain [156–159]. The HRV analysis was performed on the six minute signal obtained from each difficulty level during the experiment. In order to have a point of comparison, the same signal length was extracted from the center of the resting phases.

9.3.2.1 Time Domain Analysis

Within the HRV analysis in the time domain, we differentiate between three major types of features: statistical, geometrical and non-linear. We implemented parameters from all three types. Among the statistical parameters, we included most of the popular features such as the mean RR interval (mean RR), the standard deviation of the normal RR intervals (SDNN),

Table 9.1: Summary of the most relevant ECG features for the assessment of mental workload in this research project. We listed the features extracted from the HRV and from the ECG morphology together with a short description of each parameter. A complete list of HRV features can be found in [9] and [155]. This table was reprinted from publication [33] with permission from the publisher.

ECG feature	Unit	Description
RR	[ms]	Time distance between two subsequent beats (R peaks) in the ECG. A collection of consecutive RR intervals is called RR time series.
NN	no unit	Normal RR intervals.
$\triangle$RR	[ms]	Difference between two subsequent RR intervals.
HR	[bpm]	Instantaneous heart rate obtained from the reciprocal of each RR interval.
mean RR	[ms]	Average RR interval.
SDNN	[ms]	Standard deviation of the RR intervals.
SDANN	[ms]	Standard deviation of mean RR intervals when splitting the series into one minute segments.
SDNN index	[ms]	Average of the standard deviations of RR when splitting the series into one minute segments.
rMSSD	[ms]	Root mean square of the difference of all subsequent RR intervals.
SDSD	[ms]	Standard deviation of the difference of all subsequent RR intervals.
pNN20	[%]	Percentage of RR intervals in which the change of successive NN exceeds 20 ms
pNN50	[%]	Percentage of RR intervals in which the change of successive NN exceeds 50 ms
VLF	[ms^2]	Spectral power of the RR time series in the band [0; 0.04 Hz].
LF	[ms^2]	Spectral power of the RR time series in the band [0.04 Hz; 0.15 Hz].
HF	[ms^2]	Spectral power of the RR time series in the band [0.15 Hz; 0.4 Hz].
LF/HF	no unit	Ratio between LF and HF.
TINN	[ms]	Base of the triangle used to approximate the histogram of the RR time series.
SD1/SD2	no unit	Ratio between the standard deviations SD1 and SD2 obtained from the Poincaré plot.
SaEn	no unit	Measure of irregularity or complexity in the series called sample entropy.
ApEn	no unit	Measure of irregularity or complexity in the series called approximate entropy.
WPAband2	[NU]	Normalized spectral power of the RR time series in the band [0.0375 Hz; 0.0750 Hz] otained using WPA.
WPAband4	[NU]	Normalized spectral power of the RR time series in the band [0.1125 Hz; 0.1500 Hz] otained using WPA.
T amplitude	[NU]	Measure of the T wave peak amplitude.
T width	[NU]	Measure of the T wave width.
T symmetry	[NU]	Measure of the T wave symmetry.
T kurtosis	[NU]	Measure of the T wave tailedness.

the standard deviation of the mean RR interval of portions of the RR time series when it is divided into subseries of a given length (SDNN index), the mean of the standard deviations of RR intervals when it is divided into subseries of a given length (SDANN). The latter two were calculated dividing the RR time series into six intervals of one minute of length. Slow variations in the RR time series are characterized by these features. Rapid variations, on the other hand, are quantified by parameters such as the root mean squared difference of subsequent normal RR intervals (rMSSD), the standard deviation of the difference of subsequent normal RR intervals (SDSD) and the percentage of normal RR intervals with a variation larger than 20 ms (pNN20) and 50 ms (pNN50) with respect to the previous RR interval [127].

For the calculation of the most common geometrical features, a histogram of the RR time series was created first. This histogram was approximated by a triangle and the features TINN and HRV triangular index were computed. These parameters have been demonstrated to characterize slow variations in the series in a similar manner to SDNN [36]. However, they may be more robust when artifacts and ectopic beats are present in the RR time series. Additionally, from the Poincaré plot, which is a phase space representation of the RR time series in the two dimensions $[RR_{i-1}, RR_i]$, the standard deviations SD1 and SD2 and their ratio were computed. SD1 is also related to slow variations of the series while SD2 captures rapid changes.

From the field of non-linear parameters, we implemented the sample entropy (SaEn), the approximate entropy (ApEn) and the Shannon entropy which are all measures of complexity in the RR time series. The fluctuation analysis was also used to compute the two parameters α_1 and α_2 which are both measures of irregularity or roughness of the signal.

From the time domain, a total of 17 parameters were calculated.

9.3.2.2 Frequency Domain Analysis

The frequency domain parameters in HRV are obtained from the PSD of the RR time series. For each phase of the experiment, we estimated the PSD from a six minute interval. Welch's method was used for this purpose. This approach requires an equally sampled series. Thus, we interpolated using the RR time series using cubic splines to 4 Hz leading to a signal of 360 s·4 Hz=1440 sample points. For the Welch's method, we used a Hann window of 64 s (256 samples) and an overlap of 50 % between subsequent windows. The fast Fourier transform (FFT) was computed extending the 256 sample to 1024 with zero padding to achieve a higher resolution in spectrum.

The parameters in the frequency domain are primarily based on the spectral power in three standard frequency bands. These bands are: the very low frequency band (VLF) below 0.04 Hz, the low frequency band (LF) in the interval 0.04 to 0.15 Hz and the high frequency band (HF) ranging from 0.15 to 0.4 Hz. The power in each of these bands is calculated as the area under the curve of the PSD. The total spectral power (TP) is the sum of the VLF, LF and HF.

In addition, normalized powers LFn and HFn were also computed using as normalizing power the sum of LF and HF. As measure of the balance between the sympathetic and the parasympathetic systems, the ratio LF/HF was introduced [127]. The frequencies at which the maximal power was located in every band were also defined as features because these maxima have been shown to be related to other physiological phenomena. For example, as shown in the previous chapter, the normal breathing frequency of a healthy subject is around 0.3 Hz and often appears as a maximum in the HF band [160]. Some of the time domain parameters are known to be related to their frequency domain counterparts. For example, SDNN correlates strongly with TP, while rMMSD is known to be related to HF. In addition, LF is believed to quantify the sympathetic activity while HF is supposed to be a measure of vagal tone.

The PSD of the RR time series displayed in figure 9.4 (b) can be seen in figure 9.5 (a). Some of the features introduced in this section are depicted in figure 9.5 (a). A total of 10 frequency domain parameters were obtained.

9.3.2.3 Wavelet Packet Analysis

We created with the WPA a time-frequency representation of the RR time series. For this purpose, we used the symlet 12 wavelet because it is a good compromise between the computational cost to calculate the transform and the localization of the wavelet in the time

frequency plane. Furthermore, the almost symmetrical shape of the symlet is characterized by a close to linear phase that reduces asymmetrical distortion in the computation of the wavelet coefficients [161].

Similar to the frequency domain analysis, for the computation of the WPA, an interpolation of the RR time series was also carried out to achieve equidistant sampling. The sampling rate used was 2.4 Hz and a decomposition level of five was chosen to achieve a spectral resolution of 0.0375 Hz. The symlet 12 has the property of having 12 vanishing moments, which means that all polynomials up to an order of 12 do not correlate with this symlet. Thus, the frequency band below 0.0375 Hz contains not only the lowest frequency component of the signal but also all polynomials with an order up to 12. For this purpose, this band tends to have a significant amount of power. We removed this band from our analysis and concentrated on all the bands above 0.0375 Hz [162].

The wavelet coefficients were also squared and summed up over all times to create a wavelet spectrum comparable to the Fourier PSD. This spectrum had again a resolution of 0.0375 Hz but it was possible to combine neighboring sub-bands to achieve the same LF and HF bands typically used in HRV analysis. It was also possible to compute analogous parameters to the ones obtained from the standard frequency domain.

By synthesizing the wavelet coefficients from any given frequency band, we were also able to create band specific RR time series. From these time series, we calculated the equivalent statistical, non-linear and geometrical time domain parameters. Figure 9.5 (b) shows the time-frequency representation of the RR time series displayed in figure 9.4 (b), while figure 9.5 (c) presents the WPA based PSD of the same RR time series. A total of 215 features were extracted from WPA.

9.3.3 ECG Wave Morphology Analysis

In general, the morphological analysis of ECG waves is based on features that quantify the shape of each wave. As an example of the procedure, a T wave template is displayed in figure 9.5 (d) together with the kind of features that were extracted from it. The whole procedure began with the segmentation of the T wave around its peak in an interval spanning from 150 ms left from the peak to 200 ms after it. A possible constant deviation from the electric isoline (DC offset) was estimated from the last 50 ms and removed afterwards.

Once the preprocessing steps have been completed, the features were extracted. The maximal amplitude and energy of the signal were computed first. Then, the highest positive and negative slopes left and right from the peak were calculated. We also estimated the curvature of the peak and the tailedness of the wave using the kurtosis. Other similar statistical approaches were also applied to quantify the center of mass, width and symmetry of the T wave. Other rhythmical features that characterize the repolarization process such as the RT distance or the RT dispersion were also computed.

The morphology of the QRS complex was analyzed in a very analogous manner to the one used for T wave. For this purpose, the QRS complex was segmented in an interval

of 200 ms centered at its peak. The subsequent ST segment was also extracted from the interval 80 ms to 160 ms after the R peak. We approximated the ST segment with a second order polynomial and used its coefficients as features. The P wave, on the other hand, is often characterized by low signal-to-noise ratio (SNR) and may not be present in some ECG channels. Therefore, we used its stationary wavelet transform (SWT) (introduced in chapter 7) instead of the original morphology to compute the features. Due to the fact that the SWT is a linear transformation, its features should be a direct surrogate measure of the morphological properties of the original P wave.

The creation of a template for each ECG wave and the deviation from that template was a further necessary step to ensure the comparability between participants because of the different wave morphologies that appeared among all subjects. In order to create the template, only the first resting phase was considered. Here, all high quality waves having similar properties were averaged for template creation. For the template, the same morphological properties as for every wave were computed and the features in every wave were redefined as the difference from the template value. The new difference feature values were also normalized using the mean and standard deviation of the features of the waves used to create the template.

From the time domain, a total of 104 features were obtained from the morphological analysis.

9.4 Results

The results section is divided into two major parts. The results from the assessment of the driving performance and subjective evaluations are reported first, followed by the outcomes of the ECG signal processing analysis. The statistical analyses were carried out in a differentiated manner according to the standard procedures of each field of research (ergonomics and signal processing). Thus, performance and subjective data were analyzed with repeated measures ANOVA with Bonferroni corrected post-hoc pairwise comparisons. If the assumption for sphericity was violated, it was corrected using Greenhouse Geisser. On the other hand, significance testing of the ECG features was carried out with the non-parametric Wilcoxon signed rank test. We compared every phase of the experiment with the next phase. This led to a total of four comparisons for every ECG parameter. The statistical significance level (p-value) was set to 5 %. No Bonferroni correction was performed because of the large amount of significance tests carried out in this study. In cases like this, the correction is too conservative and can prevent the detection of significant changes.

9.4.1 Subjective NASA-TLX

The results of the NASA-TLX can be seen in figure 9.6. The assumption of sphericity was proven to be violated using the Mauchlys test. The Greenhouse Geisser corrected

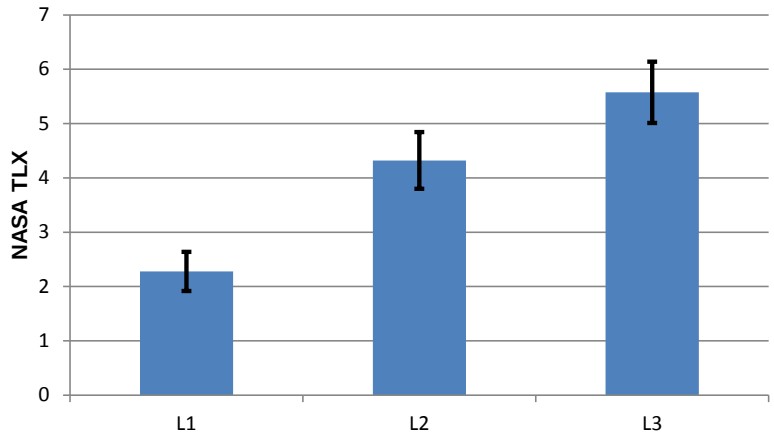

Figure 9.6: Mean value of the NASA-TLX scores for the three difficulty levels of the study. This figure was reprinted from publication [33] with permission from the publisher.

ANOVA demonstrated significantly larger NASA-TLX scores over the three levels of difficulty [$F(1.58, 41.1)=174.29$, $p<0.01$]. In addition, all three conditions were proven by the Bonferroni corrected post-hoc tests to differ significantly (difference between L1 and L2: $t(26)=11.93$, $p<0.01$; difference between L1 and L3: $t(26)=15.20$, $p<0.01$; difference between L2 and L3: $t(26)=9.10$, $p<0.01$).

9.4.2 Driving Performance

9.4.2.1 Primary Task: LCT

Sphericity could be assumed here according to Mauchlys test. The ANOVA test resulted in a significant growth of the mean deviation over the three difficulty levels [$F(2, 52)=9.09$, $p<0.01$]. However, the Bonferroni corrected post-hoc tests demonstrated a significant difference in driving performance in two comparisons and showed that there was no significant difference between L2 and L3 (difference between L1 and L2: $t(26)=3.25$, $p< 0.01$; difference between L1 and L3: $t(26)=3.72$, $p<0.01$; difference between L2 and L3: $t(26)=1.56$, $p>0.05$). The results are displayed in figure 9.7.

9.4.2.2 Secondary Task: N Back Test

Sphericity was proven to be assumable using the Mauchlys test. The results of the ANOVA tests demonstrated a significant increase of errors in all three difficulty levels. [$F(2, 52)=37.70$, $p<0.001$]. In addition, significant differences were demonstrated in all three conditions by the Bonferroni post-hoc tests (difference between L1 and L2: $t(26)=4.38$, $p<0.01$; differ-

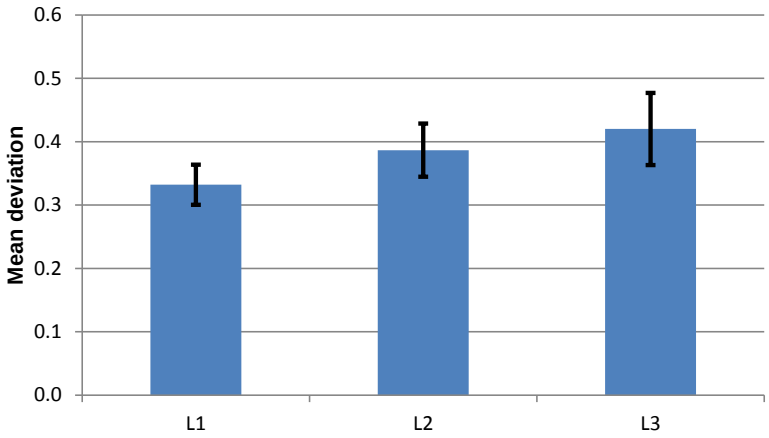

Figure 9.7: Mean deviation from the norm driven path to quantify driving performance in dependency of the three difficulty levels. This figure was reprinted from publication [33] with permission from the publisher.

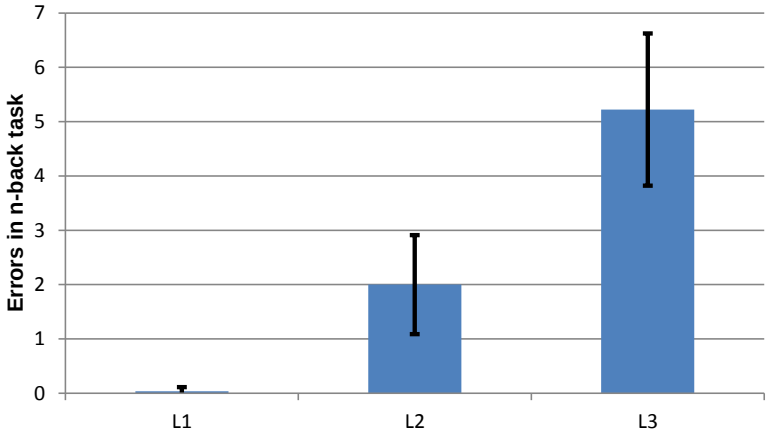

Figure 9.8: Mean errors in the n-back task in dependency of the three difficulty levels. This figure was reprinted from publication [33] with permission from the publisher.

ence between L1 and L3: $t(26)=7.61$, $p<0.01$; difference between L2 and L3: $t(26)=4.94$, $p<0.01$). The results are displayed in figure 9.8.

9.4.3 ECG Data

In this study, we created a total of 104 morphological features and another 242 rhythmical ones. They were used in an exploratory manner with the aim of finding the most relevant markers for the assessment of mental workload. For this purpose, the p-value computed from the comparison of two subsequent phases in the study helped us to identify the most relevant ECG features. We discovered that only a small group of features was indeed statistically significant. Within that group of significant features, we concentrated on the most significant

ones (lowest p-values) and summarized them in form of the boxplots displayed in figures 9.9 and 9.10 and table 9.2.

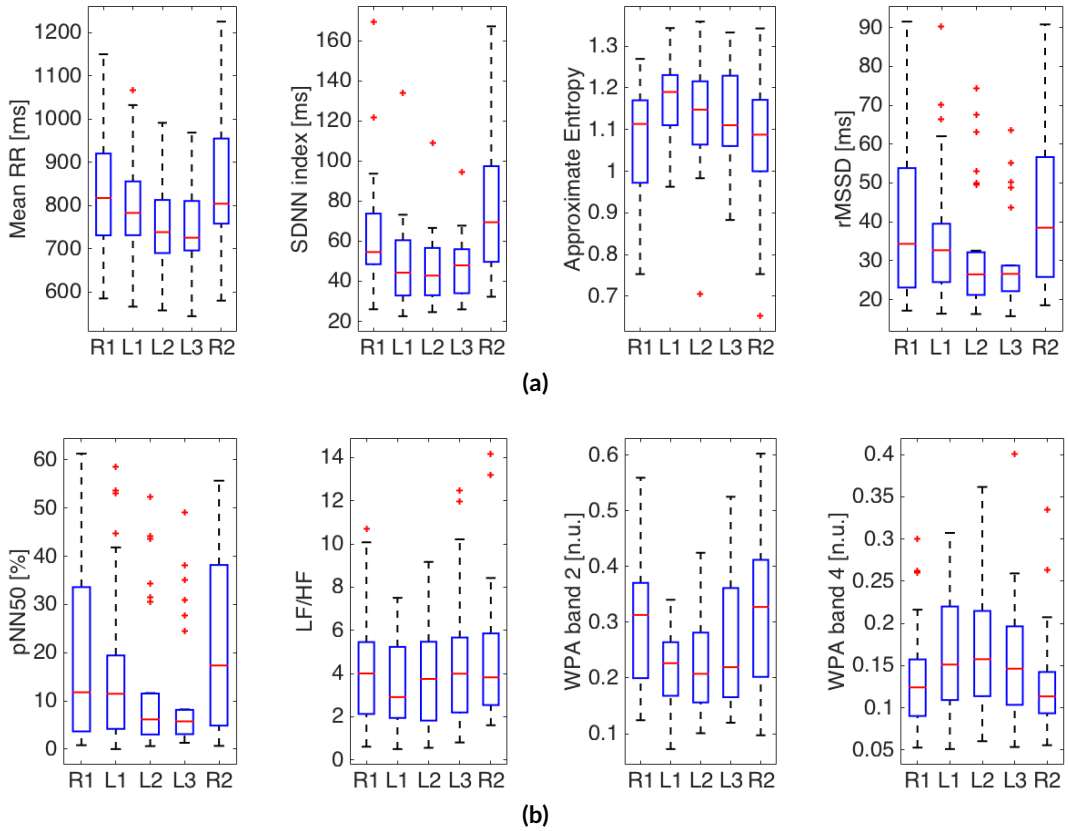

Figure 9.9: (a): Four of the most significant HRV features (lowest p-values) in this study are displyed in form of boxplots. The descriptors have different dependencies from the workload level. (b): Another four significant HRV features that also display a different dependency from the level of difficulty. This figure was reprinted from publication [33] with permission from the publisher.

9.4.3.1 HRV Analysis

From the first resting phase to the first difficulty level, a significant increase in ApEn together with a clear reduction of SDNN were observed. This demonstrated that the complexity of the RR time series is higher and the power of the slow variations in the series are diminished. Other parameters related to the low frequency components like VLF, LF, TP, SDNN, TINN and SD2 were also shown to be reduced in the first difficulty level. In addition, the mean heart rate (defined as the reciprocal of the mean RR length) was observed to increase going from a median of 73 beats per minute in the resting phase to a median of 83 beats per minute at the end of the third phase.

Table 9.2: The results obtained for the most relevant ECG features are summarized in this table. Values are presented as median ± interquantile range. This table was reprinted from publication [33] with permission from the publisher.

Feature	R1	L1	L2	L3	R2	p R1-L1	p L1-L2	p L2-L3	p R1-R2
mean RR [ms]	817.32±189.02	782.79±124.11	738.49±122.65	725.50±114.10	804.18±196.78	<**0.01**	<**0.01**	0.07	0.06
SDNN index [ms]	54.60±25.26	44.29±27.55	42.81±23.62	47.95±21.97	69.45±47.71	<**0.01**	**0.04**	0.31	<**0.01**
rMSSD [ms]	34.31±30.72	32.69±15.02	26.49±10.96	26.58±6.60	38.47±30.86	0.22	<**0.01**	0.08	0.05
SDSD [ms]	34.35±30.77	32.73±15.03	26.52±10.98	26.61±6.60	38.52±30.91	0.21	<**0.01**	0.08	0.05
pNN20 [%]	47.69±33.33	48.50±22.46	37.95±18.90	37.98±9.91	51.08±30.62	0.77	<**0.01**	0.08	0.20
pNN50 [%]	11.79±29.94	11.47±15.23	6.15±8.50	5.75±5.04	17.35±33.33	0.65	<**0.01**	**0.01**	0.09
VLF [ms^2/Hz]	701.23±558.30	433.79±595.55	446.54±596.11	496.00±577.50	937.95±1486.94	<**0.01**	0.32	0.12	<**0.01**
LF [ms^2/Hz]	869.38±779.68	544.98±616.17	462.19±407.40	489.65±421.23	975.67±1430.09	**0.02**	**0.01**	0.32	<**0.01**
HF [ms^2/Hz]	167.20±393.76	172.63±176.85	128.96±103.40	117.31±83.47	216.11±346.88	0.14	<**0.01**	0.05	0.27
LH/HF	4.00±3.33	2.91±3.29	3.75±3.65	3.99±3.47	3.82±3.32	0.22	0.74	<**0.01**	0.22
TINN [ms]	300.20±151.49	257.85±115.97	249.54±113.07	266.68±86.94	341.72±182.07	**0.01**	0.53	0.85	<**0.01**
SD1/SD2	0.27±0.15	0.32±0.12	0.29±0.09	0.27±0.12	0.26±0.07	<**0.01**	<**0.01**	0.32	0.09
SampEn	1.30±0.50	1.47±0.37	1.29±0.45	1.29±0.46	1.22±0.30	<**0.01**	<**0.01**	0.28	0.29
ApEn	1.11±0.20	1.19±0.12	1.15±0.15	1.11±0.17	1.09±0.17	<**0.01**	0.16	0.28	0.41
WPAband2 [n.u.]	0.31±0.17	0.23±0.10	0.21±0.13	0.22±0.20	0.33±0.21	<**0.01**	0.77	**0.02**	0.47
WPAband4 [n.u.]	0.12±0.07	0.15±0.11	0.16±0.10	0.15±0.09	0.11±0.05	**0.02**	0.87	0.61	0.81
T amplitude [n.u.]	0.03±0.25	-2.09±3.10	-2.35±3.12	-2.06±3.28	-0.94±1.77	<**0.01**	0.67	0.21	**0.01**
T width [n.u.]	-0.01±0.21	2.18±5.51	2.82±6.03	3.04±6.65	1.81±4.99	<**0.01**	0.12	0.83	<**0.01**
T symmetry [n.u.]	0.02±0.17	2.25±2.32	2.32±2.48	2.42±2.43	1.71±1.39	<**0.01**	<**0.01**	0.15	<**0.01**
T kurtosis [n.u.]	0.14±0.33	4.08±12.26	4.41±12.63	4.30±15.59	3.86±9.35	<**0.01**	0.05	0.67	<**0.01**

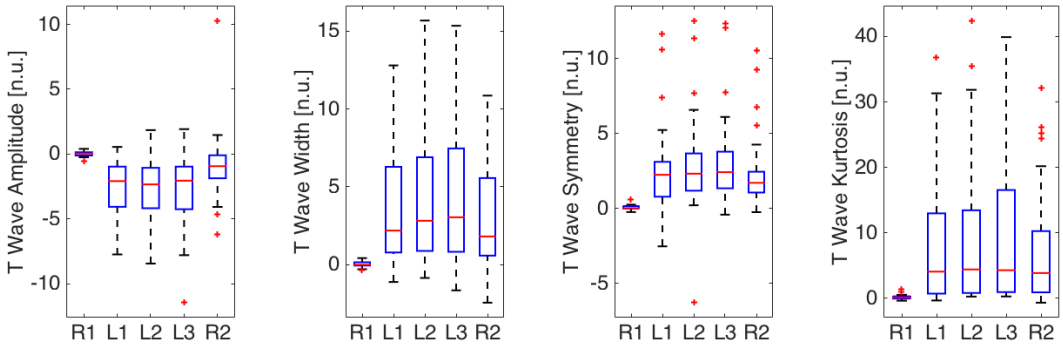

Figure 9.10: Some of the most significant morphological features for the assessment of mental workload in the ECG are displayed in the form of boxplots. The greatest changes appeared between the first resting phase and the first workload level. The changes remained then constant with increasing difficulty level. This figure was reprinted from publication [33] with permission from the publisher.

When comparing the first difficulty level with the second one, we found that HRV parameters that characterize rapid variations in the RR time series underwent a significant reduction. Even though features like rMSSD, SDSD, pNN20 and pNN50 remained unchanged from the resting phase to the first workload level, they decreased significantly during the second difficulty level. Another interesting result was observed from the non-linear parameters SaEn and SD1/SD2 that behaved similarly to ApEn. After an increase in the first difficulty level, these non-linear parameters went back to the initial levels during the first resting phase.

Significant differences between difficulty levels two and three were revealed by only three parameters among the select ones, LF/HF, pNN50, WPAband2. Furthermore, when comparing the two resting phases, we observed that VLF, LF, SDNN index and TINN were significantly different. They went from the reduced values during the three difficulty levels to values even higher than original ones observed in the first resting phase.

Using WPA, the time series was divided into smaller time frequency windows that allowed us to study the frequency domain properties of the RR time series without loosing its temporal dependency. We observed that the normalized power of the wavelet coefficients in the second frequency band (0.0375 to 0.075 Hz) underwent a significant reduction in the first difficulty level. Furthermore, we observed an increase in normalized power in the the forth band (0.1125 to 0.15 Hz). This phenomenon can be seen in figure 9.11 (a) and (b) in which the WPA of one of the participants during the first resting phase and the first workload level are displayed. In figure 9.11 (b), higher wavelet coefficients tend to appear and disappear with some regularity in the frequency band just above 0.1 Hz. This behavior was corroborated by the Fourier PSD obtained for the same participant and displayed in figure 9.11 (c).

In summary, among all rhythmical features, 84 of them were proved to undergo a significant change from the first resting phase to the first difficulty level. In the next transition from level one to level two, 64 of the rhythmical parameters were significantly modified. This number was reduced to 38 when the second workload level and the third one were

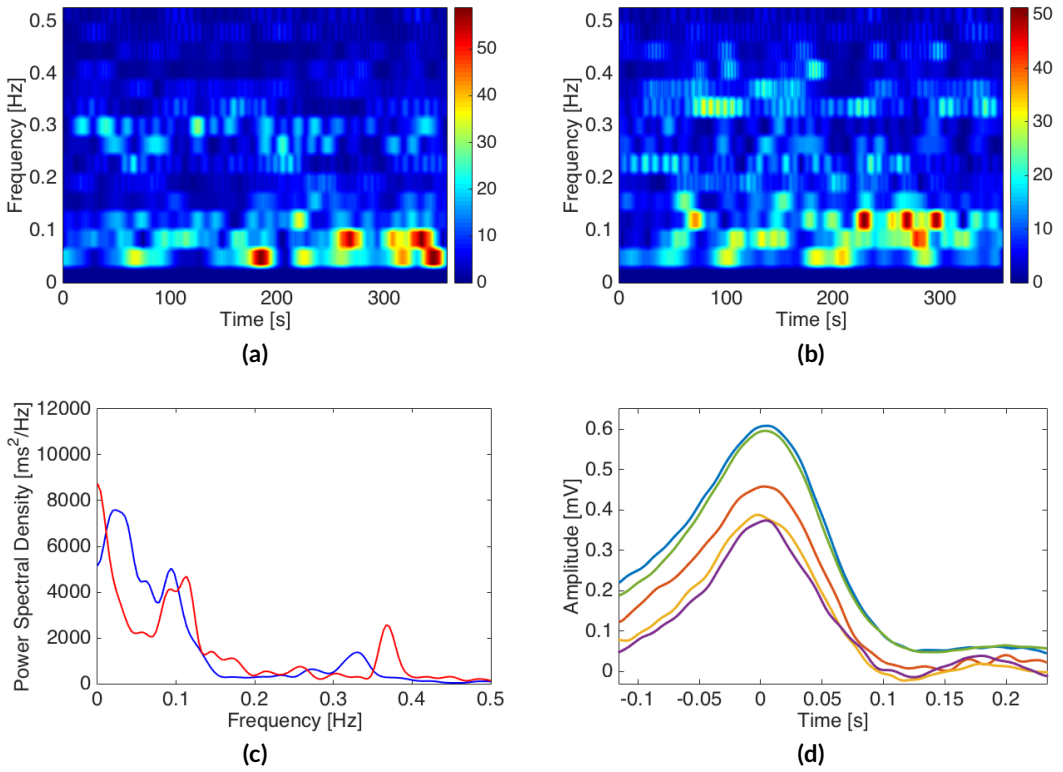

Figure 9.11: (a): Time frequency representation of the RR time series recorded from one of the participants of the study during the resting phase. (b): Time frequency representation of the RR time series recorded from the same subject during the first workload level. In the band just above 0.1 Hz, an increased power in the wavelet coefficients can be observed with some temporal regularity. (c): Fourier PSD corresponding to the same WPA representation presented from (a) (blue) and (b) (red). The increased spectral power can be seen above 0.1 Hz. (d): T waves obtained from another participant during all phases of the experiment. The color coding is given as follows: first resting phase (blue), difficulty level 1 (red), difficulty level 2 (yellow), difficulty level 3 (violet) and second resting phase (green). The shape of the T wave is strongly dependent on the workload level. This figure was reprinted from publication [33] with permission from the publisher.

compared. We also found that there was no HRV feature capable of separating all workload levels from each other.

9.4.3.2 ECG Wave Morphology Analysis

From the study of ECG wave morphology, we found that only the T wave was affected by mental workload. In the first difficulty level, all morphological properties were modified when compared to the previous resting phase. The T wave change under mental workload was characterized by a diminished amplitude, a greater width, a reduction of symmetry and an increased tailedness. In median, the shape of the wave retained this features during all three workload levels.

The interquartile range of the boxplots displayed in figure 9.10 was observed to increase with every difficulty level. This proved that the impact of the mental workload on the

morphology of the ECG is very different in every subject and these discrepancies accentuate with increasing difficulty level. An example of how a T wave changes in dependency of the workload level can be seen in figure 9.11 (d). There was no morphological feature capable of differentiating a workload level from the others. The same result was also obtained from the rhythmical features.

9.5 Discussion

9.5.1 NASA-TLX and Driving Performance

This study was characterized by an exploratory search for the most suitable ECG features for the assessment of mental workload in a simulated car driving experiment. Since the LCT remained unchanged in all three workload levels, it is plausible that learning effects may have appeared in the second and third stages diminishing again the workload level. However, the participants reported in the NASA-TLX a significantly increasing difficulty in the secondary task in all workload levels. In addition, the mean deviation from the norm driving path and the mistakes in the n-back task grew significantly with every workload level. This led us to the conclusion that the primary LCT task accompanied with the n-back task were successfully producing mental workload with increasing difficulty levels.

9.5.2 HRV Analysis

The HRV parameters showed different trends in dependency of the workload level. However, we found that in general, mental workload was characterized by a reduction in RR interval length (increased heart rate) together with a reduction of variability in the RR time series. We propose a few explanations for this observation. First, an increased sympathetic tone characterized by a higher concentration of catecholamines like adrenaline and noradrenaline in the heart. The opening of the HCN channels at cellular level is facilitated through these hormones causing an increase of Ca^{2+} current and leading to a steeper action potential in the sinus node and thus to a shorter RR interval. Furthermore, these hormones reduce the relaxation time of the heart muscle, increase contractile strength and conduction velocity facilitating the higher heart rate [163]. The increased tone of the sympathetic system would also explain the observed reduction of parameters related to the slow variations in the series.

The second possible explanation for our findings is a diminished vagal tone under the influence of mental workload. A reduction of parasympathetic activity would be conform with the decreased HRV parameters that quantify rapid variations in the series in workload level two [164]. This same results have been repored previously in literature [165]. Hence, the results suggest that mental workload, and in particular a high level of concentration performing a task, could be characterized by an initial reduction of sympathetic activity followed by a diminished vagal tone that is dependent on the degree of workload.

Another interesting result was that some HRV parameters that are related to the slow variations of the RR time series remained significantly modified even after the last n-back task was finished and the subject had the chance to relax in the second resting phase. Similar observations have been reported in literature, in which the vagal tone has been shown to remain diminished for several minutes after stress testing has finished [166]. The sympathetic dominance in that scenario causes a lower HRV.

The coupling between respiration and RR time series introduced in the previous chapter may be playing an additional role in this study. We discussed in chapter 8 that first, respiratory sinus arrhythmia (RSA) was stronger in younger subjects and second, the natural breathing rate of all subjects was around 0.3 Hz. This means that the respiration driven part of HRV is located in the HF band. However, during mental workload the coupling strength between the two time series may be lower causing a reduction in the HRV parameters that quantify rapid variations.

Directly related to respiration is also speech. Since the participants had to repeat numbers with a period of 2.2 s (equivalent to a rate of 0.45 Hz), it is possible that the breathing pattern would have been modified and this may have led to the variations in the parameters quantifying HRV power in the HF band. As a matter of fact, HRV has been proven to be affected by speech leading to an increased heart rate and a reduction in HRV [167]. Yet, speech was present during all three workload levels but HF changed only from the first workload level to the second while mean heart RR was significantly modified in the first and second workload levels. Although speech and respiration may be playing a role, they do not fully explain the results.

From the WPA, we observed that the wavelet coefficients increased and decreased with some temporal regularity in the frequency band above 0.1 Hz during all workload phases of the experiment. This finding was corroborated in the Fourier PSD with an increase of the PSD amplitude just above 0.1 Hz, too. The intermittent power of the RR time series above 0.1 Hz could be related to other physiological regulation mechanisms such as blood pressure, blood flow, cardiovascular perfusion, and body temperature located also at 0.1 Hz [164, 168]. However, another possible explanation is the LCT. In this study, the lane change was performed at a similar rate of 0.115 Hz which corresponds to the period of 8.7 s. Thus, a recurrent modulation of the driving movement could also explain the appearing power at the frequency 0.115 Hz.

9.5.3 ECG Wave Morphology Analysis

We observed from the analysis of the ECG wave morphology that only the T wave was modified in the presence of mental workload. This result has been reported in previous studies [169, 170] and we believe that this is because the repolarization of the ventricles is electrophysiologically altered at cellular level. Although the electrophysiological perturbations and variations in the heterogeneous repolarization sequence that lead to a modified T wave are not entirely understood, it is well known that an increased heart rate (like the

one observed under mental workload) leads to a modified T wave. In addition, under the influence of a larger sympathetic activity, the effect of heart rate can be potentiated [171].

Other possible explanations for a modified T wave are related to blood pressure or body temperature [80]. The baroreceptor reflex is a rapid feedback mechanism that regulates blood pressure over the variation of the heart rate [172]. Since both branches of the ANS impact directly the baroreceptor reflex, the regulation of blood pressure and thus the T wave could also be affected under mental workload. Yet, body temperature and blood pressure were not recorded in this study and these ideas can only remain a hypothesis for now. In future, other physiological signals related to the cardiovascular system such as blood pressure, respiration, oxygen saturation and temperature should be recorded and evaluated. We would expect to see modifications in the features of those signals under the influence of mental workload.

Another interesting observation from the morphological analysis was the increasing interquantile range of the T wave features with growing level of workload. This result demonstrates how mental workload affects electrophysiology of the heart in very different manners. We did not observe this kind of behaviour (or at least not this large) in the HRV parameter. An explanation for this finding could be related to the large intersubject variability in the repolarization sequence which leads to a large amount of T wave shapes in healthy subjects [76, 173]. Thus, mental workload could be a potentiator of the different repolarization schemes making them more visible and bringing subjects even further apart from each other. In any case, more research is needed to prove this hypothesis.

The T wave was also observed to retain its modified shape after the end of the workload phases during the second resting period. This finding is in accordance with other results reported in literature showing how the T wave can remain modified for several minutes after the end of a test [174]. Thus, it is plausible to believe that after mental workload testing, the T wave requires a relatively long time to recover to its original form. A longer record at the end of the experiment would probably have demonstrated the slow recovery of the T wave.

We did not see any modifications in the QRS complex and ST segment meaning that the depolarization of the ventricles was not affected by mental workload. In cardiology, an abnormal QRS complex or an elevated or depressed ST segment has been observed in combination of pathologies such as ischemia, myocardial infarction or coronary artery disease for which the ventricular tissue is severely damaged [175, 176]. Since in our study all participants were healthy young students without history of cardiac afflictions, we consider this result to be normal.

The last ECG wave in our analysis was the P wave which is the projection of the atrial electrical activity on body surface. Due to the fact that the P wave was not modified under the influence of mental workload, we conclude that the atrial depolarization was not affected either. A P wave modification would be expected under an increased heart rate. However, such changes appear at least with a heart rate of 115 beats per minute under dynamic exercise and recovery [177]. Since the heart rate of any of the participants did not go that high, we assume the unmodified P wave to be a normal result. Furthermore, atrial afflictions such as fibrillation or flutter lead also to a modified P wave but they can be excluded because of the healthy young population participating in the study.

Finally, we carried out a subject specific normalization of the morphological features but we did not normalize the rhythmical ones. It would be interesting to extend the participant specific analysis in a future investigation and to study the new results. An analysis specially tailored for each subject could deliver new insights about the effects of mental workload on the heart.

9.5.4 Limitations and Outlook

A large amount of significance tests were performed in the analysis of ECG features. This is a limiting factor because it can lead to a proportional amount of type one errors. In total, $364 \cdot 4 = 1384$ tests were carried out and since we set the significance level at 5 %, it would be plausible to expect 69 test to be significant just by chance. Therefore, it is very important to recheck visually those significant features and evaluate the results critically. In parameters such as ApEn, WPAband4 and SDNN index, we saw notoriously different medians of the distributions but also a trend in which the median showed a clear dependency of the increasing workload level. This led us to believe, that these changes were not random but rather a true effect of mental workload on the ECG. Furthermore, since the intention of this study was to explore the possibilities of the ECG features for this application, this kind of statistical analysis can help to postulate hypotheses for future prospective studies.

A further limitation of this study is the fact that we did not record other cardiovascular signals such as respiration. Thus, it is impossible to investigate the impact that breathing frequency or speech have on the HRV while repeating the numbers of the n-back task. Since respiration and speech couple to the HF band of HRV, they could impact the parameters responsible for the rapid variations in the RR time series. Nevertheless, speech should have remained constant among all workload levels and we assumed that it should not lead to any significant change from one workload level to the next one. On the other hand, respiration is definitely a biosignal that should be recorded in a future study in order to better understand its role in this experiment.

Another important aspect that can be considered for a future study are the characteristics of the population participating in the experiment. Our subjects were predominately male students of ages between 18 to 30 years. This distribution could have led to a biased statistic. To avoid this problem in future, a more heterogeneous population in respect to age and gender would be recommended.

Finally, the appearance of recurring spectral power above 0.1 Hz was postulated to be related to the LCT. It would be interesting to investigate in future, if this signal arrives from a learning effect that becomes clear when the participant gets used to the lane changing at a fixed period of time or if the signal is rather the consequence of the physical exercise required to move the steering wheel. In order to clarify this point, the study would need to be conceived differently. Instead of a steering wheel, a keyboard could be used and another rate of lane changing would be recommended as well.

9.5.5 Conclusion

The results obtained from this study suggest that the ECG, and in concrete its rhythmical and morphological features, can be successfully used for the ergonomic application of assessing the impact of mental workload on a subject while driving a car. We found that in general, an increasing workload level leads to a reduction of the variability in the RR time series and an increase of heart rate. This is because in every workload level we observed a change of different ECG features. Yet, there was no single parameter capable of differentiating all three difficulty levels but many features were able to discriminate between at least two of them. Thus, the combination of different parameters is required to achieve the best characterization of the different workload levels.

PART VI

CLOSING REMARKS

CHAPTER 10

Ideas for Future Work

In the final chapter of this thesis, we reflect on the signal processing techniques presented in the previous chapters and propose new ideas for future research projects. Some of the methods that will be discussed in this chapter have been part of recent investigations in our research group. The initial results obtained so far look promising and we believe they are worth mentioning here.

10.1 Preprocessing the Electrocardiogram

One of the fundamental steps, when performing any signal processing tasks is to prepare the signal by removing all kind of artifacts and noise. The signal preprocessing algorithms play a decisive role in the field of electrocardiogram (ECG) because they are capable of eliminating baseline wander, power line hum, and high frequency random noise and allow the physician to perform a correct diagnose based on a reliable signal. However, there are particular cases for which the filtering algorithms have to be chosen very precisely in order to remove the artifact but maintain the relevant information. A challenging example in this regard is the removal of baseline wander from the ECG in patients with acute coronary syndrome caused by ischemia or myocardial infarction. Ischemia can be diagnosed in the ECG because it is characterized by an elevation or depression of the ST segment [178]. This is a particularly difficult task because the baseline wander has similar spectral properties as the ST segment. Therefore, applying a too strong filter would also eliminate the ST change. The need for a best performing filter that does not modify the ECG is thus an important task. Figure 10.1 (b) demonstrates this effect.

In order to shed more light on this topic, we carried out a large simulation study, generated 5.5 million signals and compared different filtering methods. As golden truth for the performance quantification of the algorithms, a full torso bidomain simulation was perfomed in which the ischemic heart was represented at a multiscale level from the cardiac myocyte to the surface ECG. A faithful model of baseline wander was also created to mimic

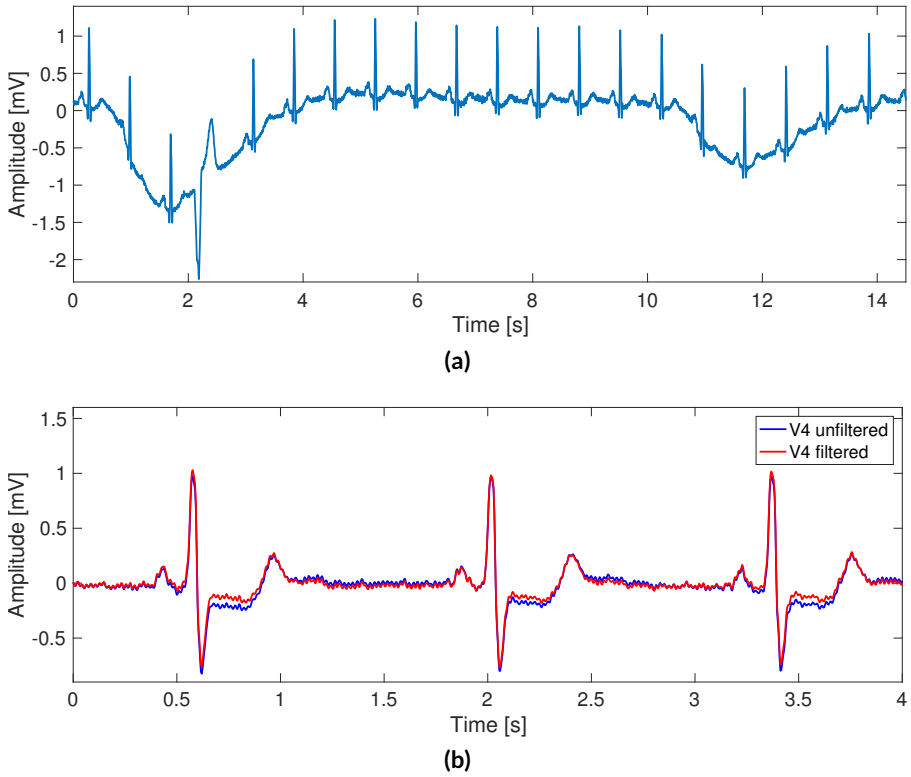

Figure 10.1: (a): ECG signal corrupted by baseline wander. The removal of this artifact is necessary to diagnose ST changes. Yet, a too strong filter can modify the ST segment as shown in figure 10.1 (b). (b): An ST depression is clearly seen in this ECG. After high-pass filtering at 1 Hz, the ST depression is slightly reduced even though the rest of the signal looks the same. The signal in blue is the original one while the red one is obtained after filtering. These signals were retrieved from the database in *physionet.org* [31]. This figure was reprinted from publication [90] with permission from the author.

this artifact and corrupt the ischemic ECG. Figure 10.2 (a) shows an example of a simulated signal with baseline wander. The spectrum of the baseline wander and the spectrum of the distorted signal are diplayed in figures 10.2 (b) and (c). This study was published in form of a journal paper and a conference contribution [90, 109].

According to the results we obtained in those publications, we believe that there is a great potential in the combination of cardiac modelling and signal processing approaches. It would be also interesting to study other major cardiac pathologies such as ventricular tachycardia, atrial fibrillation or atrial flutter and investigate how the ECG must be preprocessed to deliver a signal suitable for diagnosis. Other fields of research such as electrocardiographic imaging (ECGI) could also profit from an optimized signal preprocessing algorithm [179].

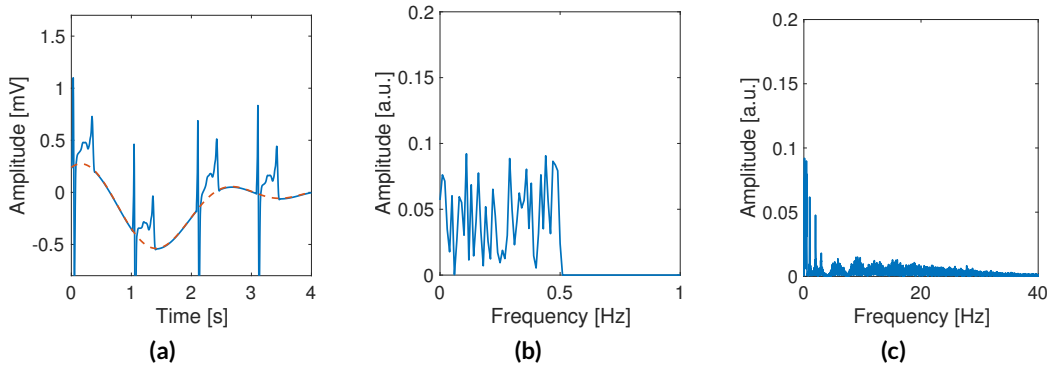

Figure 10.2: (a): Simulated ECG signal with ST elevation. Synthetic baseline wander has been added to generate an SNR of - 3 dB. The baseline wander is marked with the red dasehd line. (b): PSD of the baseline wander signal. The spectrum of the artifact ranges from 0 to 0.5 Hz. (c): PSD of the ECG signal with baseline wander. This figure was reprinted from publication [90] with permission from the author.

10.2 Signal Processing Methods for the Intracardiac Atrial Electrogram

The field of signal processing of the intracardiac electrogram (EGM) is a research area that has gained a lot of momentum in our research group over the last years [26, 110, 114, 180]. The main focus of these projects has laid on a deeper understanding of the highly complex nature of atrial arrhythmias such as fibrillation and flutter, and on helping the cardiologist to better understand the meaning of the signals acquired in the atria. Also in this field of research, signal preprocessing methods similar to the ones used for ECG analysis are required.

The unipolar intracardiac EGM is typically corrupted by the same artifacts found in the surface ECG (baseline wander, high frequency noise and power line hum). However, the filters used for intracardiac applications must be adjusted to match the spectral properties of the atrial extracellular potentials. As it turns out, the spectral properties of intracardiac EGM signals can vary strongly depending on the kind of pathology being threated [181]. However, we have successfully adapted our signal processing methods to remove the "standard" perturbations found in atrial recording during flutter. Figure 10.3 shows the filtering steps required to obtain a clean unipolar EGM suitable for further analysis.

In addition to these "standard" artifacts, atrial EGM signals are often distorted by other sources such as heart movement, respiration and ventricular far field (VFF). These perturbations should be also removed prior to further analysis. We made possible the removal of VFF during atrial flutter using a method called periodic component analysis (πCA) and we have proved this method to deliver a superior performance than the one obtained from the traditionally applied principal component analysis (PCA). Figure 10.4 demonstrates the functionality of the algorithm based on πCA to remove VFF.

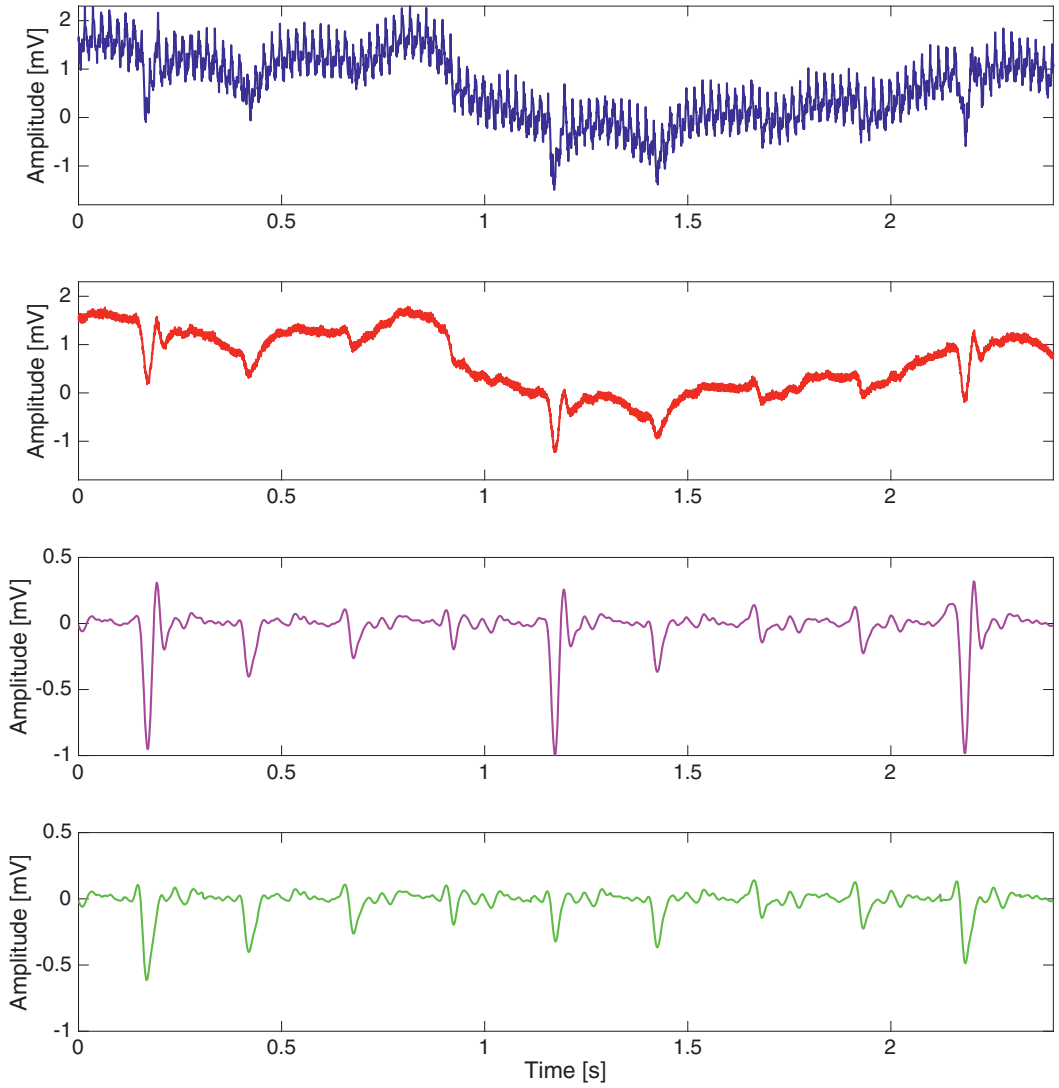

Figure 10.3: Signal processing algorithm to prepare the intracardiac signal for further analysis. (a): Unfiltered signal recorded with an intracardiac catheter. (b): In the first filtering step, the powerline hum is eliminated. (c) In the second processing step, the baseline wander and the high freqeuncy noise is filtered. (d): After the first two steps, the resulting signal is very clean but it still contains VFF (large peaks). (d): VFF removal is carried out using πCA to reconstruct the pure atrial activity. This figure was reprinted from publication [182] with permission from the publisher.

Yet, πCA can only work if the signal being processed is perfectly periodic which is the case in atrial flutter. To overcome this limitation, a different approach based on a new method called orthogonal component analysis (OCA) has also been tested on a theoretical level delivering promising results. Our developments in the field of preprocessing of atrial EGM signals have been published in form of three journal papers and an international conference contribution [113, 182–184].

Nevertheless, the removal of VFF for other atrial arrhythmias and even in the case of sinus rhythm has not been possible so far, or at least not without affecting the underlying atrial activity. In addition, the artifacts appearing on the signal caused by other effects such

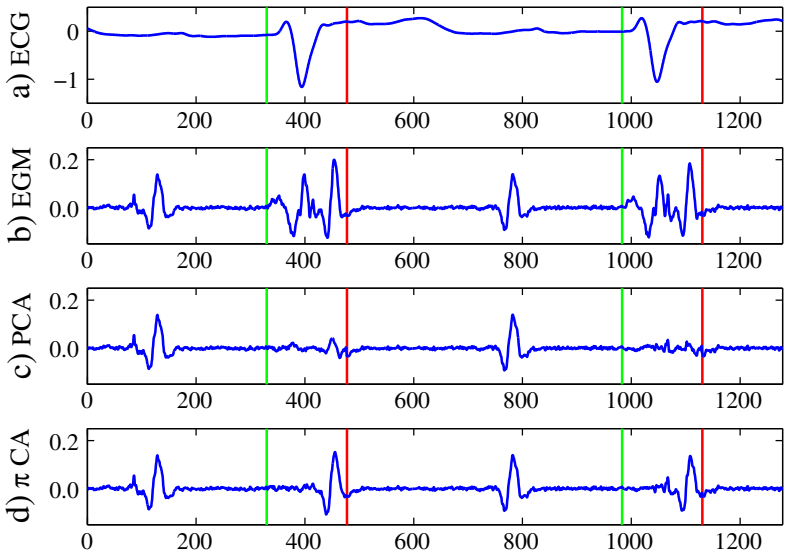

Figure 10.4: Comparison of VFF removal techniques applied on clinical recordings. The signals are characterized by stable conduction during atrial flutter. (a): Surface ECG. (b): Atrial EGM with VFF. (c): VFF removal using PCA. The atrial activity is also canceled. (d) VFF removal using πCA. Time is given in ms and amplitudes in mV. The atrial activity is retained. This figure was reprinted from publication [183] with permission from the publisher.

as varying electrode contact with the heart wall or fibrotic tissue still need more research to be fully understood. This is an area in which electrophysiological modeling and signal processing could come together to improve the current state of the art.

10.3 Machine Learning Methods in the Field of ECG Signal Processing

In chapter 4, we introduced postextrasystolic T wave change (PEST) and mentioned that the ventricular ectopic beat (VEB)s were classified using a support-vector-machine (SVM). As a matter of fact, classification tasks are very common in the field of cardiology since physicians are often interested in the diagnosis of a given disease or detecting high risk patients. Furthermore, in chapter 6, we proposed that PEST could be used to identify patients of chronic heart failure (CHF) of dying of pump failure progression death (PFD) but the results were negative. A different approach would be to combine already existing risk predictors using machine learning methods and try to achieve a higher sensitivity (SEN) and specificity (SPE). In this regards, we had the chance to contribute to a research project carried out by the group BSICoS at the University of Zaragoza in which an SVM was used to successfully combine the ECG markers turbulence slope (TS), T-wave alternans (IAA) and dispersion of repolarization ($\Delta\alpha$) to discriminate sudden cardiac death (SCD) and PFD in the patients suffering from CHF in a more powerful fashion. This research project was publish as a journal paper [185].

Apart from the identification of high risk patients, the machine learning algorithms can be used to solve inverse problems such as the one arising in ECGI. As a matter of fact, we have applied succesfully a support-vector-regression for the localization of ventricular ectopic beats (VEBs) using features computed from the body surface potential map [186]. Figure 10.5 demonstrates this approach. In figure 10.5 (a), a ventricular geometry with the origin of two VEBs can be seen. In figure 10.5 (b) and (c), their corresponding body surface potential maps are displayed. Since the two origins lay close to each other, their body surface potentials recorded in the ECG are very similar. The challenge here is to train a machine-learning algorithm capable of locating the two origins.

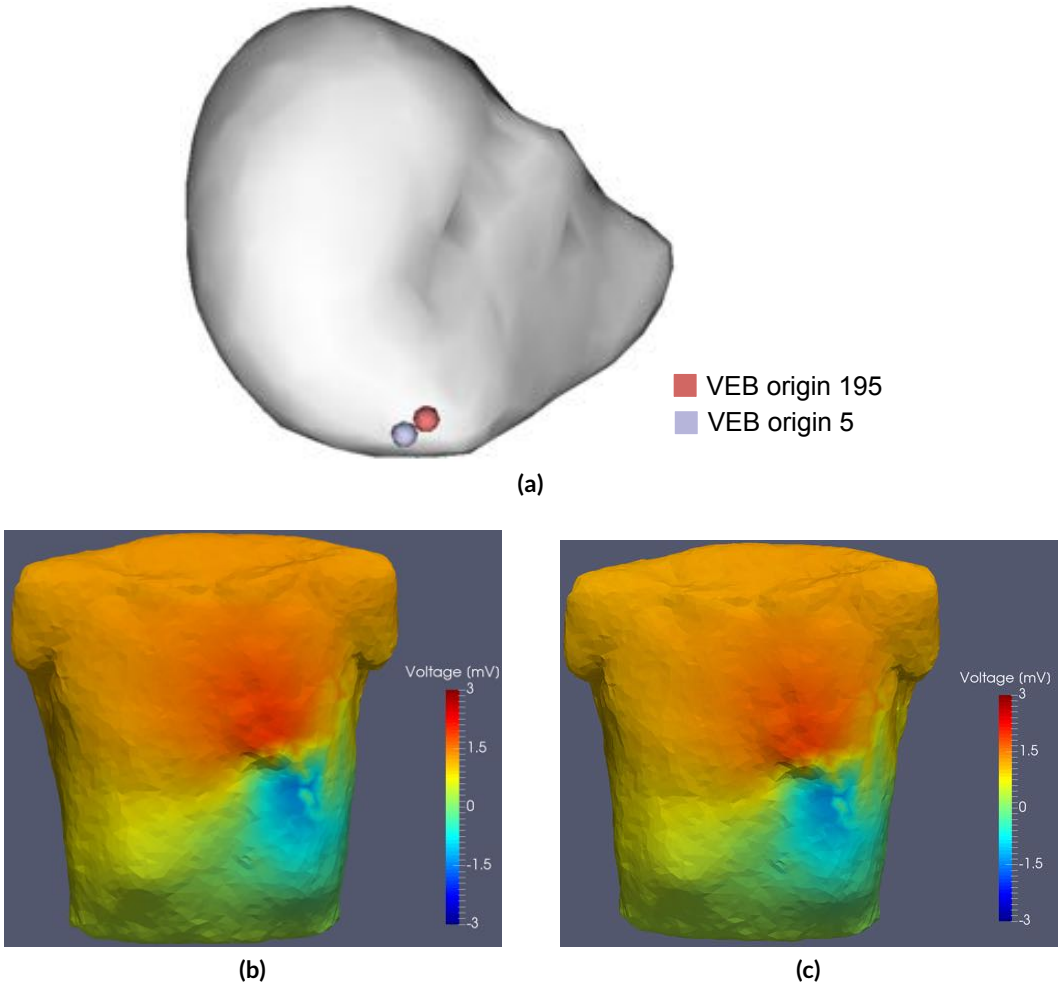

Figure 10.5: (a): Origin of two VEB with little distance from each other. (b): Body surface potential map corresponding to the focal ventricular activity labeled as"VEB origin 5" (c): Body surface potential map corresponding to the focal ventricular activity labeled as "VEB origin 195". The two body surface potentials are very similar to each other what makes an automatic localization of their origin a challenging task. Machine learning methods could help in this kind of problems. This figure was reprinted from publication [187] with permission from the author.

In a different project, we developed an artificial neural network capable of reconstructing accurately the concentration in plasma of calcium and potassium [188]. Even though these two methods have been tested only on simulated data so far, we believe that it should be possible to generalize their applicability to real recordings. This kind of research projects is a good opportunity to test, if a method that learns from simulated data can indeed be applied for real life problems.

References

[1] P. A. Iaizzo, *Handbook of cardiac anatomy, physiology, and devices*. New Jersey: Springer Science & Business Media, 2009.

[2] A. Luthra, *ECG made easy*. New Dehli: Jaypee Brothers Medical Publishers (P) Ltd, 2012.

[3] R. Lozano, M. Naghavi, K. Foreman, et al., "Global and regional mortality from 235 causes of death for 20 age groups in 1990 and 2010: a systematic analysis for the global burden of disease study 2010," *The Lancet*, vol. 380, no. 9859, pp. 2095–2128, 2013.

[4] World Health Organization, "The top 10 causes of death," Web: http://www.who.int/mediacentre/factsheets/fs310/en, 2014, [Online; accessed: 2017-01-01].

[5] C. Roehrig, G. Miller, C. Lake, et al., "National health spending by medical condition, 1996–2005," *Health Affairs*, vol. 28, no. 2, pp. w358–w367, 2009.

[6] A. J. Weiss, A. Elixhauser, and R. M. Andrews, "Characteristics of operating room procedures in us hospitals, 2011," Web: http://www.who.int/mediacentre/factsheets/fs310/en, 2014, [Online; accessed: 2017-01-01].

[7] J. Francis, M. A. Watanabe, and G. Schmidt, "Heart rate turbulence: a new predictor for risk of sudden cardiac death," *Annals of Noninvasive Electrocardiology*, vol. 10, no. 1, pp. 102–109, 2005.

[8] J. Nolan, P. D. Batin, R. Andrews, et al., "Prospective study of heart rate variability and mortality in chronic heart failure results of the united kingdom heart failure evaluation and assessment of risk trial (uk-heart)," *Circulation*, vol. 98, no. 15, pp. 1510–1516, 1998.

[9] M. Malik, "Heart rate variability," *Annals of Noninvasive Electrocardiology*, vol. 1, no. 2, pp. 151–181, 1996.

[10] G. Schmidt, M. Malik, P. Barthel, et al., "Heart-rate turbulence after ventricular premature beats as a predictor of mortality after acute myocardial infarction," *The Lancet*, vol. 353, no. 9162, pp. 1390–1396, 1999.

[11] Y. Castro-Torres, R. Carmona-Puerta, and R. E. Katholi, "Ventricular repolarization markers for predicting malignant arrhythmias in clinical practice," *World Journal of Clinical Cases*, vol. 3, no. 8, p. 705, 2015.

[12] A. J. Camm, P. Kirchhof, G. Y. Lip, et al., "Guidelines for the management of atrial fibrillation: the task force for the management of atrial fibrillation of the european society of cardiology (esc)." *European Heart Journal*, vol. 31, no. 19, pp. 2369–429, 2010.

[13] T. M. Munger, L.-Q. Wu, and W. K. Shen, "Atrial fibrillation," *Journal of Biomedical Research*, vol. 28, no. 1, pp. 1–17, 2014.

[14] S. Wolowacz, M. Samuel, V. Brennan, et al., "The cost of illness of atrial fibrillation: a systematic review of the recent literature," *Europace*, vol. 13, no. 10, pp. 1375–1385, 2011.

[15] P. E. Dilaveris and J. E. Gialafos, "P-wave dispersion: a novel predictor of paroxysmal atrial fibrillation," *Annals of Noninvasive Electrocardiology*, vol. 6, no. 2, pp. 159–165, 2001.

[16] B. Pomeranz, R. Macaulay, M. A. Caudill, et al., "Assessment of autonomic function in humans by heart rate spectral analysis," *American Journal of Physiology - Heart and Circulatory Physiology*, vol. 248, no. 1, pp. H151–H153, 1985.

[17] M. T. La Rovere, G. D. Pinna, R. Maestri, et al., "Short-term heart rate variability strongly predicts sudden cardiac death in chronic heart failure patients," *circulation*, vol. 107, no. 4, pp. 565–570, 2003.

[18] C. R. D. O'Donnell and F. T. Eggemeier, "Workload assessment methodology," in *Handbook of Perception and Human Performance*. New York: Wiley, 1986, pp. 42–1 – 42–49.

[19] K. Ryu and R. Myung, "Evaluation of mental workload with a combined measure based on physiological indices during a dual task of tracking and mental arithmetic," *International Journal of Industrial Ergonomics*, vol. 35, no. 11, pp. 991–1009, 2005.

[20] K. A. Brookhuis and D. de Waard, "Monitoring drivers' mental workload in driving simulators using physiological measures," *Accident Analysis & Prevention*, vol. 42, no. 3, pp. 898–903, 2010.

[21] A. H. Taylor and L. Dorn, "Stress, fatigue, health, and risk of road traffic accidents among professional drivers: the contribution of physical inactivity," *Annual Reviews of Public Health*, vol. 27, pp. 371–391, 2006.

[22] K. S. Saladin, *Anatomy & physiology*. New York: WCB/McGraw-Hill, 1998.

[23] P. Tate, *Seeley's principles of anatomy and physiology*. New York: McGraw-Hill Education, 2011.

[24] M. Wilhelms, *Multiscale modeling of cardiac electrophysiology: adaptation to atrial and ventricular rhythm disorders and pharmacological treatment*. KIT Scientific Publishing, 2013.

[25] M. Courtemanche, R. J. Ramirez, and S. Nattel, "Ionic mechanisms underlying human atrial action potential properties: insights from a mathematical model," *Am J Physiol*, vol. 275, no. 1 Pt 2, pp. 1522–1539, 1998.

[26] A. Loewe, *Modeling human atrial patho-electrophysiology from ion channels to ECG-substrates, pharmacology, vulnerability, and p-waves*. KIT Scientific Publishing, 2016.

[27] R. F. Schmidt and F. Lang, *Physiologie des Menschen - mit Pathophysiologie*. Heidelberg: Springer, 2007.

[28] L. Sherwood, *Human physiology: from cells to systems*. Boston: Cengage Learning, 2015.

[29] F. H. Martini, M. J. Timmons, and R. B. Tallitsch, *Human anatomy: International edition*. Essex: Benjamin Cummings, 2012.

[30] T. Fritz, "Biomechanical modeling of the human heart - modeling of the ventricles, the atria and the pericardium and the inverse problem of cardiac mechanics," PhD thesis, Institute of Biomedical Engineering (IBT), Karlsruhe Institute of Technology (KIT), 2015.

[31] A. L. Goldberger, L. A. N. Amaral, L. Glass, et al., "PhysioBank, PhysioToolkit, and PhysioNet: Components of a new research resource for complex physiologic signals," *Circulation*, vol. 101, no. 23, pp. e215–e220, 2000.

[32] H.-P. Schuster and H.-J. Trappe, *EKG-Kurs für Isabel*. Stuttgart: Georg Thieme Verlag, 2005.

[33] G. Lenis, T. Heine, P. Reichensperger, et al., "Electrocardiographic features for the measurement of drivers' mental workload," *Journal of Applied Ergonmics*, vol. 61, pp. 31–43, 2017.

[34] J. Malmivuo and R. Plonsey, *Bioelectromagnetism: principles and applications of bioelectric and biomagnetic fields*. Oxford: Oxford University Press, USA, 1995.

[35] E. Mutschler, H.-G. Schaible, P. Vaupel, et al., *Anatomie, physiologie, pathophysiologie des menschen*. Stuttgart: Wissenschaftliche Verlagsgesellschaft, 2007.

[36] U. R. Acharya, K. P. Joseph, N. Kannathal, et al., "Heart rate variability: a review," *Medical and Biological Engineering and Computing*, vol. 44, no. 12, pp. 1031–1051, 2006.

[37] A. Ben-Tal, S. Shamailov, and J. Paton, "Evaluating the physiological significance of respiratory sinus arrhythmia: looking beyond ventilation–perfusion efficiency," *The Journal of Physiology*, vol. 590, no. 8, pp. 1989–2008, 2012.

[38] F. Yasuma and J. Hayano, "Respiratory sinus arrhythmia: why does the heartbeat synchronize with respiratory rhythm?" *Chest Journal*, vol. 125, no. 2, pp. 683–690, 2004.

[39] J. A. Hirsch and B. Bishop, "Respiratory sinus arrhythmia in humans: how breathing pattern modulates heart rate," *American Journal of Physiology - Heart and Circulatory Physiology*, vol. 241, no. 4, pp. H620–H629, 1981.

[40] M. Kircher, "Separating the effect of respiration on the heart rate variability and quantifying the medical impact of the new uncoupled parameters," Master's thesis, Karlsruhe Institut of Technology (KIT), Karlsruhe, 2015.

[41] G. Lenis, T. Baas, and O. Dössel, "Ectopic beats and their influence on the morphology of subsequent waves in the electrocardiogram," *Biomedizinische Technik / Biomedical Engineering*, vol. 58, no. 2, pp. 109–119, 2013.

[42] M. A. Watanabe, "Heart rate turbulence: a review," *Indian Pacing and Electrophysiology Journal*, vol. 3, no. 1, pp. 10–22, 2003.

[43] H. P. Hsu, *Schaums outline of theory and problems of signals and systems*, Schaum's Outline Series. New York: Mc Graw-Hill, 1995.

[44] F. Puente León, U. Kiencke, and H. Jäkel, *Signale und Systeme*. Munich: Oldenbourg Wissenschaftsverlag GmbH, 201.

[45] H. D. Lüke, *Signalübertragung: Grundlagen der digitalen und analogen Nachrichtenübertragungssysteme*. Aachen: Springer-Verlag, 2013.

[46] U. Kiencke, M. Schwarz, and T. Weickert, *Signalverarbeitung: Zeit-Frequenz-Analyse und Schätzverfahren*. Munich: Oldenbourg Verlag, 2008.

[47] P. S. Addison, *The illustrated wavelet transform handbook*. Bristol: IOP Publishing Ltd, 2002.

[48] G. P. Nason and B. W. Silverman, "The stationary wavelet transform and some statistical applications," in *Wavelets and statistics*. Springer, 1995, pp. 281–299.

[49] S. Mallat, *A wavelet tour of signal processing*. Cambridge: Academic press, 1999.

[50] H. P. Hsu, *Theory and problems of probability, random variables, and random processes*, Schaums Outline Series. New York: McGraw-Hill, 1997.

[51] F. Puente León, *Messtechnik*. Heidelberg: Springer-Verlag, 2015.

[52] G. E. Box and G. M. Jenkins, *Time series analysis forecasting and control*. San Francisco: Holden Day, 1970.

[53] A. A. Goshtasby, *Image registration: principles, tools and methods*. London: Springer Science & Business Media, 2012.

[54] A. J. Izenman, *Modern multivariate statistical techniques: Regression, classification and manifold learning*. New York: Springer, 2008.

[55] I. Jolliffe, *Principal component analysis*. New York: Wiley Online Library, 2002.

[56] G. Lenis, "Analysing rhythmical and morphological ECG properties to detect the influence of ectopic beats," Diplomarbeit, Karlsruhe Institut of Technology (KIT), Karlsruhe, 2012.

[57] V. Kecman, *Learning and soft computing: support vector machines, neural networks, and fuzzy logic models*. Cambridge: MIT press, 2001.

[58] C. Cortes and V. Vapnik, "Support-vector networks," *Machine learning*, vol. 20, no. 3, pp. 273–297, 1995.

[59] C. Weiß, *Basiswissen medizinische Statistik*. Heidelberg: Springer-Verlag, 2013.

[60] R. Schlittgen and B. H. Streitberg, *Zeitreihenanalyse*. Munich: Oldenbourg Verlag, 2001.

[61] E. J. Hannan, *Multiple time series*. New York: John Wiley & Sons, 2009.

[62] E. J. Hannan and M. Deistler, *The statistical theory of linear systems*. Philadelphia: SIAM, 2012.

[63] G. Lenis, M. Kircher, J. Lázaro, et al., "Separating the effect of respiration on the heart rate variability using granger's causality and linear filtering," *Biomedical Signal Processing and Control*, vol. 31, pp. 272–287, 2017.

[64] A. Arya, M. Haghjoo, and M. Ali Sadr-Ameli, "Risk stratification for arrhythmic death after myocardial infarction: Current perspective and future direction," *International Journal of Cardiology*, vol. 108, no. 2, pp. 155–164, 2006.

[65] A. Berkowitsch, W. Zareba, T. Neumann, et al., "Risk stratification using heart rate turbulence and ventricular arrhythmia in MADIT II: Usefulness and limitations of a 10-minute holter recording," *Annals of Noninvasive Electrocardiology*, vol. 9, no. 3, pp. 270–279, 2004.

[66] G. Lenis and O. Dössel, "T wave morphology during heart rate turbulence in patients with chronic heart failure," in *Biomedical Engineering / Biomedizinische Technik*, vol. 58, no. s1, 2013.

[67] G. Lenis, T. Baas, and O. Dössel, "Rhythmical and morphological features of the ECG following a premature ventricular contraction," in *Biomedical Engineering / Biomedizinische Technik*, vol. 57, no. s1, 2012.

[68] A. Khawaja, *Automatic ECG analysis using principal component analysis and wavelet transformation*. Karlsruhe: Universitätsverlag, 2006.

[69] T. Baas, *ECG based analysis of the ventricular repolarisation in the human heart*. Karlsruhe: KIT Scientific Publishing, 2012.

[70] P. Stoica and R. Moses, *Introduction to spectral analysis*, vol. 89. Prentice Hall Upper Saddle River, NJ, 1997.

[71] R. Schneider, A. Röck, P. Barthel, et al., "Heart rate turbulence: rate of frequency decrease predicts mortality in chronic heart disease patients," *Pace Pacing And Clinical Electrophysiology*, vol. 22, 1999.

[72] M. Zabel, B. Acar, T. Klingenheben, et al., "Analysis of 12-lead T-wave morphology for risk stratification after myocardial infarction," *Circulation*, vol. 102, no. 11, pp. 1252–1257, 2000.

[73] A. Bauer, M. Malik, G. Schmidt, et al., "Heart rate turbulence: standards of measurement, physiological interpretation, and clinical use: International society for holter and noninvasive electrophysiology consensus," *Journal of the American College of Cardiology*, vol. 52, no. 17, pp. 1353–1365, 2008.

[74] P. De Chazal, M. O'Dwyer, and R. Reilly, "Automatic classification of heartbeats using ECG morphology and heartbeat interval features," *IEEE Transactions on Biomedical Engineering*, vol. 51, no. 7, pp. 1196–1206, 2004.

[75] P. de Chazal and R. Reilly, "A patient-adapting heartbeat classifier using ECG morphology and heartbeat interval features," *IEEE Transactions on Biomedical Engineering*, vol. 53, no. 12, pp. 2535–2543, 2006.

[76] D. U. J. Keller, D. L. Weiss, O. Dössel, et al., "Influence of IKs heterogeneities on the genesis of the T-wave: A computational evaluation," *IEEE Transactions on Biomedical Engineering*, vol. 59, no. 2, pp. 311–322, 2012.

[77] P. D. White, "Alternation of the pulse: a common clinical condition," *American Journal of Medical Sciences*, vol. 150, pp. 82–97, 1915.

[78] T. R. Engel, S. G. Meister, and W. S. Frankl, "Postextrasystolic T wave changes and angiographic coronary disease." *British Heart Journal*, vol. 39, no. 4, pp. 371–374, 1977.

[79] V. N. Batchvarov, A. Bajpai, and A. J. Camm, "Post-extrasystolic changes of the T wave in a patient with congestive heart failure," *Europace*, vol. 9, no. 11, pp. 1093–1093, 2007.

[80] R. Childers, "Time-related perturbations of repolarization," *Journal of Electrocardiology*, vol. 28, pp. 124–130, 1995.

[81] J. C. Geller and M. R. Rosen, "Persistent T-wave changes after alteration of the ventricular activation sequence. New insights into cellular mechanisms of 'cardiac memory'." *Circulation*, vol. 88, no. 4, pp. 1811–1819, 1993.

[82] I. D. Fagin and J. M. Guidot, "Post-extrasystolic T wave change," *The American Journal of Cardiology*, vol. 1, no. 5, pp. 597–600, 1958.

[83] M. A. Watanabe, J. E. Marine, R. Sheldon, et al., "Effects of ventricular premature stimulus coupling interval on blood pressure and heart rate turbulence," *Circulation*, vol. 106, no. 3, pp. 325–330, 2002.

[84] G. Lenis, Y. Lutz, G. Seeman, et al., "Post extrasystolic T wave change in subjects with structural healthy ventricles - measurement and simulation," in *Computing in Cardiology 2014*, vol. 41, 2014, pp. 1069–1072.

[85] E. Gil, P. Laguna, J. P. Martínez, et al., "Heart rate turbulence analysis based on photoplethysmography," *IEEE Transactions on Biomedical Engineering*, vol. 60, no. 11, pp. 3149–3155, 2013.

[86] K. Ten Tusscher and A. Panfilov, "Cell model for efficient simulation of wave propagation in human ventricular tissue under normal and pathological conditions," *Physics in Medicine and Biology*, vol. 51, no. 23, p. 6141, 2006.

[87] G. Seemann, F. Sachse, M. Karl, et al., "Framework for modular, flexible and efficient solving the cardiac bidomain equations using PETSc," in *Progress in Industrial Mathematics at ECMI 2008*. Springer, 2010, pp. 363–369.

[88] S. A. Niederer, E. Kerfoot, A. P. Benson, et al., "Verification of cardiac tissue electrophysiology simulators using an n-version benchmark," *Philosophical Transactions of the Royal Society of London A*, vol. 369, no. 1954, pp. 4331–4351, 2011.

[89] A. Loewe, W. H. Schulze, Y. Jiang, et al., "ECG-based detection of early myocardial ischemia in a computational model: impact of additional electrodes, optimal placement, and a new feature for ST deviation," *BioMed Research International*, vol. 2015, 2015.

[90] G. Lenis, N. Pilia, A. Loewe, et al., "Comparison of baseline wander removal techniques considering the preservation of ST changes in the ischemic ECG," *Computational and Mathematical Methods in Medicine*, vol. 2017, 2017.

[91] T. Sørensen, "A method of establishing groups of equal amplitude in plant sociology based on similarity of species and its application to analyses of the vegetation on danish commons," *Biologiske Skripfter*, vol. 5, pp. 1–34, 1948.

[92] L. R. Dice, "Measures of the amount of ecologic association between species," *Ecology*, vol. 26, no. 3, pp. 297–302, 1945.

[93] R. E. Edmands and J. C. Bailey, "The postextrasystolic T wave change," *The American Journal of Cardiology*, vol. 28, no. 5, pp. 536–540, 1971.

[94] K. H. ten Tusscher and A. V. Panfilov, "Alternans and spiral breakup in a human ventricular tissue model," *American Journal of Physiology - Heart and Circulatory Physiology*, vol. 291, no. 3, pp. H1088–H1100, 2006.

[95] D. R. Leachman, G. J. Dehmer, B. G. Firth, et al., "Evaluation of postextrasystolic T wave alterations in identification of patients with coronary artery disease or left ventricular dysfunction," *American Heart Journal*, vol. 102, no. 4, pp. 658–663, 1981.

[96] G. Lenis, R. Menges, I. Ramirez, J.and Cygankiewicz, et al., "Post extrasystolic T wave change to stratify risk of pump failure death in patients with chronic heart failure," in *Computing in Cardiology 2016*, vol. 43, 2016, pp. 33–36.

[97] R. Vazquez, A. Bayes-Genis, I. Cygankiewicz, et al., "The MUSIC risk score: a simple method for predicting mortality in ambulatory patients with chronic heart failure," *European Heart Journal*, vol. 30, no. 9, pp. 1088–1096, 2009.

[98] D. Dawson, H. Yang, M. Malshe, et al., "Linear affine transformations between 3-lead (frank xyz leads) vectorcardiogram and 12-lead electrocardiogram signals," *Journal of Electrocardiology*, vol. 42, no. 6, pp. 622–630, 2009.

[99] G. Lenis, N. Pilia, T. Oesterlein, et al., "P wave detection and delineation in the ECG based on the phase free stationary wavelet transform and using intracardiac atrial electrograms as reference," *Biomedical Engineering / Biomedizinische Technik*, vol. 61, no. 1, pp. 37–56, 2016.

[100] R. Kohavi, "A study of cross-validation and bootstrap for accuracy estimation and model selection," in *Proceedings of the 14th International Joint Conference of Artificial Intelligence*, vol. 14, no. 2, 1995, pp. 1137–1145.

[101] M. Haissaguerre, P. Jaïs, D. Shah, et al., "Spontaneous initiation of atrial fibrillation by ectopic beats originating in the pulmonary veins," *New England Journal of Medicine*, vol. 339, no. 10, pp. 659–666, 1998.

[102] A. Goette, C. Honeycutt, and J. J. Langberg, "Electrical remodeling in atrial fibrillation time course and mechanisms," *Circulation*, vol. 94, no. 11, pp. 2968–2974, 1996.

[103] G. Schreier, P. Kastner, and W. Marko, "An automatic ECG processing algorithm to identify patients prone to paroxysmal atrial fibrillation," in *Computers in Cardiology 2001*, vol. 28, 2001, pp. 133–135.

[104] L. Clavier, J.-M. Boucher, R. Lepage, et al., "Automatic P-wave analysis of patients prone to atrial fibrillation," *Medical and Biological Engineering and Computing*, vol. 40, no. 1, pp. 63–71, 2002.

[105] A. de Sisti, J. F. Leclercq, M. Stiubei, et al., "P wave duration and morphology predict atrial fibrillation recurrence in patients with sinus node dysfunction and atrial-based pacemaker," *Pacing and Clinical Electrophysiology*, vol. 25, no. 11, pp. 1546–1554, 2002.

[106] J. M. S. Lee and S. P. Fynn, "P wave morphology in guiding the ablation strategy of focal atrial tachycardias and atrial flutter," *Current Cardiology Reviews*, pp. 103–110, 2015.

[107] M. H. Hamdan, J. M. Kaiman, H. V. Barron, et al., "P-wave morphology during right atrial pacing before and after atrial flutter ablation – A new marker for success," *The American Journal of Cardiology*, vol. 79, no. 10, pp. 1417–1420, 1997.

[108] A. Martínez, R. Alcaraz, and J. J. Rieta, "Automatic electrocardiogram delineator based on the phasor transform of single lead recordings," in *Computing in Cardiology 2010*, vol. 37, 2010, pp. 987–990.

[109] N. Pilia, G. Lenis, A. Loewe, et al., "The impact of baseline wander removal techniques on the ST segment in simulated ischemic 12-lead ECGs," *Current Directions in Biomedical Engineering*, vol. 1, no. 1, pp. 96–99, 2015.

[110] T. Oesterlein, "Multichannel analysis of intracardiac electrograms: supporting diagnosis and treatment of cardiac arrhythmias," PhD thesis, Institute of Biomedical Engineering (IBT), Karlsruhe Institute of Technology (KIT), 2017.

[111] P. Laguna, R. G. Mark, A. Goldberg, et al., "A database for evaluation of algorithms for measurement of QT and other waveform intervals in the ECG," in *Computers in Cardiology 1997*. IEEE, 1997, pp. 673–676.

[112] L. Sörnmo and P. Laguna, *Bioelectrical signal processing in cardiac and neurological applications*. Academic Press, 2005.

[113] M. Keller, S. Schuler, M. Wilhelms, et al., "Characterization of acute radiofrequency ablation lesion development based on simulated and measured intracardiac electrograms," *IEEE Transactions on Biomedical Engineering*, vol. 64, no. 4, pp. 2467–2468, 2014.

[114] C. Schilling, "Analysis of atrial electrograms," PhD thesis, Karlsruhe Institute of Technology (KIT), Karlsruhe, 2012.

[115] J. P. Martínez, R. Almeida, S. Olmos, et al., "A wavelet-based ECG delineator: evaluation on standard databases," *IEEE Transactions on Biomedical Engineering*, vol. 51, no. 4, pp. 570–581, 2004.

[116] J. Dumont, A. I. Hernandez, and G. Carrault, "Parameter optimization of a wavelet-based electrocardiogram delineator with an evolutionary algorithm," in *Computing in Cardiology 2005*, vol. 32, 2005, pp. 707–710.

[117] A. Ghaffari, M. R. Homaeinezhad, M. Akraminia, et al., "A robust wavelet-based multi-lead electrocardiogram delineation algorithm," *Medical Engineering & Physics*, vol. 31, no. 10, pp. 1219–1227, 2009.

[118] C. Lin, G. Kail, J. Y. Tourneret, et al., "P and T wave delineation and waveform estimation in ECG signals using a block Gibbs sampler," in *IEEE International Conference on Acoustics, Speech and Signal Processing 2011*. IEEE, 2011, pp. 537–540.

[119] D. Widjaja, A. Caicedo, E. Vlemincx, et al., "Separation of respiratory influences from the tachogram: a methodological evaluation," *PloS ONE*, vol. 9, no. 7, p. e101713, 2014.

[120] M. Kircher, G. Lenis, and O. Dössel, "Separating the effect of respiration from the heart rate variability for cases of constant harmonic breathing," *Current Directions in Biomedical Engineering*, vol. 1, no. 1, pp. 46–49, 2015.

[121] G. Baselli, A. Porta, O. Rimoldi, et al., "Spectral decomposition in multichannel recordings based on multivariate parametric identification," *IEEE Transactions on Biomedical Engineering*, vol. 44, no. 11, pp. 1092–1101, 1997.

[122] K. C. Bilchick and R. D. Berger, "Heart rate variability," *Journal of Cardiovascular Electrophysiology*, vol. 17, no. 6, pp. 691–694, 2006.

[123] E. Bowers, P. Langley, M. Drinnan, et al., "Simulation of cardiac RR interval time series," in *Computers in Cardiology 2002*. IEEE, 2002, pp. 233–236.

[124] M. V. Pitzalis, F. Mastropasqua, F. Massari, et al., "Effect of respiratory rate on the relationships between rr interval and systolic blood pressure fluctuations: a frequency-dependent phenomenon," *Cardiovascular Research*, vol. 38, no. 2, pp. 332–339, 1998.

[125] J. Lázaro, R. Bailón, P. Laguna, et al., "Respiratory rate influence in the resulting magnitude of pulse photoplethysmogram derived respiration signals," in *Computing in Cardiology 2014*, vol. 41, 2014, pp. 289–292.

[126] N. Iyengar, C. Peng, R. Morin, et al., "Age-related alterations in the fractal scaling of cardiac interbeat interval dynamics," *American Journal of Physiology-Regulatory, Integrative and Comparative Physiology*, vol. 271, no. 4, pp. R1078–R1084, 1996.

[127] A. J. Camm, M. Malik, J. Bigger, et al., "Heart rate variability. standards of measurement, physiological interpretation, and clinical use," *European Heart Journal*, vol. 17, no. 3, pp. 354–381, 1996.

[128] C. W. Granger, "Investigating causal relations by econometric models and cross-spectral methods," *Econometrica: Journal of the Econometric Society*, pp. 424–438, 1969.

[129] C. Croarkin, P. Tobias, and C. Zey, *Engineering Statistics Handbook*. Published online: NIST iTL, 2002.

[130] A. Porta, V. Bari, A. Marchi, et al., "Effect of variations of the complexity of the target variable on the assessment of Wiener–Granger causality in cardiovascular control studies," *Physiological Measurement*, vol. 37, no. 2, p. 276, 2016.

[131] J. K. Ghosh, M. Delampady, and T. Samanta, *An introduction to bayesian analysis: theory and methods*. New York: Springer Science & Business Media, 2007.

[132] U. Richter, L. Faes, A. Cristoforetti, et al., "A novel approach to propagation pattern analysis in intracardiac atrial fibrillation signals," *Annals of Biomedical Engineering*, vol. 39, no. 1, pp. 310–323, 2011.

[133] P. Welch, "The use of fast Fourier transform for the estimation of power spectra: a method based on time averaging over short, modified periodograms," *IEEE Transactions on Audio and Electroacoustics*, vol. 15, no. 2, pp. 70–73, 1967.

[134] F. N. Fritsch and R. E. Carlson, "Monotone piecewise cubic interpolation," *SIAM Journal on Numerical Analysis*, vol. 17, no. 2, pp. 238–246, 1980.

[135] A. Porta, T. Bassani, V. Bari, et al., "Model-based assessment of baroreflex and cardiopulmonary couplings during graded head-up tilt," *Computers in Biology and Medicine*, vol. 42, no. 3, pp. 298–305, 2012.

[136] J. B. Hellman and R. W. Stacy, "Variation of respiratory sinus arrhythmia with age," *Journal of Applied Physiology*, vol. 41, no. 5, pp. 734–738, 1976.

[137] W. Hrushesky, D. Fader, O. Schmitt, et al., "Respiratory sinus arrhythmia: a measure of cardiac age," *Science*, vol. 224, pp. 1001–1005, 1984.

[138] E. B. Schroeder, L. E. Chambless, D. Liao, et al., "Diabetes, glucose, insulin, and heart rate variability," *Diabetes Care*, vol. 28, no. 3, pp. 668–674, 2005.

[139] P. G. Guyenet, "The sympathetic control of blood pressure," *Nature Reviews Neuroscience*, vol. 7, no. 5, pp. 335–346, 2006.

[140] S. Webb, A. Adgey, and J. Pantridge, "Autonomic disturbance at onset of acute myocardial infarction," *British Medical Journal (London)*, vol. 3, no. 5818, pp. 89–92, 1972.

[141] G. Grassi, G. Seravalle, B. M. Cattaneo, et al., "Sympathetic activation and loss of reflex sympathetic control in mild congestive heart failure," *Circulation*, vol. 92, no. 11, pp. 3206–3211, 1995.

[142] N. Moray, *Models and measures of mental workload*. New York: Springer, 1979.

[143] F. T. Eggemeier, G. F. Wilson, A. F. Kramer, et al., *Workload assessment in multi-task environments*. London: Taylor & Francis, 1991.

[144] S. Cohen, D. Janicki-Deverts, and G. Miller, "Psychological stress and disease," *Jama*, vol. 298, no. 14, pp. 1685–1687, 2007.

[145] J. K. Lenneman and R. W. Backs, "Diagnosticity of cardiac modes of autonomic control elicited by simulated driving and verbal working memory dual-tasks," in *Engineering Psychology and Cognitive Ergonomics*, Lecture Notes in Artificial Intelligence. Berlin: Springer-Verlag, 2007, pp. 541–550.

[146] L. J. M. Mulder, D. de Waard, and K. A. Brookhuis, "Estimating mental effort using heart rate and heart rate variability," in *Handbook of Human Factors and Ergonomics Methods*. Boca Raton: CRC Press, 2004, pp. 20–1–20–8.

[147] D. Ginopoulos, I. Mavrepis, K. Stampoulidis, et al., "QT dispersion and mental stress testing," *Hellenic J Cardiol*, vol. 44, pp. 180–186, 2003.

[148] J. Gottdiener, D. Krantz, R. Howell, et al., "Induction of silent myocardial ischemia with mental stress testing: Relation to the triggers of ischemia during daily life activities to ischemic functional severity," *Journal of the American College of Cardiology*, vol. 24, no. 7, pp. 1645–1651, 1994.

[149] S. Mattes, "The Lane-Change-Task as a Tool for Driver Distraction Evaluation," in *Quality of Work and Products in Enterprises of the Future*. Stuttgart: Ergonomia Verlag, 2003, pp. 57–60.

[150] I. O. for Standardization, "Road vehicles. Ergonomic aspects of transport information and control systems. Simulated lane change test to assess in-vehicle secondary task demand," 2010.

[151] B. Mehler, B. Reimer, and J. A. Dusek, "Mit AgeLab delayed digit recall task (n-back)," *MIT AgeLab White Paper*, 2011.

[152] S. G. Hart and L. E. Staveland, "Development of NASA-TLX (Task Load Index): Results of empirical and theoretical research," *Advances in Psychology*, vol. 52, pp. 139–183, 1988.

[153] S. G. Hart, "NASA-Task Load Index (NASA-TLX): 20 Years Later," *Proceedings of the Human Factors and Ergonomics Society Annual Meeting*, vol. 50, pp. 904–908, 2006.

[154] G. Borghini, L. Astolfi, G. Vecchiato, et al., "Measuring neurophysiological signals in aircraft pilots and car drivers for the assessment of mental workload, fatigue and drowsiness," *Neuroscience and Biobehavioral Reviews*, vol. 44, pp. 58–75, 2014.

[155] H. Löllgen, "Herzfrequenzvariabilität," *Deutsches Ärzteblatt*, vol. 96, pp. A2029–A2032, 1999.

[156] P. Rani, J. Sims, R. Brackin, et al., "Online stress detection using psychophysiological signals for implicit human-robot cooperation," *Robotica*, vol. 20, no. 06, pp. 673–685, 2002.

[157] Y. Goren, L. Davrath, I. Pinhas, et al., "Individual time-dependent spectral boundaries for improved accuracy in time-frequency analysis of heart rate variability," *IEEE Transactions on Biomedical Engineering*, vol. 53, no. 1, pp. 35–42, 2006.

[158] R. Bailón, P. Laguna, L. Mainardi, et al., "Analysis of heart rate variability using time-varying frequency bands based on respiratory frequency," in *29th Annual International Conference of the IEEE Society of Engineering in Medicine and Biology 2007*, 2007, pp. 6674–6677.

[159] H. Chan, J. Lin, C. Du, et al., "Time–frequency distribution of heart rate variability below 0.05 Hz by Wigner–Ville spectral analysis in congestive heart failure patients," *Medical Engineering & Physics*, vol. 19, no. 6, pp. 581–587, 1997.

[160] F. Cottin, Y. Papelier, and P. Escourrou, "Effects of exercise load and breathing frequency on heart rate and blood pressure variability during dynamic exercise." *International Journal of Sports Medicine*, vol. 20, no. 4, pp. 232–238, 1999.

[161] L. Gamero, J. Vila, and F. Palacios, "Wavelet transform analysis of heart rate variability during myocardial ischaemia," *Medical and Biological Engineering and Computing*, vol. 40, no. 1, pp. 72–78, 2002.

[162] U. Wiklund, M. Akay, and U. Niklasson, "Short-term analysis of heart-rate variability of adapted wavelet transforms," *Engineering in Medicine and Biology Magazine, IEEE*, vol. 16, no. 5, pp. 113–118, 1997.

[163] S. Silbernagl, *Taschenatlas Physiologie*. Stuttgart: Georg Thieme Verlag, 2012.

[164] P. Stein and R. Kleiger, "Insights from the study of heart rate variability," *Annual Review of Medicine*, vol. 50, no. 1, pp. 249–261, 1999.

[165] N. Hjortskov, D. Rissén, A. K. Blangsted, et al., "The effect of mental stress on heart rate variability and blood pressure during computer work," *European Journal of Applied Physiology*, vol. 92, no. 1-2, pp. 84–89, 2004.

[166] M. Buchheit, Y. Papelier, P. B. Laursen, et al., "Noninvasive assessment of cardiac parasympathetic function: postexercise heart rate recovery or heart rate variability?" *American Journal of Physiology - Heart and Circulatory Physiology*, vol. 293, no. 1, pp. H8–H10, 2007.

[167] L. Bernardi, J. Wdowczyk-Szulc, C. Valenti, et al., "Effects of controlled breathing, mental activity and mental stress with or without verbalization on heart rate variability," *Journal of the American College of Cardiology*, vol. 35, no. 6, pp. 1462–1469, 2000.

[168] H. Kvernmo, A. Stefanovska, M. Bracic, et al., "Spectral analysis of the laser Doppler perfusion signal in human skin before and after exercise," *Microvascular Research*, vol. 56, no. 3, pp. 173–182, 1998.

[169] G. Malfatto, M. Facchini, and A. Zaza, "Characterization of the non-linear rate-dependency of QT interval in humans," *Europace*, vol. 5, no. 2, pp. 163–170, 2003.

[170] R. Almeida, S. Gouveia, A. P. Rocha, et al., "QT variability and HRV interactions in ECG: quantification and reliability," *IEEE Transactions on Biomedical Engineering*, vol. 53, no. 7, pp. 1317–1329, 2006.

[171] G. Grassi, S. Vailati, G. Bertinieri, et al., "Heart rate as marker of sympathetic activity," *Journal of Hypertension*, vol. 16, no. 11, pp. 1635–1639, 1998.

[172] C. Heesch, "Reflexes that control cardiovascular function," *Advances in Physiology Education*, vol. 277, no. 6, p. S234, 1999.

[173] C. Antzelevitch, "Modulation of transmural repolarization," *Annals of the New York Academy of Sciences*, vol. 1047, no. 1, pp. 314–323, 2005.

[174] E. Cosson, F. Paycha, J. Paries, et al., "Detecting silent coronary stenoses and stratifying cardiac risk in patients with diabetes: ECG stress test or exercise myocardial scintigraphy?" *Diabetic Medicine*, vol. 21, no. 4, pp. 342–348, 2004.

[175] A. Rozanski, C. Bairey, D. Krantz, et al., "Mental stress and the induction of silent myocardial ischemia in patients with coronary artery disease," *New England Journal of Medicine*, vol. 318, no. 16, pp. 1005–1012, 1988.

[176] W. Jiang, M. Babyak, D. Krantz, et al., "Mental stress - induced myocardial ischemia and cardiac events," *Jama*, vol. 275, no. 21, pp. 1651–1656, 1996.

[177] A. Cabasson, O. Meste, G. Blain, et al., "Quantifying the PR interval pattern during dynamic exercise and recovery," *IEEE Transactions on Biomedical Engineering*, vol. 56, no. 11, pp. 2675–2683, 2009.

[178] E. M. Antman, D. T. Anbe, P. W. Armstrong, et al., "ACC/AHA guidelines for the management of patients with ST-elevation myocardial infarction - executive summary," *Circulation*, vol. 110, no. 5, pp. 588–636, 2004.

[179] C. Ritter, G. Lenis, W. H. W. Schulze, et al., "Offset removal methods for the body surface potential map to improve the ecg imaging of ventricular ectopic beats," in *Proceedings Biosignalverarbeitung und Magnetische Methoden in der Medizin 2016*, 2016, pp. 1–4.

[180] F. M. Weber, *Personalizing simulations of the human atria: Intracardiac measurements, tissue conductivities, and cellular electrophysiology*. Karlsruhe: KIT Scientific Publishing, 2011.

[181] G. Lenis, A. Kramlich, T. Oesterlein, et al., "Development and benchmarking of activity detection algorithms for intracardiac electrograms measured during atrial flutter," in *Proceedings Biosignalverarbeitung und Magnetische Methoden in der Medizin 2016*, 2016, pp. 5–8.

[182] O. Dössel, G. Lenis, A. Loewe, et al., "Model assisted biosignal analysis of atrial electrograms," *Technisches Messen*, vol. 83, no. 2, pp. 102–111, 2016.

[183] T. G. Oesterlein, G. Lenis, D.-T. Rudolph, et al., "Removing ventricular far-field signals in intracardiac electrograms during stable atrial tachycardia using the periodic component analysis," *Journal of Electrocardiology*, vol. 48, no. 2, pp. 171–180, 2015.

[184] G. Lenis, T. Oesterlein, and O. Dössel, "Orthogonal component analysis to remove ventricular far field in non periodic sustained atrial flutter," in *Computing in Cardiology 2015*, vol. 42, 2015, pp. 669–672.

[185] J. Ramirez, V. Monasterio, A. Minchole, et al., "Automatic SVM classification of sudden cardiac death and pump failure death from autonomic and repolarization ECG markers," *Journal of Electrocardiology*, vol. 48, no. 4, pp. 551–557, 2015.

[186] N. Pilia, C. Ritter, O. Dössel, et al., "Determination of the excitation origin in the ventricles with the ecg using support vector regression," in *Current Directions in Biomedical Engineering*, 2017, ahead of print.

[187] C. Ritter, "ECG offset pattern removal and support vector regression for the ECG inverse problem," Master's thesis, Karlsruhe Institut of Technology (KIT), Karlsruhe, 2016.

[188] N. Pilia, O. Dössel, A. Loewe, et al., "Characterization and reconstruction of ionic concentrations analyzing the surface ecg," in *Computing in Cardiology 2017*, 2017, ahead of print.

List of Publications and Supervised Theses

Journal Articles

- **Gustavo Lenis**, Tobias Baas, Olaf Dössel, *Ectopic beats and their influence on the morphology of subsequent waves in the electrocardiogram*, Biomedical Engineering / Biomedizinische Technik, 2013;58(2):109–119
- **Gustavo Lenis**, Nicolas Pilia, Tobias Oesterlein, Armin Luik, Claus Schmitt, Olaf Dössel, *P wave detection and delineation in the ECG based on the phase free stationary wavelet transform and using intracardiac atrial electrograms as reference*, Biomedical Engineering / Biomedizinische Technik, 2016;61(1):37–56
- **Gustavo Lenis**, Michael Kircher, Jesús Lázaro, Raquel Bailón, Eduardo Gil, Olaf Dössel, *Separating the effect of respiration on the heart rate variability using Granger's causality and linear filtering*, Biomedical Signal Processing and Control, 2017;31:272–287
- **Gustavo Lenis**, Tobias Heine, Patrick Reichensperger, Tobias Beran, Olaf Dössel, Barbara Deml, *Electrocardiographic features for the measurement of drivers' mental workload*, Applied Ergonomics, 2017;61:31–43
- **Gustavo Lenis**, Nicolas Pilia, Axel Loewe, Walther Hermann Wolfgang Schulze, Olaf Dössel, *Comparison of baseline wander removal techniques considering the preservation of ST changes in the ischemic ECG: A simulation study*, Computational and Mathematical Methods in Medicine, 2017;2017
- **Gustavo Lenis**, Christian Ritter, Nicolas Pilia, Danila Potyagaylo, Walther Hermann Wolgang Schulze, Olaf Dössel, *Removing the direct current offset from the electrocardiogram to improve electrocardiographic imaging*, Medical & Biological Engineering & Computing, in preparation
- Matthias Walter Keller, Steffen Schuler, Matthias Wilhelms, **Gustavo Lenis**, Gunnar Seemann, Claus Schmitt, Olaf Dössel, Armin Luik, *Characterization of radiofrequency ablation lesion development based on simulated and measured intracardiac electrograms*, IEEE Transactions on Biomedical Engineering, 2014;61(9):2467–2478
- Tobias Georg Oesterlein, **Gustavo Lenis**, Dan-Timon Rudolph, Armin Luik, Bhawna Verma, Claus Schmitt, Olaf Dössel, *Removing ventricular far-field signals in intracardiac*

electrograms during stable atrial tachycardia using the periodic component analysis, Journal of Electrocardiology, 2015;48(2):171–180

- Julia Ramírez, Violeta Monasterio, Ana Mincholé, Mariano Llamedo, **Gustavo Lenis**, Iwona Cygankiewicz, Antonio Bayés de Luna, Marek Malik, Juan Pablo Martínez, Pablo Laguna, Esther Pueyo, *Automatic SVM classification of sudden cardiac death and pump failure death from autonomic and repolarization ECG markers*, Journal of Electrocardiology, 2015;48(4):551–557
- Olaf Dössel, **Gustavo Lenis**, Axel Loewe, Markus Rottmann, Gunnar Seemann, Tobias Oesterlein, *Model assisted biosignal analysis of atrial electrograms*, Technisches Messen, 2016;83(2):102–111
- Tobias Oesterlein, Rashed Karim, **Gustavo Lenis**, Kawal Rhode, Claus Schmitt, Olaf Dössel, Armin Luik, *Dynamic visualization of the cardiac excitation pattern using 2D unfold of the arial shell*, Journal of Electrocardiology, in preparation

Refereed Conference Articles

- **Gustavo Lenis**, Tobias Baas, Olaf Dössel, *Automatic detection and classification of ectopic beats in the ECG using a support vector machine*, Biomedical Engineering / Biomezinische Technik 2011;56(S1)
- **Gustavo Lenis**, Tobias Baas, Olaf Dössel, *Artefaktdetektion im Elektrokardiogramm, um eine robustere Extrasystolenerkennung und Klassifizierung zu ermöglichen*, Proceedings Biosignalverarbeitung und Magnetische Methoden in der Medizin 2012
- **Gustavo Lenis**, Tobias Baas, Olaf Dössel, *T wave morphology during heart hate turbulence in patients with chronic heart failure*, Biomedical Engineering / Biomezinische Technik 2013;58(S1)
- **Gustavo Lenis**, Heinz-Georg Jahnke, Olaf Dössel, *An algorithm to analyze extracellular field potentials measured from cardiac myocytes*, Proceedings Biosignalverarbeitung und Magnetische Methoden in der Medizin 2014
- **Gustavo Lenis**, Yannick Lutz, Gunnar Seeman, Arcadi García-Alberola, José Luis Rojo-Álvarez, Óscar Barquero-Pérez, Eduardo Gil, Olaf Dössel, *Post extrasystolic T wave change in subjects with structural healthy ventricles – Measurement and simulation*, Computing in Cardiology 2014;41:1069–1072
- **Gustavo Lenis**, Tobias Oesterlein, Dan-Timon Rudolph, Olaf Dössel, *Orthogonal component analysis to remove ventricular far field in non periodic sustained atrial flutter*, Computing in Cardiology 2015;42:669–672
- **Gustavo Lenis**, Felix Conz, Olaf Dössel, *Combining different ECG derived respiration tracking methods to create an optimal reconstruction of the breathing pattern*, Current Directions in Biomedical Engineering 2015;1(1):54–57
- **Gustavo Lenis**, Alexander Kramlich, Tobias Oesterlein, Olaf Dössel, *Development and benchmarking of activity detection algorithms for intracardiac electrograms measured*

during atrial flutter, Proceedings Biosignalverarbeitung und Magnetische Methoden in der Medizin 2016:5–8

- **Gustavo Lenis**, Robert Menges, Julia Ramírez, Iwona Cygankiewicz, Antoni Bayés de Luna, Juan Pablo Martínez, Pablo Laguna, Olaf Dössel, *Postextrasystolic T wave change to stratify risk of pump failure death in patients with chronic heart failure*, Computing in Cardiology 2016;43:33–36
- **Gustavo Lenis**, Patrick Reichensperger, David Sommer, Christian Heinze, Martin Golz, Olaf Dössel, *Detection of microsleep events in a car driving simulation study using electrocardiographic features*, Current Directions in Biomedical Engineering 2016;2(1):283–287
- Eike Moritz Wülfers, Natalia S. Torres, **Gustavo Lenis**, Hui Li, Gunnar Seemann, Olaf Dössel, John H. B. Bridge, Frank Bernd Sachse, *An automated approach to analyze microstructural remodeling from confocal microscopies of ventricular myocytes from diseased hearts*, Biomedical Engineering / Biomedizinische Technik 2012;57(S1 TB):46–49
- Martin Pfeifer, **Gustavo Lenis**, Olaf Dössel, *A general approach for dynamic modeling of physiological time series*, Biomedical Engineering / Biomezinische Technik 2013;58(S1)
- Nicolas Pilia, **Gustavo Lenis**, Olaf Dössel, *Developing a robust method to delineate the P wave using information from intracardiac electrograms*, Proceedings Biosignalverarbeitung und Magnetische Methoden in der Medizin 2014
- Tobias Georg Oesterlein, **Gustavo Lenis**, Armin Luik, Bhawna Verma, Claus Schmitt, Olaf Dössel, *Removing ventricular far field artifacts in intracardiac electrograms during stable atrial flutter using the periodic component analysis – Proof of concept study*, Proceedings of 41th International Congress on Electrocardiology 2014:171–180
- Robert Menges, **Gustavo Lenis**, Olaf Dössel, *Choosing the best rhythmical and morphological features for a QRS complex classification algorithm*, Biomedical Engineering / Biomezinische Technik 2014;59:S185–S188
- Nicolas Alessandro Pilia, **Gustavo Lenis**, Axel Loewe, Walther Hermann Wolfgang Schulze, Olaf Dössel, *The impact of baseline wander removal techniques on the ST segment in simulated ischemic 12-lead ECGs*, Current Directions in Biomedical Engineering 2015;1(1):96–99
- Michael Kircher, **Gustavo Lenis**, Olaf Dössel, *Separating the effect of respiration from the heart rate variability for cases of constant harmonic breathing*, Current Directions in Biomedical Engineering 2015;1(1):46–49
- Christian Ritter, **Gustavo Lenis**, Walther Hermann Wolfgang Schulze, Danila Potyagaylo, Olaf Dössel, *Offset removal methods for the body surface potential map to improve the ECG imaging of ventricular ectopic beats*, Proceedings Biosignalverarbeitung und Magnetische Methoden in der Medizin 2016:1–4
- Joachim Greiner, Tobias Oesterlein, **Gustavo Lenis**, Olaf Dössel, *Virtual-reality based visualization of cardiac arrhythmias on mobile devices*, Computing in Cardiology 2016; 43:1081–1084

- Joachim Greiner, Stefan Pollnow, Steffen Schuler, **Gustavo Lenis**, Gunnar Seemann, Olaf Dössel, *Simulation of intracardiac electrograms around acute ablation lesions*, Current Directions in Biomedical Engineering 2016;2(1):607–610
- Tobias Oesterlein, Alexander Kramlich, **Gustavo Lenis**, Armin Luik, Claus Schmitt, Olaf Dössel, *Automatic detection and mapping of double potentials in intracardiac electrograms*, Current Directions in Biomedical Engineering 2016;2(1):179–183
- Axel Loewe, Sebastian Debatin, **Gustavo Lenis**, Olaf Dössel, *Optimal ECG lead systems to maximize left atrial information*, Current Directions in Biomedical Engineering 2017; ahead of print
- Axel Loewe, Sebastian Debatin, **Gustavo Lenis**, Olaf Dössel, *Maximization of left atrial information through the optimization of ECG lead systems*, Current Directions in Biomedical Engineering 2017; ahead of print
- Michael Kircher, Robert Menges, **Gustavo Lenis**, Olaf Dössel, *Respiratory influence on HRV parameters analyzed during controlled respiration, spontaneous respiration and apnoe*, Current Directions in Biomedical Engineering 2017; ahead of print
- Nicolas Pilia, Axel Loewe, Olaf Dössel, **Gustavo Lenis**, *Characterization and reconstruction of ionic concentrations analyzing the surface ECG*, Computing in Cardiology 2017; ahead of print
- Carl-Jiri Gross, Stefan Pollnow, Olaf Dössel, **Gustavo Lenis**, *Automatic feature extraction algorithms for the assessment of in-vitro electrical recordings of rat myocardium*, Current Directions in Biomedical Engineering 2017; ahead of print
- Tobias Georg Oesterlein, Axel Loewe, **Gustavo Lenis**, Olaf Dössel, *Statistical assessment of cardiac excitation by morphology-based clustering of local activation waves*, Current Directions in Biomedical Engineering 2017; ahead of print
- Nicolas Pilia, Christian Ritter, Danila Potyagaylo, Walther H. W. Schulze, Olaf Dössel, **Gustavo Lenis**, *Determination of the excitation origin in the ventricles with the ECG using support vector regression*, Current Directions in Biomedical Engineering 2017; ahead of print

Refereed Conference Abstracts

- **Gustavo Lenis**, Tobias Baas, Olaf Dössel, *Rhythmical and morphological features of the ECG following a premature ventricular contraction*, Biomedical Engineering / Biomedizinische Technik, 2012;57(S1):11
- Tobias Georg Oesterlein, **Gustavo Lenis**, Armin Luik, Claus Schmitt, Olaf Dössel, *Periodic component analysis to eliminate ventricular far field artifacts in unipolar atrial electrograms of patients suffering from atrial flutter*, Biomedical Engineering / Biomezinische Technik 2014;59:S162–S165
- Tobias Georg Oesterlein, **Gustavo Lenis**, Armin Luik, Claus Schmitt, Olaf Dössel, *Optimized approach for the detection of active segments in intracardiac electrograms measured*

during atrial flutter, Proceedings of 42th International Congress on Electrocardiology 2015

- A. A. Ahmad, J. Johnson, **Gustavo Lenis**, C. Hunter, Frank Bernd Sachse, *Deconvolution of multispectral confocal microscopic images using measured point spread functions*, Annual Meeting - Biomedical Engineering Society 2016:186

Invited Talks

- Computergestützte Diagnose und Behandlung von Herzerkrankungen, Karlsruhe Instute of Technology (KIT), Karlsruhe, Germany, 28 Oktober 2016

Reports and Theses

- Gustavo Lenis, *Automatic detection and classification of ectopic beats in the ECG using a support-vector-machine*, Student Research Project, Institute of Biomedical Engineering (IBT), Karlsruhe Institute of Technology (KIT), 2010
- Gustavo Lenis, *Analyzing rhythmical and morphological ECG properties to detect the influence of ectopic beats*, Diploma Thesis, Institute of Biomedical Engineering (IBT), Karlsruhe Institute of Technology (KIT), 2012

Supervised Student Theses

- Nicolas Pilia, *Developing a robust method to detect and characterize the P wave in the electrocardiogram*, Bachelor Thesis, Institute of Biomedical Engineering (IBT), Karlsruhe Institute of Technology (KIT), 2013
- Robert Menges, *Optimizing morphological and rhythmical features for a QRS complex classification system*, Bachelor Thesis, Institute of Biomedical Engineering (IBT), Karlsruhe Institute of Technology (KIT), 2013
- Ina Morath, *Comparing the standard parameters of heart rate variability and deceleration capacity with the ARMA modeled time series of RR intervals obtained from the electrocardiogram*, Bachelor Thesis, Institute of Biomedical Engineering (IBT), Karlsruhe Institute of Technology (KIT), 2014
- Patrick Reichensperger, *Developing a robust method to detect and characterize the effect of micro-sleep episodes on the electrocardiogram*, Master Thesis, Institute of Biomedical Engineering (IBT), Karlsruhe Institute of Technology (KIT), 2014

- Felix Conz, *Developing robust methods for the electrocardiogram derived respiration and for the detection and quantification of T wave alternans*, Master Thesis, Institute of Biomedical Engineering (IBT), Karlsruhe Institute of Technology (KIT), 2014
- Dan-Timon Rudolph, *Advanced signal processing algorithms to remove ventricular far field artifacts from periodic intracardiac electrograms*, Master Thesis, Institute of Biomedical Engineering (IBT), Karlsruhe Institute of Technology (KIT), 2014
- Michael Kircher, *Removing the effect of respiration on the heart rate variability and quantifying the medical impact of the new uncoupled parameters when estimating risk of cardiac death*, Master Thesis, Institute of Biomedical Engineering (IBT), Karlsruhe Institute of Technology (KIT), 2015
- Alexander Kramlich, *Development and benchmarking of algorithms for the characterization of intracardiac electrograms measured during atrial flutter*, Master Thesis, Institute of Biomedical Engineering (IBT), Karlsruhe Institute of Technology (KIT), 2016
- Christian Ritter, *ECG offset pattern removal and support vector regression for the ECG inverse problem*, Master Thesis, Institute of Biomedical Engineering (IBT), Karlsruhe Institute of Technology (KIT), 2016
- Nicolas Pilia, *Characterization and reconstruction of ionic concentrations in the human ventricles analyzing the action potential and the surface ECG*, Master Thesis, Institute of Biomedical Engineering (IBT), Karlsruhe Institute of Technology (KIT), 2016
- Gerald Schwaderlapp, *Definition, estimation, validation and clinical value of the dominant frequency of intracardiac atrial electograms*, Bachelor Thesis, Institute of Biomedical Engineering (IBT), Karlsruhe Institute of Technology (KIT), 2017
- Carl-Jiri Gross, *Auswertung uni- und bipolarer Elektrogramme von ex-vivo Präparaten*, Bachelor Thesis, Institute of Biomedical Engineering (IBT), Karlsruhe Institute of Technology (KIT), 2017

Supervised Student Research Projects

- Eulàlia Mascareñas, *ECG Signal Processing for inverse electrocardiographic imaging of ventricular extrasystoles*, Student Research Project, Institute of Biomedical Engineering (IBT), Karlsruhe Institute of Technology (KIT), 2013
- Martin Pfeifer, *Analysing physiologic time series with ARMA models*, Student Research Project, Institute of Biomedical Engineering (IBT), Karlsruhe Institute of Technology (KIT), 2013
- Nicolas Pilia, *Delineation of the P wave in the ECG validated with intracardiac signals*, Student Research Project, Institute of Biomedical Engineering (IBT), Karlsruhe Institute of Technology (KIT), 2014
- Yannick Lutz, *Full torso mondomain simulation of the human cardiac electrophysiology during an event of heart rate turbulance*, Student Research Project, Institute of Biomedical Engineering (IBT), Karlsruhe Institute of Technology (KIT), 2014

- Robert Menges, *Detailed investigation of feature dependencies in order to improve a QRS complex classification system*, Student Research Project, Institute of Biomedical Engineering (IBT), Karlsruhe Institute of Technology (KIT), 2014
- Christian Ritter, *Removing the offset of the body surface potential map to improve the reconstruction of ventricular ectopic beats for ECG imaging*, Student Research Project, Institute of Biomedical Engineering (IBT), Karlsruhe Institute of Technology (KIT), 2016
- Nicolas Pilia, *Evaluation of the influence of highpass filters on ST-segments in the ECG*, Student Research Project, Institute of Biomedical Engineering (IBT), Karlsruhe Institute of Technology (KIT), 2016
- Robert Menges, *Quantifying PEST in Holter ECGs and evaluating its usage to stratify risk of cardiac death in patients with chronic heart failure*, Student Research Project, Institute of Biomedical Engineering (IBT), Karlsruhe Institute of Technology (KIT), 2016
- Gerald Schwaderlapp, *Signalanalyse fluoreszenz-optischer Messdaten*, Student Research Project, Institute of Biomedical Engineering (IBT), Karlsruhe Institute of Technology (KIT), 2017

Awards & Grants

- International research visit grant of the Karlsruhe House of Young Scientist, 2012
- 3rd place in the student presentation competition, Workshop Innovative Verarbeitung Bioelektrischer und Biomagnetischer Signale, 2014, Nicolas Pilia, **Gustavo Lenis**, Olaf Dössel, *Developing a new method to delineate the P wave using information from intracardiac electrograms*
- Young Investigator Award, 41st International Congress on Electrocardiology, 2014, Tobias Georg Oesterlein, **Gustavo Lenis**, Armin Luik, Bhawna Verma, Claus Schmitt, Olaf Dössel, *Removing ventricular far field artifacts in intracardiac electrograms during stable atrial flutter using the Periodic Component Analysis – Proof of Concept Study*
- 3rd place in student competition, 48th DGBMT Annual Conference, 2014, Tobias Georg Oesterlein, **Gustavo Lenis**, Armin Luik, Claus Schmitt, Olaf. Dössel, *Periodic component analysis to eliminate ventricular far field artifacts in unipolar atrial electrograms of patients suffering from atrial flutter*
- Studies Award in recognition to the scientific achievements and contribution to the Coburger Convent, Coburger Convent, 2014
- International research stay grant, Karlsruhe House of Young Scientist, 2014
- Bill and Gary Sanders Poster Award, Computing in Cardiology, 2014, **Gustavo Lenis**, Yannick Lutz, Gunnar Seeman, Arcadi García-Alberola, José Luis Rojo-Álvarez, Óscar Barquero-Pérez, Eduardo Gil, Olaf Dössel, *Post extrasystolic T wave change in subjects with structural healthy ventricles -âĂŞ measurement and simulation*

- Faculty teaching award for excellent teaching and the creation of the video exercises for the mandatory undergraduate class Lineare Elektrische Netze, Faculty of Electrical Engineering and Information Technologies, Karlsruhe Institute of Technology, 2016
- 2nd place in the young investigator competition, Workshop Innovative Verarbeitung Bioelektrischer und Biomagnetischer Signale, 2016, **Gustavo Lenis**, Alexander Kramlich, Tobias Oesterlein, Olaf Dössel, *Development and benchmarking of activity detection algorithms for intracardiac electrograms measured during atrial flutter*
- Mortara Fellowship, Computing in Cardiology, 2016
- Bill and Gary Sanders Poster Award, Computing in Cardiology, 2016, Joachim Greiner, Tobias Oesterlein, **Gustavo Lenis**, Olaf Dössel, *Virtual reality visualization of arrhythmias on a smartphone*
- 2nd place in student competition, 50th DGBMT Annual Conference, 2016, Joachim Greiner, Stefan Pollnow, Steffen Schuler, **Gustavo Lenis**, Gunnar Seemann, Olaf Dössel *Simulation of intracardiac electrograms around acute ablation lesions*